Journal of Plasma and Fusion Research SERIES, Volume 10

Proceedings of the 4th Japan-China Workshop on Fusion-Related Tritium Science and Technology May 9–11, 2012, Toyama, Japan

Yukino Otani in Tateyama Kurobe Alpine Route

Tulip in Tonami

The Japan Society of Plasma Science and Nuclear Fusion Research

Contents

Preface

It is our great pleasure that the publication of the contributed papers to the 4th Japan-China Workshop (JCW) on Fusion-Related Tritium Science and Technology held in Toyama, Japan, during May 9-11, 2012, has been completed here as the Journal of Plasma and Fusion Research Series published by the Japan Society of Plasma Science and Nuclear Fusion Research.

This meeting is the 4th tritium workshop, formerly held at Mianyang in 2006, 2nd at Sendai in 2008, and 3rd at Kunming in 2010. The Workshop on fusion-related tritium science and technology provides the opportunity for discussion about tritium science and technology including tritium handling, tritium confinement, tritium breeding for establishment of a thermonuclear fusion reactor and environment effects, and other related areas for fission as well as fusion.

The present workshop was focused on the following four topics: (1) Fusion-related tritium science and technology, (2) Breeding blanket technology, (3) Environment effects, and (4) Other related tritium science and technology. The total number of the participants was 53 (30 from Japan, 19 from China, 2 from US and 2 form Korea), and 35 invited and contributed papers were presented. Among these papers, 19 excellent papers are finally published in this proceeding after reviewing by the publication committee.

I would be grateful to all the members of the Japanese and Chinese Organizing Committee and Local Committee. Finally, I would express my sincere appreciation to the members of the Local Organizing Committee and the voluntarily supporting staff of the Hydrogen Isotope Research Center (HRC) of University of Toyama, who have let to the success of this workshop.

Organizing Committee
for the 4th JCW, Chair
Kenji Okuno

Guest Editorial Board

Improvement of Hydrogen Isotope Release on Lithium Orthosilicate Ceramic Pebble by Catalytic Metals

Chengjian XIAO [a], Chunmei KANG [b], Xingbi REN [a], Xiaoling GAO [a], Xiaojun CHEN [a], Heyi WANG [a], Xiaolin WANG [c, *]

[a]*Institute of Nuclear Physics and Chemistry, CAEP, Box 919-214, Mianyang, Sichuan 621900, P. R. China*

[b]*Science and Technology Information Center, CAEP, Box 919-803, Mianyang, Sichuan 621900, P. R. China*

[c]*China Academy of Engineering Physics, Box 919-214, Mianyang, Sichuan 621900, P. R. China*

(Received: 9 May 2012 / Accepted: 26 October 2012)

Lithium Orthosilicate (Li_4SiO_4) ceramic pebble is considered as a candidate tritium breeding material of Chinese helium cooled solid breeder test blanket module（CH HCSB TBM）for the International Thermonuclear Experimental Reactor (ITER). In this paper, Li_4SiO_4 ceramic pebbles deposited with catalytic metals, including Pt, Pd, Ru and Ir, were prepared by wet impregnation method. The metal particles on Li_4SiO_4 pebble exhibit a good promotion of hydrogen isotope exchange reactions in H_2-D_2O gas system, with conversion equilibrium temperature reduction of 200−300 °C. The out-of-pile tritium release experiments were performed using 1.0 wt% Pt/Li_4SiO_4 and Li_4SiO_4 pebbles irradiated in a thermal neutron reactor. The results showed that Pt was effective to increase the tritium release rate at lower temperatures, and the ratio of tritium molecule (HT) to tritiated water (HTO) of 1.0 wt% Pt/Li_4SiO_4 was much more than that of Li_4SiO_4, which released mainly with HTO. Thus, catalytic metals deposited on Li_4SiO_4 pebble may help to accelerate the recovery of bred tritium particularly in low temperature region, and increase the tritium molecule form released from the tritium breeding materials.

Keywords: Lithium Orthosilicate (Li_4SiO_4); Hydrogen Isotope Exchange Reaction; Catalytic Metal; Tritium

1. Introduction

Lithium-containing ceramics，such as Li_2O, $LiAlO_2$, Li_2ZrO_3, Li_2TiO_3 and Li_4SiO_4, are considered as tritium breeding materials for securing an adequate tritium supply to sustain the D-T fusion reaction in a fusion reactor [1-4]. Tritium is produced via $^6Li(n,\alpha)T$ in the lithium ceramic pebbles, and extracted by a helium sweep gas with a fraction of hydrogen or deuterium from the surface of the pebbles. Considering the reduction for the residence time of tritium in the breeder blankets, the bred tritium must be carried out with a fast recovery rate over a broad range of temperatures, so some means shall be developed to accelerate the tritium release rate.

The mass transfer mechanism of tritium released from lithium-containing ceramics is complicated, but it is developed and assumed commonly that tritium is bred in grain interior, diffuses to the surface layer, and then transfer to the surface water layer which consists of physical, chemical and structural adsorbed water. Finally, tritium at the surface water discharges to the purge gas through such surface reactions as desorption, isotope exchange reactions between hydrogen and water vapor in purge gas [5]. However, the isotope exchange reactions at the interface between solid surface and sweep gas are very slow at low temperature, only fast at relatively elevated temperatures (>700 °C) [6, 7]. When isotope exchange reactions contribute strongly to tritium release rate, it is difficult to reflect tritium diffusion in the bulk of grain. Then, platinum and palladium were tried to deposit on lithium-containing ceramics, and exhibited a promotion of hydrogen isotope exchange reactions at low temperatures [6-9]. Considering the practical application of neutron activity materials in a fusion reactor, many problems need systematic study, such as comparison of different metals, the optimization of catalytic metal content and catalyst poisoning.

Now, Li_4SiO_4 ceramic pebble is considered as a candidate tritium breeder of Chinese helium cooled solid breeder test blanket module for the international thermonuclear experimental reactor（ITER）[4]. In order to investigate the energetic tritium moving mechanism in the crystal grain of Li_4SiO_4 ceramic pebble, study the isotope exchange reactions on the gas/solid interface of the pebble, and search some way to enhance the tritium release at low temperaure, it is necessary to investigate the behavior of hydrogen isotope exchange influenced by catalytic active metal. In this work, Li_4SiO_4 ceramic pebbles deposited with four kinds of catalytic metals, Pt, Pd, Ru and Ir, were prepared. The effects of different Pt content and different metal role on the hydrogen isotope exchange reactions were examined in H_2/D_2O gas system. The tritium release behavior of the neutron-irradiated 1.0 wt% Pt/Li_4SiO_4 and Li_4SiO_4 was compared through the out-of-pile tritium release experiments.

author's e-mail: xiaocj@hotmail.com

2. Experimental

2.1 Preparation of Sample

Li_4SiO_4 ceramic pebbles were fabricated by freeze-sintering process[10]. The preparation process included mixing Li_4SiO_4 powder, polyvinylalcohol solution and antifoam agent, dropping the prepared mixture into liquid nitrogen through a nozzle to generate spheres, freeze-drying the spheres in a freeze dry system, and calcinating the spheres programedly to get ceramic pebbles.

Li_4SiO_4 ceramic pebbles (av. 0.9 mm in diameter) were selected to be deposited with noble metals by wet impregnation method. The pebbles were dried in a vacuum drier at 150°C for 3h. Then the metal-containing solution, H_2PtCl_6, H_2IrCl_6, $PdCl_2$ and $RuCl_3$, was dripped on the pebbles respectively, and was adsorbed swiftly by the pebbles. When the pebbles were saturated with the solution, they were dried for 1-2 h by infrared ray. After repeating the above steps until the pebbles had adsorbed a predetermined content, they were transferred to deoxidize in a 5 vol% H_2/N_2 mixture gas at 400-450 °C for 3h. Finally Li_4SiO_4 ceramic pebbles with catalyst were obtained.

2.2 Physical Characterization

Powder X-ray diffraction (XRD) patterns of 1.0 wt% Pt/Li_4SiO_4 were determined on a DX-2600SSC diffractometer (Cu Kα radiation at 40 kV and 30 mA) at a scanning speed of $1.2^o\,min^{-1}$ from 15 ° to 95 °. Pt particle size was analyzed by Philips- CM30 transmission electron microscope at an acceleration voltage of 200 kV. Pt particles more than 100 were chosen randomly to test the metal particle size by Photoshop CS2 software.

Table1 Experimental conditions

Group	Sample mass (g)	Flow rate of D_2/He	Flow rate of H_2/ He
Li_4SiO_4; 1.0 wt% Pt/Li_4SiO_4	0.2	100	100
0.1~1.0 wt% Pt/Li_4SiO_4	0.35	50	50
0.1 wt% M/Li_4SiO_4 (M = Pt, Pd, Ru and Ir)	0.35	50	50

2.3 Hydrogen Isotope Exchange Reactions

The samples were dried at 150 °C for 2h in a vacuum drier, and then installed in a settled reactor (ϕ = 8 mm) made of stainless steel. A mixture gas of 1.08 % H_2/He and 1.12 vol% D_2O/He was introduced into the reactor. The concentration of D_2O was controlled by D_2/He gas passing through a CuO bed of 350 °C. The deuterium concentration of HD in the outlet stream was measured by gas chromatogram (Agilent 6890N). 601 column was used as the column material. The HD peak could be obtained depending on the thermal conductivity coefficient when hydrogen was used as a carrier gas. All the experiments were conducted under steady state conditions at ambient atmosphere pressure. The experimental conditions and the expeimental flow chart for hydrogen isotope exchange reactions are shown in Table1 and Fig.1 respectively.

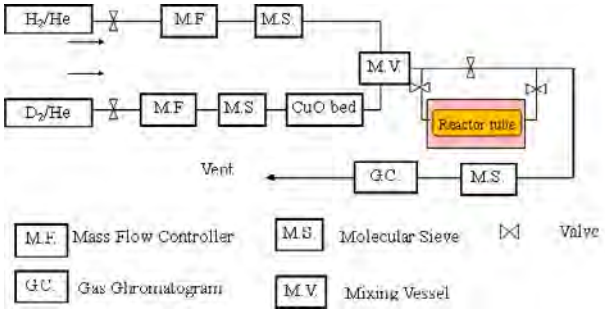

Fig.1 Experimental flow chart for hydrogen isotope exchange reactions

2.4 Tritium Thermal Desorption

Li_4SiO_4 and 1.0 wt% Pt/Li_4SiO_4 ceramic pebbles, which had been dried at 150 °C for 2 h in vacuum, were sealed in quartz capsules with He gas less than 10 Pa. Then the encapsulated samples were irradiated in a reactor with a neutron flux of 7.1×10^{12} $cm^{-2}s^{-1}$ for 100min at ambient temperature (29-36 °C). Tritium was produced by thermal neutron capture of lithium via the reaction of $^6Li(n, \alpha)T$. After irradiation, the samples were placed at room temperature for two years. The quartz capsules were broken in a glove bag filled with He gas. Some pebbles about 0.01-0.02 g were transferred into a reactor tube made of quartz for tritium thermal desorption, and the others were removed into a small test tube which was stored in a desiccator for stand-by.

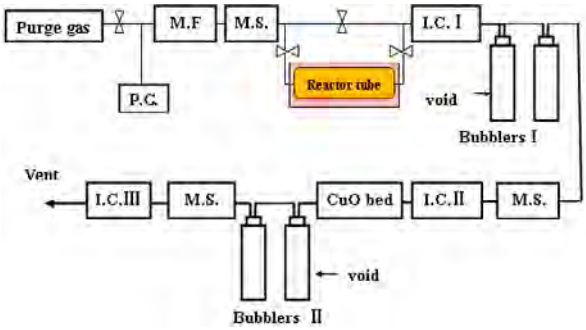

Fig.2 Experimental flow chart for tritium release

Tritium release experiments were performed by applying the out-of-pile temperature programmed desorption technique. The flow chart of the experimental system is shown in Fig.2.The reactor tube was heated in a tube furnace at a heating rate of 5 °C min^{-1} from room temperature to 800 °C, while a purge gas of He containing 1vol% H_2 carried the released tritium (HT and HTO) through the experimental system at a flow rate of 50 ml

min^{-1}. The first ionization chamber measured total tritium released from the ceramic pebbles, the second ionization chamber measured tritium released as HT. The amount of tritium in the bubblers, which were used to adsorb HTO (T_2O) with glycol solution as adsorbent, was measured by liquid scintillation counting. Details of the experiments were cited in the previous literature[11,12].

3.Results and Discussions

3.1 Preparation of Sample

As the data shown in Table 2, Li_4SiO_4 ceramic pebble fabricated by freeze-sintering process has good sphericity, high density and material phase purity .

Table 2 Characteristics of Li_4SiO_4 ceramic pebble

Raw materials	Density (%T.D.)	Phase purity of Li_4SiO_4 (%)	Sphericity	Diameter (mm)	Grain size (μm)
Li_2CO_3+SiO_2	80～85	>97	1.04(a.v.)	0.5～1	4.5(a.v.)

Fig.3 Appearance of 1.0 wt% Pt/Li_4SiO_4 pebble

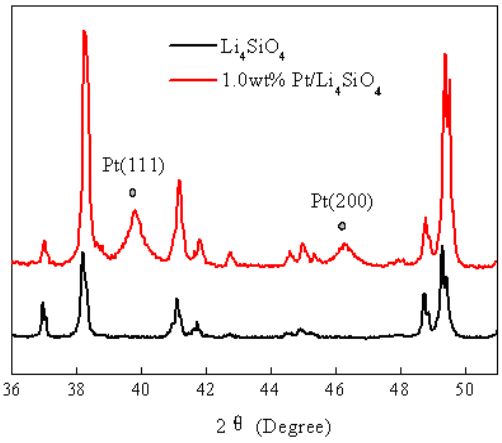

Fig.4 XRD patterns of Li_4SiO_4 and 1.0 wt% Pt/Li_4SiO_4

0.1−1.0 wt% Pt/Li_4SiO_4 and 0.1 wt% M/Li_4SiO_4 (M =Pd, Ru, Ir) ceramic pebbles were obtained by the wet impregnation method. When the catalytic metals were deposited on Li_4SiO_4, the surface color changed from white to grey（0.1 wt% Pt）, brown (0.5 wt% Pt) or black （1.0 wt% Pt） as shown in Fig.3. It is determined by X-ray diffraction that Pt particles on the pebble surface belong to face centered cubic structure with the crystalline planes of Pt (1 1 1) and Pt (2 0 0) in Fig.4. TEM analysis in Fig.5 shows that the agglomeration of Pt particles is obvious, but the maximal size of Pt particles is less than 20 nm as shown in Fig.6. The mean size of Pt particles is 6.7 nm.

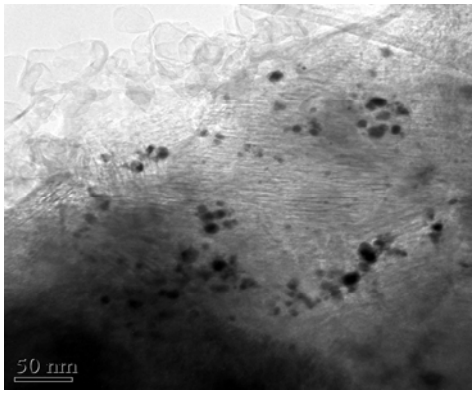

Fig.5 TEM micrograph of 1.0 wt% Pt/Li_4SiO_4 pebble

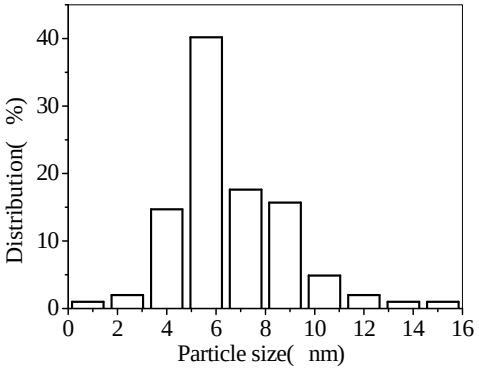

Fig.6 Distribution of Pt particles on the surface of 1.0 wt% Pt/Li_4SiO_4 pebble

3.2 Isotope Exchange Reactions on pebble

The mixture gas of H_2, D_2O and He was feeded into the reaction bed, D_2O was adsorbed on the grain surface of the sample, and then the isotope exchange reactions took place over the grain surface between the adsorbed D_2O and H_2 in the gas. The exchange reactions on the basis of the simplified model were expressed as

$$D_2O(s) + H_2(g) \Leftrightarrow HD\ (g) + HDO(s) \quad (1)$$
$$HDO(s) + H_2(g) \Leftrightarrow HD\ (g) + H_2O(s) \quad (2)$$

The deuterium concentration in the outlet stream was measured with gas chromatogram, and the

conversion of D-atoms for the isotope exchange reaction was defined as the formula (3) , where $C_{D,out}$ was the concentration of HD in the outlet stream, and $C_{D,in}$ was the concentration of D-atoms in the inlet stream.

$$R = \frac{C_{D,\ out}}{C_{D,\ in}} \qquad (3)$$

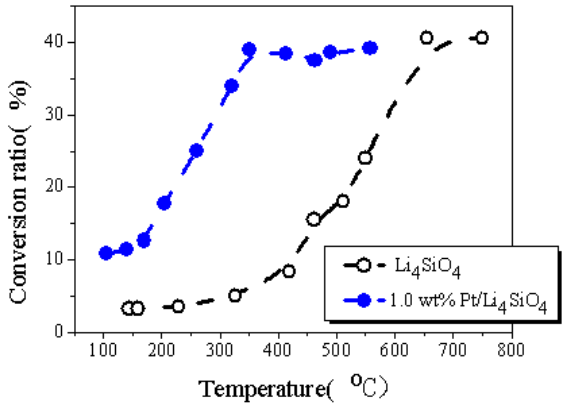

Fig.7. Conversion ratio of hydrogen isotope exchange reactions

With respect to the virgin Li_4SiO_4, the rate of the isotope exchange reaction taking place on the surface was quite slow, and the conversion ratio reached equilibrium above 650 °C. However, the conversion ratio of 1.0 wt% Pt/Li_4SiO_4 ceramic pebble increased rapidly between 200 °C and 300 °C, and reached equilibrium above 300 °C. The experimental curves in Fig.7 indicate that the conversion equilibrium temperature decreased about 300 °C if 1.0 wt% Pt was deposited on the surface.

Catalytic metal deposited on Li_4SiO_4 ceramic pebbles would provide active adsorption sites for H_2 in the gas, and had a tendency to decompose H_2(ads) into H(ads). The H(ads) atom had higher reactivity and quicker transfer capability, so the activation energy for the exchange reaction was reduced, and it's easy to occur hydrogen isotope exchange between the H(ads) atom and D_2O molecule adsorbed on the surface of ceramic pebbles [6-9]. The hydrogen isotope exchange reaction process may be expressed as follows.

$$H_2\,(g) + 2M\,(s) \Leftrightarrow 2M\text{-}H\,(s) \qquad (5)$$

$$M\text{-}H(s) + D_2O(ads) \Leftrightarrow M\text{-}H(D_2O) \Leftrightarrow M\text{-}D(HDO) \Leftrightarrow M\text{-}D(s) + HDO(ads) \qquad (6)$$

$$M\text{-}H(s) + M\text{-}D(s) \Leftrightarrow 2M(s) + HD(g) \qquad (7)$$

, where M(s) is the catalytic metal deposited on solid surface.

To investigate the catalytic effect depended on different metal content, the Li_4SiO_4 ceramic pebbles were deposited with 0.1 wt%, 0.5 wt% and 1.0 wt% content of Pt respectively. According to the experimental results shown in Fig.8, the content of Pt on the surface could influence the enhancement of the isotope exchange reactions. The conversion ratio of 0.1 wt% Pt/Li_4SiO_4 reached equilibrium after 350 °C, and that of 0.5-1.0 wt% Pt/Li_4SiO_4 reached around 300 °C. It indicates that more content of Pt on the pebble surface would provide more active adsorption localities, and the lower equilibrium temperature for the isotope exchange reaction would be obtained. However, the efficiency of noble metals of the surface should depend on the surface coverage for the samples having different specific surface area. Y. Narisato and K. Mochizuki reported that the better content range of Pd on lithium ceramic pebbles was 0.15-1.6 wt% or 0.02-0.2 wt% [5, 13].

Pd, Ru, and Ir were also deposited on Li_4SiO_4 respectively, and exhibited to enhance the isotope exchange reactions as shown in Fig.9. It is suggested that many catalytic metals could be used to promote hydrogen isotope exchange reactions on Li_4SiO_4 ceramic pebble.

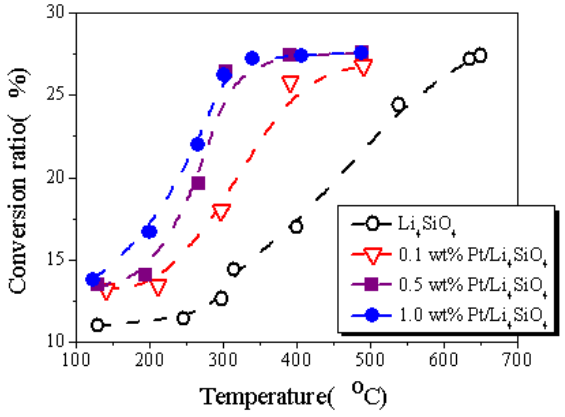

Fig.8. Conversion ratio of isotope exchange reactions on Pt/Li_4SiO_4 pebble

According to the thermodynamic functions, hydrogen isn't adsorbed on catalytic active metal surface in intact molecule, and it combines with metal atoms in single atom [13, 14]. Water vapor molecule exists in intact molecule on Pt surface, but has a tendency to be dissociated to OH(ads) and H(ads) on Ir or Ru surface. So there were different hydrogen isotope exchanging processes on the surface of M/Li_4SiO_4 pebbles. It indicates that if Pt or Pd with rational intermingles of Ru, Ir or Fe, deposited on Li_4SiO_4 pebbles together, would incease the catalytic activity. In that case, the amount of the noble metal could be reduced in the tritium breeder materials.

3.3 Tritium Thermal Desorption

Fig.10 and 11 present the tritium release behavior of neutron-irradiated Li_4SiO_4 and 1.0 wt% Pt/Li_4SiO_4 pebbles under the 1.0 vol% H_2/He purge gas flow. After

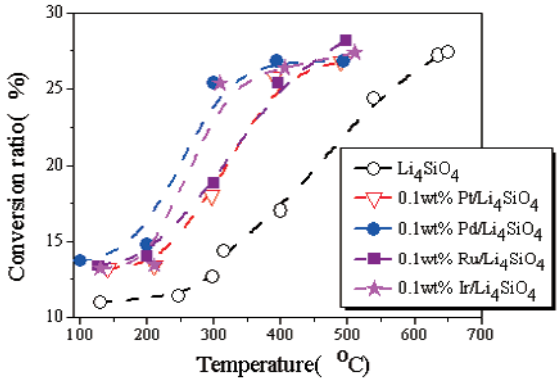

Fig.9. Conversion ratio of isotope exchange reactions on M/Li_4SiO_4 pebble

the specimens were swept by pure He gas to wipe off the tritium adsorbed physically on the pebble, the purge gas was changed to 1.0 vol% H_2/He, and then the reactor tube was heated at a rate of 5 °C /min. The blue curve represents the total tritium concentration denoted as HT&HTO released from the pebbles, and the red curve represents the molecular form of tritium denoted as HT.

Fig. 10 shows the tritium release curves of virgin Li_4SiO_4. There are two large peaks of total tritium from R.T to 800 °C. One peak, appeared at around 259 °C, and the second one, relatively larger than the former, appeared at 418 °C. It's evidently that tritiated water, denoted as HTO, is much more than HT in the annealing course, especially at low temperature less than 400 °C. As shown in Table 3, the fraction of HTO was 96.2 % of the total tritium, but HT was 3.8 %. It indicated that tritium was released mainly as the chemical form of tritiated water in the experimental conditions of this paper.

Fig.11 shows the tritium release curves of 1.0 wt% Pt/Li_4SiO_4. There are two peaks for both the total tritium and the tritium molecular form during the annealing course. With regard to the total tritium curve, the larger peak was observed at 218 °C, and the smaller peak appeared at 468 °C. It means that most of tritium was released at lower temperature less than 400 °C. The tritium release curve of HT had a similar shape as that of the total tritium. Table 3 shows that the fraction of HTO was 36.9 %, but HT was increased to 63.1%. The fraction of chemical forms was quite different from that of the virgin Li_4SiO_4. It indicates that the tritium molecular form (HT) became the main component when noble metal deposited on the surface of Li_4SiO_4.

To compare the tritium release amount of Li_4SiO_4 and 1.0 wt% Pt/Li_4SiO_4, 37.4% of the total amount of tritium was released at 350 °C for Li_4SiO_4, but 66.9% for 1.0 wt% Pt/Li_4SiO_4. The largest peak of total tritium was at 418 °C for Li_4SiO_4, but 218 °C for 1.0 wt% Pt/Li_4SiO_4. So the catalytic effect of Pt was evidently. Even at temperature less than 200 °C, the tritium concentration in the outlet stream of the reactor tube increased rapidly

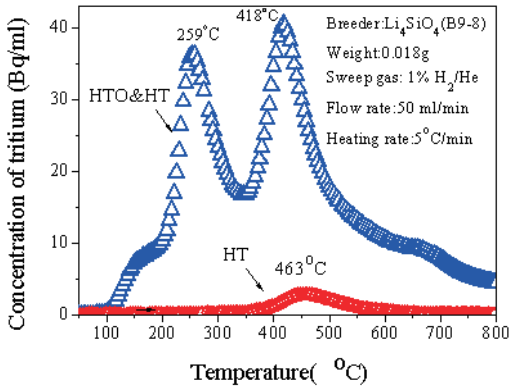

Fig.10 Tritium release of neutron-irradiated Li_4SiO_4 pebble

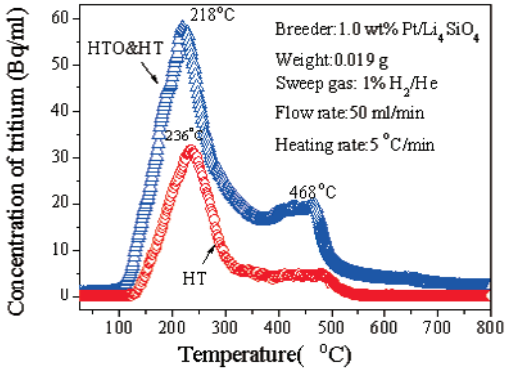

Fig.11 Tritium release of neutron-irradiated 1.0 wt% Pt/Li_4SiO_4 pebble

Table 3 Fraction of tritium released from samples

Sample	Fraction of Chemical forms in TDS process (%)		Fraction of tritium (HTO&HT) released in TDS process (%)		
	HTO	HT	25-350 °C	350-550 °C	550-800 °C
Li_4SiO_4	96.2	3.8	37.4	44.0	18.6
1.0 wt% Pt/Li_4SiO_4	36.9	63.1	66.9	25.8	7.3

from 1.0 wt% Pt/Li_4SiO_4. It means that when catalytic metal was deposited on the surface of Li_4SiO_4, the hydrogen isotope exchange reactions were enhanced between H_2 in the purge gas and tritium adsorbed on the solid surface.

With regard to the tritium chemical form, 3.8 % of the total tritium was released as HT from room temperature to 800 °C for Li_4SiO_4, and a small peak of HT appeared at 463 °C. However, the fraction of HT was 63.1 % for 1.0 wt% Pt/Li_4SiO_4 with only one large peak at 236°C. The HT curve strongly influenced the shape of the total tritium curve for 1.0 wt% Pt/Li_4SiO_4. It indicated when 1.0 wt% Pt was deposited on Li_4SiO_4, the hydrogen isotope exchange reactions, expressed as (5)-(7),were easy to proceed at the temperatures less than 460 °C.

The isotope exchange reactions on 1.0 wt%

Pt/Li_4SiO_4 proceeded much faster than that on virgin Li_4SiO_4 , and the chemical forms of the released tritium changed. It was attributed to the catalytic effect of noble metal on the solid surface. Without the effect of catalyst, the exchange reaction rates of (1) and (2) were far smaller than the desorption rate or the rate of isotope exchange reaction (8), then the conversion of tritium (HTO into HT) was quite slow.

$$H_2O(g) + HTO(s) \Leftrightarrow HTO(g) + H_2O(s) \qquad (8)$$

With the help of catalyst, it's easy to occur hydrogen isotopes exchanging between H(ads) atoms and T adsorbed on the surface of ceramic pebbles at lower temperature as the formula(6). As soon as T exchanged with H(ads) and migrated to the active adsorption locality, it would discharge quickly combined with another H(ads).

Considering the high neutron activity in practical application, the content of noble metals should be reduced on lithium ceramic pebble, and some new metal with low neutron activity need to discover.

Conclusions

Wet impregnation method has been used to fabricate Li_4SiO_4 ceramic pebbles deposited with catalytic active metals including Pt, Pd, Ru and Ir.

Lithium orthosilicate pebble deposited with noble metals exhibite a promotion of hydrogen isotope exchange reactions in H_2/D_2O gas system. With respect to virgin Li_4SiO_4, the rate of the isotope exchange reaction taking place on the surface was quite slow, and the conversion ratio reached equilibrium after 650 ^oC. However, the conversion ratio of M/Li_4SiO_4 was increased obviously from 200 ^oC and 300 ^oC. More content of the catalytic metal provided more active adsorption localities on the pebble, so the conversion ratio of 0.1 wt% M/Li_4SiO_4 reached equilibrium after 350 ^oC, and that of 0.5-1 wt% M/Li_4SiO_4 reached equilibrium after 300 ^oC.

Most tritium was released at lower temperatures from neutron-irradiated 0.1 wt% Pt/Li_4SiO_4, and the chemical form of HT was increased remarkably compared with that of Li_4SiO_4. The result indicates that catalytic metal deposited on Li_4SiO_4 ceramic pebble could reduce activation energy, facilitate H-T(D) isotope exchange reaction, and influence the tritium release mechanism. Consequently, the deposition of catalytic metal on Li_4SiO_4 is an effective way to promote the tritium release from the breeder materials, and is in favor of the design of tritium cycle system about extracting, separating and purifying in a D-T fusion reactor.

Acknowledgements

This work is financially supported by the Development Fund of China Academy of Engineering Physics (2010B0301035) and the National Magnetic Confinement Fusion Science Program (2010GB112004).

References

[1] N. Rouxa, et al, Fusion Eng. Des. 41 (1998) 31-38.
[2] C. E. Johnson, et al, J. Nucl. Mater. 258-263 (1998) 140-148.
[3] C. Xiao, et al, Progress in Chem. 23 (2011) 1906-1914.
[4] X. Chen,et al, Fusion and Plasma Phys. 26(2006) 210-216.
[5] T. Kinjyo, et al, Fusion Eng. Des. 81 (2006) 573–577
[6] Y. Narisato, et al, J. Nucl. Mater. 329-333(2004) 1370-1373.
[7] K. Munakata, et al, J. Nucl. Mater. 307-311(2002) 1451-1455
[8] K. Munakata, et al, J. Nucl. Mater. 386-388 (2009) 1091-1094.
[9] K. Munakata, et al, Fusion Eng. Des. 58-59 (2001) 683-687.
[10] X Gao, et al, Atomic Energy Sci. and Tech. 44(2010) 1099-1104
[11] C. Kang, et al, J. Nucl. Mater. 412 (2011) 62–65.
[12] C. Xiao, et al. Fusion and Plasma Phys. 31(2011) 224-227.
[13] K. Mochizuki, et al, Fusion Eng. Des. 85(2010) 1185-1189.
[14] S. Hu, et al, International Jornal of Hydrogen Energy. 19(2010) 10118-10126

Effects of Li_4TiO_4 Structure on Tritium Release Kinetics from Lithium-Enriched $Li_{2+x}TiO_3$

Makoto KOBAYASHI[1], Kiyotaka KAWASAKI[1], Katsuyoshi TATENUMA[2], Masanori HARA[3], Masao MATSUYAMA[3], Toshiyuki FUJII[4], Hajimu YAMANA[4], Yasuhisa OYA[1] and Kenji OKUNO[1]

[1]*Radioscience Research Laboratory, Faculty of Science, Shizuoka University, Japan*

[2]*Kaken Co. Ltd., 1044, Hori, Mito-city, Ibaraki, 310-0903, Japan*

[3]*Hydrogen Isotope Research Center, University of Toyama, Toyama, Japan*

[4]*Research Reactor Institute: Kyoto University, Kumatori, Japan*

(Received: 10 May 2012 / Accepted: 3 December 2012)

Keywords : Tritium, Li_2TiO_3, Li_4TiO_4, diffusion, de-trapping, TDS

The release kinetics of tritium for $Li_{2+x}TiO_3$ (x = 0, 0.2, 0.4) and Li_4TiO_4 were studied by means of Thermal Desorption Spectroscopy (TDS). Tritium-TDS spectrum at the heating rate of 0.5 K / min for $Li_{2+x}TiO_3$ irradiated with thermal neutron consisted of two release stages at 480 K and 580 K, namely Peaks 1 and 2, respectively. The activation energy of Peak 1 was estimated to be around 0.37 eV, while that of Peak 2, about 0.63 eV. The latter corresponded to the activation energy of tritium diffusion in Li_2TiO_3. For Li_4TiO_4 exposed to tritium-deuterium mixture gas, two tritium release stages named as Peaks A and B were also observed at 450 K and 600 K, respectively, in tritium-TDS spectrum at the heating rate of 0.5 K / min. As the release temperature regions of Peak 1 and Peak A were almost the same, tritium releases of these peaks were considered to be originated from a same process. O-T bonds formed on the surface of Li_4TiO_4 were decomposed as Peak B in TDS spectra.

1. Introduction

For the development of D-T fusion reactors, it is important to establish an effective fuel recycling system and a comprehensive model of tritium migration processes in solid tritium breeding materials. In the test blanket module for ITER, lithium titanate (Li_2TiO_3), one of ternary lithium oxides, is a candidate of tritium breeding materials because of good tritium release property, chemical stability, and so on [1]. During the operation of D-T fusion reactor, energetic tritium is generated by the reactions of $^6Li(n, \alpha)T$ and $^7Li(n, n\alpha)T$ in Li_2TiO_3 and lithium will be consumed by these reactions, resulting in lithium-depletions in Li_2TiO_3. As lithium-depletion in Li_2TiO_3 induces lower tritium generation rate, the lithium-depleted tritium breeding materials will be replaced after certain periods of operations.

The use of $Li_{2+x}TiO_3$ (x=0.2, 0.4), which is the lithium-enriched Li_2TiO_3, is proposed recently to improve the life cycle of tritium breeding materials with respect to tritium generation property [2-4]. $Li_{2+x}TiO_3$ consists of Li_2TiO_3 structure and excess lithium: i.e. Hara *et al.* [5], reported that both of $Li_{2.2}TiO_3$ and $Li_{2.4}TiO_3$ were the mixture of Li_2TiO_3 and Li_4TiO_4 structures, indicating that excess lithium induced the formation of Li_4TiO_4 structure in Li_2TiO_3 structure during fabrication.

In our previous study, tritium release behaviors and their kinetics for $Li_{2+x}TiO_3$ irradiated with thermal neutron were investigated by means of TDS [6]. Tritium-TDS spectrum for $Li_{2.0}TiO_3$ at the heating rate of 0.5 K/min consisted of single release stage at around 580 K. An additional release stage was observed at around 480 K for the tritium-TDS spectra for $Li_{2.2}TiO_3$ and $Li_{2.4}TiO_3$, although the major release stage was located at 580 K, which was assigned to the tritium release controlled by tritium diffusion in Li_2TiO_3 structure from kinetic analyses. In addition, the amount of tritium released at 480 K was increased with increasing lithium concentration. It was considered that this additional tritium release stage would be associated with excess lithium, that is, Li_4TiO_4 structure. However, the effects of Li_4TiO_4 structure on tritium release for $Li_{2+x}TiO_3$ are still unclear because tritium release mechanisms for Li_4TiO_4 have not been studied in detail. Therefore, in this study, tritium release behavior for Li_4TiO_4 was studied by means of TDS. Tritium was generated in Li_4TiO_4 by thermal neutron irradiation or introduced by thermal tritium gas absorption. The tritium release kinetics for $Li_{2+x}TiO_3$ irradiated with thermal neutron was also evaluated for comparison.

2. Experimental

Powders of Li_4TiO_4 and $Li_{2+x}TiO_3$ purchased from Kaken Co. were used as samples. The average grain diameters of Li_4TiO_4, $Li_{2.0}TiO_3$, $Li_{2.2}TiO_3$ and $Li_{2.4}TiO_3$ measured by SEM (Scanning Electron Microscope) were 12, 3.0, 1.0 and 1.0 μm, respectively. For thermal neutron irradiation experiments, 0.3 g of these samples were introduced into

f5144008@ipc.shizuoka.ac.jp

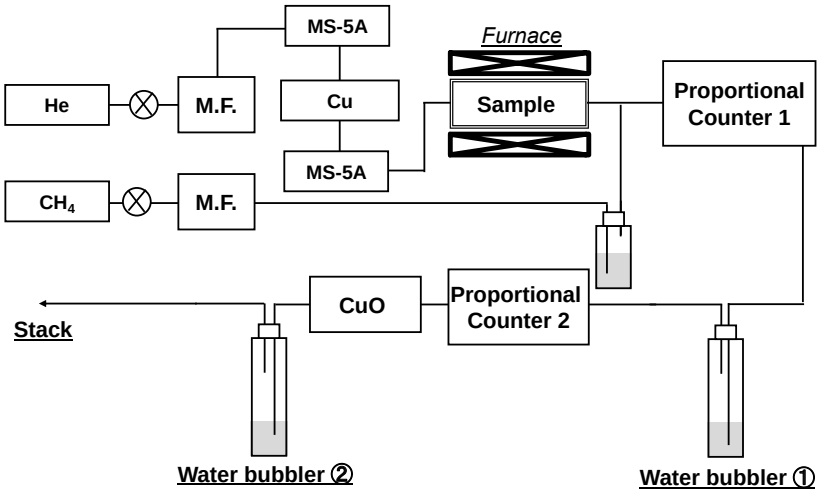

Fig. 1 Schematic drawing of TDS system

quartz tubes individually and annealed at 1073 K for Li_4TiO_4 and 1173 K for $Li_{2+x}TiO_3$ under He gas with the pressure of less than a few Pa for 3 h. After heating, these tubes were sealed under vacuum. Thermal neutron irradiations were conducted at Pneumatic tube 2 (Pn-2) of Research Reactor Institute, Kyoto University (KURRI). The thermal neutron flux was 5.5×10^{12} n cm^{-2} s^{-1}. The thermal neutron irradiation was carried out for 10 min, corresponding to the thermal neutron fluence of 3.3×10^{15} n cm^{-2}. The temperatures of the samples during irradiation were estimated to be lower than 350 K.

For hydrogen isotope gas exposure, Li_4TiO_4 sample was heated at 1073 K for 3 h in vacuum under the pressure around 10^{-5} Pa, then sample temperature was kept at 673 K. Thereafter, the tritium-deuterium mixture gas consisting of D_2 and DT (T/D = 0.005) or the pure D_2 (isotopic purity: 99.4%) gas was introduced into the sample with the total pressure of 200 Pa for 1 day. After the hydrogen isotope gas exposure, the sample was quickly cooled down by water and liquid nitrogen.

Out-of-pile tritium release experiments were performed in tritium-TDS system at Shizuoka University as shown in Fig. 1. The sample put in Mo crucible was set in quartz tube surrounded by a ceramic furnace. The He gas at the flow rate of 15 sccm was introduced into MS-5A and a heated Cu at 623 K to exclude impurities such as water and oxygen in He gas, and then purged into the system during experiments. The released tritium is recovered by purge gas and is carried to the first proportional counter (PC1). The volume of PC is 30 cm^3, and the voltage of 2.4 kV was applied to PC during measurement. After PC1, purge gas with tritium passes through first water bubbler (WB1) to trap the water-form tritium such as HTO and T_2O, named as "oxidized T". The second proportional counter (PC2) set after WB1 measures gas-form tritium such as HT and T_2, named as "reduced T". Thereafter, the reduced T are oxidized by heated CuO at 623 K after PC2 and trapped by second water bubbler (WB2). The amounts of oxidized T and reduced T trapped in WB1 and WB2, respectively, are quantified by a Liquid Scintillation Counter (ALOKA LSC-5100). The CH_4 gas at the flow rate of 25 sccm was used as a counting gas for the proportional counters. The CH_4 gas was humidified by passing through another water bubbler for reduction of memory effect in proportional counters. The humidified CH_4 gas was converged to He gas flow just before PC1 so that humidified CH_4 is not purged directly to Mo crucible with sample during heating. The quartz tube, stainless tubing of this system and the proportional counters were also heated at around 373 K to reduce the memory effect.

In the tritium-TDS experiments, the samples were heated up to 1173 K. Isothermal heating experiments were also conducted around 600-700 K.

FT-IR (Fourier Transform Infrared Spectroscopy) measurements were also carried out for Li_4TiO_4 exposed to pure D_2 gas at Shizuoka University to reveal chemical states of deuterium in Li_4TiO_4. Changes of crystal structure of Li_4TiO_4 by D_2 gas exposure were also investigated by X-ray diffraction (XRD) technique at University of Toyama.

3. Results and discussion

Fig. 2 shows the tritium-TDS spectra for $Li_{2+x}TiO_3$ at the heating rate of 0.5 K / min measured by PC1, representing the overall release of tritium. These spectra can be separated into two release stages, namely Peak 1 at 480 K and Peak 2 at 580 K. The TDS spectra for $Li_{2.0}TiO_3$ consisted of one release stage as Peak 2, although additional release stage of Peak 1 was also found for $Li_{2.2}TiO_3$ and $Li_{2.4}TiO_3$. The amount of tritium for Peak 1 was increased with increasing lithium concentration. To understand the tritium release kinetics for these peaks, the heating rate dependence experiments were carried out. In this analysis, Kissinger-Akahira-Sunose (KAS) model-free-kinetics method [6] which has been widely applied to analyze TDS spectra was adopted in the present

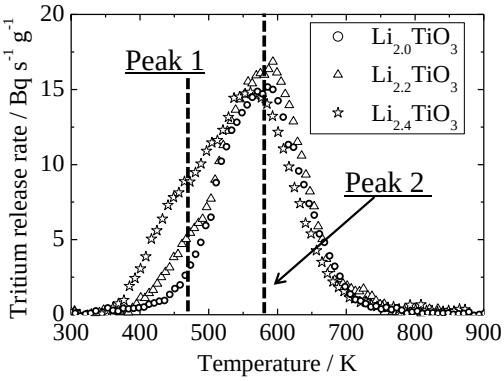

Fig. 2 Tritium-TDS spectra of $Li_{2+x}TiO_3$ at the heating rate of 0.5 K / min

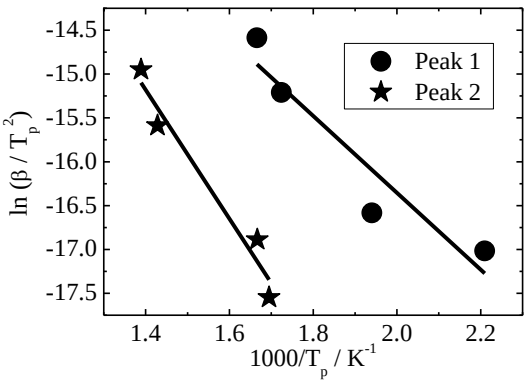

Fig. 3 Analytical results of release kinetics for Peaks 1 and 2 in $Li_{2.4}TiO_3$

study. In this method, $\ln(\beta/T_P^2)$ are plotted against $1/T_P$ for the determination of activation energy, where β is the heating rate and T_P is the peak temperature, based on following equation,

$$\ln\left(\frac{\beta}{T_p^{\,2}}\right) = \ln\left(\frac{RA}{E_a g(\alpha)}\right) - \frac{E_a}{RT_P} \qquad (1)$$

where R is gas constant, A is pre-exponential factor, E_a is activation energy of reaction. The term of $g(\alpha)$ is a model-function determined by rate limiting process of reaction. The linear relation between $\ln(\beta/T_P^2)$ and $1/T_P$ was deduced as Eq. 1, and the slope of which is representing $-E_a/R$. The peak separation analysis was done for TDS spectra of $Li_{2.2}TiO_3$ and $Li_{2.4}TiO_3$ under various heating rates, then peak temperatures for Peaks 1 and 2 in each spectrum were estimated. Table 1 summarizes the peak temperatures of Peaks 1 and 2 for $Li_{2.4}TiO_3$ at various heating rates. The peak temperatures were shifted toward higher temperature region with increasing heating rate. Fig. 3 shows the $\ln(\beta/T_P^2)$ vs $1/T_P$ plot for Peaks 1 and 2 for $Li_{2.4}TiO_3$. Liner relations between $\ln(\beta/T_P^2)$ and $1/T_P$ were found for each peak. The obtained activation energies of these release peaks were evaluated to be 0.37 eV and 0.63 eV for Peaks 1 and 2, respectively. The similar activation energies were also obtained for $Li_{2.2}TiO_3$. Especially, the activation energy of Peak 2 was consistent with that of tritium diffusion for Li_2TiO_3 obtained in our previous study and other works [7, 8]. The activation energy around 0.4 eV has not been reported for Li_2TiO_3 with neutron irradiation [8-10]. In addition, the activation energy for desorption of hydrogen isotopes adsorbed on the surface of Li_2TiO_3 was reported as about 1.2 eV [11], indicating that Peak 1 would not be associated with Li_2TiO_3.

Table 1 Peak temperatures of each peak for $Li_{2.4}TiO_3$ at various heating rates

Heating rate (K / min)	*T_P for Peak 1 (K)*	*T_P for Peak 2 (K)*
0.5	**453**	**591**
1	**515**	**603**
5	**580**	**705**
10	**601**	**718**

Fig. 4 shows the tritium-TDS spectrum for Li_4TiO_4 irradiated with thermal neutron measured at the heating rate of 0.5 K / min. This spectrum was measured by PC1 and no tritium release was found by PC2, indicating that almost all of tritium was released as water form. The tritium-TDS spectrum of Li_4TiO_4 can be separated into two release stages at 450 K and 600 K, and named as Peak A and Peak B, respectively. Especially, FWHM of Peak B was quite narrow compared to the other spectra as shown in Fig. 2. The peak temperature of Peak A was almost consistent with that of Peak 1.

Isothermal heating experiments were done for Li_4TiO_4 exposed to tritium-deuterium mixture gas to determine the tritium release kinetics for Li_4TiO_4. Because of the exposure temperature of 673 K, which is higher than the release temperature of Peak A, the release kinetics of Peak B was examined in these experiments especially. Two probable processes which control the tritium release in Li_4TiO_4 are considered as diffusion and de-trapping processes. In the diffusion limited release process, tritium would diffuse slowly toward the surface and release on the surface quickly. In the de-trapping limited one, tritium would be initially trapped strongly by the trapping sites. Tritium release would be initiated by de-trapping from the

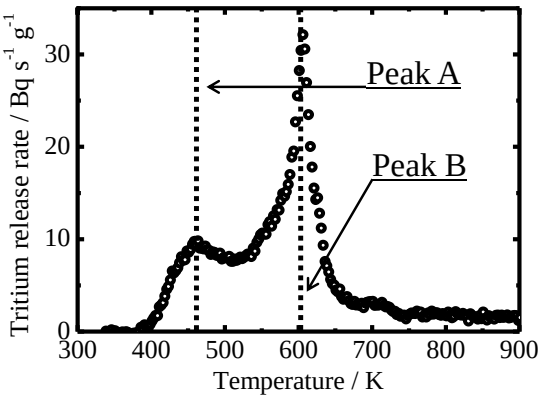

Fig. 4 Tritium-TDS spectrum of Li_4TiO_4 with thermal neutron irradiation

trapping sites. The other processes are quite faster than the de-trapping process, so these processes are not apparent on tritium release kinetics. The tritium release controlled by diffusion process is expressed by Fick's diffusion equation [12]. In particular for tritium release via diffusion in spherical media, tritium release with respect to elapsed time, t can be expressed in the following equation,

$$\alpha = 1 - \frac{6}{\pi^2}\sum_{n=1}^{\infty}\frac{1}{n^2}\exp\left(\frac{-Dn^2\pi^2 t}{a^2}\right) \qquad (2)$$

where α is fraction of released tritium to total amount, a is the radius of media, namely grain radius and D is diffusivity. On the other hand, the rate of de-trapping limited release should be controlled only by the concentration of trapped tritium in the material, indicating that de-trapping limited release is the first-order reaction, which is expressed as follows,

$$\frac{d\alpha}{dt} = k(1-\alpha) \qquad (3)$$

where k is the rate constant of reaction [13]. Comparing the theoretical curve derived from Eqs. 1 and 2 with tritium release by isothermal heating, the rate limiting process on tritium release was determined. Fig. 5 shows the isothermal tritium release behavior at various temperatures for Li_4TiO_4 exposed to tritium-deuterium mixture gas. The theoretical curves by de-trapping limited release model and diffusion limited release model were also shown in this figure. As shown in Fig. 5, theoretical curves based on diffusion limited release model could hardly reproduce isothermal tritium release for Li_4TiO_4. The theoretical curves by de-trapping limited release model could reproduce tritium release curve in the temperature region around 600-700 K, as shown in Fig. 6, indicating that tritium release for Li_4TiO_4 was controlled by de-trapping process.

The activation energy of tritium de-trapping was derived to be about 1.2 eV from the de-trapping rate constants at various temperatures, which was close to the

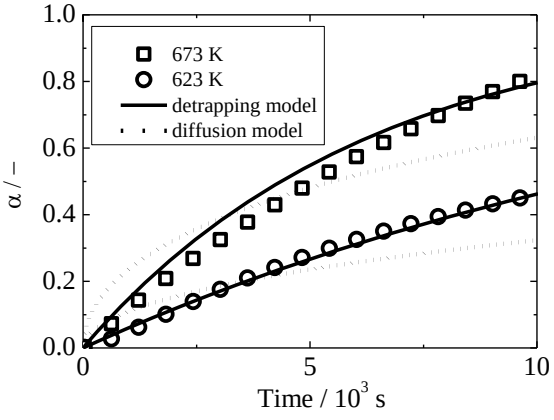

Fig. 5 Comparison of isothermal tritium release to theoretical curves derived from de-trapping and diffusion processes

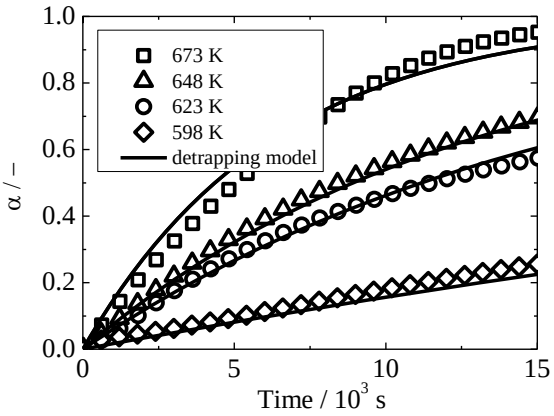

Fig. 6 Isothermal tritium release for Li_4TiO_4 exposed to tritium-deuterium mixture gas

decomposition energy of hydrogen from O-H bonds [14]. A FT-IR spectrum for Li_4TiO_4 exposed to pure D_2 gas showed the IR absorption in the wavenumber range of 2450-2750 cm^{-1} (not shown here). It was reported that O-D bonds in lithium ceramics showed IR absorption in this wavenumber region[15], indicating that O-D bonds were formed in Li_4TiO_4 by D_2 gas exposure. Therefore, it was considered that tritium trapped as O-T bonds were de-trapped by the decomposition of O-T bonds and released as Peak B for Li_4TiO_4.

However, the activation energy of Peak 2 in $Li_{2+x}TiO_3$ was different from that of the decomposition of O-T bonds in Li_4TiO_4. In addition, the tritium retentions as Peak 2 in $Li_{2+x}TiO_3$ were almost similar to that of Li_2TiO_3, although more than half of tritium was retained as O-T bonds in Li_4TiO_4 with neutron irradiation. These facts would indicate that the tritium releases derived from O-T bonds should be small in $Li_{2+x}TiO_3$.

The crystal structure of Li_4TiO_4 before and after D_2 gas exposure were compared by XRD method as shown in Fig. 7. In the measurements, silicon was used for reference. The diffraction patterns of Li_4TiO_4 exposed to D_2 gas were quite similar to that without D_2 gas exposure, indicating that the crystal structure was not changed by D_2 gas exposure. These results indicated that LiOD structure (crystal) was not formed in Li_4TiO_4. It was reported that Li_4TiO_4 is reactive with water vapor and forms O-H bonds on the surface [4], considering that water vapor as impurity was adsorbed on the surface of Li_4TiO_4 during air exposure or TDS measurements, which would induce the formation of O-H bonds. Similar results have been obtained in Li_2O [13]. The rate limiting process of tritium release for Li_2O was changed by heating temperature: i.e. in a lower temperature region, tritium release was controlled by decomposition of surface O-T bonds. In a higher temperature region, tritium release was governed by diffusion process. The rate limiting process was changed at 570 K, and this temperature was closed to Peak B appearing in this study, indicating that O-T bonds was mainly formed on the surface of Li_4TiO_4 and decomposed

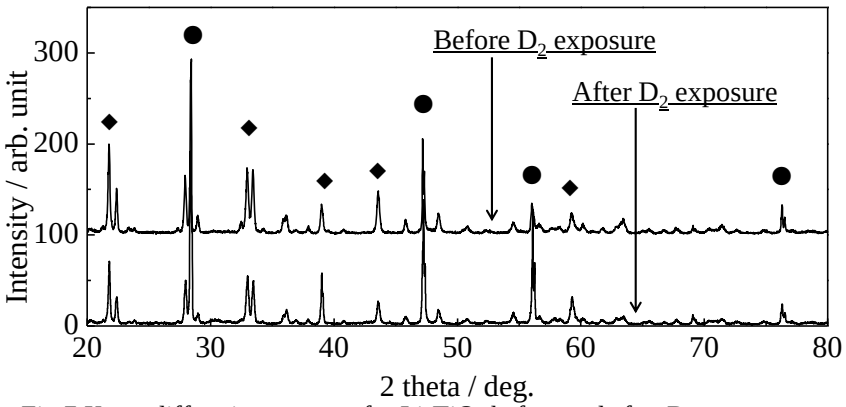

Fig.7 X-ray diffraction patterns for Li_4TiO_4 before and after D_2 gas exposure
◆ indicates Li_4TiO_4 structure and ● indicates reference silicon [5]

as observed as Peak B. The small tritium retention as O-T bonds in $Li_{2+x}TiO_3$ would imply that the amount of water on the surface of Li_4TiO_4 in $Li_{2+x}TiO_3$ was small. Because the $Li_{2+x}TiO_3$ was the mixtures of Li_2TiO_3 and Li_4TiO_4, the effective surface area of Li_4TiO_4 in $Li_{2+x}TiO_3$ should be small, resulting in the small retention of tritium as O-T bonds.

Peak B appearing in the TDS spectrum of Li_4TiO_4 could be assigned to the release of tritium as O-T bonds in this study. However, the assignment for Peak A was not completed although this peak also appeared in TDS spectra of $Li_{2+x}TiO_3$. The water vapor on the surface of Li_4TiO_4 may provide trapping sites for tritium as O-T bonds. A part of tritium migrated from bulk region of Li_4TiO_4 at lower temperatures, corresponding to tritium release as Peak A, would be trapped on the surface at lower temperature region. Li_4TiO_4 would easily react with water vapor in air, therefore, the experiments for Li_4TiO_4 without any air exposure are required to elucidate the tritium retention and release as Peak A, and consequently the relations of tritium retention as Peak 1 and the amount of excess lithium in $Li_{2+x}TiO_3$. The experiments in vacuum system would be a promising way to exclude the effects of surface O-T bonds. Therefore, it was considered that hydrogen isotope gas exposure and subsequent TDS experiments in the same vacuum system would reveal the tritium release mechanisms from Li_4TiO_4 in detail.

4. Conclusions

The release kinetics of tritium for $Li_{2+x}TiO_3$ and Li_4TiO_4 were studied by means of TDS. Tritium-TDS spectrum with the heating rate of 0.5 K / min for $Li_{2+x}TiO_3$ irradiated with thermal neutron consisted of two release stages at 480 K and 580 K, namely Peaks 1 and 2, respectively. The activation energy of Peak 1 was estimated to be around 0.37 eV, while that of Peak 2 was about 0.63 eV. The latter one corresponded to the activation energy of tritium diffusion in Li_2TiO_3. For Li_4TiO_4 irradiated with thermal neutron, two tritium release stages named as Peaks A and B were also observed at 450 K and 600 K, respectively, in tritium-TDS spectrum at the heating rate of 0.5 K / min. As the release temperature regions of Peak 1 and Peak A were almost the same, tritium releases of these peaks were considered to be originated from the same process. The O-T bonds were easily formed on the surface of Li_4TiO_4, appearing as Peak B in TDS spectrum.

Acknowledgements

This work was supported by the Grant-in-Aid for Scientific Research (A), KAKENHI 20246131.

References

[1] N. Roux *et al.*, J. Nucl. Mater., **233**, 1431 (1996).
[2] T. Hoshino *et al*., J. Nucl. Mater. **386–388**, 1098–1101 (2009)
[3] T. Hoshino *et al*., Fusion Eng. Des. **84**, 956–959 (2009)
[4] T. Hoshino *et al*., Fusion Eng. Des. **82**, 2269–2273 (2007).
[5] M. Hara *et al*., J. Nucl. Mater. **404**, 217–221 (2010).
[6] T. Ozawa, Netsu Sokutei **31(3)**, 133 (2004).
[7] M. Kobayashi *et al.*, Fusion Eng. Des., **87**, 471 (2012).
[8] T. Kulsartov *et al*., Fusion Sci. Technol., **60** 1139 (2011).
[9] C. Alvani *et al*., Fusion Eng. Des., **69**, 275 (2003)
[10] S. Casadio *et al.*, J. Nucl. Mater., **329**, 1252 (2004).
[11] K. Hashimoto *et al.*, Fusion Eng. Des., **61** 375 (2002).
[12] K. Okuno and H. Kudo, Fusion Eng. Des. **8**, 355 (1989).
[13] H. Kudo and K. Okuno, J. Nucl. Mater., **101** 38 (1981).
[14] K. Okuno and H. Kudo, J. Nucl. Mater., **133**, 192 (1985).
[15] T. Oda *et al*., J. Nucl. Mater. **346**, 306 (2005).

Release behavior of hydrogen isotopes in Li_2TiO_3 pellet

Deqiong Zhu, Takuji Oda and Satoru Tanaka

Department of Nuclear Engineering and Management, The University of Tokyo

(Received: 25 May 2012 / Accepted: 20 August 2012)

Release behavior of hydrogen isotopes thermally sorbed in Li_2TiO_3 pellet was studied by thermal desorption spectroscopy (TDS). As microstructure (grain size, surface condition, open and closed pores) of pellet samples were changed by high-temperature sintering, the release behavior of hydrogen isotopes was changed. The amount of hydroxyl groups chemically adsorbed on the surface was found to increase with the specific surface area. The gas migration in open pores was delayed to high temperature region (450~650 K), for which Knudsen diffusion and interaction between gas molecules and walls of narrow open pore channels is considered to be the main mechanism. The release of hydroxyl groups absorbed in the bulk was delayed due to the existence of closed pores, and these hydroxyl groups have to undergo bulk diffusion and trapping in closed pores several times before desorption.

Keywords: tritium breeder, hydrogen isotopes, Li_2TiO_3, pellet, microstructure

1. Introduction

The tritium release in ceramic breeder materials is a complex process, in which the contributions of bulk diffusion, surface processes and interaction with radiation defects were included as investigated in previous studies [1-4]. Just a few literatures were reported on the influence of porosity on tritium release behavior. Tanifuji et al. investigated the porosity dependence of tritium release in neutron-irradiated Li_2O sintered pellets. It was shown that the tritium release behavior is significantly affected even by a slight porosity change in pellet sample with densities above 87% T.D., and that tritium release can be delayed due to trapping in closed pores [5]. Peeters et al. compared the tritium residence time of different Li_2TiO_3 sample materials in the experiments EXOTIC-8 and EXOTIC-9/1, and suggested that tritium release improves with increasing open porosity and the closed porosity has no effect on tritium release behavior [6]. Tam et al. developed a random-lattice approach to study the tritium percolation through porous ceramic breeders by modeling the short range transport in pores via a convection-diffusion-reaction approach and long range transport via a matrix technique [7].

In the present work, Li_2TiO_3 pellet samples with different microstructure (grain size, specific surface area, open and closed pores) were prepared. The release behavior of hydrogen isotopes thermally sorbed in pellet samples was studied by thermal desorption spectroscopy (TDS). Scanning electron microscope (SEM, JSM-6510LA, JEOL, Ltd.) was used to observe the pore morphology and grain size. Mercury intrusion porosimetry (autopore(R) IV 9520, Micromeritics Instrument Corporation) was adopted to measure the open porosity, open pore size distribution. The specific surface area was measured by BET (Kr adsorption at 77 K) on an Autosorb-1-C (Quantachrome.Co). The influence of microstructure (grain size, specific surface area, open and closed pores) on hydrogen isotopes release behavior was discussed.

2. Experiment

Li_2TiO_3 pellet samples were prepared by pressing the powder into pellet and sintering. The starting materials of Li_2TiO_3 poly crystal powder, PVA (5 wt%) and stearic acid (5 wt%) were ball-milled for 6 h and mixed homogeneously. The mixture of powders was pressed into pellets stepwise at 20 kN (2 minutes), 40 kN (2 minutes) and 60 kN (2 minutes) per 1.3 cm^2. By sintering the as-prepared pellets in air at different temperatures for 12 h, five pellet samples of various apparent densities (% of theoretical density: 3.43 $g.cm^{-3}$ for Li_2TiO_3) were obtained: (a) 76% T.D., 1173 K, (b) 83.5% T.D., 1223 K, (c) 86.6% T.D., 1273 K, (d) 88.6% T.D., 1373 K and (e) 88.6% T.D., 1473 K. Note that these apparent densities were evaluated by measuring the mass and size of pellets. The color of all the pellet samples is white after sintering in air at high temperatures.

Deuterium was incorporated into pellet samples by heating in 100 Pa D_2O vapor at 1073 K for 1 h in absorption system. After cooling down and evacuation, the samples were transferred into a high-vacuum TDS system, and then were heated to 973 K at 5 K/min for TDS experiment. TDS spectra of released gas versus temperature or time were obtained during the heating process. Figure 1 shows the photographs of five pellet

zhudeqiong@flanker.n.t.u-tokyo.ac.jp

samples after TDS experiments. The gray color in samples (a) and (b) and darker color in samples (c) to (e) were observed. It was reported that Li containing species (Li and LiOD) were observed in mass spectra for Li_2TiO_3 by heating above 973 K in D_2O atmosphere. And the color of Li_2TiO_3 changed from white to light blue after heated in D_2O atmosphere, which was attributed to be due to the oxygen defects induced by LiOD vaporization [8]. In the present work, the color of Li_2TiO_3 pellet samples changed to gray or black after heated in 100 Pa D_2O vapor, which is similarly considered to be induced by reduction.

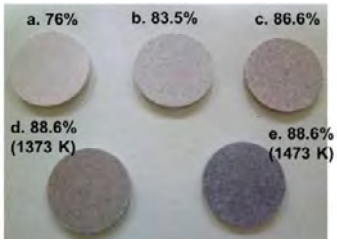

Fig. 1 Photographs of pellet samples after TDS experiment

3. Results and discussion

3.1. Release behavior of hydrogen isotopes

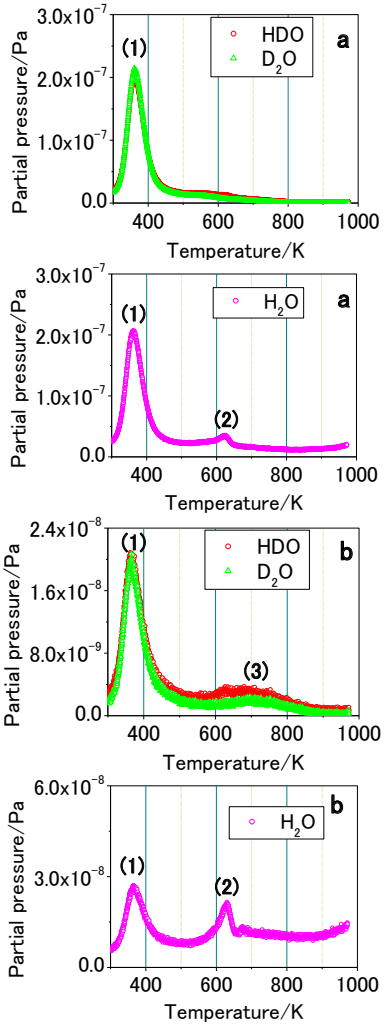

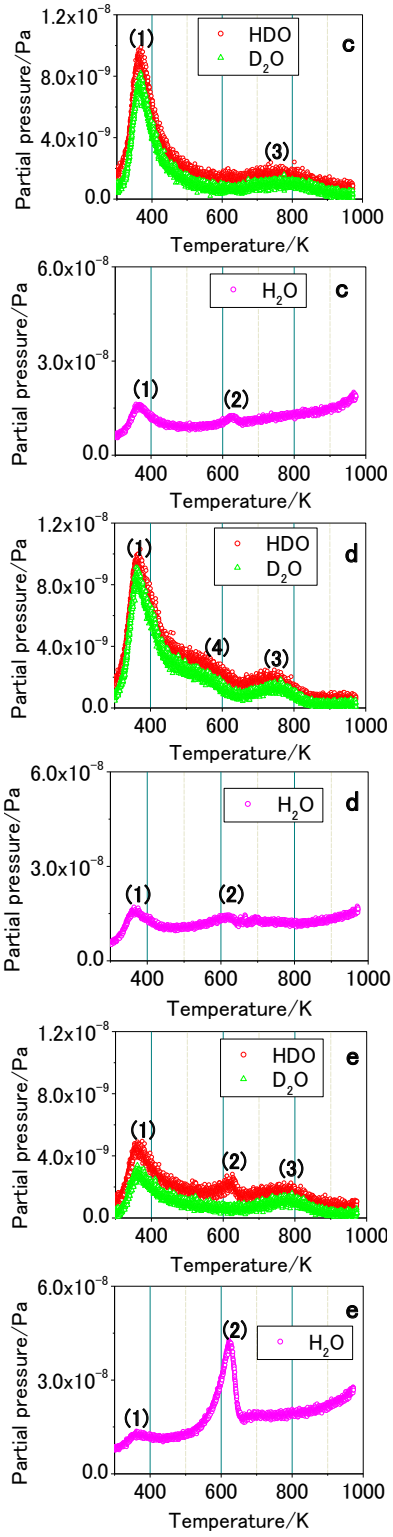

Fig. 2 TDS spectra for Li_2TiO_3 pellet samples: (a) 76% T.D., (b) 83.5% T.D., (c) 86.6% T.D., (d) 88.6% T.D. (1373 K), (e) 88.6% T.D. (1473 K)

Figures 2 show the TDS spectra for Li_2TiO_3 pellet samples. Deuterium thermally sorbed in pellet samples was released mainly in HDO and D_2O. One peak was observed at around 360 K for HDO, D_2O and H_2O, named peak (1). For H_2O, one more peak was observed at around 625 K, named peak (2). Except sample (e), no obvious HDO

release corresponding to peak (2) was observed. A peak for HDO and D_2O was observed at 650~900 K in samples (b) to (e), named peak (3). In sample (d), a broad peak between peak (1) and peak (3) was observed at 450~650 K for HDO and D_2O, named peak (4). For peak (3) and peak (4), no obvious H_2O peak was observed.

Based on the previous studies [9, 10], peak (1) is assigned to molecules physically adsorbed on the surface, which is released through desorption of physically adsorbed water molecules and migration along open pore channels, and peak (2) to hydroxyl groups chemically adsorbed on the surface, which is released by recombination desorption or isotope exchange reactions. In order to assign peak (3) and peak (4), the D/H ratios for peaks (1) to (4) were calculated and compared in Table 1. For peaks (3) and (4), no H_2O peak was obviously observed, which could be submerged in the high-level background. In order to give more precise evaluation of D/H ratios for peaks (3) and (4), the H_2O peak was estimated from HDO and D_2O peaks by assuming the equilibrium for the following reaction:

$$H_2O + D_2O = 2HDO \quad (1)$$

The D/H ratios for peaks (4) and (5) evaluated without (shown in brackets) and with considering the estimated H_2O peaks were compared.

Table 1 D/H ratios for peak (1) to peak (4)

Sample	D/H ratio			
	peak (1) ~ 360 K	peak (2) ~ 625 K	peak (3) 650~900 K	peak (4) 450~650 K
a	0.96	-	-	-
b	0.91	-	1.8 (2.8)	-
c	0.82	-	1.9 (2.9)	-
d	0.89	-	1.9 (2.9)	1.9 (2.9)
e	0.86	0.01	1.9 (2.9)	-

The D/H ratio reflects the probability of isotope exchange reaction between deuterium species (D_2O, HDO, -OD) and H_2O residue in TDS system. For peak (1), isotope exchange reaction between released molecules (HDO, D_2O) and H_2O/-OH residue in TDS system partially occurred. For peak (2) with the lowest D/H ratio of around 0.01, it is considered that isotope exchange reaction between –OD on the sample surface and H_2O residue in TDS system largely happened. The D/H ratios for peak (3) and peak (4) are larger than that for peak (1) and peak (2), and similar to that of D_2O tank (D/H ratio=1.8). It indicates that the probability of isotope exchange reaction is much smaller in peak (3) and peak (4), which suggests that the origins of peak (3) and peak (4) are located at some places where residual H_2O gas in TDS system hardly reaches. In the present experiment, obvious H_2O peak with higher level than HDO and D_2O was observed at around 625 K. Three possibilities were considered for this H_2O peak: (i) –OH formed due to H_2O residue in D_2O tank and then desorbed as H_2O after recombination, (ii) –OH formed by isotope exchange reaction between –OD on the sample surface and H_2O residue in TDS system and then desorbed as H_2O after recombination, and (iii) isotope exchange reaction between released molecules (HDO, D_2O) and H_2O residue in TDS system.

The quantitative analysis for peak (1), peak (2) and peak (3), and assignment of peak (3) and peak (4) will be discussed in detail in section 3.4.

3.2. SEM observation

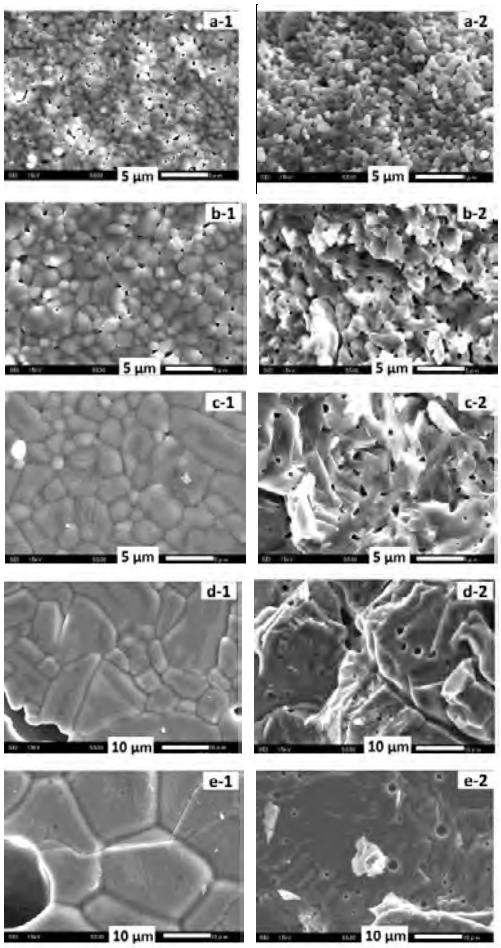

Fig. 3 SEM observation for Li_2TiO_3 pellet samples: (a) 76% T.D., (b) 83.5% T.D., (c) 86.6% T.D., (d) 88.6% T.D. (1373 K), (e) 88.6% T.D. (1473 K); 1- surface, 2- cross section

SEM observation for Li_2TiO_3 pellet samples is shown in Fig. 3. With the density increasing, grain sizes increased, and the porosity decreased. A broad grain size distribution was observed in sample (c) and especially obvious in sample (d) (Fig. 3.c-1 and d-1). Small pores with dead-end appeared in samples (b) to (e), and especially obvious in samples (d) and (e) (Fig. 3.b-2, c-2, d-2 and e-2). In samples (d) and (e), the grains in the bulk melted to form

big grain (Fig. 3.d-2 and e-2).

3.3. Mercury intrusion porosimetry

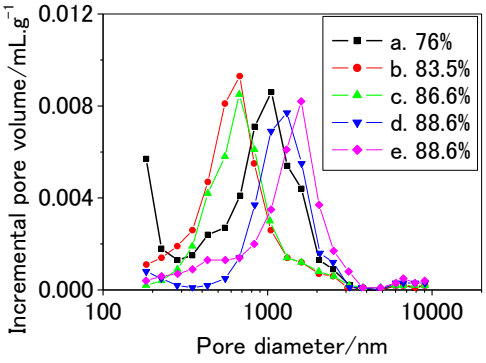

Fig. 4 Open pore size distribution for Li_2TiO_3 pellet samples: (a) 76% T.D., (b) 83.5% T.D., (c) 86.6% T.D., (d) 88.6% T.D. (1373 K), (e) 88.6% T.D. (1473 K)

The open porosity and open pore size distribution were measured by mercury intrusion porosimetry under the pressure of 6.8 MPa, for which pores smaller than 183 nm could not be measured. As a result, the open porosity and open pore size distribution could be underestimated to some extent. The open porosity was calculated from the open pore volume (volume of mercury intruded into sample) and external sample volume. The open porosity for pellet samples is: (a) 12.7%, (b) 11.9%, (c) 10.9%, (d) 9.8% and (e) 10.6%, which decreased from sample (a) to sample (d), and slightly increased in sample (e). Figure 4 shows the open pore size distribution, which was determined from the mercury pressure by the Washburn equation assuming that the geometry of pore channels can be approximated by cylindrical capillaries [11]. It seems that there are some pores smaller than 168 nm existing in pellet samples especially in sample (a). With the density increasing, the open pore size decreased in samples (b) and (c), and then increased in samples (d) and (e). With the sintering temperature increasing, the pores shrank first in samples (b) and (c), then expanded in samples (d) and (e) due to over-sintering at high temperature (1373 K and 1473 K). A small fraction of pores with larger size around several microns were also observed in sample (e). The closed porosity was evaluated from the measured open porosity and apparent density for pellet samples as *[closed porosity] = (1- [apparent density/theoretical density]) - [open porosity]*: (a) 11.3%, (b) 4.6%, (c) 2.5%, (d) 2.4% and (e) 0.8%. Due to the underestimation of open porosity by mercury intrusion porosimetry, the closed porosity might be overestimated especially in sample (a).

3.4. Discussion

3.4.1. Quantitative analysis for peak (1) and (2)

Table 2 shows the correlation between the specific surface area of pellet and the amount of peak (1) and peak (2). The amount of peak (1) (molecules physically adsorbed on the surface) was evaluated from the area of D_2O, HDO and H_2O peaks at around 360 K, and the amount of peak (2) (hydroxyl groups chemically adsorbed on the surface) was evaluated from the area of H_2O peak at around 625 K (HDO peak was added in sample (e)). The specific surface area of pellet samples was measured by BET.

Table 2 Correlation between specific surface area and amount of peak (1) and peak (2)

Sample	Specific surface area of pellet / $m^2 \cdot g^{-1}$	Peak (1) molecules/ 10^{17} g^{-1}	Peak (2) hydroxyl groups/ 10^{16} g^{-1}
a	0.762	22.5	11.2
b	0.120	2.2	6.4
c	0.035	0.9	1.3
d	0.058	1.1	1.5
e	0.039	0.4	19.8

The amount of molecules physically adsorbed on the surface (peak (1)) is proportional to the specific surface. Except sample (e), the amount of hydroxyl groups chemically adsorbed on the surface (peak (2)) is roughly proportional to the specific surface area in samples (a) to (d). It is considered to be due to that the concentration of surface defects induced by vaporization of Li-containing species is different in sample (e) sintered at the highest temperature (1473 K).

The vaporization characteristics of Li_2TiO_3 have been investigated by the mass spectrometric Knudsen effusion method, and it was shown that the vaporization of lithium-containing species increased with the temperature increasing [8, 12]. Hoshino et al. investigated the vaporization of lithium containing species under different atmospheres (D_2, D_2O, vacuum and O_2) from 973 to 1473 K [8], and the sum of partial pressures of Li-containing species (Li, LiO, Li_2O and LiOD) was found to be: D_2 = D_2O > vacuum > O_2. In the present study, pellet samples were prepared by sintering in air, where Li_2TiO_3 should show an intermediate vaporization behavior between O_2 atmosphere and D_2O atmosphere due to the existence of moisture (H_2O, similar to D_2O) and O_2. In another work [13], the non-stoichiometry of Li_2TIiO_3 heated in reduction atmosphere was quantitatively analysed by thermogravimetry. The mass of Li_2TiO_3 was found to decrease with time and the weight loss due to Li_2O and O vaporization reached the maximum after heating at 1273 K for around 16 h in H_2 atmosphere. And the maximum weight loss due to Li_2O vaporization was found to be 0.982 mg of 288.5 mg, which results in Li_2O deficiency with molar fraction of 0.01. The amount of defects induced by sintering in air (without O vaporization) is considered to be smaller than this value in samples (a) to

(d), for which the influence from the defects on the release behaviour of hydrogen isotopes is considered to be negligible. However, the molar fraction of Li_2O might be close to or larger than 0.01 in sample (e) which was sintered at higher temperature (1473 K), and the influence of surface defects on the amount of surface hydroxyl groups is expected in sample (e).

Oda et al. [14] studied the influence of radiation defects on hydrogen isotope behavior in Li_2O by in situ IR absorption analysis, and suggested that hydrogen isotopes were stabilized in Li_2O through an interaction with the Li vacancy or mutual aggregation. Bikondoa et al. [15] used STM to image the reaction of water molecules with bridging-oxygen vacancies on rutile TiO_2 (110) and oxygen vacancies were visually observed being transformed into OH species as a water molecule dissociates in the vacancy. It indicates that oxygen vacancies act as active sites for hydroxyl groups. In the present work, defects induced by Li species vaporization might facilitate relatively larger amount of hydroxyl groups adsorbed on the surface, especially in sample (e).

3.4.2. Assignment of peak (3)

Peak (3) was observed at higher temperature region (650~900 K) than the peak due to hydroxyl groups chemically adsorbed on the surface in high-density pellet samples (d) to (e) and might located at some places where residual H_2O gas in TDS system hardly reaches. Here two kinds of possible origins for peak (3) are considered: (i) hydroxyl groups absorbed in the bulk, (ii) molecules trapped in closed pores. In order to clarify the origin of peak (3), the amount of molecules/hydroxyl groups for peak (3) was estimated from the area of D_2O and HDO peaks in TDS spectra, which is around 10^{15}.

In the case of (ii) molecules trapped in closed pores, the pressure needed to trap 10^{15} molecules was roughly estimated. By assuming the closed porosity in high-density pellet samples (d) to (e) to be 5%, the volume of closed pores is estimated to be around 0.005 cm^3 (the volume of pellet is around 0.1 cm^3). Based on the ideal gas law equation, around 800 Pa of D_2O vapor is needed to trap 10^{15} molecules at 300 K. However, 100 Pa D_2O vapor was applied in the present experiment. Here we can infer that molecules trapped in closed pores are not a main source of peak (3).

In the previous study, 7.8×10^{16} cm^{-3} hydroxyl groups were thermally absorbed in the bulk of Li_2TiO_3 single crystal plate after heating in 100 Pa D_2O vapor at 1073 K for 1 h [10]. The amount of hydroxyl groups for peak (3) is at the same level, which convinced us that peak (3) can be assigned mainly due to (i) hydroxyl groups absorbed in the bulk.

In order to make clear the release path for peak (3), the "effective grain size" is defined to be an effective diffusion length needed to reach the surface (or open pores). The "effective grain size" is calculated from temperature of peak (3) by using a simple diffusion model, the detail of which was reported in the previous study [9]. The real grain size of pellet samples was decided by SEM observation. Table 3 shows the correlation between the real grain size and "effective grain size". The "effective grain size" is several times larger than the real grain size. It indicates that hydroxyl groups might experience bulk diffusion in multiple grains due to the existence of closed pores. It is generally known that the migration along the grain boundaries is fast. The surface processes are considered to proceed fast at the temperature region of peak (3) (650~900 K) (the peak was observed at 625 K in the present work). Besides, peak (3) was not observed in 5 μm and 50 μm single crystal powder samples [10]. Accordingly, the release of hydrogen isotopes is considered to be jointly controlled by diffusion in the bulk, trapping in the closed pores and dissolution in the grains at the temperature region of peak (3). When the hydroxyl groups come to the surface of closed pores, molecules desorbed from the grain surface can be trapped in the closed pores, dissolve in grain and diffuse in the grain bulk again. After several-times bulk diffusion and trapping in closed pores, the hydroxyl groups can arrive at the surface of pellet or open pores and finally be released to the TDS system. No obvious dependence of hydrogen isotopes release temperature on the grain sizes decided by SEM was observed in the present work.

Table 3 Correlation between the real grain size and "effective grain size" for peak (3)

Sample	Real grain size/ μm	Peak temperature / K	"Effective grain size"/ μm	"Effective grain size"/ real grain size
a	~ 1	-	-	-
b	1~3	700	12	4~12
c	3~10	775	50	5~14
d	>5	750	32	<6
e	>10	780	55	1~5

3.4.3. Assignment of peak (4)

For peak (4) detected in sample (d), a similar peak also appeared between peak (1) and peak (2) in 5 μm (av.) Li_2TiO_3 single crystal powder sample, in which sever agglomeration was observed [10]. The possible origin of water molecules physically adsorbed on the surface of inner open pores is considered, which is released through migration along complicated-structure pore channels. In the simulation by using the random-lattice approach

developed by Tam, in which convection-diffusion-reaction approach was considered for short range transport in open pores, a sharp pulse of tritium-bearing species was injected at the center of interconnected pores. And the release of injected tritium-bearing species exhibited a broad distribution with the long tail, which indicates many different pathways through which the gas molecule can reach the outlet from the source [7]. In the present work, two kinds of open pore channels are assumed: (I) pore size much larger than molecule mean free path, (II) pore size smaller than molecule mean free path. In the case (I), interaction between gas molecules and walls of pore channels is negligible, and the gas diffusion is fast, which is released in peak (1). In the case (II), interaction between gas molecules and walls of pore channels has to be taken into account. The broad peak (4) is considered to be mainly due to Knudsen diffusion and interaction between gas molecules and walls of different-shape narrow open pore channels [16, 17]. It was reported that Knudsen diffusion is dominant in pores with size of several (tens) nm [18, 19]. In the present study, no obvious peak (4) was observed except sample (d). Hence, we may think that narrow pore channels were evolved in the sintering condition of sample (d). However, small pore channels of several (tens) nm could not be measured by mercury intrusion porosimetry. The detailed mechanism for peak (4) needs further study.

4. Summary and Future work

The release behavior of hydrogen isotopes thermally sorbed in Li_2TiO_3 pellet was studied by TDS. The release behavior of hydrogen isotope was obviously changed due to the change in the microstructure of materials by high-temperature sintering. The amount of hydroxyl groups chemically adsorbed on the surface increases with the specific surface area. The release of hydroxyl groups in the bulk was delayed due to the existence of closed pores through undergoing bulk diffusion in multi-grains and trapping in closed pores several times. The peak related to gas migration in open pores was observed at relatively high temperature region (450~650 K), which is considered to be due to Knudsen diffusion and interaction between gas molecules and walls of narrow open pore channels, which needs further study.

References

[1] Peter C. BERTONE, The kinetics that govern the release of tritium from neutron-irradiated lithium oxide, J. Nucl. Mater. 151 (1988) 281-292.

[2] A. RENÉ RAFFRAY, Seungyon CHO, Mohamed A. ABDOU, Modeling of tritium transport in ceramic breeder single crystal, J. Nucl. Mater. 210 (1994) 143-160.

[3] M. Oyaidzu, H. Kimura, A. Yoshikawa, et al., Correlation between annihilation of irradiation defects and tritium release in neutron-irradiated lithium zirconate, Fusion Eng. Des. 81 (2006) 583–588.

[4] Makoto Oyaidzu, Yusuke Nishikawa, Taichi Suda, et al., Detrapping behavior of tritium trapped via hot atom chemical process in neutron-irradiated ternary lithium oxides, J. Nucl. Mater. 375 (2008) 1-7.

[5] Takaaki Tanifuji, Daiju Yamaki, Tadashi Takahashi, Akira Iwamoto, Tritium release from neutron-irradiated Li_2O sintered pellets: porosity dependence, J. Nucl. Mater. 283-287 (2000) 1419-1423.

[6] M.M.W. Peeters, A.J. Magielsen, M.P. Stijkel, J.G. van der Laan, In-pile tritium release behaviour of lithium metatitanate produced by extrusion–spheroidisation–sintering process in EXOTIC-9/1 in the high flux reactor, Petten, Fusion Eng. Des. 82 (2007) 2318–2325.

[7] S.W. Tam, V. Ambrose, Tritium percolation through porous ceramic breeders – A random-lattice approach, Fusion Eng. Des.17 (1991) 43-48.

[8] T. Hoshino, et al., Vapor species evolved from Li_2TiO_3 heated at high temperature under various conditions, Fusion Eng. Des. 81 (2006) 555–559.

[9] Deqiong Zhu, Takuji Oda and Satoru Tanaka, Effect of grain size on hydrogen isotope behavior in $LiNbO_3$, Fusion Sci. Technol. 60 (2011) 1147-1150.

[10] Deqiong Zhu, Takuji Oda, Yohei Shono, Satoru Tanaka, Study of hydrogen isotopes inventory in Li_2TiO_3, J. Nucl. Mater. Submitted.

[11] J. Van Brake1, S. Modrý, M. Svatá, Mercury Porosimetry: State of the Art, Powder Technol. 29 (1981) 1-12.

[12] Hamazo Nakagawa, Mitsuru Asano, Kenji Kubo, Mass Spectrometric Investigation of the Vaporization of Li_2TiO_3, J. Nucl. Mater. 110 (1982) 158-163.

[13] T. Hoshino, M. Dokiya, T. Terai, et al., Non-stoichiometry and its effect on thermal properties of Li_2TiO_3, Fusion Eng. Des. 61-62 (2002) 353-360.

[14] Takuji Oda, Yasuhisa Oya, Satoru Tanaka, Dynamic observation of the behavior of 3 keV D_2^+ irradiated into Li_2O using IR absorption spectroscopy, J. Nucl. Mater. 346 (2005) 306-311.

[15] Oier Bikondoa, Chi L. Pang, Roslinda Ithnin, et al., Direct visualization of defect-mediated dissociation of water on TiO_2 (110), Nat. Mater. 5 (2006) 189-192.

[16] Jaime Benítez, Principles and Modern Applications of Mass Transfer Operations (A JOHN WILEY&SONS,INC., New Jersey, 2009), p.59.

[17] Douglas M. Ruthven, Principles of Adsorption and Adsorption processes (A Wiley & Sons, New York, 1984), p 136.

[18] Kourosh Malek, Marc-Olivier Coppens, Knudsen self- and Fickian diffusion in rough nanoporous media, J. Chem. Phys. 119 (2003) 2801-2811.

[19] Aaron W. Thornton, Tamsyn Hilder, Anita J. Hill, James M. Hill, Predicting gas diffusion regime within pores of different size, shape and composition, J. Membrane. Sci. 336 (2009) 101-108.

Mass loss of Li_2TiO_3 pebbles in atmosphere containing hydrogen

Hideaki Kashimura[a,*], Masabumi Nishikawa[a], Kazunari Katayama[a], Shohei Matsuda[a], Satoshi Fukada[a], Tsuyoshi Hoshino[b]

[a]*Interdisciplinary Graduate School of Engineering Science, Kyushu University, 6-10-1, Hakozaki, Higashi-ku, Fukuoka 812-8581, Japan*

[b]*Blanket Irradiation and Analysis Group, Fusion Research and Development Directorate, Japan Atomic Energy Agency, 2-166, Oaza-Obuchi-Aza-Omotedate, Rokkasho-mura, Kamikita-gun, Aomori 039-3212, Japan.*

(Received: 8 May 2012 / Accepted: 24 September 2012)

It has been found that water vapor is released from the ceramic breeder materials into the purge gas due to desorption of adsorbed water and the water formation reaction, and affects the tritium release behavior. Additionally, the release of water vapor possibly promotes the mass loss of Li from the ceramic breeder materials. In this study, we investigated the changes in the mass of Li_2TiO_3 (NFI, CEA) and Li_2TiO_3 with additional Li (JAEA) at elevated temperatures. In hydrogen atmosphere (10,000 ppm H_2/Ar), the Li mass loss is close to be related to the amount of adsorbed water and amount of water formation in each Li_2TiO_3, and the Li mass loss of Li_2TiO_3 (CEA) is about three times larger than that of the other Li_2TiO_3 pebbles. It is considered that the chemical form of released Li different whether there is the adsorbed water and the water vapor by the water formation reaction in the gas phase or not.

Keywords: ceramic breeders, Li mass loss, surface water, water formation reaction, hydrogen atmosphere

1. Introduction

The present authors have developed an estimation model to represent the tritium release behavior from ceramic breeder materials, which is valid for out-of-pile and in-pile conditions [1, 2]. Tritium release curves estimated by the tritium release model gave good agreements with experimental curves from the ceramic breeder materials under various purge gas conditions [3]. Fig. 1 shows the tritium release model constructed by the present authors. In the model, the tritium diffusion in a breeder grain, tritium transfer to surface water at interfacial layer, and surface reactions on grain surface as adsorption / desorption of physisorbed and chemisorbed water, isotope exchange reaction with hydrogen in purge gas (isotope exchange reaction 1), isotope exchange reaction with water vapor in purge gas (isotope exchange reaction 2), and water formation reaction of hydrogen in purge gas with oxygen in the material are taken into account.

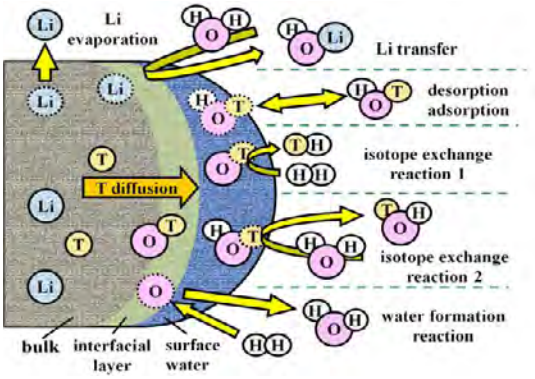

Fig. 1 The tritium release model from ceramic breeder materials

The tritium release behavior from the ceramic breeder materials packed in the blanket module under ITER-like operational condition is estimated based on the tritium release model using parameters obtained in our studies [2]. It is assumed in this estimation that purge gas is He gas mixed with 100Pa H_2 and that physisorbed water is removed completely before operation. The operational condition of ITER is repetition of a burning time of 400 seconds with dwell time of 1400 seconds. This model simplifies the condition of the ITER test blanket module suggested by Japan Atomic Energy Agency (Fig. 2). Fig. 3 shows the tritium release behavior from Li_2TiO_3 (NFI) under the operational condition of ITER. It was estimated that the partial pressure of water vapor in gas phase was about 20Pa and it is kept for about 100hour. This water vapor affects the chemical form of the released tritium. The reaction of released water vapor with the ceramic breeder materials may promote the Li mass transfer. When the ceramic breeder materials are placed at high temperature conditions, a certain amount of Li may evaporate. If non-negligible Li transfer is caused, it would possibly lead to serious issues such as stuffing and erosion of pipes, and drop of TBR. However, the Li mass transfer in a packed bed of the ceramic breeder materials has not been sufficiently understood to date. In the present study, we investigated the changes in the Li mass loss of Li_2TiO_3 (NFI, CEA), and Li_2TiO_3 with additional Li (JAEA) at elevated temperatures in hydrogen atmosphere, and compared them.

kashimura@aees.kyushu-u.ac.jp

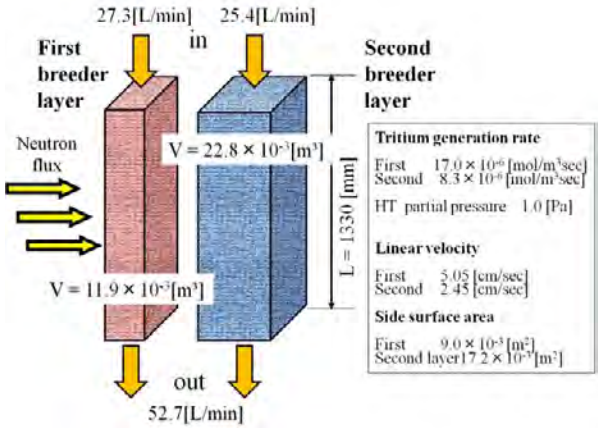

Fig. 2 The ITER-TBM type model

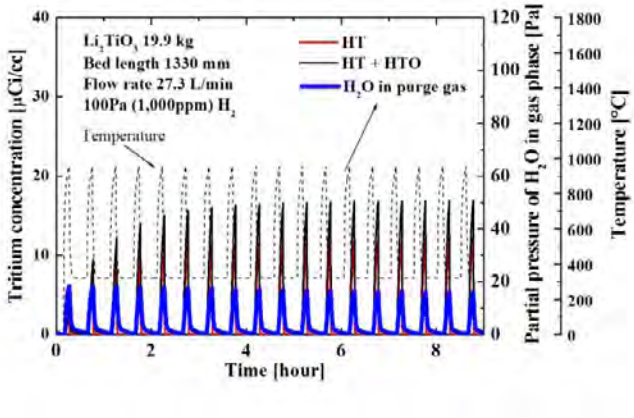

Fig. 3 The simulation result of tritium and water release curve under the operational condition of ITER

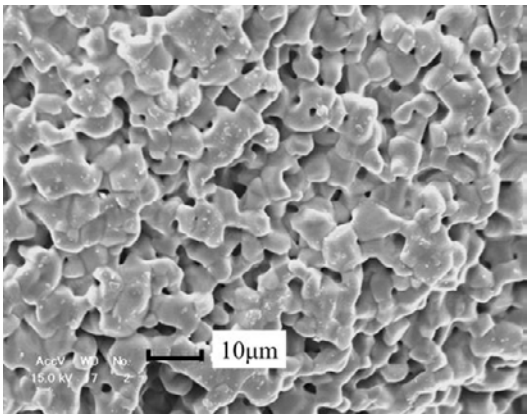

Fig. 4 The SEM picture of as-received Li_2TiO_3 (NFI)

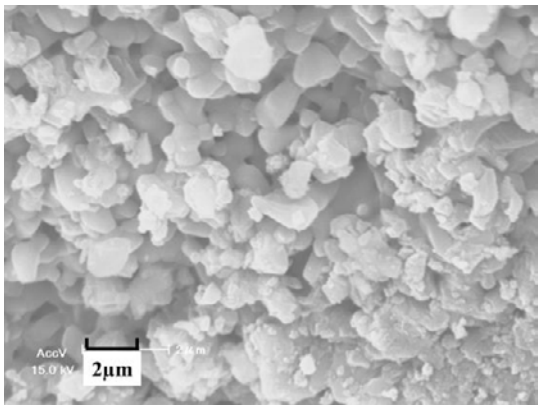

Fig. 5 The SEM picture of as-received Li_2TiO_3 (CEA)

2. Experimental

In this experiment, Li_2TiO_3 pebbles produced by Nuclear Fuel Industry (NFI), Commissariat à l'énergie atomique (CEA), and Li_2TiO_3 with additional Li, 2.06 in Li/Ti ratio, produced by Japan Atomic Energy Agency (JAEA) were used. The Li_2TiO_3 with additional Li is in developmental stage in JAEA as an advanced tritium breeder material for DEMO blanket. The sample pebbles of 0.5 g were packed in a quartz tube, 4 mm in inner diameter, and 36 mm long for Li_2TiO_3 (NFI) and 29 mm for Li_2TiO_3 (CEA), and 29mm for Li_2TiO_3 with additional Li (JAEA) in bed length. Fig. 4, 5 shows a SEM picture of the inside of Li_2TiO_3 (NFI) and Li_2TiO_3 (CEA) pebble. It was estimated from SEM observation that the grain diameter of Li_2TiO_3 is 5μm for NFI, 1μm for CEA, and 30μm for JAEA. Each pebble diameter is 2mm, 1mm, and 1mm, respectively. The details of the experimental procedures were reported in the previous paper [4]. After the desorption of physisorbed water from the sample pebbles by introduction of H_2/Ar (1000PaH_2/Ar) gas at room temperature, the sample bed was heated to 900 °C, or 600 °C with a ramp rate of 5 °C/min, and the temperature was held. The water vapor concentration at outlet was measured by a hygrometer (MAH-50, SHIMAZU Co.). The weight changes of sample pebbles were measured before and after the experiment. It is considered that the weight loss of sample pebbles is caused by desorption of adsorbed water vapor, disassociation of oxygen with water formation reaction and release of Li-containing species. In this study, weights of released water vapor and oxygen are subtracted from the weight loss of sample pebbles and the rest is defined as Li mass loss.

3. Result and Discussion

Fig. 6 shows the concentration of water vapor at outlet of the quartz tube when Li_2TiO_3 (NFI) sample bed was heated with a ramping rate of 5 °C/min to 900 °C. It is observed that when H_2/Ar gas is introduced, physisorbed water can be released at room temperature and chemisorbed water is almost removed by elevating temperature to about 400 °C. At over 500 °C, the water vapor is released by the water formation reaction between H_2 and oxygen in the material. The weight of chemisorbed water and oxygen are obtained to be 6.52×10^{-3}g and 1.55×10^{-3}g on average.

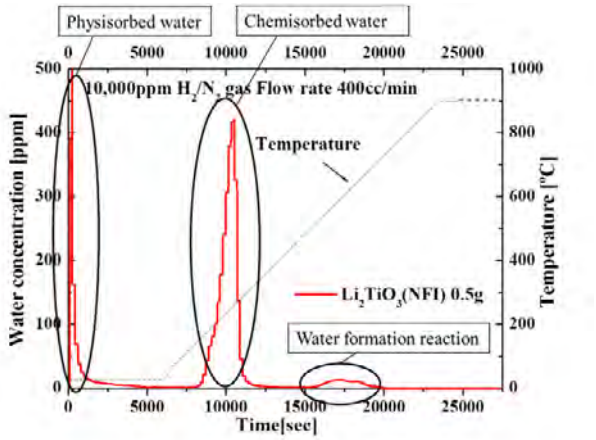

Fig. 6 Example of the water release curve from Li_2TiO_3 (NFI)

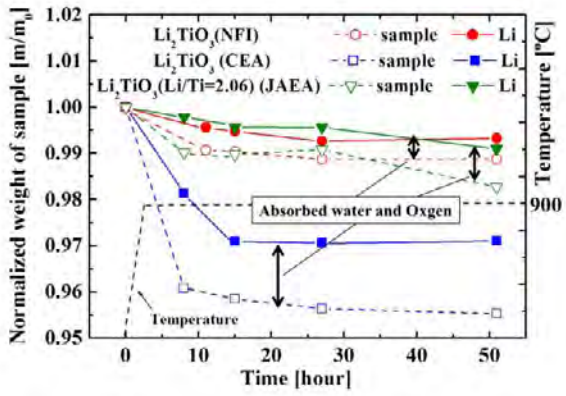

Fig. 7 Result of the experiment to the weight changes of sample and mass loss of Li at 900 °C

Fig. 7 shows the weight changes of sample pebbles and the Li mass loss. In the case of Li_2TiO_3 (NFI), the weight loss of sample pebbles is about 1.0 wt% and the Li mass loss is about 0.7wt% after 50hours. The weight of sample seems to be almost steady after 24hours. For the data of Li_2TiO_3 (CEA), a huge mass loss is observed after 8hours. After 50hours, the weight loss of sample pebbles is about 4.0 wt% and the Li mass loss is about 3.0 wt%. In the case of Li_2TiO_3 with additional Li, the weight loss of sample pebbles is 2.0 wt%, and the Li mass loss is about 1.0 wt% after 50hours. It seems that the Li mass loss still continues.

The Li mass loss per gram of Li_2TiO_3 (CEA) is about three times larger than those of Li_2TiO_3 (NFI) and Li_2TiO_3 with additional Li. It is considered that the amount of Li mass loss is related to the difference of surface area and the amount of released water. It is found by the present authors that the amount of chemisorbed water per surface area of Li_2TiO_3 (NFI) are about twice larger than that of Li_2TiO_3 (CEA) and, the amount of generated water per surface area of Li_2TiO_3 (CEA) and that of Li_2TiO_3 (NFI) are almost same. Therefore it is considered that the Li mass loss of Li_2TiO_3 (NFI) is promoted by the release of water vapor, but we use Li_2TiO_3 (CEA) which surface area is smaller than that of Li_2TiO_3 (NFI) in this experiment, the Li mass loss of Li_2TiO_3 (CEA) is promoted. Fig. 8 shows the relationship between the amount of released water and the Li mass loss. In this figure, the Li mass loss of Li_2TiO_3 (CEA) is three times larger than that of the others, and the amount of released water of Li_2TiO_3 (CEA) is also about three times larger. It is suggested that the Li mass loss is closely associated with the amount of released water from the sample pebbles. The water formation reaction is promoted at high temperatures in hydrogen atmosphere. Therefore it is predicted that the amount of Li mass loss in hydrogen atmosphere is larger than that in dry gas condition, but it is not carried out yet.

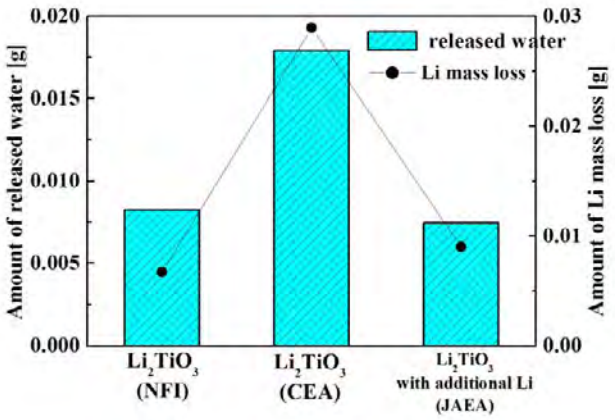

Fig. 8 Comparison between the amount of released water and the amount of the Li mass loss

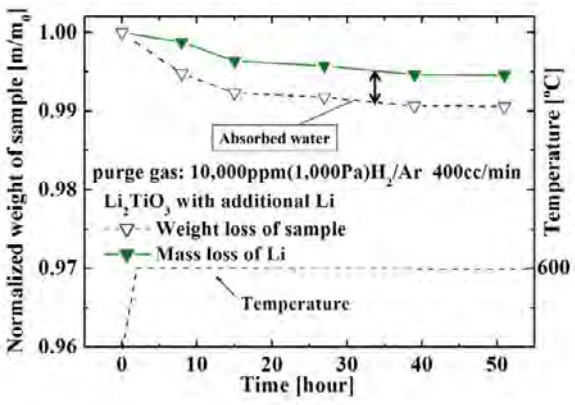

Fig. 9 Result of the experiment to the weight changes of sample pebbles and mass loss of Li at 600 °C

Fig. 9 shows the weight changes of sample pebbles when Li_2TiO_3 with additional Li were heated to 600 °C. In this figure, the weight loss of the sample pebbles is 1.0 wt%, and the Li mass loss is 0.5 wt% after 50hours. It is about one-half of the Li mass loss at 900 °C. In the previous studies, it has been found that the amount of generated water by the water formation reaction at 600 °C is smaller

than that at 900 °C for Li_2TiO_3 [5,10]. Therefore it can be said that the Li mass loss at 600 °C is smaller than that at 900 °C because the release of Li by the reaction with generated water at 600 °C is smaller. The weight of sample pebbles seems to be almost steady after 40 hours.

We are also considering that the amount of released water is associated with the method of Li_2TiO_3 manufacturing. By the present authors, Li_2TiO_3 (NFI) is made by the wet process, and Li_2TiO_3 (CEA) is made by the extrusion-spheronization-sintering process. [6, 7] It is considered that the amount of released water is related to whether water is used or not in manufacturing process.

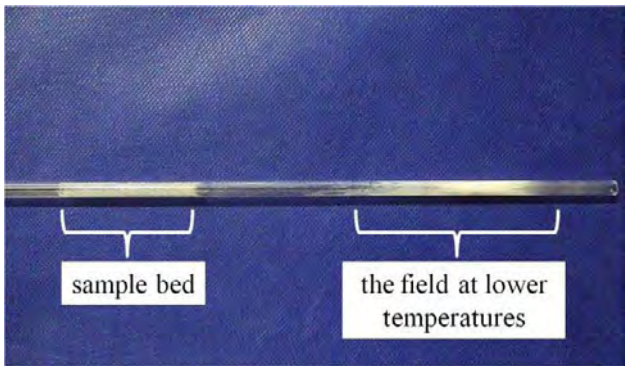

Fig. 10 Picture of the quartz tube after the experiment

Fig. 10 shows the picture of quartz tubes when Li_2TiO_3 (NFI) was used for sample bed after experiment. In this picture, the wall of the quartz tube after experiment is stained with the Li compounds. White turbidity is formed around the sample bed and the downstream region where the temperature is lower than that at the sample bed. It is speculated that Li reacts with the water vapor on the surface of the breeder material and vaporized as LiOH, and then deposits at lower temperature region. White turbidity around the sample bed may be caused by just Li evaporation. It has been observed by Hoshino et al. that Li partial pressure is higher than LiOD partial pressure at high temperature under D_2 atmosphere [8]. When the sample bed is held at high temperature for a long time and adsorbed water and the generated water by the water formation reaction expended completely, and Li would evaporate as Li atoms from the surface of the breeder material slowly.

4. Conclusions

The Li mass loss of Li_2TiO_3 in hydrogen atmosphere is close to be related to the amount of adsorbed water and amount of water formation in each breeder material. The Li mass loss of Li_2TiO_3 (CEA) is about three times larger than that of Li_2TiO_3 (NFI) or Li_2TiO_3 with additional Li (JAEA).

It is obtained that the Li mass loss of Li_2TiO_3 with additional Li (JAEA) at 600 °C is half times larger than that of Li_2TiO_3 with additional Li at 900 °C. It is supposed that the rate of water formation velocity is low at 600 °C, and the amount of released water is less than that of 900 °C.

In hydrogen atmosphere, the chemical form of released Li is different whether there is the adsorbed water and the water vapor by the water formation reaction in the gas phase or not. If there is the absorbed water and the water vapor by the water formation reaction in the gas phase, the chemical form of released Li is LiOH, and there is no water vapor in the gas phase, Li could evaporate from the surface of Li_2TiO_3.

References

[1] T. Kinjyo, et al., Fusion Eng. Des. **83**, (2008) 580 - 587.
[2] T. Kinjyo, et al., J. Nucl. Mater. **367 - 370**, (2007) 1361 - 1365.
[3] T. Kinjyo, et al., Fusion Eng. Des. **82**, (2007) 15 - 24.
[4] M. Nishikawa et al., J. Nucl. Mater., **325**, (2004) 87 - 93.
[5] T. Hanada, et al., J. Nucl. Mater., **417**, (2011) 735-738.
[6] K. Tsuchiya, et al., J. Nucl. Mater., 258-263, Part 2, (1998) 1985 - 1990.
[7] J. D. Lulewicz and N. Roux, J. Nucl. Mater. **307-311**, Part 1, (2002) 803-806.
[8] T. Hoshino, et al., Fusion Eng. Des. **81**, (2006) 555-559.
[9] T. Kinjyo, et al., Fusion Eng. Des. **83**, (2008) 580-587.
[10] K. Katayama, et al., Fusion Eng. Des. **87**, (2012) 927-931.

Flibe-Tritium Research for Fission or Fusion Reactors at Kyushu University

Satoshi FUKADA

Department of Advanced Energy Engineering Science, Kyushu University

(Received: 7 May 2012 / Accepted: 6 August 2012)

There is increasing interest in using ionic molten-salt Flibe not only as self-cooled tritium(T)-breeding material in a fusion reactor blanket but also as fuel solvent of molten-salt fission reactors. Application of Flibe to T-breeding fluid for a stellarator-type fusion reactor operated at a high magnetic field brings large simplification of its blanket structure, allowing continuous operation under high-beta plasma conditions. Using mixed Flibe-ThF_4+UF_4 fuel in molten salt fission reactors permits stable long-term operation without fuel exchange. When Flibe or Flinak is irradiated by neutrons, however, acid and corrosive TF is generated, and some T permeates through structural walls. In order to solve these problems, chemical conditions of Flibe are changed using the redox-control reaction, Be+2TF=BeF_2+T_2. In addition, permeation of hydrogen isotopes is lowered by enhancing T recovery rates. Part of Flibe-tritium researches are performed at Idaho National Laboratory (INL) under the Japan-US collaboration work of JUPITER-II. Our own contributions to the topics are shortly introduced in this paper.

Keywords: Flibe, tritium, fusion reactor, molten salt fission reactor, permeation

1. Introduction

Flibe is a stable mixed molten salt composed of 2LiF+BeF_2 in molar ratio (2:1) with melting point of 459ºC. Flinak (LiF+NaF+KF) is also a stable molten salt with 0.465:0.115:0.42 in molar ratio and a similar m.p. of 454ºC. The Flibe and Flinak ionic salts are planned to be used not only for a tritium(T)-breeding blanket in fusion reactors such as FFHR-2 at National Institute for Fusion Sciences (NIFS) in Japan [11,13,15,17] but also as fuel solvent in small molten salt fission reactors such as FUJI [21]. The former is intensively investigated under the direction of Prof. Sagara of NIFS [11,13,15,17]. Flibe is chemically and physically stable even at high temperature. Its low electric conductivity makes more suitable when utilizing in stellarator-type fusion reactors, which can be operated under conditions of a high beta magnetic field. Flibe can achieve the T self-sufficient condition of tritium breeding ratio *TBR*>1 [20], which is required for a fusion blanket. Flinak also gives a higher *TBR* value with use of Be [21].

Since Flibe heated to above m.p. can dissolve ThF_4 and UF_4 in any composition, it is used as fuel solvent in molten salt fission reactors. ^{232}Th is a fertile material which can be converted into fissile ^{233}U by a sequence of neutron-absorption reactions and the two beta decays, *i.e.* $^{232}Th + n \rightarrow {}^{233}Th \rightarrow {}^{233}Pa \rightarrow {}^{233}U$. The earliest molten salt reactor was set up in Oak Ridge National Laboratory (ORNL) in the 1960's. China is recently interested in its application to fuel solvent for the Thorium Molten Salt Reactor (TMSR), because of their large possible reserves and less generation of radioactive waste. TMSR can be operated for extended time without fuel discharge. The experimental fission reactor will be constructed in Shanghai Institute of Applied Physics, China Academy of Engineering Physics (SINAP, CAEP) in the near future. In this context, a

Fig. 1 Photos of solid Flibe at room temperature and transparent molten salt when its melts

author's e-mail: sfukada@nucl.kyushu-u.ac.jp

collaboration work on tritium release and measurement in the TMSR was recently initiated between researchers of SINAP, CAEP and our Kyushu University.

Generally, molten ionic salts of Flibe and Flinak are stable even under air at high-temperature. They become transparent when they are melted as shown in Fig. 1. When Flibe or Flinak is used for fusion or fission reactors under a high-intensity neutron flux or high-temperature conditions, various advantages and disadvantages are observed. The advantages of Flibe or Flinak can be summarized as follows: (i) comparatively low reactivity with O_2 or H_2O, (ii) low electric conductivity, (iii) low T solubility, and (iv) easy T recovery. On the other hand, the disadvantages when using Flibe or Flinak are (i) generation of chemically reactive TF under neutron irradiation, (ii) comparatively high viscosity (8.6 mPa・s at 600ºC of Flibe compared with 1.0 mPa・s at 20ºC of H_2O), which leads to high pumping power, (iii) the experimental increase of viscosity with increase of BeF_2 content, and (iv) high T permeability through some metals.

Many experiments have been carried out under the Japan-US collaboration work called JUPITER-II in 2001-2006 and our contributions within the frame of the domestic collaboration have continued since then. Part of the tritium research was performed in the Safety and Tritium Applied Research (STAR) facility of Idaho National Laboratory (INL). Many achievements are summarized in the references of the present paper [1-18]. Our T-related experimental or design-based research on applications of the molten salts Flibe and Flinak to fusion or fission reactors is briefly introduced in the present paper. The introduction is mainly devoted to our own studies due to the limit of paper length.

2. Redox Control

When mixed molten salt of Flibe or Flinak is exposed to neutron flux in fission or fusion reactors, tritium fluoride (TF) is generated by the reaction of LiF with neutrons as follows:

$^6LiF + n = TF + {}^4He$

$^7LiF + n = TF + {}^4He + n'$

The reaction cross-section of ^6Li with thermal neutrons is very large. On the other hand, that with ^7Li is small and has the threshold energy of 2.47 MeV. Therefore, enrichment of ^6Li is often necessary to achieve high *TBR*, when applied in a fusion reactor blanket. Since the reaction product TF is a strong acid, it corrodes metallic walls. Consequently, TF is converted into molecular T_2 or HT, which is chemically compatible with metallic walls and the fluorine is allowed to react with metallic Be. The reduction/oxidation (redox) control reaction in the liquid phase of Be (dissolved in Flibe) + 2TF (HF) ⟶ BeF_2 + T_2 (H_2) is used for the purpose. The experimental results are summarized in Fig. 2. It is assumed in the calculation that the Be dissolution rate is constant, the above reaction is second-order in HF concentration and contributions of the reverse reaction are negligibly small. As seen in the figure, close agreement is obtained between experiment and calculation regardless of the HF concentration and the Be dissolution concentration. A reaction rate constant is obtained from fitting between experimental results and calculations as shown in Fig. 2.

Since the solubility of T_2 generated by the reaction in Flibe is very low, T easily permeates through structural materials of fusion or fission reactors. Therefore, highly efficient procedures for T recovery from the Flibe flow in fission or fusion reactors and an effective T permeation protection are necessary in order to operate safely fusion or

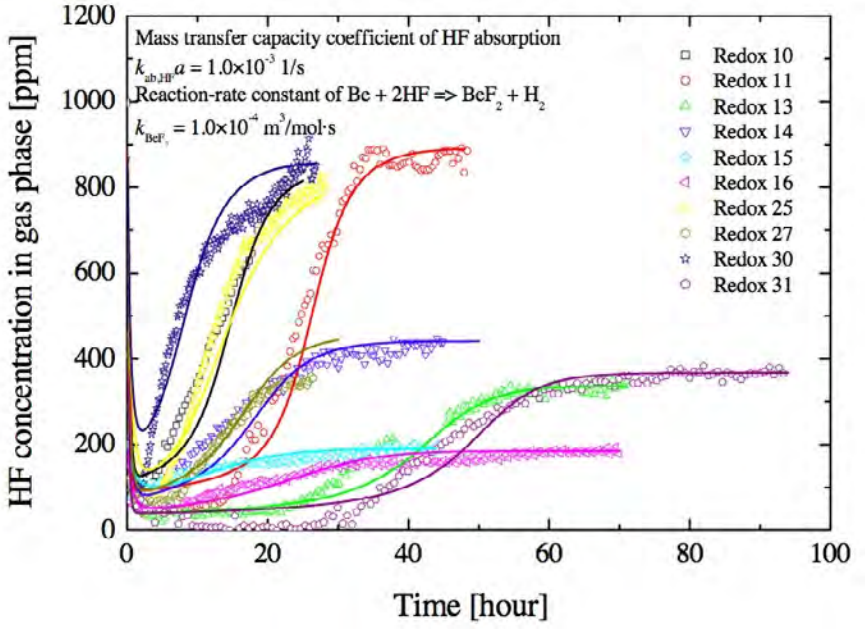

Fig. 2 Comparison between experiment and calculation of reaction of 2HF+Be⟶BeF_2+H_2 in liquid Flibe

fission reactors. Our previous work on T recovery and permeation through Flibe covers the following five topics, (i) diffusivity and solubility of hydrogen isotopes in Flibe or Flinak, (ii) Flibe purification and redox control by Be, (iii) chemical analysis of T in Flibe, (iv) design of equipment to recover T from Flibe, (v) design of Flibe blanket, *etc*. Many of these results are described in the references [1-18]. In the next section we focus on the solubility and permeability of hydrogen isotopes in Flibe or Flinak.

3. Solubility and Permeability of H Isotopes in Flibe or Flinak

Fusion or fission communities are much interested in two liquid breeders Flibe and Flinak, and many of their various properties have been investigated experimentally. Solubility and permeability of H isotopes in Flibe or Flinak molten salts are very important factors for the design of fusion reactors and to estimate the T-breeding performance. Solubility is related to the T inventory and permeability to T leakage through boundaries. Fig. 3 correlates solubility constants for various gases in Flibe and Flinak. Dissolution of gases in Flibe or Flinak follows Henry's law described by $c_k = K_{H,k} p_k$, where c_k and p_k are the concentration of gas k dissolved in the molten salt and the partial pressure of gas k, respectively. $K_{H,k}$ (k=H_2, He, Ar, Xe) is the Henry constant of gas k. These gases are dissolved in atomic or molecular form in Flibe and Flinak, and the major force acting between molten salt and dissolved inert gas is surface tension. Therefore, the solubility constant $K_{H,k}$ is given by the following equation regardless of Flibe and Flinak:

$$K_{H,k} = \exp\left(-\frac{E_0 + 4\pi N_A r_{b,k}{}^2 \gamma}{R_g T}\right) \qquad (1),$$

where $r_{b,k}$ is the atomic or molecular radius of the gaseous species k, N_A the Avogadro number, R_g the gas law constant, T temperature and γ the surface tension of Flibe or Flinak. Although E_0 is a constant for inert gases, in case of H_2 another attractive force between this molecule and the molten salt plays a role. Therefore the solubility of H_2 shows different tendency from that of inert gases (see Fig. 3).

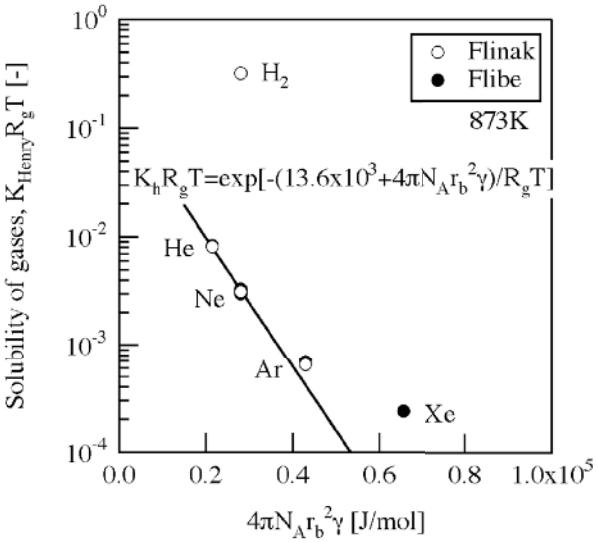

Fig. 3 Solubilities of H_2, He, Ar, Xe in Flibe or Flinak

The product of diffusivity D_{H2} and solubility $K_{H,H2}$ is equal to the permeability when no retardation on material-gas interface occurs. The steady-state H_2 permeation rate denoted by j_{H2} is proportional to the partial pressure difference between the upstream and downstream sides denoted by $p_{H2,up}$ and $p_{H2,down}$, respectively, and is expressed as follows:

$$j_{H_2} = \frac{K_{H,H_2} D_{H_2}}{\delta}\left(p_{H_2,up} - p_{H_2,down}\right) \qquad (2),$$

where δ is the thickness of the molten salt layer and D_{H2} is the diffusivity of H_2 in Flibe or Flinak.

4. Recovery of Tritium from Flibe or Flinak

The equilibrium partial pressure of T dissolved in Flibe or Flinak and vapor pressure of Flibe are shown in Fig. 4 together with other liquid blanket candidates. As seen there, the T equilibrium pressure over Flibe is the highest, being about 10^5 Pa for 1ppm T dissolved in Flibe. Therefore, simple He gas purge is promising to recover T in Flibe if direct contact between gas and liquid is possible. If direct contact is unsuitable, the problem is avoided by means of a

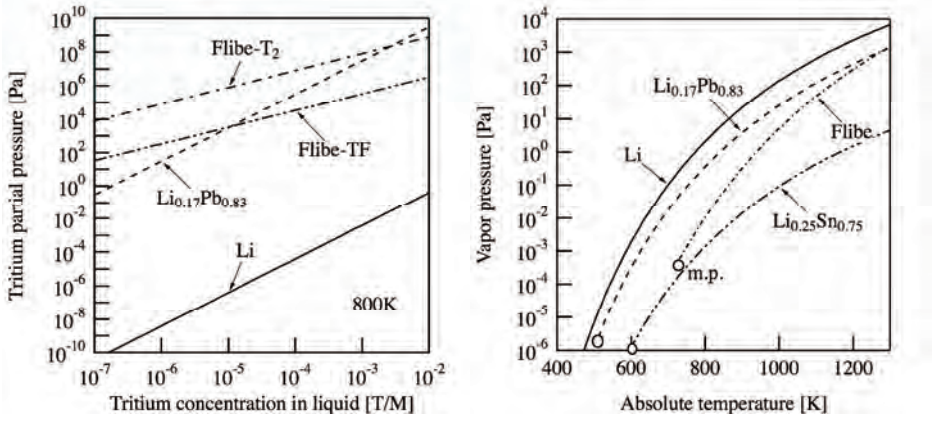

Fig. 4 Comparison of T equilibrium pressure and vapor pressure among Li, $Li_{17}Pb_{83}$ and Flibe

permeation window. If the redox control is not successful, the chemical form of tritium remains to be TF. The equilibrium pressure of TF is, however, about 1/200 of T_2. Therefore the efficiency of gas purge is reduced.

Fig. 5 shows a schematic view of a He-Flibe counter-current extraction tower. Tritium dissolved in Flibe at the tower inlet diffuses from the Flibe bulk to the Flibe-He interface. When it arrives at the surfaces, T desorbs to the He side. Then T_2 gas diffuses through the He-side boundary layer. T_2 in He is purged out to the gas outlet. In order to keep good contact between He and Flibe, inert metal packing is placed inside of the tower. Rashig ring, Dixon ring or equivalents can be used as usually packed in commercial gas-liquid extraction towers such as distillation process. Analytical study on T recovery from Flibe using the counter-current tower is being performed in Japan and China, but no experimental result has been presented.

Here, we compare Li chemical activity in the liquid blanket candidates among Li, Flibe, $Li_{17}Pb_{83}$ and $Li_{25}Sn_{75}$ eutectic alloys. Li has the highest vapor pressure among them. Since the chemical activity of Li is high, its use in fusion reactors may be limited for safety reasons even though its *TBR* is the largest among the four candidates. The vapor pressure of $Li_{17}Pb_{83}$ is lower than that of Li. The chemical activity of Li in the $Li_{17}Pb_{83}$ eutectic alloy decreases with increasing temperature as one can see when comparing the difference in vapor pressure between Li and $Li_{17}Pb_{83}$, which slightly spreads with increasing temperature. Judging from the viewpoint of vapor pressure, Flibe and $Li_{25}Sn_{75}$ are the lower group. The chemical activity of Li is low. Since the vapor pressure of Flibe is about 10^{-2} Pa at 800 K, its vaporization is negligibly small even when its accidental release happens (see Fig. 4). Therefore, Flibe is the safest materials among the four candidates. $Li_{25}Sn_{75}$ cannot constitute any blanket design of *TBR*>1.

5. Thorium as Fertile Material for Molten Salt Reactor

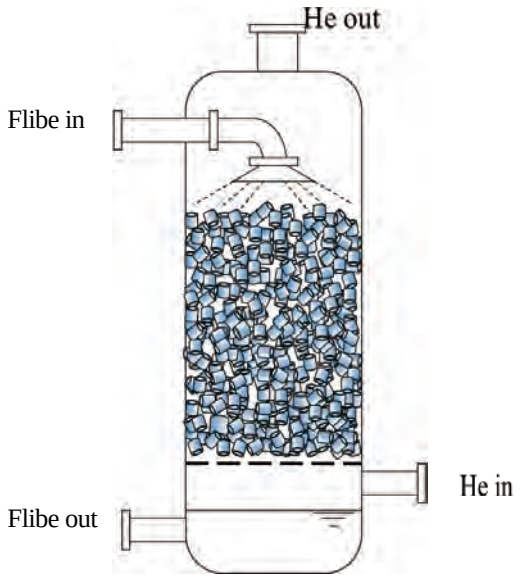

Fig. 5 Overview of He-Flibe counter-current extraction tower

When a Flibe molten salt mixed with UF_4 and TF_4 is used as fuel of a molten salt fission reactor, the largest disadvantage is the strong gamma ray originated from ^{232}U or its daughter nuclei ^{208}Tl. The gamma ray energy from ^{208}Tl is 2.8MeV. Therefore, the designed molten salt reactor should be buried under the ground in order to decrease non-necessary exposure to gamma rays (see Fig. 6). The figure shows an example for the molten salt reactor cited in the reference [19]. One generation path of ^{232}U from ^{232}Th fuel is considered to be $^{232}Th(n,2n)^{231}Th$, $^{231}Th \rightarrow ^{231}Pa$, $^{231}Pa(n,\gamma)^{232}Pa$, and finally $^{232}Pa \rightarrow ^{232}U$. The first (n,2n) reaction occurs only with fast neutrons. The threshold energy is 6.5MeV. Therefore, neutron slow-down using a resonable moderator is effective in order to decrease the generation of ^{232}U. Another path for the generation of ^{231}Th is the neutron capture reaction of ^{230}Th. This isotope is present as a natural impurity in ^{232}Th. ^{230}Th is a daughter

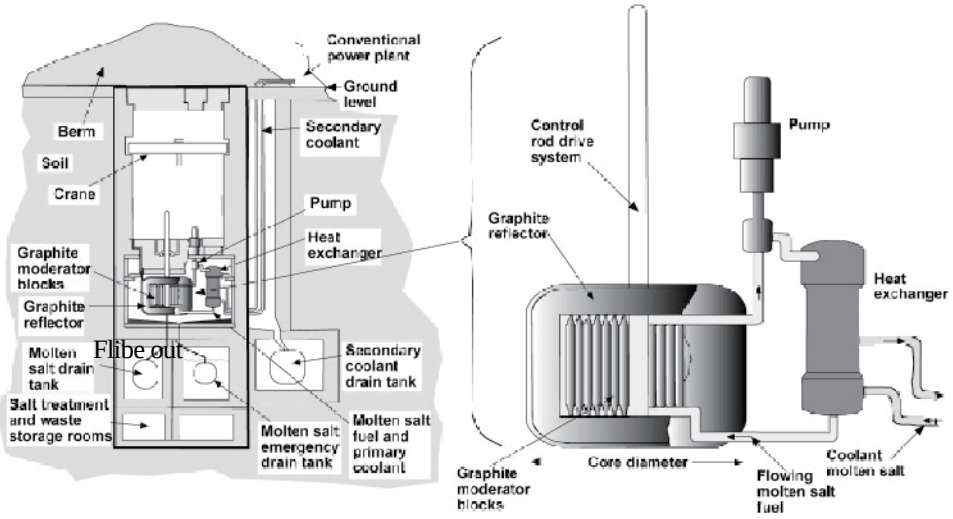

Fig. 6 Conceptual design of underground molten salt fission reactor. Figure is cited from the address [19].

product of the alfa decay of ^{238}U. When ^{231}Th is generated, as described above, the same path works to generate ^{208}Tl. Therefore, it is effective to separate natural U from natural Th (almost 100% ^{232}Th) beforehand in order to minimize the generation of high intensity gamma ray. The chemical separation between U and Th will be performed by a solvent extraction technique using Tributyl phosphate (TBP) as solvent.

6. Conclusions

Applications of molten salt Flibe or Flinak to fusion or fission reactors and our previous research on these topics were presented. Since Flibe and Flinak show not only proper T breeding ability for fusion reactors but also less reactivity with O_2 or H_2O regardless of slightly larger viscosity than other breeding materials, they can be used as a blanket fluid of a FFHR-2 fusion reactor. The advantages of molten salts were discussed here. On the other hand, corrosive TF acid is generated when exposed to neutrons. In order to solve this problem, the Be redox control reaction was shown to be effective. Since the solubility of T_2 (H_2) is comparatively small, although it is larger than that of inert gases, the T_2 recovery is readily carried out with a He-Flibe counter-current extraction tower. When Flibe mixed with fertile Th is exposed to neutrons, strong gamma rays are emitted from the Th fuel. The problem of strong gamma radiation is mitigated by placing the whole Th fission reactor under the ground. Impurity removal in natural Th can decrease the strong gamma ray originated from ^{208}Tl.

7. References

(i) Redox control and Flibe purification study:

[1] S. Fukada, R.A. Anderl, Y. Hatano, *et al.*, "Initial studies of tritium behavior in Flibe and Flibe-facing material", *Fusion Engineering and Design*, 61-62 (2002) 783-788.

[2] R.A. Anderl, S. Fukada, G.R. Smolik, *et al.*, "Deuterium/tritium behavior in Flibe and Flibe-facing materials", *Journal of Nuclear Materials*, 329-333 (2004) 1327-1331.

[3] M.F. Simpson, G.R. Smolik, J.P. Sharpe, *et al.*, "Quantitative measurement of beryllium-controlled redox of hydrogen fluoride in molten salt", *Fusion Engineering and Design*, 81 (2006) 541-547.

[4] D.A. Petti, G.R. Smolik, M.F. Simpson, *et al.*, "JUPITER-II molten salt Flibe research: An update on tritium mobilization and redox chemistry experiments", *Fusion Engineering and Design*, 81 (2006) 1439-1449.

[5] S. Fukada, M.F. Simpson, R.A. Anderl, *et al.*, "Reaction rate of beryllium with fluorine ion for Flibe redox control", *Journal of Nuclear Materials*, 367-370 (2007) 1190-1196.

(ii) Solubility, diffusivity, and permeability of hydrogen isotopes through Flibe and Flinak:

[6] S. Fukada, R.A. Anderl, R.J. Pawelko, *et al.*, "Flibe-D_2 permeation experiment and analysis", *Fusion Science and Technology*, 44 (2003) 410-414.

[7] S. Fukada, R.A. Anderl, T. Terai, *et al.*, "Diffusion coefficient of tritium through a molten salt Flibe blanket and evaluation of tritium leak from fusion reactor system", *Fusion Science and Technology*, 48 (2005) 666-669.

[8] S. Fukada, A. Morisaki, "Hydrogen permeability through a mixed molten salt of LiF, NaF and KF (Flinak) as a heat-transfer fluid", *Journal of Nuclear Materials*, 358 (2006) 235-242.

[9] Y. Edao, S. Fukada, H. Noguchi, A. Sagara, "Tritium release from neutron-irradiated Flibe purged out by Ar-H_2 or Ar at elevated temperature", *Fusion Science and Technology*, 55 (2009) 140-151.

(iii) Design study of tritium recovery from Flibe blankets:

[10] S. Fukada, M. Nishikawa, A. Sagara, "Calculation of recovery of tritium from a Flibe blanket", *Fusion Technology*, 39 (2001) 1073-1077.

[11] A. Sagara, H. Yamanishi, T. Uda, *et al.*, "Studies on Flibe blanket designs in helical reactor FFHR", *Fusion Technology*, 39 (2001) 753-757.

[12] S. Fukada, M. Nishikawa, A. Sagara, T. Terai, "Mass-transport properties to estimate rates of tritium recovery from Flibe blanket", *Fusion Science and Technology*, 41 (2002) 1054-1058.

[13] A. Sagara, T. Tanaka, T. Muroga, *et al.*, "Innovative liquid blanket design activities in Japan", *Fusion Science and Technology*, 48 (2005) 524-529.

[14] S. Fukada, A. Morisaki, A. Sagara, T. Terai, "Control of tritium in FFHR-2 self-cooled Flibe blanket", *Fusion Engineering and Design*, 81 (2006) 477-483.

[15] A. Sagara, O. Mitarai, S. Imagawa, *et al.*, "Conceptual design activities and key issues on LHD-type reactor FFHR", *Fusion Engineering and Design*, 81 (2006) 2703-2719.

[16] S. Fukada, K. Katayama, T. Terai, A. Sagara, "Recovery of tritium from Flibe blanket in fusion reactor", *Fusion Science and Technology*, 52 (2007) 677-681.

[17] A. Sagara, O. Mitarai, T. Tanaka, *et al.*, "Optimization activities on design studies of LHD-type reactor FFHR", *Fusion Engineering and Design*, 83 (2008) 1690-1695.

[18] S. Fukada, Y. Edao, A. Sagara, "Effects of simultaneous transfer of heat and tritium through Li-Pb or Flibe blanket", *Fusion Engineering and Design*, 85 (2010) 1314-1319.

[19] http://energyfromthorium.com/2010/12/07/not-so-fast-with-thorium/moirteller/

[20] H. Yamanishi *et aI.*, "Design studies on nuclear properties on the Flibe blanket for helical-type fusion reactor FFHR", *Fusion Engineering and Design*, 41 (1998) 583-588.

[21] H.Yamanishi, A.Sagara, Annual Report of National Institute for Fusion Science, April 1999–March 2000 (2000) 177.

Experimental and computational studies on tritium permeation mechanism in erbium oxide

Wei Mao[1),*], Takumi Chikada[1)], Akihiro Suzuki[2)], Takayuki Terai[1)] and Kenji Yamaguchi[3)]

1) *Department of Nuclear Engineering and Management, School of Engineering, The University of Tokyo, 7-3-1 Hongo, Bunkyo-ku, Tokyo 113-8656, Japan.*

2) *Nuclear Professional School, School of Engineering, The University of Tokyo, 2-22, Shirakata-shirane, Tokai, Naka, Ibaraki 319-1188, Japan.*

3) *Quantum Beam Science Directorate, Japan Atomic Energy Agency, 2-4 Shirakata-shirane, Tokai, Naka, Ibaraki 319-1195, Japan.*

(Received: 10 May 2012 / Accepted: 3 October 2012)

A tritium permeation barrier (TPB) is much required in fusion blankets to reduce the loss of fuel and minimize radiological hazard. However, the detailed mechanism of tritium permeation through TPB coatings has not yet been clarified because of their complicated crystal structures. To understand the microscopic mechanism, we have not only prepared and characterized nanostructured ceramic Er_2O_3 thin films, but also studied the energetics and mobility of interstitial deuterium in cubic bulk Er_2O_3 using *ab initio* density-functional calculations. The estimated diffusion activation energy (E_a) of interstitial deuterium is somewhat higher than the diffusion energy barrier observed experimentally at 873 K. This result shows that grain boundary structures existing in the TPB of Er_2O_3 significantly lower the diffusion barrier and change the diffusion pathway. Transport of hydrogen and its isotopes through the Er_2O_3 coatings are likely to be dominated by grain boundaries rather than by grains.

Keywords: Hydrogen isotope permeation measurement, Erbium oxide, Density functional theory calculations, Nudged elastic band

1. Introduction

There is no doubt that the environmental and economic acceptability of presently conceived D-T fueled fusion power plants will be dependent on the ability to contain and handle tritium within the reactor building and to control tritium releases to the environment without incurring into exorbitant costs [1, 2]. The problems of tritium leakage have been studied since 1970`s [3], and tritium permeation barrier (TPB) coating has been one of the most important subjects in the development of liquid lithium blanket for fusion systems. As to coating materials, a great many ceramics such as $Y_3Al_2O_{12}$, CaO, MgO, AlN (aluminum nitride), Al_2O_3, Y_2O_3 and Er_2O_3 were initially considered potentially eligible. Of these Er_2O_3 was selected as one of the most preferable candidate materials for TPB coatings because of its high permeation reduction factor (PRF) [4], high thermodynamic stability at high temperatures and in air, good compatibility with liquid Li, and high electrical resistivity [5]. Additionally, Er_2O_3 has one of the lowest Gibbs free energy of formation among all binary oxide ceramics [6]. Recently, Er_2O_3 is attracting more and more attentions in the application of TPB coatings for fusion systems.

Up to now, we have made rapid progress in the fabrication of TPB coatings by different methods such as sputtering deposition (SD) [7] and metal-organic decomposition (MOD) [8], but complex crystal structures and many surface defects still exist in the coatings, which make it difficult to investigate the detailed mechanism of hydrogen isotope permeation. At present, a high-quality ceramic Er_2O_3 thin film with nanostructures is successfully synthesized by arc source plasma assisted deposition (ASPAD). The ceramic shows grain boundary structures which are regarded as large defects in terms of permeation of hydrogen isotopes. Consequently, we place more and more emphasis on investigating hydrogen isotope behavior in this nanostructured thin film because of its slightly simpler structures compared to those prepared by SD and MOD methods.

In addition to experimental studies, ab-initio calculations based on density functional theory (DFT) have been applied to complement the established

author's e-mail: mao@nuclear.jp

experimental methods to investigate the energetics and mobility of atomic deuterium (D) in cubic bulk Er_2O_3. In recent years, DFT calculations have become a very valuable tool to elucidate the structures and determine the dynamics of interstitial H in metals, alloys, ceramics and other solids such as heterogeneous catalysts [9]. It is reported that DFT can be used to predict the precise mechanism of H diffusion or reaction events in condensed phases [10]. It is, therefore, essential to apply DFT calculations to the diffusion of hydrogen and its isotopes in Er_2O_3 for the verification of experimental data. As a result, a comparison between diffusion experiments and DFT simulations can provide useful information on the mechanism of hydrogen isotope permeation.

In this study, the objective is to compare the diffusion activation energies of interstitial D derived by DFT calculations with the diffusion energy barriers obtained from the experiments, and to study the relationship between the microstructure and hydrogen isotope behavior in Er_2O_3 for the mechanism of tritium permeation.

2. Methodology

2.1. Preparation and characterization of Er_2O_3 coatings

A mirror polished disk-shaped substrate of 20 mm in diameter and 0.5 mm in thickness was coated by arc source plasma assisted deposition (ASPAD), described in Ref. [7]. The substrate materials were made from reduced activation ferritic/martensitic (RAFM) steels, including JLF-1 (0.10% C; 0.05% Si; 0.45% Mn; 0.003% P; 0.002% S; 0.003% Al; 8.85% Cr; 1.99% W; 0.20% V; 0.080% Ta; 0.0231% N; 0.0002% B; < 0.01% Ni; < 0.05% Cu; <0.001% Mo; < 0.002% Nb; balance Fe) and F82H (7.65% Cr; 2.00% W; 0.50% Mn; 0.20% V; 0.04% Ta; 0.10% Si; 0.10% C; balance Fe) steels. Er_2O_3 coating about 1.3 μ m thick was deposited on one side of the substrate. Subsequently, deuterium permeation through the coated sample was carried out in the temperature range 573-973 K at driving pressures of 10^3-10^5 Pa [7].

2.2 Ab initio density-functional calculations in bulk Er_2O_3

At room temperature, Er_2O_3 exhibits cubic rare-earth bixbyite (C phase, space group *Ia*3) structure with a large complex unit cell comprising 16 Er_2O_3 sequioxide units with an experimental lattice parameter of 1.0543 nm [11]. In this structure, the O anions approximately occupy three-quarters of all the tetrahedral interstices while the Er cations lie in a face centred cubic arrangement. Apart from rotation symmetry, the bixbyite structure is different from that of the fluorite in missing one-fourth of the sites in the anion sublattice in the < 111 > direction. That is, it possesses two vacancies (16c) at the corners of the oxygen cube, as shown in Fig. 1.

Ab initio density-functional calculations are used to investigate the diffusion behavior of interstitial deuterium in bulk Er_2O_3. We employ Vienna *ab initio* Simulation Package (VASP) for our total energy and DFT calculations. All calculations were performed using the full-potential frozen-core all-electron projected augmented wave (PAW) method within the Generalized Gradient Approximation (GGA) of Perdew and Wang (PW91), as implemented in VASP [12]. The cut-off energy of plane wave was set to 500.0 eV. According to the Monkhorst-Pack scheme [13], we performed the tests with the k-point grid of 2x2x2 in the integration over the Brillouin zone. In the initial configuration of the crystal lattice, we have chosen the experimental cubic structure of Er_2O_3 unit cell with a = 1.0543 nm, 32 erbium atoms (occupying the 8a and 24d equipoints) and 48 oxygen atoms (occupying 48e equipoints). We conducted *ab initio* DFT calculations in the unit cell of Er_2O_3 for the geometry optimization of lattice parameters and atom positions. The geometry relaxations were terminated when residual forces on each atom and energy changes on each atom were less than 0.001 eV/Å and $1x10^{-5}$ eV, respectively. All calculations below referring to interstitial D were performed by inserting an individual D into the cell optimized by DFT methods. It is worth noting that the parameters of cut-off energies and k-point meshes were tested under the convergence criteria of energy changes on each atom less than 0.001 eV, and found sufficient to give reliable convergent results in the *ab initio* DFT calculations.

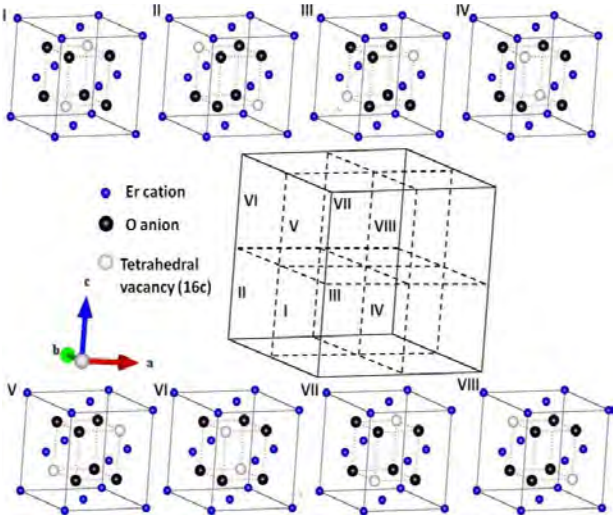

Fig. 1. Cubic bixbyite structure of Er_2O_3 unit cell. The cell is subdivided into eight small units, in which tetrahedral vacancies (16c) are virtually depicted as obtained from a comparison between the bixbyite and fluorite structures.

3. Results and discussions

3.1 Microstructures of Er_2O_3 coatings

Er_2O_3 coatings of 1.3 μ m in thickness were prepared using JLF-1 substrate and the ASPAD method. The coatings were found to possess a high-quality grain boundary nanostructure, as shown in Fig. 2. This grain boundary is regarded as the largest defect because of almost complete absence of other defects such as vacancies and dislocations. The average grain size of the coatings is about 200 nm.

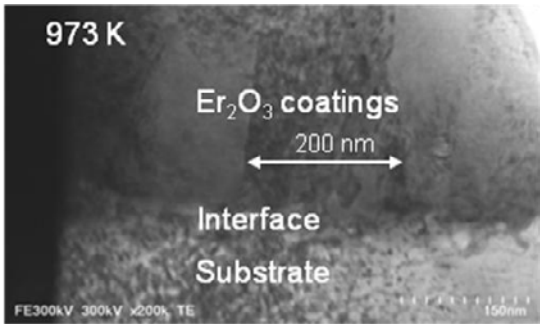

Fig. 2. STEM image of the Er_2O_3 coating fabricated by arc sputtering plasma assisted deposition (ASPAD) at room temperature and annealed at 973 K.

Given no change of grain sizes with instant increase of temperatures, the relationship between grain size and deuterium permeation flux was investigated in the Er_2O_3 coatings by permeation measurements carried out at 773, 873, and 973 K, as shown in Fig. 3. The average grain sizes of the coatings as deposited, after the measurements at 773, 873, and 973 K are 20, 90, 250, and 280 nm, respectively. Apparently, the deuterium permeation flux decreases with increasing grain size when the temperatures are kept constant, in good agreement with previous results [14]. In other words, a decrease of grain sizes results in an increase of the permeation flux of deuterium through the Er_2O_3 coatings.

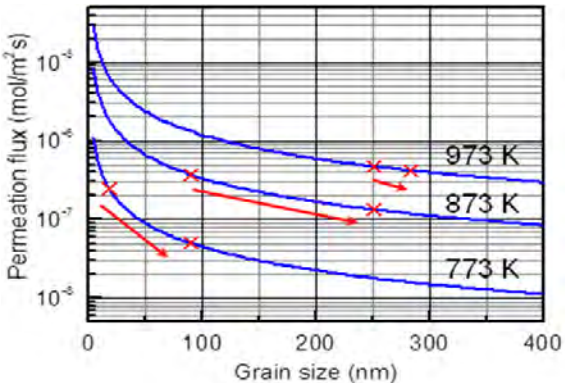

Fig. 3. Grain size dependence of deuterium permeation flux through the 1.3 μ m thick Er_2O_3 coatings. The grain sizes of the coatings were estimated by TEM images. The permeation measurements were carried out at a pressure of 8.00 x 10^{-4} Pa. In the figure, X is the permeation flux-grain size point in the plot, and the red rash arrows represent the change at constant temperatures of 773, 873, and 973 K.

3.2 Calculations of Er_2O_3 lattice constant

As initial configuration we have selected the experimental cubic structure of Er_2O_3 with a lattice constant of 1.0543 nm. The lattice parameter corresponds to a volume of 1.1719 nm^3. After relaxations of the structure with a different lattice constant approaching the experimental one (forces on atoms are less than 0.001 eV/Å), we obtained the cubic unit cell with a series of values of lattice constant and corresponding volume as a function of total energy shown in Fig. 4. After fitting with Birch-Murnaghan 3rd-order equation of state (EOS) [15], we obtained the balanced volume of 1.1727 nm^3 corresponding to the lowest total energy and the optimized lattice constant equal to 1.0545 nm, in good agreement with the experimental ones [11].

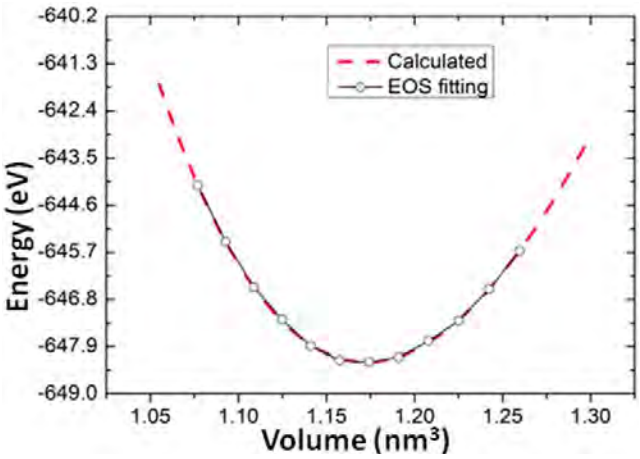

Fig. 4. Total energy configurations as a function of volume in the unit cell of Er_2O_3. The configurations are performed by ab initio calculations and Birch-Murnaghan 3rd-order EOS fitting.

3.3 Individual D atom in bulk Er_2O_3

In the lattice model described in Section 2.2, we theoretically occupied the initial positions of tetrahedral vacancies in the oxygen anion sublattice, based on a comparison of the fluorite and bixbyite structures. After relaxing the cell consisting of two primitive units, we introduced an individual neutral hydrogen atom into the cubic bixbyite structure to simulate dilute loadings of interstitial D, and calculate directly its motion by DFT. Considering a great number of interstitial sites (the tetrahedral vacancies of oxygen anion are included) in the structure, we found that D binding energy is mainly dependent on the type of the surrounding atoms, especially the nearest neighboring ones. The binding energy of an interstitial D atom in host lattice can be defined as follows:

$$E_{bind} = E_{(D/S)} - E_{(S)} - E_{(D)} \quad (1)$$

where $E_{(D/S)}$ and $E_{(S)}$ are the total energy of the system with and without an interstitial D atom, respectively. $E_{(D)}$ is the energy of D atoms in free space with spin polarization. With regard to the DFT calculations, the D binding energy

in the tetrahedral vacancies of oxygen anion sublattice were found to be strongest among the interstitial sites, equal to - 10 kJ/mol representing an exothermic reaction. This indicates that an individual interstitial deuterium atom is easily trapped in the tetrahedral vacancies. In other words, the tetrahedral interstitial site of oxygen anion sublattice belongs to the local minima position surrounded by the interstitials filled with O anions.

It is worthwhile to look into the effect of spin polarization because the total energy goes down 14~18 kJ/mol when a deuterium atom is inserted into the interstitial site of the tetrahedral. We therefore include spin polarization in the present computational scheme and apply it to an individual H_2 molecule. The calculated binding energy / cohesive energy and bond length of H_2 are 4.55 eV and 0.740 Å, corresponding well to the experimentally obtained values of 4.48 eV and 0.741 Å [16], respectively. Such calculations confirm the fact that the computational scheme considering spin polarization is reliable and sufficient to give fully converging results.

3.4 Diffusion behavior of deuterium in bulk Er_2O_3

To investigate the diffusion behavior of deuterium in bulk Er_2O_3, we employed the DFT calculations to examine trapping binding sites, diffusion pathways and diffusion activation energies for an individual D atom hopping from one local minima position to its nearest neighboring site. The diffusion activation energies (E_a) were determined by the energy difference between the local minima position and the activated state site. The hopping distance between the two energy minima in the bulk Er_2O_3 was measured to be 3.787 Å. The activated states were found by the nudged elastic band (NEB) [17] method using nine images as well as the symmetry consideration, in which forces on atoms are zero and any infinitesimal change of deuterium initial coordinate causes a finite change of atomic coordinates. The identical position of the activated states lies in the Er layer at the point equidistant from Er cations, derived by the above two methods.

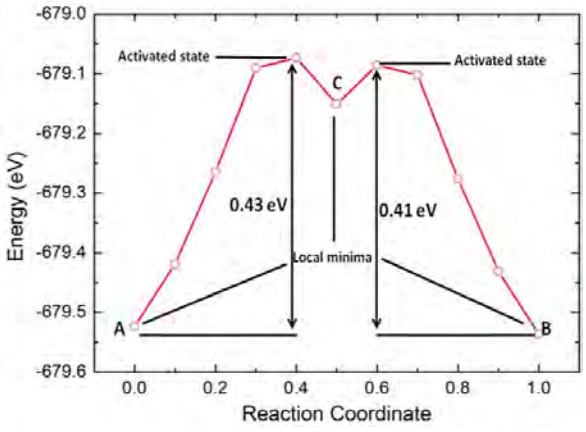

Fig. 5. Energy versus reaction coordinate obtained by the NEB method in bulk Er_2O_3. The initial separation distance between the two local minima sites is 3.787 Å.

The overall minimum energy pathway (MEP) shown in Figure 5 indicates another new local minima position (C) and barriers (A-C*, C-B*) along the path connecting the initial local minima position (A) and its crystallographic equivalent position (B). The migration barriers from A to C and from C to B are 41.5 kJ/mol (0.43 eV) and 39.6 kJ/mol (0.41 eV), respectively. Furthermore, we have as well calculated a migration barrier of 157.3 kJ/mol (1.63 eV) in the minimum energy pathway of deuterium diffusion along the direction from C to C`s crystallographic equivalent site. The maximum (157.3 kJ/mol) in the MEPs corresponds to the position where D diffuses through the highest number of bond making/breaking events in Er_2O_3, in which the corresponding activated state locates the O-layer at the site equidistant from O anions.

3.5 Relationship between diffusion and permeation of hydrogen and its isotopes through erbium oxide

The permeability of hydrogen isotopes is generally defined as the steady state diffusional transport of atoms through a material supporting a pressure difference. According to the theory reported in the paper of Marchi et al. [18], the permeability and diffusivity of hydrogen isotopes through single-layer material can be expressed in the general form as follows:

$$\Phi = \Phi_0 \exp(-\frac{E_\Phi}{RT}) \quad (2)$$

$$D = D_0 \exp(-\frac{E_D}{RT}) \quad (3)$$

where Φ (mol/m/s/$Pa^{1/2}$) and D (m^2/s) are the permeability and diffusivity of hydrogen, respectively. R (8.314 J/mol/K) is the gas constant; T (K) is the sample temperature; and E_Φ (J/mol) and E_D (J/mol) are the activation energy of permeation and diffusion of hydrogen and its isotopes, respectively. Φ_0 and D_0 are the corresponding coefficients of diffusion and permeation. Equations (2) and (3) indicate that diffusivity can represent permeability to a large extent since they are similar in magnitude over a wide range of temperatures in the transport of hydrogen and its isotope atoms through the material.

According to Ref. [14], the permeation flux under steady-state conditions through a single layer barrier can be expressed as

$$J = KD\frac{P^{1/2}}{d} \quad (4)$$

where J is the permeation flux per unit area of material of thickness d (m); K is the Sieverts` constant and P the driving pressure of hydrogen and its isotopes. Since $\Phi = KD$, Eq. (4) in combination with Eq. (2) gives the relationship between the permeation flux (J) and the activation energy (E_D) of diffusion under steady-state conditions, i.e.

$$J = \Phi P^{1/2} / d = \Phi_o \exp(-\frac{E_D + E_S}{RT}) P^{1/2} / d \quad (5)$$

where E_s (J/mol) is the heat of solution of hydrogen atoms in the single-layer material or oxide with a thickness of d (m), and E_Φ is defined as the sum of E_S and E_D. It is obvious that diffusion plays an important role in the process of permeation of hydrogen and its isotopes based on the relationship of permeation flux J and diffusion activation energy E_D given in Eq. (5). With the aim of understanding the mechanism of permeation it is therefore reasonable to study first the diffusion behavior of hydrogen and its isotopes through erbium oxide.

In experiments on the permeation of deuterium, the diffusion activation energy was estimated from an Arrhenius plot of temperature versus diffusivity, D being obtained by measuring the time-lag t_l(s) with relationship t_l (s) = $d^2/6D$, as described in [19]. The measured activation energy of approximate 20.0 kJ/mol [14] is of similar order of magnitude with the D diffusion energy barrier of 157.3 kJ/mol evaluated by the NEB method as implement in *ab initio* DFT calculations. The discrepancy in activation energies is partly attributed to the fact that nanostructured Er_2O_3 thin films were used in the experiments while bulk Er_2O_3 was adopted in the computational simulations. Although the Er_2O_3 thin films were prepared by the ASPAD method with the aim of achieving good performance as TPB coatings, they had very large defects, i.e. grain boundaries (GB`s) within the nanostructure as revealed by Fig. 1. A GB represents an environment where the symmetry of a crystal is terminated. Apart from the diffusion of hydrogen and its isotopes through the bulk of erbia, diffusion is likely to occurs also via the large defect GB`s.

In order to elucidate the hydrogen behavior in erbium oxide, we purposely conducted *ab initio* DFT calculations in the bulk Er_2O_3 assuming an ideal crystal structure. The volume and geometry relaxations in the calculations show that an individual interstitial D prefers to bind in the tetrahedral interstitial sites of O anion sublattice (local minima). MEP found by the NEB method shows the diffusion pathway of deuterium hopping from one local minima to the nearest neighboring one. Most important, the maximum energy difference between the minimum site and the estimated transition state (saddle point) determined in this way is 157.3 kJ/mol, and somewhat higher than the experimental value of 20.0 kJ/mol. This indicates that at the grain boundary the activation energy for hydrogen isotope (deuterium) diffusion decreases because of the different diffusion pathway as predicted by MEP. In other words, the diffusivity of deuterium will be increased if we introduce GB into the perfect bulk Er_2O_3. On the basis of Eq. (5), which relates the permeation flux J to the diffusivity D, the permeability will increase correspondingly. Actually, GB's existing in Er_2O_3 coatings degrade the grain sizes due to loss of bulk area and lead to an increase of permeation flux, in good agreement with the experimental data given in Fig. 3. It is intuitively considered that diffusion and permeation of hydrogen and its isotopes through erbium oxide are likely to occur predominately through grain boundaries rather than grains. In addition, it is worth noting that the activation energy obtained in the deuterium permeation is still large and high concentration to that derived by the DFT calculations. This suggests that the Er_2O_3 coatings prepared by the ASPAD method possess high performance as required for TPB coatings. As shown in Fig. 3, the growth of grain size enhances the ability of the coatings to suppress deuterium diffusion and permeation. As the grains become very large, the permeability of deuterium will decrease because of the absence of grain boundaries. That is, the activation energy is maximized when the Er_2O_3 coatings become a perfect crystal without any grain boundary as assumed in the DFT calculations.

4. Conclusions

In this study, the mechanism of tritium permeation through Er_2O_3 has been investigated by the experimental measurements and the computational simulations. We have prepared Er_2O_3 coatings of 1.3 μ m in thickness by the ASPAD method and characterized the coatings via deuterium permeation measurements. From the experiments, we concluded that a grain boundary nanostructure exists in the Er_2O_3 coating and estimated the diffusion activation energy to be 20.0 kJ/mol. Additionally, *ab initio* DFT calculations based on transition state theory were carried out for interstitial deuterium in an ideal supercell assuming cubic bixbyite Er_2O_3. Calculated and fitted lattice constants of Er_2O_3 showed good agreement with the experimental data. Also the minimum energy sites, diffusion pathways and diffusion activation barriers for an individual D atom were found by MEP calculations. The local minima position is found located in the tetrahedral interstitial site of oxygen anion sublattice. The results indicate that the preferred hopping path of individual D atoms is from one local minima position to its nearest neighboring site. The maximum diffusion activation energy resulting from the MEP calculation is 157.3 kJ/mol and higher than that obtained experimentally (20.0 kJ/mol). This discrepancy is attributed to grain boundary structures found in the Er_2O_3 coatings. GB`s lead to pathways of hydrogen diffusion different from MEP derived by DFT calculations. They provide useful information on tritium permeation mechanism in erbium oxide. Additionally, it appears that diffusion and permeation of hydrogen and its isotopes through the Er_2O_3 coatings will probably take place through grain boundaries rather than grains. This

conclusion is drawn from *i*) the comparison of the activation energy between diffusion experiments and DFT simulations *ii*) the interdependence of hydrogen and its isotope diffusion and permeation, and *iii*) the relationship between the permeation flux and grain size during the measurement of deuterium permeation.

Acknowledgements

This work was supported in part by GoNERI, the Global Center of Excellence (G-COE) Program of the Nuclear Education and Research Initiative of the Japan Society for the Promotion of Sciences (JSPS).

References

[1] V.A. Maroni, Tritium Processing and Containment Technology for Fusion Reactors: Perspective and status, Proc. Second Topical Meeting on the Technology of Controlled Nuclear Fusion, USERDA Report CONF -760935-P3 (1976) P. 799.
[2] F. N. Flakus, At. Energy Rev. **13**, 587 (1975).
[3] G.W. Hollenberg, E.P. Simonen, G. Kalinin, A. Terlain, Fusion Eng. Des. **28**, 190 (1995).
[4] Z. Yao, A. Suzuki, D. Levchuk, T. Chikadaa, T. Tanaka, T. Muroga, T. Terai, J. Nucl. Mater. **386-388**, 700 (2009).
[5] Z. Yao, A. Suzuki, T. Muroga, K. Katahira, J. Nucl. Mater. **329-333**, 1414 (2004).
[6] MATL2 (Materials oriented Little Thermodynamic database 2), Version 1.06, The Japan Society of Calorimetry and Thermal Analysis (Kagaku Gijutsu Sha, Japan, 1992).
[7] T. Chikada, A. Suzuki, Z. Yao, A. Sawada, T. Terai, T. Muroga, Fusion Eng. Des. **82**, 2572 (2007).
[8] T. Chikada, A. Suzuki, T. Tanaka, T. Terai, T. Muroga, Fusion Eng. Des. **85**, 1537 (2010).
[9] K. Honkala, A. Hellman, I.N. Remedeiakis, Á. Logadóttir, A. Carlsson, S. Dahl, C.H. Christensen, J.K. Nørskov, Science **507**, 555 (2005).
[10] D.S. Sholl, J. Alloy. Compd. **446-447**, 462 (2007).
[11] Y.E. Bogatov, A.K. Molodkin, M.G. Safronenko, Y.Y. Nevyadomskaya, Russ. J. Inorg. Chem. **39**, 211 (1994).
[12] G. Kresse, J. Furthmuller, Phys. Rev. B **54**, 11169 (1996).
[13] H.J. Monkhorst, J.D. Pack, Phys, Rev. B **13**, 5188 (1976).
[14] T. Chikada, A. Suzuki, H. Maier, T. Terai, T. Muroga, Fusion Sci. Technol. **60**, 389 (2011).
[15] F. Birch, Phys. Rev. **71**, 809 (1947).
[16] B.G. Johnson, P.M.W. Gill, J.A. Pople, J. Chem. Phys. **98**, 5612 (1993).
[17] H. Jónsson, G. Mills, K. W. Jacobsen, C*lassical and Quantum Dynamics in Condensed Phase Simulations*, edited by B. J. Berne, G. Ciccotti and D. F. Coker (World Scientific, Singapore, 1998), pp. 385-404.
[18] C. San Marchi, B.P. Somerday, S.L. Robinson, Int J Hydrogen Energy, **26**, 597 (2001).
[19] T. Chikada, A. Suzuki, T. Kobayashi, H. Maier, T. Terai, T. Muroga, J Nucl. Mater. **417**, 1241 (2011).

Solubility of hydrogen isotopes in zirconia ceramics

Kenichi HASHIZUME[1)], Kosuke OGATA[1)], Satoshi AKAMARU[2)], and Yuji HATANO[2)]

1) *Interdisciplinary Graduate School of Science and Engineering, Kyushu University, Hakozaki 6-10-1, Fukuoka 812-8581, Japan.*

2) *Hydrogen Isotope Research Center, University of Toyama, Gofuku 3190, Toyama 930-8555, Japan.*

(Received: 25 May 2012 / Accepted: 5 October 2012)

The hydrogen solubility in zirconia (yttria stabilized zirconia, YSZ) using a tritium imaging plate (IP) technique has been measured in a temperature region ranging from 673K to 973K. The tritium distribution in the zirconia specimens was nearly uniform suggesting an equilibrated dissolution. The hydrogen solubility in specimens were rather low (around ppm or below) and showed Arrhenius type temperature dependence, while it seemed to be independent of Y contents.

Keywords: Zirconia, YSZ, Tritium Gas Exposure, Imaging Plate Technique, Hydrogen Solubility

1. Introduction

Oxide materials are used in fusion reactors as plasma diagnosis windows, electric insulators and tritium permeation barriers [1-7]. Tritium dissolution and permeation in the oxide materials are a significant issue from a stand point of tritium retention and leakage. However, compared with metals and alloys, tritium (hydrogen) solubilities in oxides have not been studied well, because very low hydrogen solubility in oxides made difficult to detect hydrogen in them [8].

In this study, we have tried to examine the hydrogen solubility in Y_2O_3 stabilized ZrO_2(YSZ) using a rather high concentration tritium gas and an imaging plate (IP) technique. The single- and poly-crystalline YSZ specimens were used in order to clarify the influences of grain boundary and Y content on hydrogen solubility.

2. Experimental

Mirror polished single crystal plates ($10 \times 5 \times 0.5$ mm^3) of cubic zirconia (13%Y_2O_3-ZrO_2(100)) from Dalian Keri Optoelectronic Technology Co. Ltd. were used as specimens. Polycrystalline specimens were prepared with conventional sintering process using PSZ powders manufactured by Toso Co. Ltd (grades: TZ-3Y, TZ-4Y, TZ-6Y, TZ-8Y and TZ-10Y, Y contents of which ranged from 6 % (TZ-3Y) to 20 % (TZ-10Y)). The each grade powder was die-pressed into disks and then isostatically pressed at 200 MPa. The disks were sintered at 1773 K for 20 h. The size of the disk specimens was about 8 mm in diameter and 1 mm in thickness. The densities of the disks exceeded 95 % of theoretical ones for all grades. The crystal structure of the disk specimens characterized by X-ray diffraction was tetragonal for TZ-3Y, the mixture of tetragonal and cubic for TZ-4Y, and cubic for TZ- 6Y, 8Y and 10Y as shown in Fig.1. The single- and poly-crystalline specimens were heated at 873 K for 1 h in a vacuum to remove an initially dissolved hydrogen, and then exposed to 133 Pa of tritium-deuterium gas mixture (T/(T+D)~ 0.17) at temperatures ranging from 673 to 973 K for 1-5 h. No apparent pressure change was observed during the tritium gas exposure. After that, the specimens

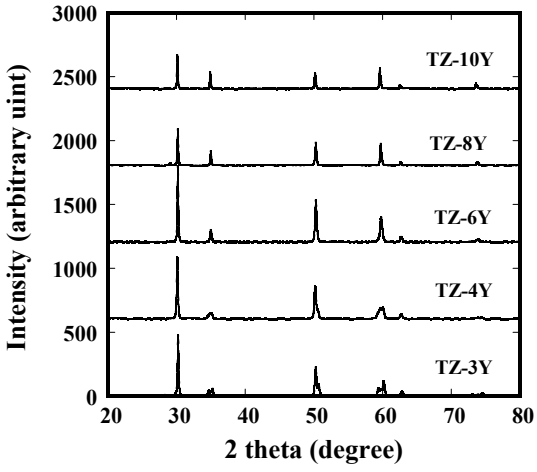

Fig.1 XRD spectra of polycrystalline specimens

author's e-mail:hashi@nucl.kyushu-u.ac.jp

were quenched down to fix tritium distribution. After the specimen surfaces were exposed to IP (TR2025, GE Health Care Co.) for 15 min in order to measure surface tritium densities, the specimens were cut in halves with a diamond saw, and the cross sections of the specimens were exposed to IP for 15 h. The details of this procedure were described in elsewhere [7]. Photo-stimulated luminescence (PSL) intensities were obtained from IP Reader (FLS7000, Fujifilm). The PLS values were converted to tritium activities by calibration with a tritium standard sample (ART 123A, American Radiolabeled Chemicals, Inc.). Hydrogen surface density and solubility were evaluated from the tritium activity and isotope abundance ratio.

3. Results and Discussion

Figure 2 shows the examples of the PSL images of specimen surface and cross section. The PSL intensities (tritium activities) seemed to be rather uniform except for much intense parts which should be surface contaminations, particularly in specimen edges where were not polished. Since the high PSL intensity area was limited around the edges, these PSD data were omitted. The errors without the contaminations were estimated to be ±30 % for all specimens. The PSL images of the cross sections suggested an equilibrated dissolution of tritium.

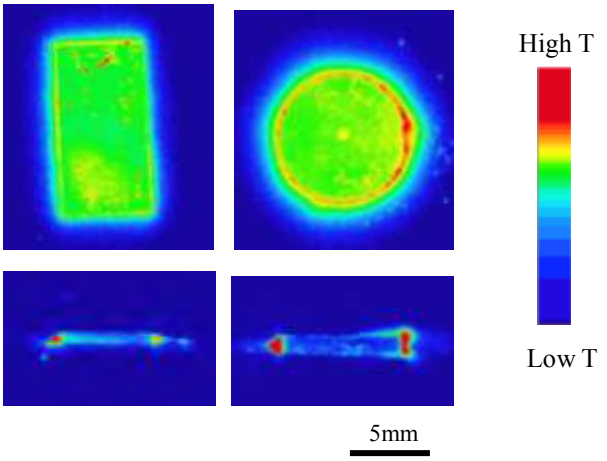

Fig. 2 PSL images of surface and cross section. Single crystal plate (left) and polycrystalline disk (right) exposed to D-T gas at 873 K for 1 h.

Figure 3 shows the tritium activities (hydrogen surface densities) on the specimens exposed to the tritium gas. The amount of tritium uptaken on the specimen surface increased with increasing temperature up to 2×10^5 Bq/cm^2 (equivalently ~10^{15} H/cm^2) and almost saturated at 873 K. At 973 K the tritium density on the single crystalline surface decreased, where tritium desorption should be more dominated than its adsorption. In any case, no clear difference appeared among the specimens.

Figure 4 shows the tritium activities in the single- and poly-crystalline specimens which increase with the exposure temperature, which appear to be very similar to that of its surface density. Figure 5 also shows the tritium activities in poly-crystalline specimens against an oxygen deficiency x which was simply calculated from Y contents of YSZ. No clear difference in tritium activities appeared for the single- and poly-crystalline specimens. Several studies previously suggested that the hydrogen solubility in grain boundary was high, compared with the oxide grain inside. Unfortunately, the spatial resolution of IP technique is not high enough to detect tritium only in the grain boundary. The influence of grain boundary would be examined in the future study. In any case, it should be safely concluded that no clear influence of grain boundary and O deficiency (Y content) in the present experimental condition.

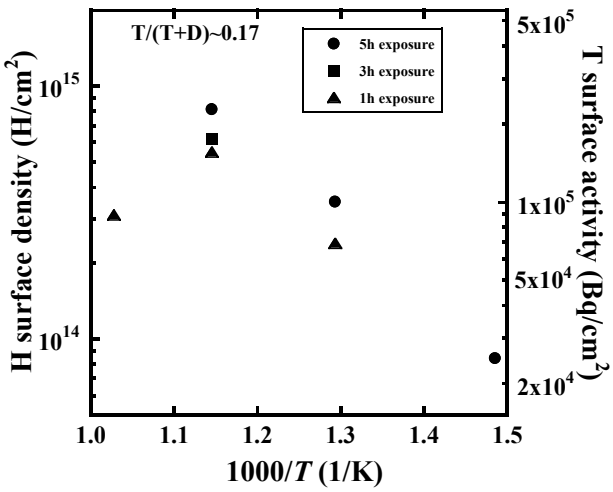

Fig. 3 Hydrogen isotope surface density (T surface activity) on single crystal specimen.

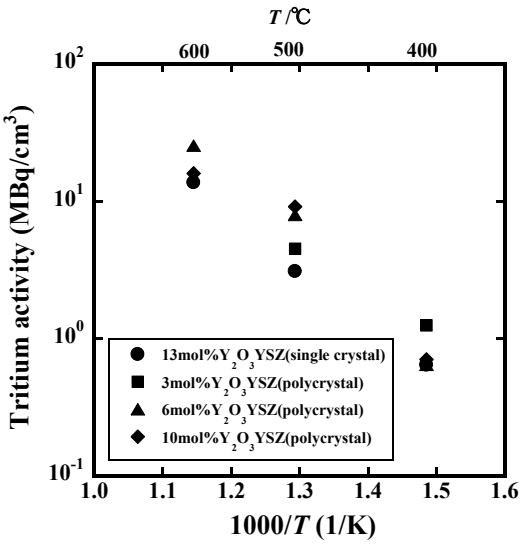

Fig. 4 Tritium activities in single- and poly-crystalline specimens (5 h exposure to D-T gas).

The color of the specimens after the tritium gas exposure slightly changed to be brownish. Not only the characteristics of surface but that of bulk might be influenced by the reductive reaction. However, the effect of this reaction is not discussed here because the adsorption reaction of hydrogen is too complicated to make a quantitative analysis.

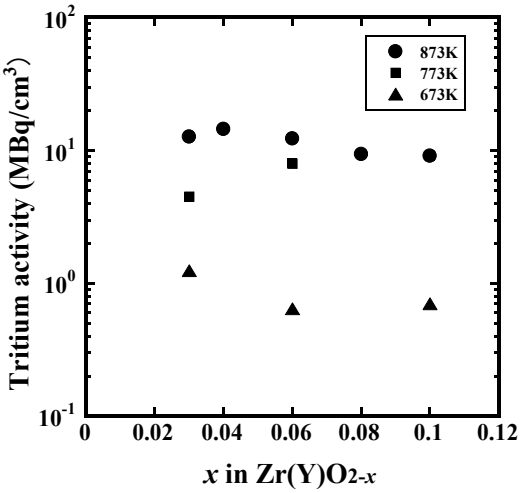

Fig. 5 Tritium activities vs O deficiency x in poly-crystalline specimens.

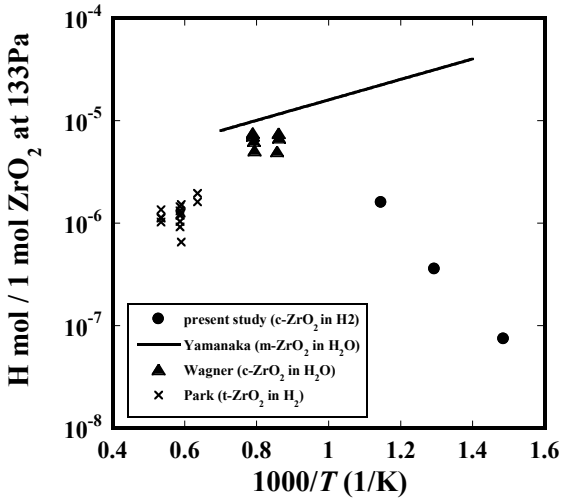

Fig. 6 Comparison of hydrogen solubility in zirconia (5h-exposed single-crystal for the present data).

The present data on hydrogen solubility are compared with literature data [9-12] in Fig. 6. The all literature data have been converted to those at a pressure of 133 Pa of hydrogen containing gases (H_2 or H_2O), based on relations $s \propto p_{H_2}^{1/2}$ and $s \propto p_{H_2O}^{1/2}$. As shown in Fig. 6, the values of solubility and its temperature dependence are rather scattered. Reasons of the scattering are not clear at present stage, but might be attributed to differences in experimental conditions such as dissolution temperatures, crystal structures of zirconia (monoclinic, tetragonal and cubic) and hydrogen containing gas species (H_2 or H_2O).

The present study focused on the solubility of hydrogen in zirconia ceramics. The dependence of hydrogen amounts uptaken on surface and bulk in the oxides becomes clear using the IP technique. This also indicates that the IP technique was a useful tool to study the kinetics of hydrogen dissolution and hydrogen solubility in various oxides.

4. Summary

Using an imaging plate (IP) technique and high concentration tritium gas (T/(T+D)~0.17), tritium solubility in zirconia ceramics (YSZ) was measured in a temperature region ranging from 673 K to 973 K. The surface activity of tritium on the specimens increased with increasing temperature and almost saturated at 873 K, which reached 2×10^5 Bq/cm^2 (equivalently ~10^{15} H/cm^2).

The hydrogen solubility in the oxides also increased with increasing temperature. No clear difference in the solubility appeared between single crystal and polycrystalline specimens and among the specimens with various Y contents.

5. Acknowledgements

The present study was partly supported by the usage/research program of the Hydrogen Isotope Research Center, University of Toyama (HRC2010-04) and by the Sohoko Research Program of National Institute for Fusion Science (NIFS11KUR014) .

6. References

[1] F. W. Clinard, Jr., G. F. Hurley, J. Nucl. Mater., **103&104**, 705 (1981).
[2] W. Dienst, T. Fett, R. Heidinger, H.D. Rhörig, B. Shultz, J. Nucl. Mater., **174**, 102 (1990).
[3] R. Heidinger, J. Nucl. Mater., 179-181 (1991) 64.
[4] E.R. Hodgson, Nucl. Instr. Met. Phys. Res., **B191**, 744 (2002).
[5] A. Ibarra, E.R. Hodgson, Nucl. Instr. Met. Phys. Res., **B218**, 29 (2004) .
[6] Y. Hatano, K. Zhang, K. Hashizume, Physica Scripta, **T145**, 0140144 (2011).
[7] K. Hashizume, K Ogata, M. Nishikawa, T. Tanabe, A. Abe, S. Akamaru, Y Hatano, Proceeding of ICFRM-15, to be published.
[8] T. Norby, Solid State Ionics, **40/41**, 857 (1990) .
[9] V.C. Wagner, Ber. Bunsenges. Physik Chem., **72**, 778 (1968) .
[10] K. Park, D.R. Olander, J. Am. Ceram. Soc., **74**, 72 (1991) .
[11] S. Yamanaka, T. Nishizaki, M. Uno, M. Katsura, J. Alloys Compd., **293-295**, 38 (1999) .
[12] M. Miyake, M. Uno, S. Yamanaka, J. Nucl. Mater., **270**, 233 (1999) .

Numerical Simulation of Detritiation System for NIFS with Commercial Catalyst and Adsorbent

K. Munakata[a,*], K. Hara[a], T. Sugiyama[b], K. Kotoh[c], M. Tanaka[d] and T. Uda[d]
*kenzo @gipc.akita-u.ac.jp
[a] Faculty of Engineering and Resource Science, Akita University, Tegata-gakuen-machi 1-1, AKITA 010-8502 Japan
[b] Nagoya University, Furo-cho Chikusa-ku, Nagoya464-8603, Japan
[c]Kyushu University, Motooka 744, Nishi-ku, Fukuoka 819-0395, Japan
[d]National Institute for Fusion Science, Oroshi-cho 322-6, Toki, Gifu 509-5292 Japan

(Received: 9 May 2012 / Accepted: 18 August 2012)

Establishment of tritium recovery system is necessary to prevent its leakage to the working area. The catalytic oxidation and adsorption is the most reliable method to recover tritium released into the working area of those facilities. Therefore, there is a necessity that the tritium recovery system with large-scale and higher integrity is developed and constructed. For this purpose, it is required to obtain and accumulate updated database for chemical engineering design based on most recently commercial and available catalysts and absorbents. In this work, we selected a catalyst and an adsorbent, and examined their adsorption characteristics for water vapor and performance of catalytic oxidation of hydrogen. Adsorption isotherms were studied with a volumetric gas adsorption instrument. Various adsorption models were tested to correlate the experimental isotherms. Breakthrough experiments were also performed to assess adsorption performances. Furthermore, numerical simulations were performed based on the obtained experimental results.

Keywords: detritiation, catalyst, adsorbent, membrane dehumidifier, numerical simulation, mass balance

1. Introduction

A large amount of tritium would be handled as fuel in nuclear fusion power plants. In these facilities, tritium is confined in multiple confinement barriers. However, if unexpected accidents take place, tritium leaks to the working areas. Thus, establishment of tritium recovery system is necessary to prevent its leakage to the working area. The catalytic oxidation and adsorption is the most reliable method to recover tritium released into the working area of those facilities. In this method, tritium gas is oxidized with catalysts, and then tritiated water vapor is collected by adsorbents.

It is planned to conduct deuterium plasma experiments in National Institute for Fusion Science (NIFS). In these experiments, D-D fusion reactions take place and tritium is produced, and thus the release of tritium to the environment has to be minimized. Therefore, there is a necessity that the tritium recovery system with large-scale and higher integrity is developed and constructed. However the previous experimental and engineering database [1] obtained by several researchers on absorbents cannot be applied to the design of updated tritium recovery system since the absorbents used in the previous studies are not been produced any longer in the industry. Therefore, it is required to obtain and accumulate updated database for chemical engineering design by testing most recently commercial and available catalysts and absorbents in experiments. In this work, we selected an adsorbent and examined its adsorption characteristics for water vapor.

2. Catalyst and adsorbent

The authors went through previous literature and inquired about catalysts or adsorbents used for detritiation systems that are being used in several research institutes. However, the result of such survey reveals that the production or model number of the materials such as catalyst and adsorbent is not clear, and they are not considered to be available in the present industrial market. Additionally, conduction of new screening tests, in order to search feasible catalysts or adsorbents, is time consuming. It should be also noted that feasibility tests of catalysts and adsorbents are not limited within catalytic activity or adsorption performance; durability in long-time use, mechanical stability, ease in their procurement with large quantities are important points as well.

For this reason, the authors selected a catalysts and an adsorbent, which are ones of the most widely and generally used in industries and are credited and reputed by engineers and designers as well.

In terms of catalyst, the authors selected a Pt/alumina catalyst, DASH520, manufactured by N. E. Chemcat Co., which is widely used in industries for various purposes. The catalyst was deposited with 4.1g/L of platinum. The average diameter of the catalyst is 3.25 mm. the packing density was 770 g/L.

With regard to the adsorbent, the author selected a MS5A adsorbent that is produced by Union Showa Co. in Japan (subsidiary company of Union Carbide Co.) and is widely used in industries. The production of zeolites in Union Showa Co. is licensed by Union Carbide Co, and the pellet-type MS5A adsorbent could be one of the world-standard adsorbents.

Corresponding author: kenzo@gipc.akita-u.ac.jp

3. Experimental

3.1 Catalytic oxidation of hydrogen

The experiments were performed under the steady state condition. The catalysts were packed in a reactor made of quartz. The temperature of the reactor was controlled with the constant temperature bath. Argon gas was used as a carrier gas. The argon gas containing hydrogen (about 300-800 ppm) and oxygen (20%) was introduced to the reactor.

Experiments were also performed using wet process gases which contained water vapor (about 300-1000 Pa) in order to study the influence of coexistent water vapor on the catalytic activity for oxidation of hydrogen. The concentrations of hydrogen at inlet and outlet stream of the reactor were measured with a gas-chromatograph (GC-8A) manufactured by SHIMAZU Co.

3.2 Water adsorption

The authors studied adsorption behavior of water vapor on the DASH520 catalyst and MS5A adsorbent, as well. The adsorption isotherms of water vapor on the DASH520 catalyst and MS5A adsorbent were measured using a volumetric gas adsorption instrument, BELSORP-max, manufactured by BEL Japan Inc. The instrument is designed for measurement of wide range of adsorption isotherms on surface area and pore size distribution analysis.

3.3 Summary of experimental results

Conversion rate R_c and over all mass transfer capacitance for oxidation (based on surface reaction) in dry condition $k_{r,ox,0}$a were computed to assess catalytic performance. R_C and $K_{F,ox}$ are defined as

$$S_V = Q / V \tag{1}$$

$$R_C = 100 \times (C_{in} - C_{out}) / C_{in} \tag{2}$$

Table 1 Parameters optimized for L-F equation.

	m	DASH520	MS5A
$q_{s,m}$ [mol/g]	1	1.52×10^{-4}	19.8
$b_{0,m}$ [(mol/(g·Pa))$^{1/u_i}$]		3.86×10^{-13}	2.02×10^{-15}
E_m [J/(mol·K)]		39100	44700
v_m [-]		3.16	0.908
$q_{s,m}$ [mol/g]	2	4.58	0.00703
$b_{0,m}$ [(mol/(g·Pa))$^{1/u_i}$]		1.49×10^{-22}	8.90×10^{-20}
E_m [J/(mol·K)]		75100	92000
v_m [-]		1.76	2.67
$q_{s,m}$ [mol/g]	3	3.57×10^{-4}	0.00191
$b_{0,m}$ [(mol/(g·Pa))$^{1/u_i}$]		1.43×10^{-7}	1.42×10^{-9}
E_m [J/(mol·K)]		38800	36100
v_m [-]		3.25	4.05
$q_{s,m}$ [mol/g]	4	1.70×10^{-5}	0.000485
$b_{0,m}$ [(mol/(g·Pa))$^{1/u_i}$]		6.62×10^{-10}	4.98×10^{-12}
E_m [J/(mol·K)]		34800	64400
v_m [-]		1.93	6.33
$q_{s,m}$ [mol/g]	5	2.12×10^{-3}	-
$b_{0,m}$ [(mol/(g·Pa))$^{1/u_i}$]		9.85×10^{-9}	-
E_m [J/(mol·K)]		32800	-
v_m [-]		2.09	-

$$k_{r,ox,0}a = S_V \ln\left(C_{in} / C_{out}\right) \tag{3}$$

The mass transfer capacitances for oxidation of hydrogen (based on surface reaction) of DASH520 is expressed as

$$k_{r,ox,0}a = 1.16\times10^5 \exp\left(-25400/(RT)\right) \tag{4}$$

The experimental adsorption isotherms of water vapor on the DASH520 catalyst and MS5A adsorbent were found to be successfully correlated using a sort of multi-site Langmuir-Freundrich equation:

$$q_{ad} = \sum_{m=1}^{n} \frac{q_{ad,s,m} b_m p^{v_m}}{1 + b_m p^{v_m}} \tag{5}$$

$$b_m = b_{0,m} \exp(E_m / RT) \tag{6}$$

Parameters (optimized by non-linear least squares analysis) for DASH520 catalyst (n=5) and MS5A adsorbent (n = 4) are listed in Table 1.

Experimental results on the catalytic oxidation of hydrogen in wet gases reveal that coexistence of water vapor severely inhibits the catalytic oxidation of hydrogen. It was found that the mass transfer coefficient for catalytic oxidation in wet gases is expressed as a function of the amount of water adsorbed on the catalyst substrate:

$$\frac{k_{r,ox}a}{k_{r,ox,0}a} = 0.476\exp\left[-\left(643 q_{ad}\right)^{25.1}\right] + 0.524\exp\left[-\left(456 q_{ad}\right)^{5.00}\right] \tag{7}$$

4. Simulation procedure and mass balance

The basic assumption on catalyst and adsorption bed is one-dimensional dispersed plug flow in packed bed [2]. Chemical reactions such as catalytic oxidation of hydrogen isotopes, adsorption of water vapor, isotope exchange reaction were taken into consideration. The mass balance equations in catalyst beds are expressed as follows (for adsorption bed, catalytic reactions are not considered):

・Mass balance of Q_2 (i = H, D or T) in gas phase

$$\frac{\partial(uC_{Q2,i})}{\partial z} + \varepsilon\frac{\partial C_{Q2,i}}{\partial t} + \varepsilon\frac{\partial}{\partial z}\left(D_L\frac{\partial C_{Q2,i}}{\partial z}\right) = -k_{F,ox}aC_{Q2,i} \tag{8}$$

$$\frac{1}{k_{F,ox}a} = \frac{1}{k_{r,ox}a} + \frac{1}{k_g a} \tag{9}$$

・Mass balance of Q_2O (i = H, D or T) in gas phase

$$\frac{\partial(uC_{Q2O,i})}{\partial z} + \varepsilon\frac{\partial C_{Q2O,i}}{\partial t} + \varepsilon\frac{\partial}{\partial z}\left(D_L\frac{\partial C_{Q2O,i}}{\partial z}\right) \tag{10}$$

$$= k_{F,ox} a C_{Q2,i} - k_{F,ad,i} a\left(c_{Q2O,H} + c_{Q2O,D} + c_{Q2O,T}\right)\theta_1 + k_{F,ex} a \theta_2$$

・Mass balance of Q_2O (i = H, D or T) in solid phase

$$\gamma \frac{\partial \bar{q}_{Q2O,i}}{\partial z} = k_{F,ad,i} a\left(c_{Q2O,H} + c_{Q2O,D} + c_{Q2O,T}\right)\theta_1 - k_{F,ex} a \theta_2 \tag{11}$$

$$\bar{q}_{Q2O,i} = q_{ad,Q2O,i} + q_{st,Q2O,i} \tag{12}$$

$$\theta_1 = c_{Q2O,i} - \frac{\left(c_{Q2O,H} + c_{Q2O,D} + c_{Q2O,T}\right)\bar{q}_{Q2O,i}}{\bar{q}_{Q2O,H} + \bar{q}_{Q2O,D} + \bar{q}_{Q2O,T}} \tag{13}$$

$$\begin{aligned} &when\ \ c_{Q2O,H} + c_{Q2O,D} + c_{Q2O,T} \geq 0 \\ &\theta_2 = c_{Q2O,i} / \left(c_{Q2O,H} + c_{Q2O,D} + c_{Q2O,T}\right) \\ &when\ \ c_{Q2O,H} + c_{Q2O,D} + c_{Q2O,T} < 0 \\ &\theta_2 = \bar{q}_{Q2O,i} / \left(\bar{q}_{Q2O,H} + \bar{q}_{Q2O,D} + \bar{q}_{Q2O,T}\right) \end{aligned} \tag{14}$$

The heat balance equation is given as

$$\begin{aligned} &\frac{\partial\left(u\rho_g c_{p,g} T\right)}{\partial z} + \varepsilon \frac{\partial\left(\rho_g c_{p,g} T\right)}{\partial t} + \gamma \frac{\partial\left(c_{p,s} T\right)}{\partial t} \\ &+ \frac{\partial}{\partial z}\left(\lambda_{eff} \frac{\partial T}{\partial z}\right) \\ &= (k_{F,ox,H} C_{Q2,H} + k_{F,ox,D} C_{Q2,D} + k_{F,ox,T} C_{Q2,T}) a \Delta H_{ox} \\ &+ k_{F,ad,T} a (C_{Q2O,H} + C_{Q2O,D} + C_{Q2O,T} - C^*) \Delta H_{ad} \\ &- 4 h_w (T - T_{air}) / D_b \end{aligned} \tag{15}$$

The assumptions used in the modeling of membrane dehumidifier are: (i) the feed gas is a binary mixture of water vapor and air, (ii) the pressure drops and diffusive mass transfer in the feed side and permeation side are negligible, (iii) laminar films on the surface of the membrane are negligible and (iv) the system is adiabatic and the temperature of the gas mixture is constant [3]. The molar fluxes of penetrants through the dense and porous layers can be expressed as,

$$\begin{aligned} N_{d,i} = D_{d,i} \frac{dC_{d,i}}{dl} &= \frac{D_{d,i} S_w}{\delta_d}\left(p_{h,i} - p_{l,i}\right) \\ &= P_{d,i}\left(p_{h,i} - p_{l,i}\right), \end{aligned} \tag{16}$$

$$N_{2,i} = D_{2,i} \frac{dC_{2,i}}{dl}. \tag{17}$$

In Eq. (16), a constant pressure gradient is assumed and a permeance is applied because the thickness of the dense layer is very thin and the value is not disclosed by the vendor. The diffusion coefficient $D_{2,i}$ in Eq. (17) is estimated as Knudsen's diffusion coefficient.

Polyimide membranes absorb moisture easily at high pressures of water vapor. The sorption capacity of water vapor in equilibrium increases almost linear with the activity of water vapor [5]. In the present study, water vapor content in the matrix of support layer in equilibrium is expressed by the following equation.

$$\bar{C}'_{2,w} = a_{sorp}\left(p_{2,w}/p_s\right) \tag{18}$$

Sorption rate of water vapor is, then, expressed as

$$r = \varepsilon V'_2 k_{sorp}\left(\bar{C}'_{2,w} - C'_{2,w}\right). \tag{19}$$

It is known that a very low partial pressure of a condensable species, such as water vapor in the feed stream, can significantly reduce the permeability of the other constituent relative to its permeability as a pure component. In the present study, the permeance of air is expressed by the following equation at relatively low water vapor activity.

$$P_{d,a} = P_{d,a,0} - a_p\left(p_{h,w}/p_s\right) \tag{20}$$

The membrane is divided into small sections along the axis, and a kind of plate model was applied. The total mass balances are expressed as

$$V_{1,j} \frac{dC_1}{dt} = 0 = q_{1,j} - q_{1,j+1} - N_{12,j} S_1, \tag{21}$$

$$\varepsilon V_{2,j} \frac{dC_{2,j}}{dt} = N_{12,j} S_1 - N_{23,j} S_2 - r_j \tag{22}$$

and

$$V_{3,j} \frac{dC_3}{dt} = 0 = q_{3,j+1} - q_{3,j} + N_{23,j} S_2. \tag{23}$$

The mass balances for each component are, then,

$$V_{1,j} C_1 \frac{dx_{1,j}}{dt} = q_{1,j} x_{1,j} - q_{1,j+1} x_{1,j+1} - N_{12,w,j} S_1, \tag{24}$$

$$\varepsilon V_{2,j} \frac{dC_{2,w,j}}{dt} = N_{12,w,j} S_1 - N_{23,w,j} S_2 - r_j, \tag{25}$$

$$\varepsilon V_{2,j} \frac{dC_{2,a,j}}{dt} = N_{12,a,j} S_1 - N_{23,a,j} S_2, \tag{26}$$

$$(1 - \varepsilon) V_{2,j} \frac{dC'_{2,w,j}}{dt} = r_j \tag{27}$$

and

$$V_{3,j} C_3 \frac{dx_{3,j}}{dt} = q_{3,j+1} x_{3,j+1} - q_{3,j} x_{3,j} + N_{23,w,j} S_2. \tag{28}$$

Equations (25) and (26) represent the mass transfers in the pore of the support layer. On the other hand, Eq. (27) represents the concentration change of water vapor in the matrix of the support layer. Equations (29)-(31) and the relationships, $N_{12,w,j} = N_{A,w} = N_{B,w}$ and $N_{23,w,j} = N_{C,w}$ give Eqs. (32) and (34) as fluxes in which the mass conservations across the membrane is taken into account. In the same way, Eqs. (33) and (35) are obtained for the air.

$$\begin{aligned} N_{A,w} &= \frac{D_{d,w}}{\delta_d}\left(S_w p_h x_{1,j} - S_w C^{int}_{2,w,j} RT\right) \\ &= P_{d,w}\left(p_h x_{1,j} - C^{int}_{2,w,j} RT\right) \end{aligned} \tag{29}$$

$$N_{B,w} = \frac{2D_{2,w}}{\delta_2}\left(C_{2,w,j}^{int} - C_{2,w,j}\right) \quad (30)$$

$$N_{C,w} = \frac{2D_{2,w}}{\delta_2}\left(C_{2,w,j} - \frac{p_l x_{3,j}}{RT}\right) \quad (31)$$

$$N_{12,w,j} = \frac{2D_{2,w}P_{d,w}}{P_{d,w}\delta_2 RT + 2D_{2,w}}\left(p_h x_{1,j} - C_{2,w,j}RT\right) \quad (32)$$

$$N_{12,a,j} = \frac{2D_{2,a}P_{d,a}}{P_{d,a}\delta_2 RT + 2D_{2,a}} \times \left\{p_h\left(1 - x_{1,j}\right) - C_{2,a,j}RT\right\} \quad (33)$$

$$N_{23,w,j} = \frac{2D_{2,w}}{\delta_2 RT}\left(C_{2,w,j}RT - p_l x_{3,j}\right) \quad (34)$$

$$N_{23,a,j} = \frac{2D_{2,a}}{\delta_2 RT}\left\{C_{2,a,j}RT - p_l\left(1 - x_{3,j}\right)\right\} \quad (35)$$

$$N_{12,j} = N_{12,w,j} + N_{12,a,j} \quad (36)$$

$$N_{23,j} = N_{23,w,j} + N_{23,a,j} \quad (37)$$

The mass balance equations discredited and then matrices generated were solved by direct methods such as LU decomposition method. The generalized Crank-Nicholson scheme was applied for time-marching procedure.

5. Results and discussion

5.1 Detritiation system design of NIFS

In D-D experiments in NIFS, (a) detritiation of downstream of outgas generated in cleaning of plasma container (vacuum vessel purge gas) and (b) plasma exhaust gases is required. Thus, it is necessary to develop a detritiation system to recover low-concentration tritium generated in LHD (Large Helical Device). The schematics of the detritiation system designed at present are shown in Fig. 1. Representative operational conditions are summarized in Table 2. With regard to the vacuum vessel purge gas, the process gas is first introduced to 100 kg of catalyst bed and then tritiated water vapor is collected by condenser and polymer membrane-type dehumidifier. In contrast, the plasma exhaust gases are treated using catalyst and adsorption beds. One of the major differences is throughput of the gases processed. The concentrations of tritium and deuterium are considerably higher in the plasma exhaust gas. Numerical simulations were performed for both cases described above.

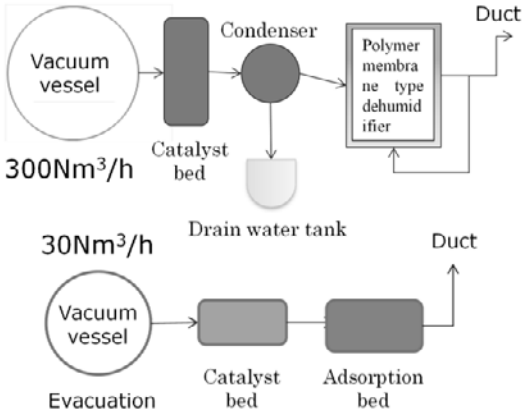

Fig. 1 Detritiation systems designed in NIFS

(a) outgas generated in cleaning of plasma container
(b) downstream of plasma exhaust gases.

Table 2 Operational condition of detritiation system.

Detritiation of vacuum vessel purge gas	Detritiation of plasma exhaust
$C_{Q2,H}$: 0.5 ppm	$C_{Q2,H}$: 130.0ppm
$C_{Q2,D}$: 90.0 ppm	$C_{Q2,D}$: 2983.3 ppm
$C_{Q2,T}$: 1×10^{-8} ppm	$C_{Q2,T}$: 9.25×10^{-6} ppm
$C_{Q2O,H}$: 1500.0 ppm	$C_{Q2O,H}$: 3.6667 ppm
$C_{Q2O,D}$: 90.0 ppm	$C_{Q2O,D}$: 28.667 ppm
$C_{Q2O,T}$: 1×10^{-8} ppm	$C_{Q2O,T}$: 6×10^{-8} ppm
Amount of catalyst: 100 kg	Amount of catalyst: 100 kg
Temp. of catalyst: 30℃, 100℃, 200℃	Temp. of catalyst: 30℃, 100℃, 200℃, 400℃
Heating: heat exchanger, adiabatic	Heating: heat exchanger, adiabatic
Recovery: Polymer membrane-type dehumidifier UM-XC5 (Φ90 mm×710 mm), 60 sets, high pressure 0.6 MPa, low presasure0.1 MPa, 30 ℃, 100 L/min	Recovery: MS5A adsorbent,100 kg
Dehumidifier cooling: heat exchanger, adiabatic	Adsorbent cooling: heat exchanger, adiabatic

5.2 Results of numerical simulation for detritiation of vacuum vessel purge gas

Figure 2 shows changes in the concentration of molecular form of tritium in the outlet stream of the catalyst bed. With regard to the temperature of inlet gas, three cases (30 °C, 100 °C and 200 °C) were tested. It can be seen in the figure that catalytic activity is considerably decreased in the cases where the inlet gas temperatures are 30 °C and 100 °C. This is because that water vapor contained in the process gas inhibits

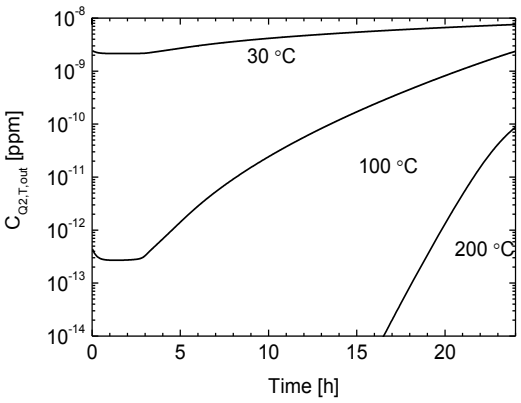

Fig. 2 Change in concentration T_2 in outlet stream of Pt/alumina catalyst beds.

catalytic activity with increase in the amount of water adsorbed on the catalyst substrate. However, this effect could be considerably avoided if the inlet gas temperature is raised to 200 °C as shown in the figure. Thus, preheating of the process gas with heat exchangers is necessary for the treatment of vacuum vessel purge gas.

Subsequent numerical simulation for condenser and polymer membrane-type dehumidifier was performed in the case where the inlet gas temperature is raised to 200 °C. The transient variations of chemical components such as hydrogen isotopes and isotopes of water vapor in the outlet stream of the catalyst bed were used as the inlet condition of the polymer membrane-type dehumidifier. Figure 3 shows changes in amounts of bulk water and concentration of tritiated water in drain tank. The amount of bulk water increases almost linearly with lapse time. The concentration of tritiated water increases in the same trend. Figure 4 shows changes in concentrations of molecular form of tritium and tritiated water vapor at the outlet of the duct. The concentration of tritiated water vapor increases almost linearly with lapse time. The molecular form of tritium sharply increases 20 h after the commencement of operation of the detritiation system, since the inhibition of catalytic activity by water vapor becomes a dominant factor. However, the result of this simulation indicates that regulatory level of tritium concentration at the outlet of the duct is fulfilled.

5.3 Results of numerical simulation for detritiation of plasma exhaust gas

Figure 5 (a) shows changes in T_2 concentration in outlet stream of the catalysts bed. In this case, preheating of the process gas before the catalyst bed is unnecessary because of the help of higher concentration of D_2; its reaction can generate heat and raise the reactor

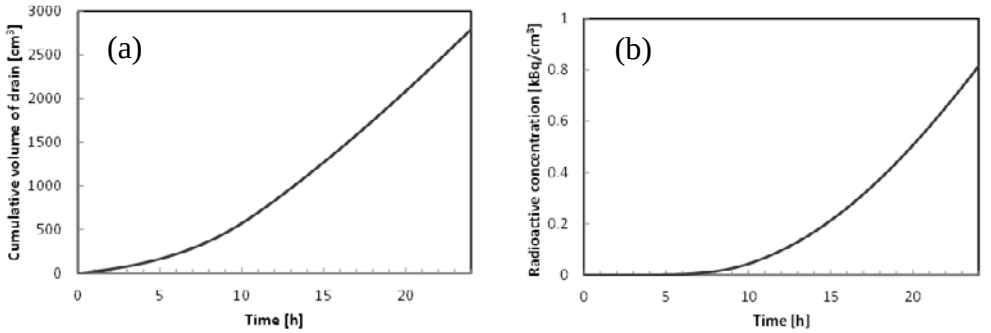

Fig. 3 Change in (a) amount of bulk water and (b) concentration of tritium in drain tank.

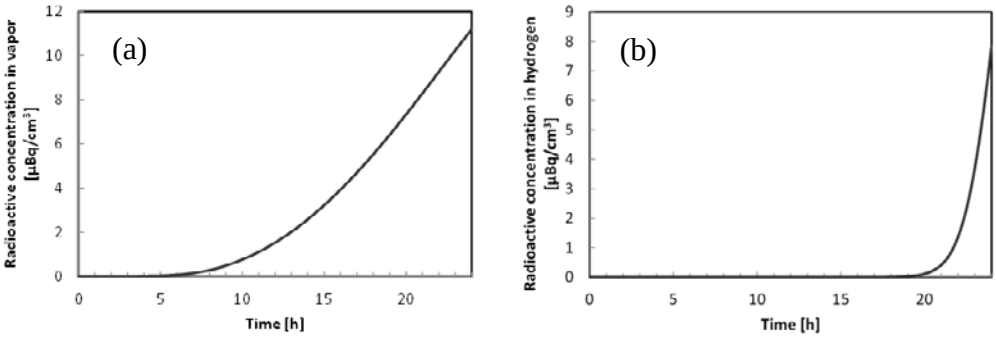

Fig. 4 Change in (a) concentration of molecular form of tritium and (b) concentration of tiritiated water vapor on outlet stream of duct.

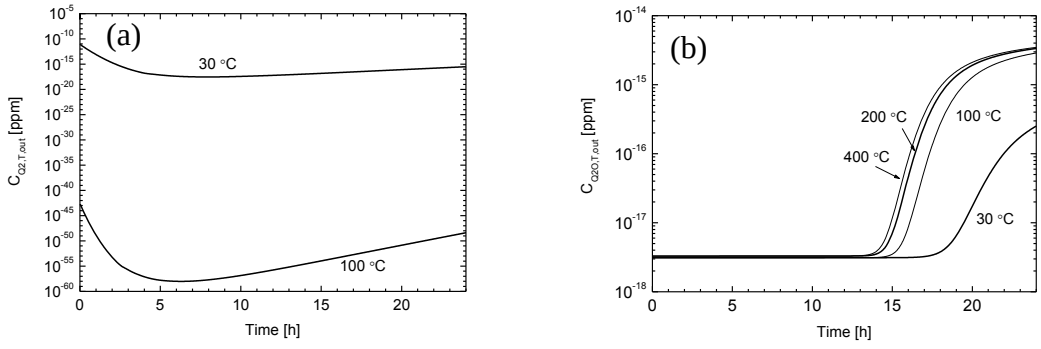

Fig. 5 Change in (a) concentration of molecular form of tritium in outlet gas of catalysts bed and (b) concentration of tiritiated water vapor on outlet stream of adsorption bed.
(Temperatures shown in the figures represent the temperature of the process as at inlet of the catalyst bed.)

temperature. Figure 5 (b) shows breakthrough curve for T_2O vapor, which indicates that breakthrough starts at 10 h after the start of operation of 100 kg of MS5A adsorbent regardless of variation in temperature of process gas at the inlet of the catalyst bed.

6. Conclusion

Catalytic oxidation rate of hydrogen and water adsorption characteristics are investigated with regards to commercial catalyst and adsorbent. Based on the experimental results, simulation models were constructed for catalyst bed, adsorption bed and polymer-type membrane dehumidifier. Test process simulations were carried out on the basis of the detritiation systems designed in NIFS.

Nomenclature

a	Specific surface area [m^2 m^{-3}]
a_{sorp}	Slope of the adsorption isotherm [mol m^{-3}]
a_p	Coefficient in Eq. (20) [mol m^{-2} s^{-1} Pa^{-1}]
b_0	Constant related to Langmuir-Freundrich equation [arbitrary]
$c_{p,g}$	Specific heat of gas [J g^{-1} K-1]
$c_{p,s}$	Specific heat of solid phase [J kg^{-1} K-1]
C	Molar concentration [mol m^{-3}]
D	Diffusion coefficient [m^2 s^{-1}]
D_b	Bed diameter [m]
ΔH_{ad}	Adsorption heat [J mol^{-1}]
ΔH_{ox}	Reaction heat for catalytic oxidation [J mol^{-1}]
$k_{F,ad}$	Overall mass transfer coefficient for adsorption [m/s]
$k_{F,ox}$	Overall mass transfer coefficient for catalytic oxidation [m/s]
K_g	Mass transfer coefficient for gas film layer [m/s]
$k_{r,ox}$	Mass transfer coefficient for catalytic oxidation based on surface reaction [m/s]
$k_{r,ox,0}$	Mass transfer coefficient for catalytic oxidation based on surface reaction in dry condition[m/s]
k_{sorp}	Rate constant of the adsorption [s^{-1}]
l	Position in the permeate direction [m]
N	Permeation flux [mol m^{-2} s^{-1}]
p	Pressure or partial pressure [Pa]
P	Permeance [mol m^{-2} s^{-1} Pa^{-1}]
q	Flow rate [mol s^{-1}]
q_{ad}	Concentration of water adsorbed [mol g^{-1}]
q_{st}	Concentration of water strongly bound to surface (structural water) [mol g^{-1}]
$\bar{q}$	Net Concentration of water species on the surface [mol g^{-1}]
Q	Volumetric gas velocity [m^3 s^{-1}]
r	Adsorption rate of water vapor [mol s^{-1}]
R	Gas constant [J K^{-1} mol^{-1}]
R_c	Conversion rate [-]
S	Outside wall area of a calculation cell [m^2]
S_V	Space velocity [s^{-1}]
S_w	Solubility coefficient of water [mol m^{-3} Pa^{-1}]
t	Time [s]
T	Temperature [K]
u	Superficial gas velocity [m s^{-1}]
V	Volume [m^3]
V	Constant related to Langmuir-Freundrich equation [-]
X	Mole fraction of water vapor [-]
Z	Length in axial direction [m]

Greek letters

Δ	Thickness of the layer [m]
E	Void ratio in the porous layer
λ_{eff}	Effective heat conductivity in axial direction [J m^{-1} s^{-1}]
ρ_g	Density of gas [g m^{-3}]

Overscript

Int	Interface between dense and porous layer
$\bar{}$	Equilibrium state
$'$	Matrix of the porous layer

Subscripts

0	Initial value
1	Feed side
12	From feed side to the porous layer
2	Porous layer
23	From porous layer to the permeation side
3	Permeation side
A	Air
A	Indicator in Fig. 2
B	Indicator in Fig. 2
C	Indicator in Fig. 2
D	Dense layer
H	High pressure side
I	Component (H, D or T) or (w or a)
In	inlet
J	Number of the calculation cell along the axis
L	Low pressure side
M	Adsorption site number
N	Maximum adsorption site number
Out	outlet
Q	H, D, or T (^1H, ^2H or ^3H)
S	Saturated state
W	Water vapor

References

[1] K. Kotoh and K. Kudo, "Applicability of Commercial Adsorbents to Multi-column Adsorption Systems with Condenser for Tritiated Water Vapor Removal", Journal of Nuclear Science and Technology, 34, 1099(1997)

[2] K. Munakata, M. Nishikawa, T. Takeishi, N. Mitsuishi and M. Enoeda, "Recovery of Tritium in Room Air by Precious Metal Catalysts with Hydrophilic Substrate", Journal of Nuclear Science and Technology. 25 , 383 (1988)

[3] T. Sugiyama, N. Miyahara, M. Tanaka, K. Munakata and I. Yamamoto, "A Simulation Model for Transient Response of A Gas Separation Module Using A Hollow Fiber Membrane", Fusion Engineering and Design, 86, 2743(2011).

Effects of La_2O_3, Cu and Fe addition on the catalytic performance of Ni-SiO_2 catalysts for methane decomposition

Heyi Wang,* Wenhua Wang, YongYang，Shuming Peng

Institute of Nuclear Physics and Chemistry, China Academy of Engineering Physics, Mianyang, 621900, PR China

(Received: 9 May 2012 / Accepted: 6 November 2012)

Methane decomposition over four kinds of catalysts such as Ni-SiO_2, Ni-La_2O_3-SiO_2, Ni-Cu-SiO_2 and Ni-Fe-SiO_2 prepared by co-impregnation method and sol-gel method, respectively, has been studied. The results indicated that Ni-La_2O_3-SiO_2 catalyst with La/Ni = 0.3 prepared by co-impregnation method showed better catalytic performance compared with all the other Ni-La_2O_3-SiO_2 catalysts during methane decomposition at 823 K. However, the temperature resistance of this catalyst was not very good. The introduction of Cu and Fe into Ni-SiO_2 enhanced the temperature resistance of the catalysts during methane decomposition at 923 K and the overall catalytic performance of the catalysts was Ni-Cu-SiO_2 (sol-gel method) > Ni-Fe-SiO_2 (sol-gel method) > 75%Ni-25%SiO_2 (sol-gel method) > Ni-La_2O_3-SiO_2 (co-impregnation method). XRD studies of Ni-La_2O_3-SiO_2, Ni-Cu-SiO_2 and Ni-Fe-SiO_2 catalysts indicated that Ni species existed in the form of Ni metal in Ni-La_2O_3-SiO_2, while Ni-Cu alloy and Ni-Fe alloy appeared in Ni-Cu-SiO_2 and Ni-Fe-SiO_2 catalysts. The structure of the carbon filaments formed during methane decomposition changed a lot with the introduction of Cu and Fe. At 923 K, “bifurcate carbon filaments” formed over Ni-Cu-SiO_2 during methane decomposition, while “bamboo-shaped carbon filaments” formed over Ni-Fe-SiO_2 catalysts.

Keywords: Methane decomposition, Ni-SiO_2, Ni-La_2O_3-SiO_2, Ni-Cu-SiO_2, Ni-Fe-SiO_2

1. Introduction

If graphite and carbon fiber composite are employed as plasma facing components for ITER, the deuterated and tritiated methane may be a considerable constituent of the impurity gas stream [1-6]. Methane decomposition is a safe and simple method for recovering deuterium and tritium from the deuterated and tritiated methane and an optional catalyst bed for methane decomposition is currently included into the design of the tokamak exhaust processing system (TEP) [7,8].

Lots of research on methane decomposition has been done by many researchers [9-11]. The ZrCo powder has already been found to decompose methane slowly at 573 K. A product of 0.05 molC/mol ZrCo was obtained after 80 h when the getter was exposed to 430 torr CH_4 [9]. Watanabe [10] *et al* investigated the decomposition of methane on Zr_7Ni_{10}, ZrNi, Zr_2Ni, Zr_4Ni and Zr in the temperature range 573 K–823 K and the alloy of Zr_4Ni removed methane over 99% efficiently in 105 s at 673 K. Baker [11] et al discovered that a St 909 getter (Zr–Mn–Fe) could effectively remove 99% of NH_3, CO_2 and O_2 at 673 K, CO at 873 K, and CH_4 at 973 K from an inert gas stream.

However, methane decomposition for recovering deuterium and tritium which was studied by the above researchers all focused on the static systems and the unsupported alloy catalysts, while the dynamic systems were hardly investigated. Above all, the unsupported alloy catalysts in the dynamic systems will deactivate quickly. Methane decomposition over the supported catalysts to prepare H_2 and carbon filament in the dynamic system has been studied by many researchers and many achievements have been obtained in recent years [12-16]. However, the effects of the rare metal oxide, Fe and Cu addition on the temperature resistance of the Ni-based catalysts were little investigated. In view of this, methane decomposition over supported catalysts such as Ni-SiO_2, Ni-La_2O_3-SiO_2, Ni-Cu-SiO_2 and Ni-Fe-SiO_2 catalysts in dynamic systems has been studied in this work. The influences of the preparation method, the reaction temperature and the contents of La, Cu and Fe in Ni-SiO_2 on methane decomposition were investigated.

2. Experimental

2.1. Catalyst preparation

Ni-La_2O_3-SiO_2 catalysts were prepared by co-impregnation method [17] which was done through impregnating SiO_2 with the mixed aqueous solution of $Ni(NO_3)_2$ and $La(NO_3)_3$ for 1.5 h, and then drying up the impregnated samples at 413 K for 12 h, and finally calcined them at 873 K for 6 h. The Ni content in all the catalysts was Ni/Si = 0.67 (molar ratio) and the La contents in the catalysts were La/Ni = 0, La/Ni = 0.1,

author's e-mail:hywang@caep.ac.cn

La/Ni = 0.3, La/Ni = 0.45 and La/Ni = 0.6 (molar ratio), respectively.

75%Ni-25%SiO_2, 65%Ni-10%Fe-25%SiO_2, 35%Ni-40%Fe-25%SiO_2, 65%Ni-10%Cu-25%SiO_2, and 35% Ni-40%Cu-25%SiO_2 catalysts (mass fraction) were prepared by sol-gel method [18,19]. The method was based on mixing the active components such as NiO or the mixtures of NiO and CuO (or Fe_2O_3) in this case, with alcosol containing silica in a certain amount. The suspends of the active components with alcosol were dried in flowing air at room temperature and were finally calcined at 923 K for 3 h. Alcosol was prepared by mixing 50 mL of TEOS, 40 mL of ethanol, 2 mL of water and 0.5 mL of 40% HCl. Silica content in the alcosol was 0.142 g/mL and could be diluted by ethanol. The mixture of NiO and CuO (or Fe_2O_3) was originated from calcining the mixture of $Ni(NO_3)_2$ and $Cu(NO_3)_2$ (or $Fe(NO_3)_3$) at 723 K and the $Ni(NO_3)_2$ and $Cu(NO_3)_2$ (or $Fe(NO_3)_3$) mixture was obtained by evaporating the mixed solution of $Ni(NO_3)_2$ and $Cu(NO_3)_2$ (or $Fe(NO_3)_3$).

2.2 Activity tests and catalyst characterization

Methane catalytic decomposition reactions were carried out in a fixed-bed quartz reactor (10 mm i.d.) under atmospheric pressure. Before the activity tests, Ni-La_2O_3-SiO_2 catalysts were subjected to a reduction pre-treatment using pure hydrogen of 20 mL/min at 873K for 1h and Ni-Cu-SiO_2 and Ni-Fe-SiO_2 catalysts were reduced with pure hydrogen of 20 mL/min at 923 K for 1 h. The feed stream was high-purified methane (99.99%) of 15 mL/min. The gaseous reaction products were monitored by an off-line gas chromatography (GC) combined with a 5A molecular column, using a thermal conductivity detector (TCD) for hydrogen and methane analysis.

XRD patterns were recorded on a Bruker D8Advance diffractometer with Cu Kα radiation at 40 kV and 40 mA.

The detailed structure of the deposited carbons was observed using the FEI Inspect F scanning electron microscope (SEM) operated at 20 kV and the JEOL JEM-100CX Transmission electron microscopy (TEM), operated at 80 kV.

3. Results and discussion

3.1 The catalytic performance of the catalysts

Fig.1 depicts the kinetic curves of methane decomposition over Ni-La_2O_3-SiO_2 catalysts with different contents of La_2O_3 at 823 K. Only hydrogen was obtained as a gaseous product for all the catalysts. It could be observed that the catalytic activity of Ni-SiO_2 catalyst without La_2O_3 decreased gradually with the time on stream and it was completely deactivated after 450 minutes. The addition of La_2O_3 extended the lifetime

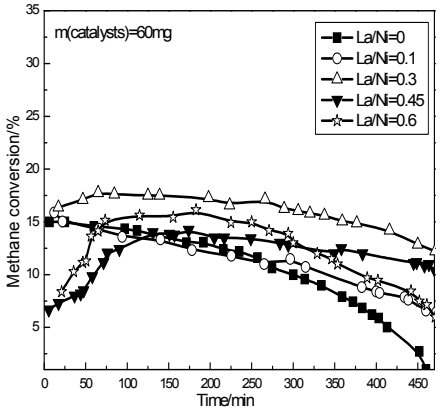

Fig.1 Kinetic curves of methane decomposition over Ni-La_2O_3-SiO_2 catalysts at 823 K.

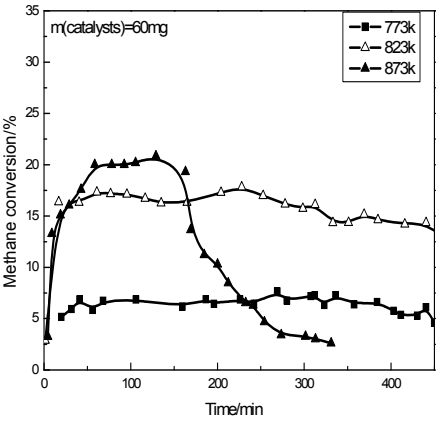

Fig.2 Effect of reaction temperature on methane decomposition over Ni-La_2O_3-SiO_2 catalysts with La/Ni = 0.3.

of Ni-SiO_2 catalyst obviously. For the Ni-La_2O_3-SiO_2 catalyst with La/Ni = 0.1, the methane conversion decreased from 16% to 7% after 450 minutes. With the increase of La_2O_3 content from La/Ni = 0.1 to La/Ni = 0.3, the catalytic performance of the catalyst was greatly improved and the methane conversion decreased from 17% to 13% with only 4% dropped after 450 minutes. However, when La_2O_3 content in the catalyst exceeded La/Ni = 0.3, the catalytic performance of the catalysts dropped slightly. The methane conversion decreased from 15% to 7.5% for Ni-SiO_2 with La/Ni = 0.6 after 450 minutes. Thus, a conclusion can be drawn that an optimum La_2O_3 content exists in Ni-La_2O_3-SiO_2 catalysts which can improve the catalytic performance of Ni-SiO_2 the most efficiently, while the introduction of more La_2O_3 into Ni-SiO_2 catalyst will impair the catalytic activity and the lifetime of the catalysts and this optimum La_2O_3 content is La/Ni = 0.3.

Fig.2 shows the effect of reaction temperature on methane decomposition over Ni-La_2O_3-SiO_2 catalyst with La/Ni = 0.3. The catalytic activity of Ni-La_2O_3-SiO_2 with La/Ni = 0.3 increased remarkably from 773 K to 823 K. When the reaction temperature increased from 823 K to 873 K, the initial methane conversion increased to 20%,

however, the lifetime of the catalyst was reduced and the methane conversion decreased to 2% after 300 minutes. Therefore, a higher reaction temperature reduced the lifetime of the catalyst and another conclusion can also be drawn that the temperature resistance of Ni-La_2O_3-SiO_2 was not so good even if the introduction of La_2O_3 into Ni-SiO_2 greatly extended the lifetime of Ni-SiO_2 at a lower reaction temperature such as 823 K.

Fig.3 compared the catalytic performance of Ni-La_2O_3-SiO_2 prepared by co-impregnation method with that of 75%Ni-25%SiO_2 prepared by sol-gel method and it demonstrated that the effect of the preparation method of the catalysts on methane decomposition was important. The catalytic activity of Ni-La_2O_3-SiO_2 with La/Ni = 0.3 which showed the best catalytic performance among the Ni-La_2O_3-SiO_2 catalysts was a little lower than that of 75%Ni-25%SiO_2. The methane conversion of 75%Ni-25%SiO_2 catalyst at 823 K remained 21% and didn't change during the reaction. However, the methane conversion of Ni-La_2O_3-SiO_2 with La/Ni = 0.3 decreased from 17% to 14% after 400 minutes. Therefore, both the catalytic activity and the stability of 75%Ni-25%SiO_2 were better than that of Ni-La_2O_3-SiO_2 with La/Ni = 0.3 which indicated that the Ni-based catalysts prepared by sol-gel method showed better catalytic performance than that prepared by co-impregnation method during methane decomposition.

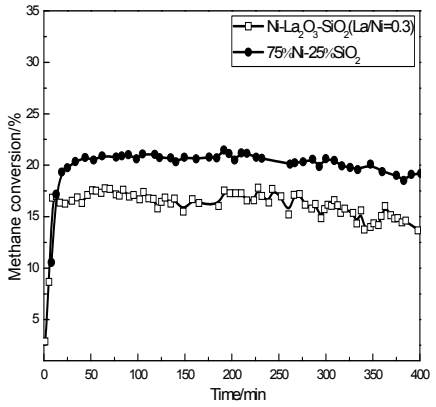

Fig.3 Effect of preparation method on methane decomposition at 823 K (m(Ni-La_2O_3-SiO_2) = 60 mg, co-impregnation method; m(75%Ni -25%SiO_2) = 30 mg, sol-gel method).

Fig.4(a) depicts the kinetic curves of methane decomposition over Ni-Cu-SiO_2 catalysts with different contents of Cu at 923 K. The lifetime of 75%Ni-25%SiO_2 catalyst was very short at 923 K unlike the catalytic behaviors at 823 K of which the methane conversion was kept at 21% for 400 minutes (Fig.3). After 70 minutes, the methane conversion of 75%Ni-25%SiO_2 decreased to around 5% and remained at this value. The addition of lower content of Cu improved the lifetime of Ni-SiO_2 catalyst apparently and the catalytic activity of Ni-Cu-SiO_2 didn't change obviously during methane decomposition. The methane conversion of 65%Ni-10%Cu-25%SiO_2 catalyst was kept at around 40%, while when the Cu content increased to 40%, the methane conversion dropped to about 19%. Therefore, it was different from Ni-La_2O_3-SiO_2 catalyst that Ni-Cu-SiO_2 catalysts could catalyze methane decomposition at a higher reaction temperature such as 923 K and the introduction of Cu into Ni-SiO_2 enhanced the temperature resistance of the catalysts.

Fig.4(b) shows the kinetic curves of methane decomposition over Ni-SiO_2 and Ni-Fe-SiO_2 catalysts at 923 K. The catalytic behaviors of Ni-Fe-SiO_2 catalysts were similar with that of Ni-Cu-SiO_2 catalysts. The introduction of Fe also improved the lifetime of Ni-SiO_2 catalysts obviously at 923 K. However, a deactivation period occurred for 65%Ni-10%Fe-25%SiO_2 catalyst and when methane decomposition over 65%Ni-10%Fe-25%SiO_2 catalyst proceeded to 200 min, the methane conversion decreased from 44% to 25%. While, the methane conversion of 35%Ni-40%Fe -25%SiO_2 was maintained at 19% all the time which indicated that with the increase of the Fe content in the Ni-Fe-SiO_2 catalysts the catalytic activity of the catalyst dropped and the stability of Ni-Fe-SiO_2 catalyst was enhanced. Therefore, Ni-Fe-SiO_2 could also catalyze methane decomposition at a higher reaction temperature such as 923 K which was similar with Ni-Cu-SiO_2. However, the catalytic performance of 65%Ni-10%Fe-25%SiO_2 was a little poorer than that of 65%Ni-10%Cu-25%SiO_2 for the poorer stability.

The research on the temperature resistance of the catalysts is very important for methane decomposition is an endothermic reaction and the conversion rises with the increase of the reaction temperature [20]. Thus, a catalyst with high temperature resistance can catalyze methane decomposition more efficiently at a higher reaction temperature [21]. According to the above results, a conclusion can be drawn that the order of the catalytic performance of the four kinds of catalysts above is Ni-Cu-SiO_2 (sol-gel method) > Ni-Fe-SiO_2 (sol-gel method) > 75%Ni-25%SiO_2 (sol-gel method) > Ni-La_2O_3-SiO_2 (co-impregnation method). Also, when methane decomposition over Ni-Cu-SiO_2 or Ni-Fe-SiO_2 catalysts is applied to TEP to recover deuterium and tritium from the deuterated and tritiated methane, a much higher reaction temperature can be adjusted to utilize the temperature resistance of the catalysts to improve the catalytic efficiency.

3.2 The characterization of the catalysts before and after methane decomposition

Fig.5(a) shows the XRD spectra of Ni-La_2O_3-SiO_2

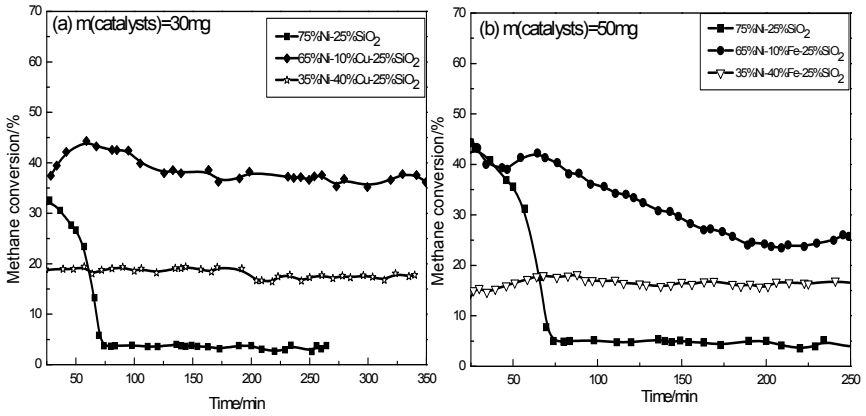

Fig.4 Kinetic curves of methane decomposition over Ni-Cu-SiO_2 and Ni-Fe-SiO_2 catalysts at 923 K.

catalysts reduced by hydrogen. The diffraction peaks at 2θ = 44.46°, 51.81° and 76.36° in the XRD spectra of Ni-SiO_2 revealed that the Ni species in the Ni-SiO_2 catalyst reduced by hydrogen existed mainly in the form of Ni metal. When lower content of La_2O_3 was introduced into the catalysts such as Ni-La_2O_3-SiO_2 with La/Ni = 0.1 and La/Ni = 0.3, no La_2O_3 peaks were detected which meant that the lower contents of La_2O_3 existed in an amorphous phase. However, as the contents of La_2O_3 exceeded La/Ni = 0.3, the La_2O_3 diffraction peaks appeared. In addition, with the increase of the La_2O_3 content, the intensity of the diffraction peaks due to Ni metal turned weaker and weaker and the FWMH of the diffraction peaks turned wider and wider which indicated that the Ni crystallite size turned smaller and smaller. Therefore, the Ni dispersion degree was enhanced with the increase of La_2O_3 content.

Fig. 5(b) shows the XRD spectra of Ni-SiO_2 and Ni-Cu-SiO_2 catalysts reduced by hydrogen. The diffraction peaks at 2θ = 44.46°, 51.81° and 76.36° in the XRD spectra of 75%Ni-25%SiO_2 also demonstrated that the Ni species in the Ni-SiO_2 catalysts reduced by H_2 existed mainly in the form of Ni metal. The diffraction peaks due to Cu were not detected in Ni-Cu-SiO_2 catalysts even if the Cu content was very high. In fact, when Ni-Cu-SiO_2 was reduced by hydrogen, the Ni species was associated with the Cu species through the formation of Ni-Cu alloy in the catalysts and only Ni-Cu alloy metal phase existed in the Ni-Cu-SiO_2 catalyst.

Fig.5(c) shows the XRD spectra of Ni-SiO_2 and Ni-Fe-SiO_2 catalysts reduced by hydrogen. The Fe in the catalysts also appeared as Ni-Fe alloy which was similar with Ni-Cu-SiO_2 catalysts. However, the Ni-Fe-SiO_2 catalysts reduced by hydrogen had two metal phases: the Ni metal phase and the Ni-Fe alloy phase which was different from Ni-Cu-SiO_2. The diffraction peaks due to Ni-Fe alloy and Ni metal overlapped with each other which indicated that the Ni-Fe alloy had identical structure with the Ni metal.

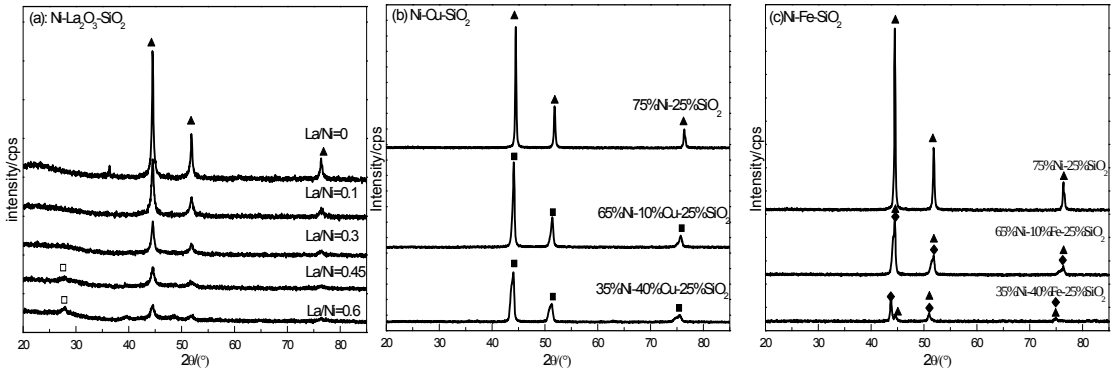

Fig.5 XRD spectra of the Ni-La_2O_3-SiO_2, Ni-Cu-SiO_2 and Ni-Fe-SiO_2catalysts reduced by hydrogen (▲-Ni, □-La_2O_3, ■-Ni-Cu alloy, ◆-Ni-Fe alloy).

Fig.6 shows the SEM images of the Ni-SiO_2, Ni-La_2O_3-SiO_2, Ni-Cu-SiO_2 and Ni-Fe-SiO_2 catalysts after methane decomposition at different reaction temperatures. It could be clearly observed that the surfaces of all the catalysts were completely covered with the interlaced carbon filaments and the structure of the carbon filaments was seriously influenced by the reaction temperature and the introduced Cu and Fe. The

fundamental structure of the carbon filaments formed over Ni-La_2O_3-SiO_2 with La/Ni = 0 and La/Ni = 0.3 at 823 K (Fig.6(a) and Fig.6(b)) was similar with that of 75%Ni-25%SiO_2 at 823 K (Fig.6(c)) except the thickness and the thickness of the carbon filaments formed over the three catalysts was 75%Ni-25%SiO_2 > Ni-La_2O_3-SiO_2 with La/Ni = 0.3 > Ni-SiO_2 with La/Ni = 0.

From the performance of methane catalytic decomposition in Fig.1 and Fig.3, the order of the catalytic performance of the three catalysts was 75%Ni-25%SiO_2 > Ni-La_2O_3-SiO_2 with La/Ni = 0.3 > Ni-SiO_2 with La/Ni = 0. It could be concluded that when thicker carbon filaments formed over the catalysts, the catalysts showed better catalytic performance during methane decomposition.

The carbon filaments formed over 75%Ni-25%SiO_2 at 923 K turned shorter and thinner compared with those formed at 823 K. Thus, the increase of the reaction temperature lowered the carbon capacity of 75%Ni-25%SiO_2. When Cu was introduced into Ni-SiO_2, the carbon filaments turned much thicker and less homogeneous. The introduction of Fe into Ni-SiO_2 also changed the fundamental structure of the carbon filaments formed during methane decomposition at 923 K. They were much longer and thinner.

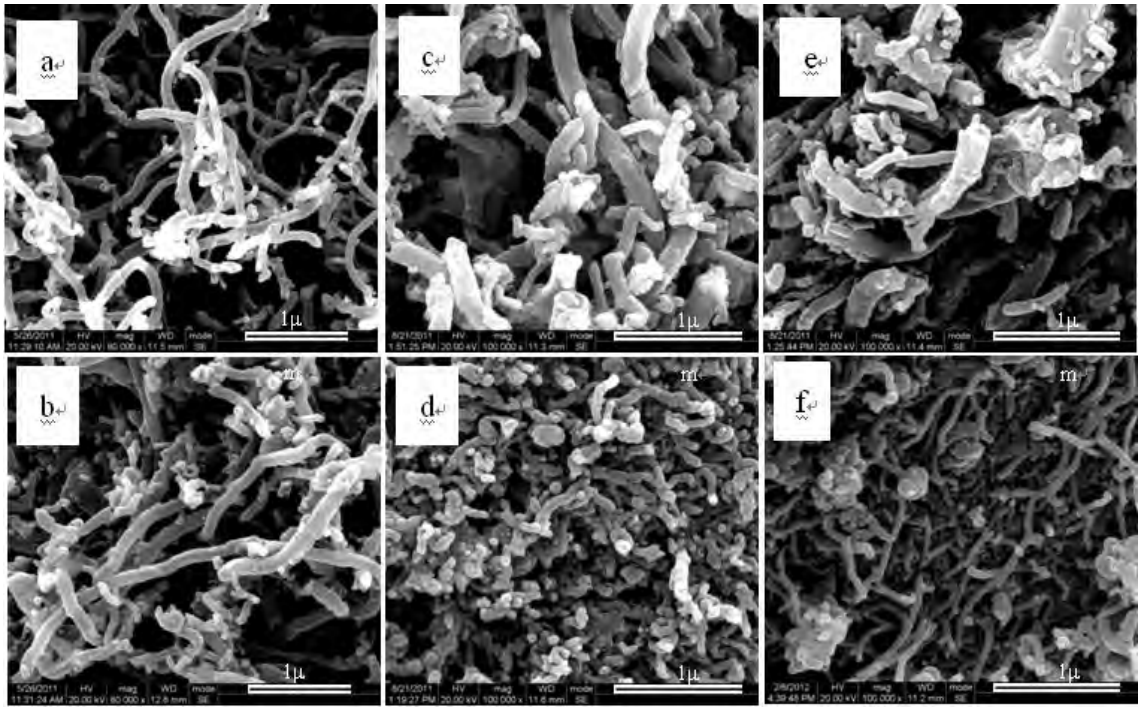

Fig. 6 SEM images of carbon filaments formed during methane decomposition (a: Ni-SiO_2 with La/Ni=0, 823 K; b:Ni-La_2O_3-SiO_2 with La/Ni=0.3, 823 K; c: 75%Ni-25%SiO_2, 823 K; d:75%Ni-25%SiO_2, 923 K; e: 65%Ni-10%Cu-25%SiO_2, 923 K; f: 35%Ni-40%Fe-25%SiO_2, 923 K).

Considering the great changes of the carbon filaments with the increase of the reaction temperature and the introduced Cu and Fe, TEM images of these carbon filaments were also investigated to analyze the differences of the detailed structure of these carbon filaments.

In the TEM images of 75%Ni-25%SiO_2 after methane decomposition at 823 K (Fig.7(a)), the carbon filaments with diameters from 70 nm to 110 nm were observed. The “pear-shaped” Ni metal particles were present at the tip of the carbon filaments. While in the TEM images of 75%Ni-25%SiO_2 catalyst formed during methane decomposition at 923 K (Fig.7(b)), the diameter range of the carbon filaments was 50 nm-90 nm and spherical Ni metal particles appeared at the tip of the carbon filaments. The diameters of both types of carbon filaments were in agreement with their diameters of the catalyst particles at the tips.

The different shapes of the Ni metal particles at different reaction temperatures reflected the different carbon diffusion mechanisms during methane decomposition. Takenaka [22] *et al* pointed out that the formation of the “pear-shaped” Ni metal particles was due to the diffusion of carbon atoms through the bulk of Ni metal particles, while the formation of the spherical Ni metal particles resulted from the diffusion of carbon atoms on the surface of Ni metal particles. Thus, it could be speculated that the carbon atoms formed during methane decomposition was preferential to diffuse through the surface of the Ni metal particles at a higher temperature.

Another phenomenon which should be paid attention

to was that when the formed carbons during methane decomposition diffused through the bulk of the active metal at 823 K, the catalyst could keep active for methane decomposition for a long time, while, when the formed carbons during methane decomposition diffused through the surface of the active metal, the catalyst lost its activity in a short time (Fig.3 and Fig.4). As a result, the diffusion of the formed carbons through the surface of the catalysts wasn't beneficial for the long time methane decomposition.

Fig.7(c) and Fig.7(d) show the TEM images of the carbon filaments formed during methane decomposition over 65%Ni-10%Cu-25%SiO_2 at 923 K. It can be observed that "bifurcate carbon filaments" formed over 65%Ni-10%Cu-25%SiO_2 catalysts and the Ni-Cu alloy particle which was active for methane decomposition was not at the tip of the carbon filaments as it was in the carbon filaments formed over Ni-SiO_2 catalyst. A few carbon filaments grew from one Ni-Cu alloy particle and the Ni-Cu alloy particle was positioned among the carbon filaments.

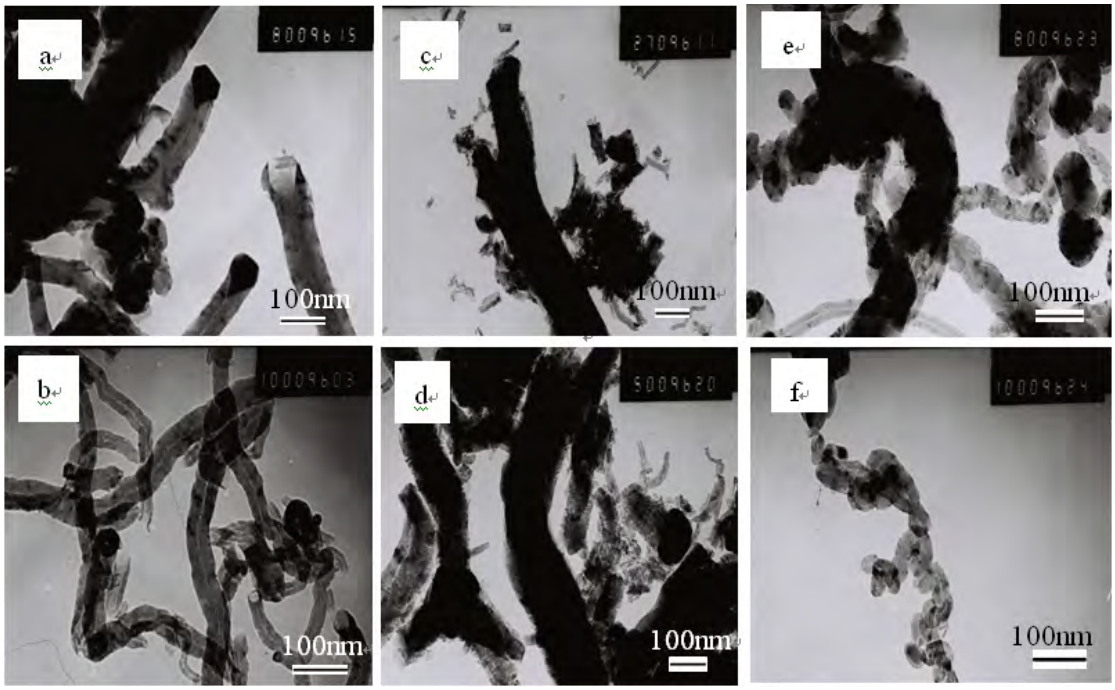

Fig.7 TEM images of carbon filaments formed over Ni-SiO_2, Ni-Cu-SiO_2 and Ni-Fe-SiO_2 during methane decomposition (a: 75%Ni-25%SiO_2,823 K; b:75%Ni-25%SiO_2, 923 K; c,d: 65%Ni-10%Cu-25%SiO_2, 923 K; e,f:35%Ni-40%Fe-25%SiO_2, 923 K).

Compared with the Ni particles in Fig.7(b) which was formed over 75%Ni-25%SiO_2 after methane decomposition at 823 K, the Ni-Cu particles were also "pear-shaped" after methane decomposition over Ni-Cu-SiO_2 catalysts at 923 K. Thus, it could be speculated that the addition of Cu into Ni-SiO_2 catalyst changed the diffusion mechanism of the formed carbons. At a higher reaction temperature such as 923 K, the diffusion of the carbons formed over Ni-Cu-SiO_2 catalyst remained through the bulk of Ni-Cu particles. This might be the reason why the lifetime of Ni-Cu-SiO_2 catalysts was also very long at a higher reaction temperature such as 923 K.

Fig.7(e) and Fig.7(f) shows the TEM images of the carbon filaments formed over Ni-Fe-SiO_2 catalysts at 923 K. Carbon filaments of "bamboo-shaped" structure formed over Ni-Fe-SiO_2 catalyst. The walls of the "bamboo-shaped carbon filaments" were uneven and the hollows of these carbon filaments were divided into many cells which was different from those formed over Ni-SiO_2 catalyst. The Ni-Fe alloy particles which were active for methane decomposition were not only present at the tip of the carbon filaments after methane decomposition, but also existed in the hollow cells of the "bamboo-shaped" structure.

Apparently, the addition of Fe also changed the carbon diffusion mechanism of Ni-SiO_2 catalyst during methane decomposition. The results of Ermakova and Takenaka [18, 23] *et al* indicated that the products of methane decomposition over Fe-SiO_2 catalysts were also "bamboo-shaped carbon filaments". Thus, the carbon diffusion mechanism of Ni-Fe-SiO_2 catalyst during methane decomposition was similar with that of Fe-SiO_2 catalyst.

Since the carbon diffusion mechanism of Ni-Fe-SiO_2 is similar with that of Fe-SiO_2 catalyst, it can also be

believed that the characterization of methane decomposition over Ni-Fe-SiO_2 catalysts should be in agreement with that of Fe-based catalysts. As the activation temperature of the Fe-based catalysts is much higher than that of the Ni-based catalysts [23], the introduction of Fe also enhanced the temperature resistance of Ni-based catalysts and the lifetime of Ni-Fe alloy catalysts was much longer than that of the single Ni-based catalysts at a higher reaction temperature such as 923 K.

In addition, the temperature resistance of Ni-Cu alloy and Ni-Fe alloy catalysts was both stronger than that of the single Ni-based catalysts, while the stability of 65%Ni-10%Fe-25%SiO_2 catalyst during methane decomposition wasn't as good as that of 65%Ni-10%Cu-25%SiO_2 (Fig.4). The reason for this might be that not all of the Ni species in 65%Ni-10%Fe-25%SiO_2 catalyst existed in the form of Ni-Fe alloy (Fig.5), while Ni and Cu could form alloys over a wide composition range and this was proved by the results of Fig.5 and other researchers [24]. When the Fe content in Ni-Fe-SiO_2 increased to 40%, the stability of the catalyst was enhanced for the Ni species in 35%Ni-40%Fe-25%SiO_2 mainly existed in the form of Ni-Fe alloy although the catalytic activity of the catalyst decreased.

4. Summary

1) The introduction of La_2O_3 into Ni-SiO_2 catalysts obviously extended the lifetime of the catalysts during methane decomposition at 823 K. However, the temperature resistance of Ni-La_2O_3-SiO_2 didn't change obviously and the catalytic activity of Ni-La_2O_3-SiO_2 with La/Ni = 0.3 disappeared at a very short time at 873 K. While the introduction of Cu and Fe into Ni-SiO_2 enhanced the temperature resistance of the catalyst. The catalytic performance of the catalysts during methane decomposition was Ni-Cu-SiO_2 (sol-gel method) > Ni-Fe-SiO_2 (sol-gel method) > 75%Ni-25%SiO_2 (sol-gel method)> Ni-La_2O_3-SiO_2 (co-impregnation method).

2) XRD studies of Ni-La_2O_3-SiO_2, Ni-Cu-SiO_2 and Ni-Fe-SiO_2 catalysts indicated that the Ni species existed in the form of Ni metal in Ni-La_2O_3-SiO_2 catalyst and Ni-Cu alloy and Ni-Fe alloy appeared in Ni-Cu-SiO_2 and Ni-Fe-SiO_2 catalysts, respectively.

3) The fundamental structure of the carbon filaments formed over Ni-La_2O_3-SiO_2 with La/Ni = 0 and La/Ni = 0.3 was similar with that of 75%Ni-25%SiO_2 at 823 K. While the carbon filaments formed over 75%Ni-25%SiO_2 at 923 K turned shorter and thinner than those formed at 823 K. "Bifurcate carbon filaments" formed over Ni-Cu-SiO_2, while "bamboo-shaped carbon filaments" formed over Ni-Fe-SiO_2 catalysts during methane decomposition at 923 K.

Acknowledgements

This work was financially supported by the National Magnetic Confinement Fusion Science Program of China (2011GB111005).

References

[1] M. Glugla, L. Dörr, R. Lässer, D. Murdoch, H.Yoshida, Fus. Eng. Des. **61-62**, 569 (2002).
[2] C. Rizzelloa, F. BT. Pinnab, S. Tosti, Fus. Eng. Des. **85**, 58 (2010).
[3] M. Glugla, D. K. Murdoch, H. Geißler, P. Herrmann, R. Kraemer, Fus. Eng. Des. **39–40**, 893 (1998).
[4] R. Lässer, M. Glugla, K. Günther, T. L. Le, D. Niyongabo, R. D. Penzhorn, K. H. Simon, Fus. Eng. Des. **58–59**, 371 (2001).
[5] S. Tosti, L. Bettinali，F. Borgognoni, D. K. Murdoch, Fus. Eng. Des. **82**,153 (2007).
[6] M. Glugla, A. Perevezentsev, D. Niyongabo, R. D. Penzhorn, A Bell, P. Herrmann, Fus. Eng. Des. **49–50**, 817 (2000).
[7] M. Glugla, D. K. Murdoch, Fus. Eng. Des. **39~40**, 893 (1998).
[8] R. Lässer, A. C. Bell, N. Bainbridge, Fus. Eng. Des.**47**,173 (1999).
[9] R. D. Penzhorn, M. Devillers, M. Sirch, J. Nucl. Mater. **170**, 217 (1990).
[10] K. Watanabe, W. M. Shu, E. Motohashi, Fus. Eng. Des. **39–40**, 1055 (1998).
[11] J. D. Baker, D. H. Meikrantz, R. J. Pawelko, R. Anderl, D. F. Tuggle, J. Vac. Sci. Technol. **A12**, 548 (1994).
[12] J. Z. Li, G. X. Lu. J. Mol. Catal. A: Chem., **221**, 105 (2004).
[13] S. Takenaka, S. Kobayashi, H. Ogihara, O. Kiyoshi, J. Catal. 217, 79(2003).
[14] L. Jerry, J. S. Kevin, Appl. Catal. **349**, 116 (2008).
[15] M. A. Ermakova, D. Y. Ermakov, Catal. Today 77, 225 (2002).
[16] Y. Echegoyen, I. Suelves, J. Power Sources **169**, 150 (2007).
[17] Z. Beatriz, A. Miguel, B. Valenzuela, P. Jorge, T. G. Enelio, Int. J. Hydrogen Energy **35**, 12091 (2010).
[18] M. A. Ermakova, D.Y. Ermakov, Catal Today **77**, 225 (2002).
[19] M. J. Lázaro, Y. Echegoyen, I. Suelves, J. M. Palacios, R. Moliner. Appl. Catal. A **329**, 22 (2007).
[20] T. V. Reshetenko, L. B. Avdeeva, Z. R. Ismagilov, A. L. Chuvilin, V. A. Ushakov, Appl. Catal. A **24**7, 51 (2003).
[21] T. V. Reshetenko, L. B. Avdeeva, Z. R. Ismagilov. Genseki, K. Otsuka, J. Catal. **238**, 353 (2006).
[22] S. Takenaka, S. Kobayashi, H. Ogihara, K. Otsuka, J. Catal. **217**, 79 (2003).
[23] S. Takenaka, M. Serizawa, K. Otsuka, J. Catal. **222**, 520 (2004).
[24] K. C. Khulbe, R. S. Mann, Catal. Rev. Sci. Eng. **24**, 311 (1982).

Measurement of Tritium Distribution in Nickel and Vanadium by Means of A Combined Technique of An Imaging Plate and Thin Absorbers

Hiroko YOSHIDA-OHUCHI, Yuji HATANO[1)], Akram MOHAMMADI[2)] and Takao KAWANO[3)]

Radioisotope Research and Education Center, Graduate School of Pharmaceutical Science, Tohoku University, Sendai 980-8578, Japan

[1)]Hydrogen Isotope Research Center, University of Toyama, Toyama 930-8555, Japan

[2)]Radiation Research Center, Shiraz University, Shiraz 85111-71946, Iran

[3)]National Institute for Fusion Science, Toki-city 509-5292, Japan

(Received: 10 May 2012 / Accepted: 21 October 2012)

A combined technique of an imaging plate (IP) and thin absorbers was applied to tritium in nickel and vanadium specimens using copper, aluminum, and gold foil as the absorber. Copper and aluminum foil are used as a K-edge filter with X-ray absorption at 9.0 keV and 1.56 keV, respectively. Gold has L-edges X-ray absorption at around 13 keV. With this technique, photostimulated luminescence (PSL) decay curves are obtained by changing absorber's thickness. In the nickel specimen, the difference in PSL decay curves between for the copper and gold absorber was clearly observed 20 days after loading, however, all curves became similar single pattern after 388 days. The same curve pattern was obtained in vanadium for all absorbers. The cross section images and depth profiles, which were taken at 468 days and 3.9 years after loading for the nickel and vanadium specimen, respectively, show no significant inclination of tritium concentration for both specimens. These results indicate that uniform tritium distribution in the specimen provides the similar single PSL decay curves pattern for the copper or aluminum and gold absorber.

Keywords: tritium, imaging plate, thin absorber, bremsstrahlung X-rays, depth distribution, non-destructive measurement

1. Introduction

Non-destructive and quantitative measurement of the amount of tritium retained on/in plasma-facing materials (PFMs) of magnetic fusion devices are of great importance for the control of fuel particles and to ensure safety for maintenance work and waste processing of PFMs in fusion systems. The tritium imaging plate (IP) technique for detecting beta particles is useful to non-destructively determine the surface tritium distribution on PFMs [1-5]. An IP made of europium-doped BaFBr(I), a photostimulated luminescence (PSL) material, is a two-dimensional radiation sensor. This IP has many excellent properties making it suitable for this purpose, including high sensitivity, wide dynamic range over five orders of magnitude, a high degree of spatial resolution, and reusability by exposing the IP to visible light between uses [6].

Tritium emits beta particles with a maximum energy of 18.6 keV, with an average of 5.7 keV. These have a range of about several micrometers in graphite, and hence the IP technique is sensitive to tritium up to a depth of a few microns. In order to obtain tritium distribution in regions deeper than the escape depth of beta rays from tritium, we have been developing a combined technique of an imaging plate (IP) and thin absorbers using the bremsstrahlung X-rays generated by the interaction between the beta particles from tritium and matter [7].

In this study, the combined technique of the IP and thin absorbers was applied to tritium in nickel and vanadium specimens using copper, gold, and aluminum foil as the absorber. Copper and aluminum foil are used as a K-edge filter with X-ray absorption at 9.0 keV and 1.56 keV, respectively. Gold has L-edges X-ray absorption at around 13 keV [7].

2. Experimental

Tritium was introduced into sheet type specimens (1.5 x 1.5 x 0.05 cm^3) of nickel by gas absorption method at 673 K on 24 Dec 2010 in the manner described in the previous paper [8]. Specimens were loaded with deuterium containing 17% tritium. For vanadium specimen (4.8 x 1.0 x 0.05 cm^3), tritium was introduced by the same method at 673 K on 27 May 2008 [9]. The tritium concentration in the specimen was controlled to be 1.0 appm; the total concentration of tritium and deuterium was 200 appm. Then all specimens were kept at room temperature.

The initial distribution of tritium in the nickel specimen was examined by β-ray induced X-ray spectroscopy (BIXS) under Ar atmosphere in the manner described in the previous paper [10]. Tritium distribution

author's e-mail: hiroko@m.tohoku.ac.jp

was measured twice, 20 and 388 days after tritium loading for the nickel specimen and 3.5 years for the vanadium specimen, respectively by the combined technique of a BAS-MS type-IP (Fujifilm Co., Ltd.) and absorbers. At the same time, tritium in the surface regions was measured by using a BAS-TR type-IP (Fujifilm Co., Ltd.). The BAS-MS type-IP was used to detect bremsstrahlung X-rays from tritium. This IP consists of a 9-μm-thick polyethyleneterephthalate protective film and a 115-μm-thick photostimulable phosphor layer affixed to a 12-μm-thick plastic back layer and a 190-μm-thick polyethyleneterephthalate base layer [11]. It has a high sensitivity to photons. The BAS-MS type-IP can detect bremsstrahlung X-rays, but not the beta particles emitted from tritium because of its thick protective film. The BAS-TR type-IP lacking a protective surface layer was developed for detection of the beta particles from tritium. This IP consists of a 50-μm-thick photostimulable phosphor layer affixed to a 250-μm-thick base layer.

The BAS-MS type-IP was irradiated with bremsstrahlung X-rays by placing the specimen directly on the IP or with inserting absorbers for 1 h. To avoid contamination of the IP during irradiation, each specimen was sandwiched with a quite thin 1.2-μm-thick film. The schematic diagram of the irradiation setup is shown in Fig. 1. During irradiation, the IP was kept inside a refrigerator with temperature controlled to 4°C, in order to decrease the fading effect, although the BAS-MS-type IP shows good fading characteristics at room temperature [12]. The IP was kept for 20 min after irradiation and then read to avoid fading effects caused by the short half-life component. A model FLA7000 IP reader (Fujifilm Co., Ltd.) was used with a spatial resolution of 100 μm and 8 bits of digital resolution dpi, followed by an image analysis with the Multi Gauge (ver.3.2). For each irradiation, the IP was simultaneously irradiated with a ^{137}Cs disk-shaped gamma-ray source and measured PSL values obtained from the specimen were corrected by that obtained by the ^{137}Cs source to minimize errors induced by the readout system and the procedure. To detect tritium in the surface regions, the BAS-TR type-IP was irradiated with the beta particles by placing the specimen directly on the IP without using the film for 20 min.

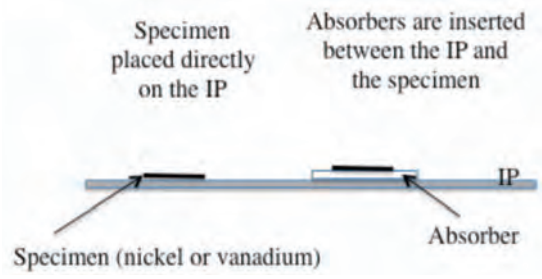

Fig.1 Schematic diagram of the irradiation setup.

3. Results and Discussion

Fig.2 shows X-ray spectrum from the nickel specimen containing tritium. A sharp intense peak of Ar Kα X-rays is at around 3 keV. Another sharp peak at 7.48 keV can be assigned to Ni Kα X-rays. It should be noted that relatively small intensity of Ni Kα peak in comparison with Ar Kα peak. Ar Kα X-rays are induced by tritium in shallow surface region, while Ni Kα X-rays are induced mainly by tritium in the bulk. The spectrum in Fig.2 indicates that tritium is concentrated in the surface regions, which is consistent with the result shown in the previous paper [8].

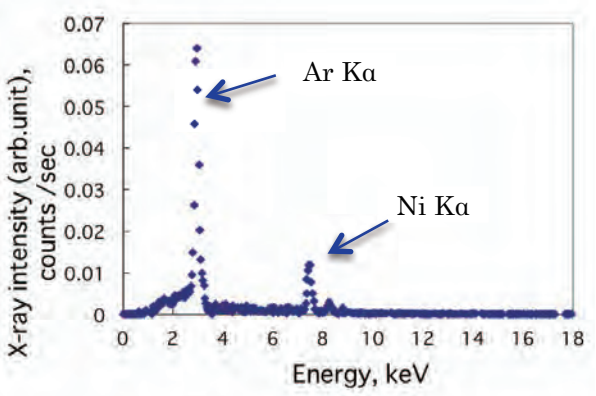

Fig.2 Characteristic BIXS spectrum of a tritium-containing nickel specimen.

Fig.3(a) shows a BAS-TR image for the nickel specimen taken at 20 days after loading, describing tritium two-dimensional distribution in the surface region. The PSL intensity along the line A and B are shown in Fig.3(b), respectively, expressing flat distributions along both lines at the same PSL intensity level except the edge. The

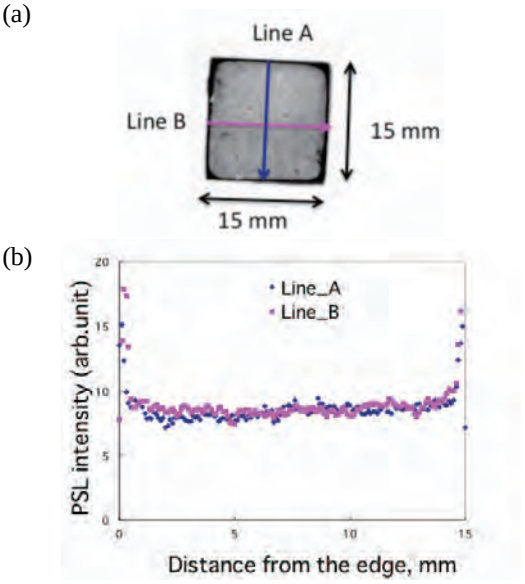

Fig.3 (a) BAS-TR image for the nickel specimen taken at 20 days after loading. (b) PSL intensity along the line A and B.

average PSL intensity per arbitrary unit is 8.4 on the flat curves. The image taken at 388 days after loading was exact the same one with that at 20 days in Fig.3(a) but with a decrease of 16.3% in the average PSL intensity.

Fig.4(a) shows BAS-MS images for the nickel specimen taken at 20 days after loading when the thickness of each absorber varied, exhibiting quite different images compared with the BAS-TR image in Fig.3(a). Each PSL value in the area of 85 mm^2 at the center of the specimen was obtained, and then PSL decay curve was obtained by normalizing the measured PSL values to the PSL value without absorber. Fig.4(b) shows PSL decay curves as a function of the effective thickness for three absorbers. The effective thickness, $\mu \cdot t$, which normalizes the thickness of each absorber by $1/\mu$, was obtained by the following equation:

$$\mu \cdot t = (\mu / \rho) \cdot \rho \cdot t \qquad (1)$$

where μ / ρ is the mass attenuation coefficient (cm^2/g) at K or L-edge X-ray absorption for copper and aluminum absorbers and gold absorber, respectively [13], ρ density (g/cm^3), and t the thickness of absorbers (cm). The scale of the effective thickness for aluminum absorber is expressed as 1/10 in Fig.4(b). When X-rays energy spectrum distribution spreads over some energies, the slope of PSL decay curve is expected to change as the thickness of the absorber increases.

(a)

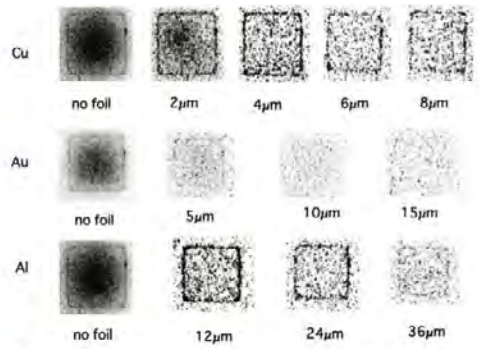

(b)

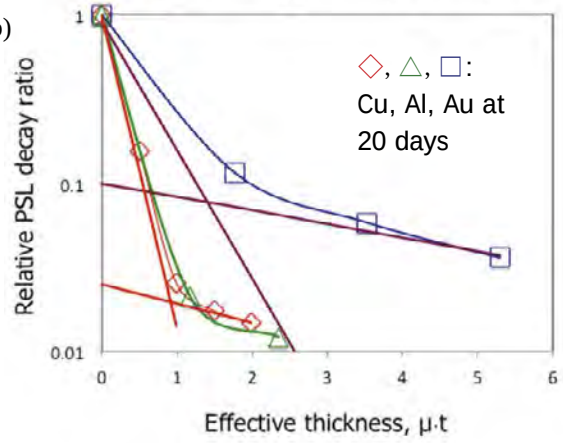

Fig.4 (a) BAS-MS type-IP images for the nickel specimen taken at 20 days after loading when the thickness of each absorber varied. (b) PSL decay curves as a function of the effective thickness for three absorbers. The scale of the effective thickness for aluminum absorber is expressed as 1/10. PSL decay curves for copper and aluminum absorbers are shown as ◇, △ respectively and that for gold is shown as □. Solid lines express two components of PSL decay curves for copper and gold absorbers .

PSL decay curves pattern for copper and aluminum absorbers (shown as ◇, △ respectively) are similar, while that for gold (shown as □□□is quite different from others. In the previous paper [7], we described the principle of the combined technique of the IP and absorbers and how each absorber works when the bremsstrahlung energy spectrum distribution changes as tritium migrates into matter, that is, PSL values derived from the lower energy range rapidly decrease as the copper and aluminum absorber thickness increase. On the other hand, the gold absorber works oppositely, rapidly reducing PSL derived from the higher energy range. Thus, PSL decay curve consists of two components, with fast and slow rates of decay, and they can be expressed in the following equation [7]:

$$f(x) = a \cdot e^{-\mu 1 x} + b \cdot e^{-\mu 2 x} \qquad (2)$$

where a and b are the relative ratio of two components, μ_1 and μ_2 penetrating coefficient of each component, and x is the thickness of the absorber. Two components of PSL decay curves for copper and gold absorbers are shown as solid lines in Fig.4(b). The differences in relative ratio of two components and penetrating coefficient of each component between two PSL decay patterns for copper and gold absorbers are summarized in Table 1. The relative ratio of two components, a and b is considered to indicate the ratio of higher and lower energy bremsstrahlung X-rays in the bremsstrahlung energy spectrum distribution [7].

Table 1 Differences in relative ratio of two components, a and b and penetrating coefficient of each component, μ_1 and μ_2 between two PSL decay patterns for copper and gold absorbers.

Absorber	a	b	μ_1	μ_2
Copper	0.98	0.020	4.0	0.15
Gold	0.90	0.10	1.7	0.19

The same measurements were repeated at 388 days after loading. BAS-MS images show a large decrease of 98% in PSL intensity in comparison with that at 20 days, which can be caused by chronic release from nickel under ambient air at room temperature [8]. PSL decay curves as a function of the effective thickness for three absorbers taken at 388 days are shown in Fig.5(a) and all PSL decay curves at 20 and 388 days after loading are summarized in Fig.5(b). It should be noted that Fig.5(a) shows no differences in the PSL decay curves pattern for three absorbers and these curves became close and similar to the

curve for the gold absorber at 20 days in Fig.5(b). The change in the PSL decay curves for copper and aluminum absorbers between 20 and 388 days can be explained by the diffusion process. Diffusion coefficient (D) at 293 K is calculated for tritium through nickel to be 2.5 x 10^{-14} (m^2/s) using literature values [14]. At 20 days after loading, tritium concentration is considered to distribute with a gradient as Dt/l^2 is calculated to be 0.3 (l=0.25 mm) and then a diffusion process ends at 388 days as Dt/l^2 is calculated to be 13 (>> 1.0) [15]. Based on the preliminary results obtained by simulating the bremsstrahlung energy spectrum with Monte Carlo N-Particle Transport Code (MCNP), the spectrum distribution spreads over lower to higher range at 20 days because tritium concentration distributes with the gradient, and the spectrum distribution changes with time, shifting its peak to higher energy with a decrease of lower energy bremsstrahlung X-rays because tritium concentration distribution loses the gradient as the diffusion process proceeds and the uniform tritium distribution is formed in the specimen after 388 days. The relative ratio, a, the component with fast rate of decay for the copper absorber at 388 days was determined as 0.72, which became smaller than that at 20 days (0.98 in Table 1), indicating PSL derived from the lower energy range decreased with time. This result is consistent with the assumed theory. On the contrary, the PSL decay curve for the gold absorber does not seem to have changed with time. This is because PSL derived from the higher energy range does not decrease through the diffusion process. Then, at a result, all PSL decay curves for three absorbers are considered to become similar at 388 days.

The combined technique of the IP and thin absorbers was applied to tritium in the vanadium specimen and PSL decay curves as a function of the effective thickness for three absorbers were obtained (shown in Fig.6), expressing the same pattern with those in the nickel specimen for three absorbers at 388 days.

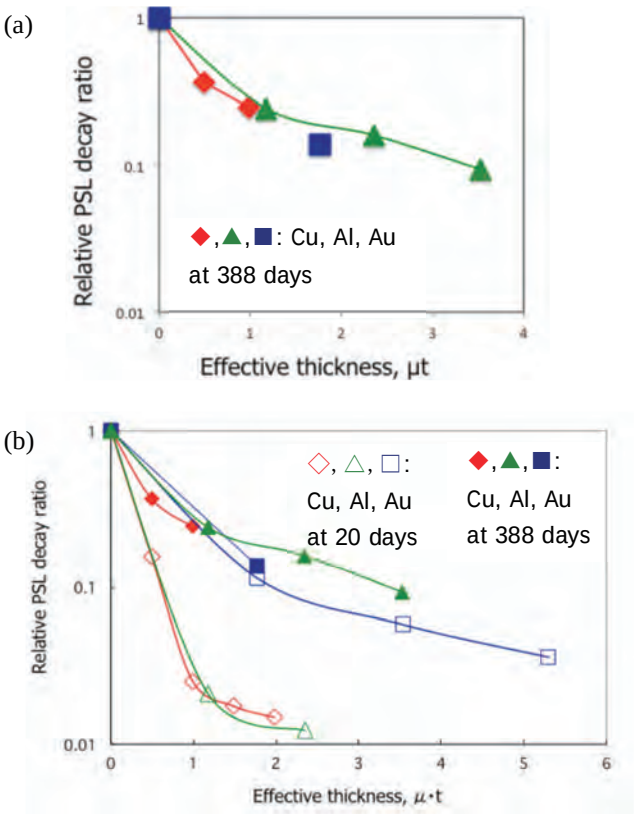

Fig.5 (a) PSL decay curves for the nickel specimen as a function of the effective thickness for three absorbers taken at 388 days after loading. (b) All PSL decay curves at 20 and 388 days after loading. Curves for copper, aluminum, and gold absorbers are shown as ♦,▲, and ■ at 388 days and ◇, △, and □ at 20 days, respectively. The scale of the effective thickness for aluminum absorber is expressed as 1/10 in both figures.

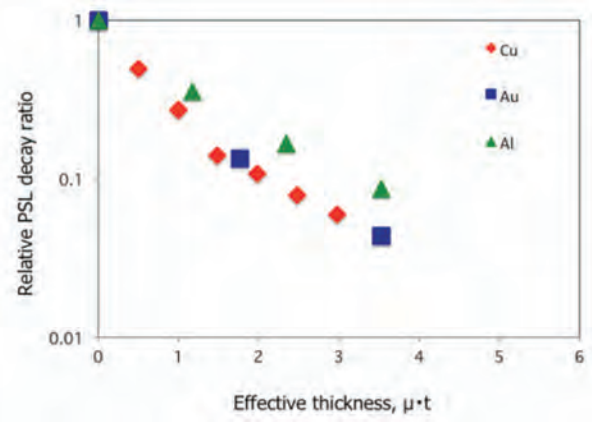

Fig.6 PSL decay curves as a function of the effective thickness for the vanadium specimen. The scale of the effective thickness for aluminum absorber is expressed as 1/10.

In order to obtain tritium distributions in the nickel and vanadium specimen, cross section images and depth profiles were obtained by autoradiography. They were taken at 468 days and 3.9 years after loading for the nickel and vanadium specimen, respectively. Both specimens were cut through the middle and the BAS-TR type-IP was irradiated by contacting the cross section of the specimen directly on the IP for 47 h. To avoid high concentrated tritium on the nickel surface, the side of the cross section was covered with tape during irradiation. The cross section images and depth profiles so obtained are shown in Fig.7(a) and (b) for the nickel and vanadium specimen, respectively. Through the cross section, no significant inclination of tritium concentration was observed in both images and depth profiles. The observation for the nickel specimen in Fig.7(a) can be explained by the diffusion

process. The process ended at 388 days as mentioned above and then tritium distribution is supposed to be uniform in the specimen except high concentrated tritium on the surface. For the vanadium specimen, the diffusivity of tritium is much larger than that in the nickel [9] and the diffusion process ended at the time when autoradiography was obtained, resulting in uniform tritium distribution in the vanadium specimen. These observations for two specimens indicate that uniform tritium distribution in the specimen provides the similar single PSL decay curves pattern for the copper or aluminum and gold absorber.

From comprehensive results, this technique can be used usefully to observe tritium depth distribution in matter nondestructively. Further investigation should be needed for the analysis about the relationship between tritium distribution in the specimen and PSL decay curves pattern by simulating the bremsstrahlung energy spectrum with MCNP Code.

(a)

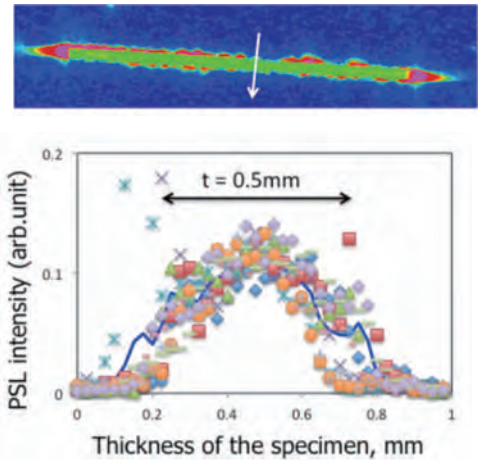

(b)

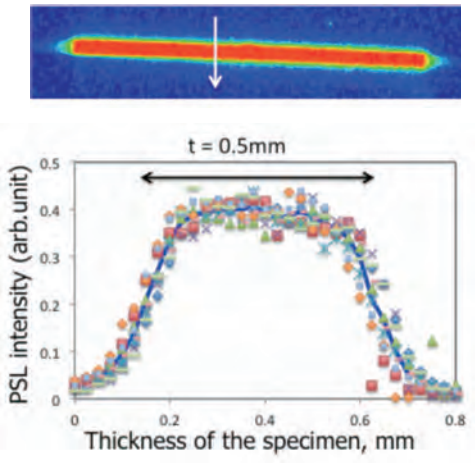

Fig.7 BAS-TR autoradiography cross section images and depth profiles for the nickel (a) and vanadium (b) specimen, respectively. In each figure, the average profile obtained from 10 profiles is shown in a line.

Acknowledgments

This study has been supported in part by KAKENHI on Priority Areas, 476, Tritium for Fusion, from MEXT, Japan, and the National Institute for Fusion Science under the Joint Work contract #NIFS12KUHR017, as a part of Bilateral Collaboration Project with University of Toyama. The author is grateful to Professor Yasuhiro Kondo of Ishinomaki Senshu University for his advice.

[1] T. Tanabe *et al*., Fus. Eng. and Des. **54**, 147 (2001).
[2] K. Miyasaka *et al*., J. Nucl. Mater. **307-311**, 1441 (2002).
[3] K. Masaki *et al*., J. Nucl. Mater. **313-316**, 514 (2003).
[4] T. Tanabe *et al*., J. Nucl. Mater. **313-316**, 478 (2003).
[5] K. Sugiyama *et al*., J. Nucl. Mater. **313-316**, 507 (2003).
[6] J. Miyahara *et al*., Nucl. Instr. and. Meth. **A 246**, 572 (1986) .
[7] H. Ohuchi-Yoshida *et al*., Fus. Eng. and Des. **87**, 423 (2012).
[8] M. Saito *et al*., Fus. Sci. Technol. **60**, 1459 (2011)
[9] Y.Hatano *et al*., Proceedings of 2nd Japan-China Workshop on Blanket and Tritium Technology 100 (2008)
[10] Y.Torikai *et al*., J. Nucl. Mater. **363-365**, 462 (2007)
[11] Fuji Film Co., Ltd. Homepage, http://www.fujifilm.com/products/life_science_systems/science_imaging/imaging_plate/faq/
[12] H. Ohuchi *et al*., Nucl. Instr. and. Meth. **A 490**, 573 (2002).
[13] NIST Homepage, http://physics.nist.gov/PhysRefData/XrayMassCoef/tab3.html.
[14] F. Reiter *et al*., EUR 15217 EN (1993).
[15] J.Crank, The mathematics on diffusion 2nd edition (Oxford university press, New York, 1975) p.50.

The R&D Status of ITER SDS

Sei-Hun YUN[1)*], Chang Shuk KIM[1)], Min Ho CHANG[1)], Hyun-Goo KANG[1)], Seungyon CHO[1)], Hyun Gon LEE[1)], Ki Jung JUNG[1)], Hongsuk CHUNG[2)], Dae Seo KOO[2)], Kyu-Min SONG[3)], Soon-Hwan SHON[3)] and Duk Jin KIM[4)]

[1)] *ITER KO, National Fusion Research Institute, Gwahangno 113, Daejeon, 205-806, Korea*

[2)] *Korea Atomic Energy Research Institute, Daedeokdaero 1045, Daejeon, 305-353, Korea*

[3)] *Korea Hydro & Nuclear Power Co., Central Research Institute, 70-1312-gil, Yeseong-daero, Daejeon, 305-343, Korea*

[4)] *TUV SUD KOCEN, 13F Kranztechno, Sangdaewon-dong, Jungwon-gu, Seongnam, 462-729, Korea*

(Received: 27 May 2012 / Accepted: 24 August 2012)

The ITER tritium storage and delivery system (SDS) is still in pre-conceptual phase. The major functions of ITER SDS are composed of tritium storage in a safe way, rapid fueling based on the plasma scenario and tritium inventory accountancy in a day schedule. The ITER SDS will be delivered to the ITER site as a set of glovebox modules which have every tritium compatible components in its space for tritium confinement and are to be assembled together at the ITER tritium building. Meanwhile there have been some reports for the ITER SDS' R&D activities and progress, the current R&D status is still on-going at the pre-conceptual design (CD) phase. The scope of current R&D has been rearranged with the depleted uranium (DU) oriented experiments for the future ITER application. This report deals with the current status and activities, especially setup of handling procedure, test devices and facility design based on DU getter material, for CD completion of the ITER SDS next year.

Keywords: ITER SDS, R&D status, getter material, ZrCo, DU, process verification, 1:1 scale test.

1. Introduction

ITER tritium storage and delivery system is one of key technologies, which are to be utilized for the fusion tritium plant construction, to provide the fusion fueling system by means of tritium storage, supply and inventory, in a safe way, in accordance with the plasma scenario and accountancy availability in a day basis, respectively. While the SDS is composed of major equipment needed further R&D for detailed design, it will be followed by the systematic R&D program. The main objective of the ITER SDS R&D—even though still on-going—is to verify not only each component's requirements in accordance with the system function, but also performance availabilities as the whole of the SDS' requirements physically and technically combined with each other components that have individual characteristics and performance in most aspects of tritium safety and compatibility. The overall project schedule of the ITER SDS is divided into three distinguishable phases: (1) pre-conceptual R&D phase, (ii) systematically programmed R&D phase (conceptual design phase, preliminary design phase), (iii) and the final design & procurement phase. This report is focused on the current R&D status in pre-conceptual phase, in addition to the further consideration on the interface relatives to the SDS in tritium plant fuel cycle as well. The R&Ds on this ITER SDS lies in the starting point of newly programmed systematic R&D phase. In this period the reference material for ITER SDS has been changed from zirconium cobalt (ZrCo) to depleted uranium (DU), because of different shortfalls in material properties and limits in technical applications [4].

There have been some reports for the SDS R&D activities and progress [1-3]. The content in the first phase, pre-conceptual R&D was focused on ZrCo as the tritium storage material; R&Ds for type and design concept of the tritium storage bed and characteristics of storage material were reported in Ref. [1]; R&D's for bed performance in terms of delivery rate, thermo hydraulic analysis of in-bed calorimetry, studies on hydride reaction using visual cell reactor, unit process verification test having 1:1 scaled ZrCo bed, transfer pump performance and its combination, and calorimeter design for the tritium accountancy at the tritium loading station (TLS) were reported in Ref. [2]; and R&D's for highly concentrated and enhanced results on every ITER SDS' component and interrelationship were also reported in Ref. [3].

From the turning point of the tritium storage material, DU, this report deals with the current status and activities

mainly issued topics, especially DU handling procedures, experimental devices and facility design, in R&D of ITER SDS.

2. Small Scale Bed Experiments and Basic Study

2.1 DU bed preparation & experiment

Various SDS beds including beds using DU has been developing [5]. Fig. 1 shows a metal hydride bed in the glovebox. The argon in the glovebox is pumped through a series of treatment devices, which remove water and oxygen from the gas. Finely divided heated copper metal is used to remove oxygen, and this oxygen removing column is regenerated by passing 4% hydrogen in an argon mixture through it while it is heated, and the water formed is passed out of the box with the excess hydrogen and argon. A 13X molecular sieve is used to remove water by adsorbing it in the pores of the molecular sieves. The hermetically sealed glovebox maintains an argon atmosphere with an H_2O concentration at 0.0 ppm, and O_2 concentration at about 0.0–0.4 ppm. The glovebox is kept at a higher pressure of about 1.25-in. H_2O than the surrounding air, so that any microscopic leaks are mostly leaking inert gas out of the box instead of letting air in. The metal hydride bed is introduced into the main chamber through a sealed antechamber on the right side of the glovebox. In the glovebox the Swagelok nut on the primary vessel is open to introduce the depleted uranium into the primary vessel of the metal hydride bed. The quantity of the depleted uranium has already been exactly measured by using a precision balance in the glovebox. The primary vessel that contains depleted uranium sealed by the Swagelok nut is withdrawn from the glovebox through the antechamber. Finally the primary vessel is assembled with the secondary vessel of the metal hydride bed.

Fig.1 Hydride bed in the glovebox [5].

Fig. 2(a), 2(b) show the equipped system picture and flow diagram of the metal hydride bed performance test rig, respectively [5]. The bed performance test rig can equip two different beds at the same time to compare their performance. The rig is used for a measurement of the hydrogen recovery and delivery rates. A hydrogen delivery scroll pump is connected to the manifold piping. The scroll pump has a desirable pumping characteristic. Its leakage rate is negligibly small. But the leakage rate is measured every time before each hydrogen delivery experiment. Because of its leakage characteristics this pump is used only for an experimental purpose. Metal powders in two bed models are activated through several repetitions of hydriding and dehydriding. The amount of hydrogen used for the initial activation and hydriding & dehydriding runs is measured by the hydrogen pressure filled in the loading vessel and the manifold. The control and data acquisition system is provided.

Fig. 3 shows a temperature transient and heating pattern of the primary vessel during the heating test. The measured and setting values of the primary vessel temperature are almost the same. Overshooting of the heater exists but is negligible. Fig. 4 shows the temperature transient of the primary vessel during the cooling test [6]. Secondary vessel was either under vacuum (case A in Fig. 4) or filled with helium (case B in Fig. 4). A series of hydriding and dehydriding tests for the ZrCo and DU beds is going to be performed further.

2.2 Visual DU hydriding reaction

The DU hydride is going to be analyzed by using a visual cell reactor as shown in Fig. 5 and thermo physical property analyzers. This kind of experimental apparatus was utilized in ZrCo hydriding system before [7-8].

The visual cell apparatus in the right-hand side of Fig. 5 was used to look at the hydride material's behavior at hydriding/dehydriding reaction and the compressibility of the expanded hydride micro-powder [7-8]. Table 1 shows the summary of experimental thermo physical properties—packing density, heat capacity, thermal diffusivity and thermal conductivity—of ZrCo hydride material [8]. This result was also applied to the theoretical analysis and simulation of heat & mass transfer phenomena in the complicated getter bed systems, and engineering design as well.

The DU hydride material is to be tested using similar apparatus (left-hand side of Fig. 5). However, the main difference of DU hydriding reaction system including a visual cell reactor comparing to ZrCo hydriding case is to apply an inert gas atmosphere using a glovebox that covers all equipment for the containment of air and moisture.

2.3 Related engineering studies

Fig. 6 shows the detailed mathematical approach to analyze and simulate the getter bed system that is composed of thin double-layered, annulus-type, ZrCo bed

to be anticipated getting a rapid absorption/desorption behavior than any other geometric type of getter bed. In comparison of thin annulus bed with the typical cylindrical bed that has same lengthy in Fig. 6 the absorption and desorption rate of the thin annulus bed shows remarkable speed in more than two times. On the other hand, the thermal mass of the getter bed was too gross to cool down. The cooling time, therefore, of the heated getter bed after desorption requires much more hours to get ready for the next cycle at absorption process. The next getter bed model should be limited to minimize the thermal mass and to maximize the heat and mass transfer rate for the ITER SDS optimization, theoretically.

(a) Equipped test rig of (b)

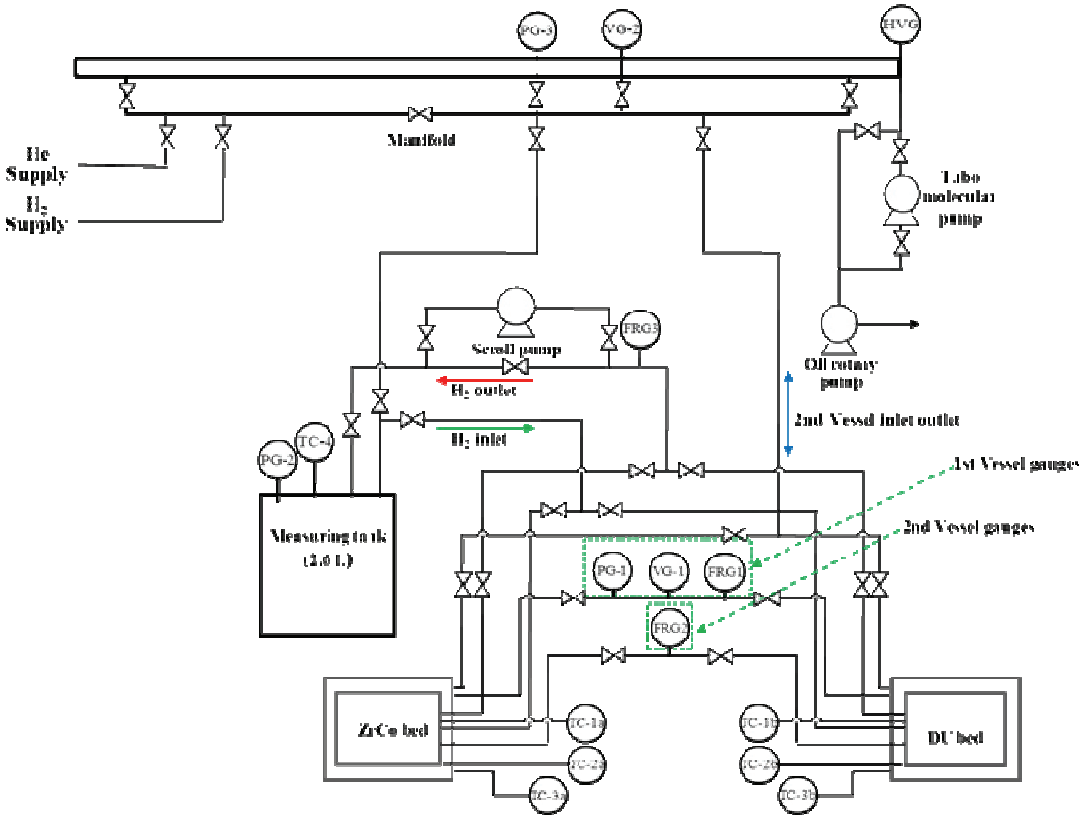

(b) Flow diagram of ZrCo and DU bed system

Fig.2 Hydride bed performance test rig [5].

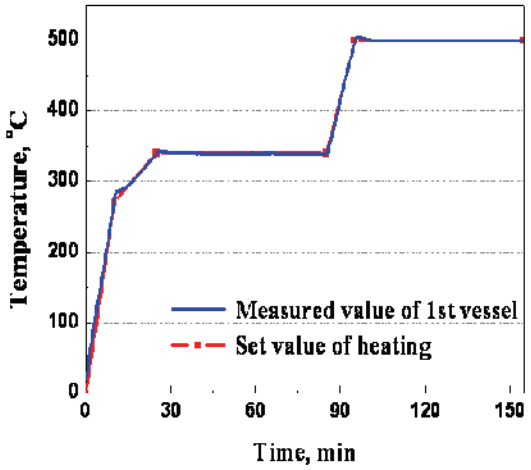

Fig.3 Heating test of the primary vessel [6].

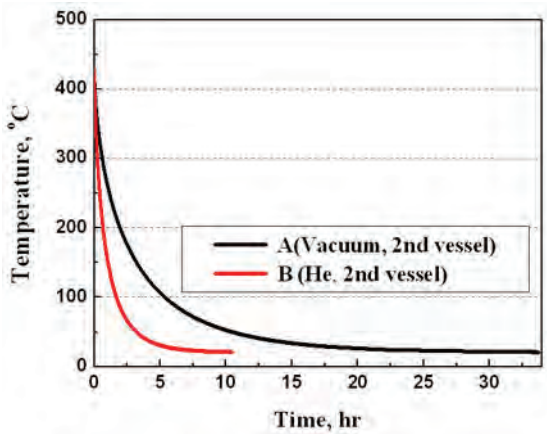

Fig. 4 Cooling test of the bed [6].

Table 1 Thermo physical properties of ZrCoHx [8].

Property	ZrCo	**ZrCo Hydride
Packing Density [g/cm³]	Baotou : 4.990 SAES G. : 3.500	Baotou : 2.389 SAES G. : 1.645
*Heat Capacity [J/g.K]	(25°C) 0.328 (100°C) 0.339 (200°C) 0.308 (300°C) 0.299 (400°C) 0.314 (500°C) 0.330	(25°C) 0.421 (100°C) 0.485 (200°C) 0.443
*Thermal Diffusivity [mm²/s]	(25°C) 0.085 (100°C) 0.074 (200°C) 0.070 (300°C) 0.071 (400°C) 0.078 (500°C) 0.081	(25°C) 0.082 (100°C) 0.077 (200°C) 0.066
*Thermal Conductivity [W/m.K]	(25°C) 0.139 (100°C) 0.125 (200°C) 0.108 (300°C) 0.081 (400°C) 0.122 (500°C) 0.133	(25°C) 0.082 (100°C) 0.089 (200°C) 0.070
*TG Mass Change [%]	Range 20~550°C Initial +0.07 Sharp Increase At 350 °C Final +1.04 DSC : No peak	Range 20~550°C 1st +0.17 (250°C) 2nd +0.37 (375°C) 3rd -0.08 (400°C) 4th +1.29 (550°C) Total +1.74 DSC : 382.6°C Exothermic
*Off-Gas (after TG)	[H_2] very small	[H_2] high amount [H_2O] a little bit

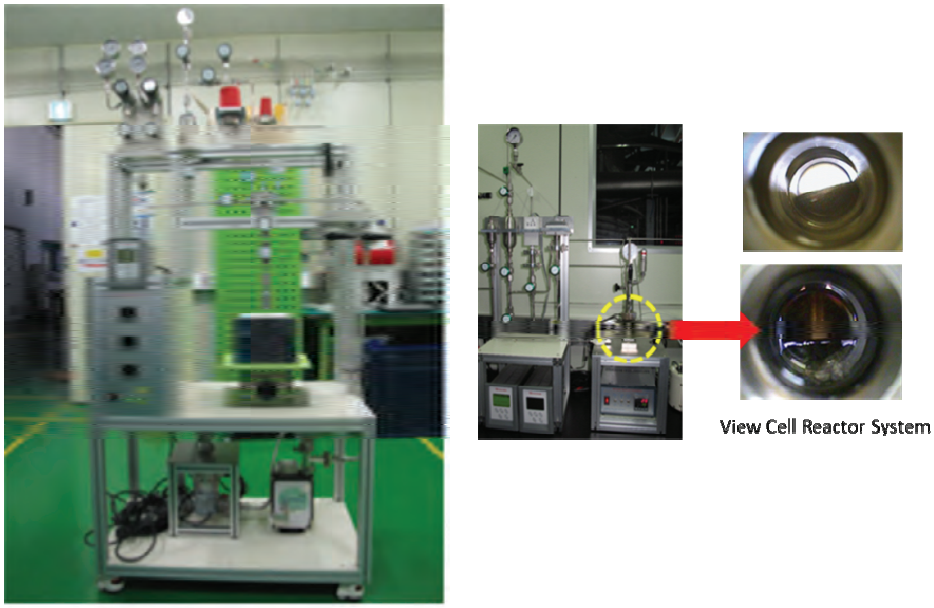

Fig. 5 Metal hydriding apparatus and a visual cell reactor.

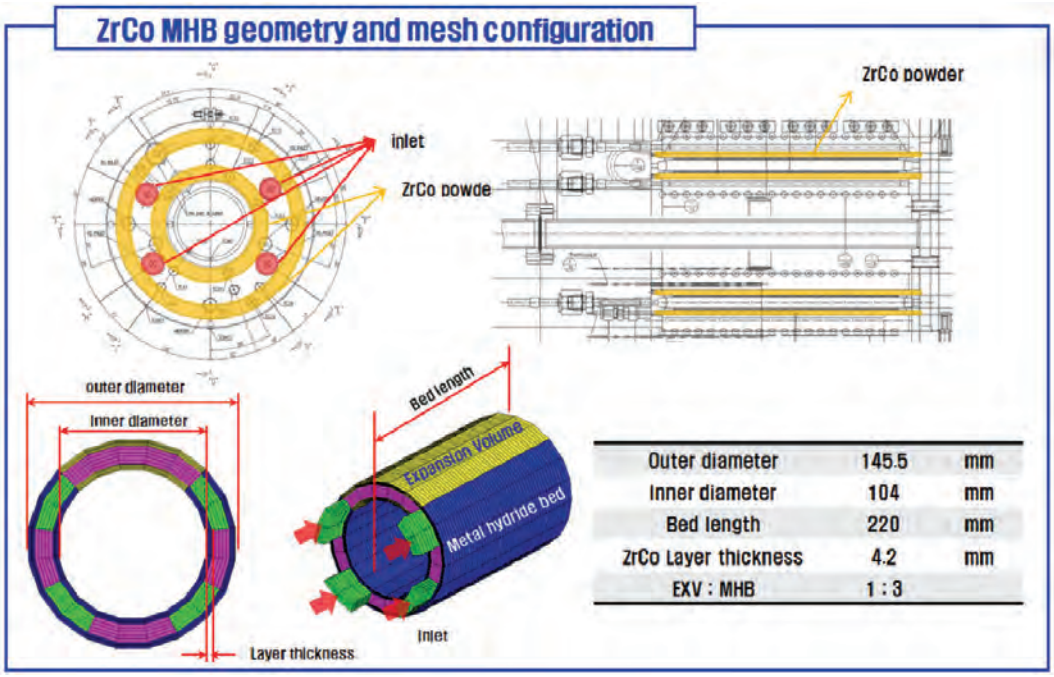

(1) Mesh Configuration

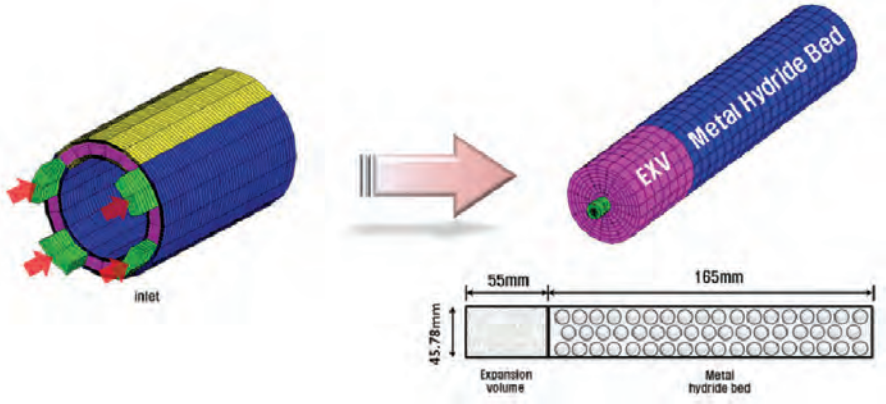

(2) Geometric details and mesh reconfiguration

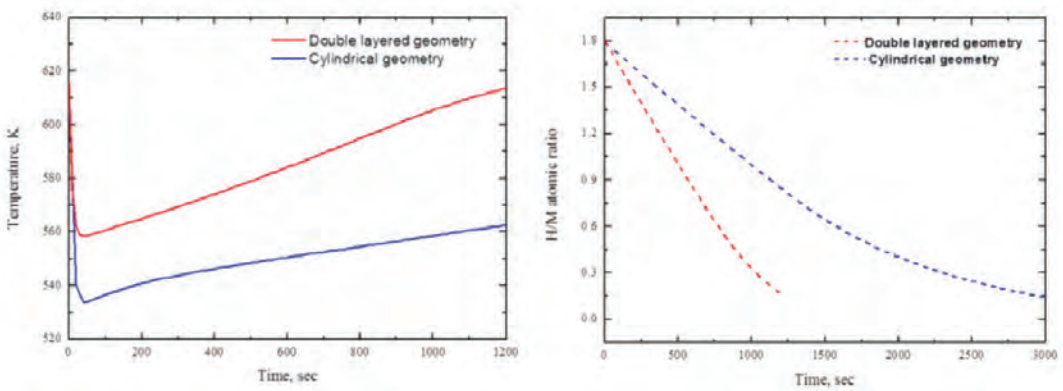

(3) Illustration of temperature and H/M ratio evolution profiles.

Fig. 6 Theoretical approach and simulation result of the annulus-type ZrCo bed (upper), and comparing absorption & desorption rate with cylindrical bed (down).

Fig. 7 shows an illustration of ITER SDS module for the tritium building installation. In general, SDS module and every component in the module glovebox keep the fire-sector rule (The maximum tritium content in every component is limited under 70 gram, and in every container under 700 gram of tritium). ITER SDS module is composed of multiple getter beds, buffer vessels, transfer pumps and many instruments as shown in Fig. 7. Tens of gloveboxes are to be assembled to compose the whole ITER SDS′s functions and requirements.

At one fuel supplying scenario a group of getter beds has to be operated simultaneously to satisfy the ITER fueling requirement. Here, another complicated problem might be occurred, such as control logic development for the optimization of getter bed system operation. Fig. 8 shows a similarity test apparatus using multiple batch-wise efflux system that seems to behave the multiple getter bed system: Efflux/desorption, recharging/ absorption, and successive cyclic operations.

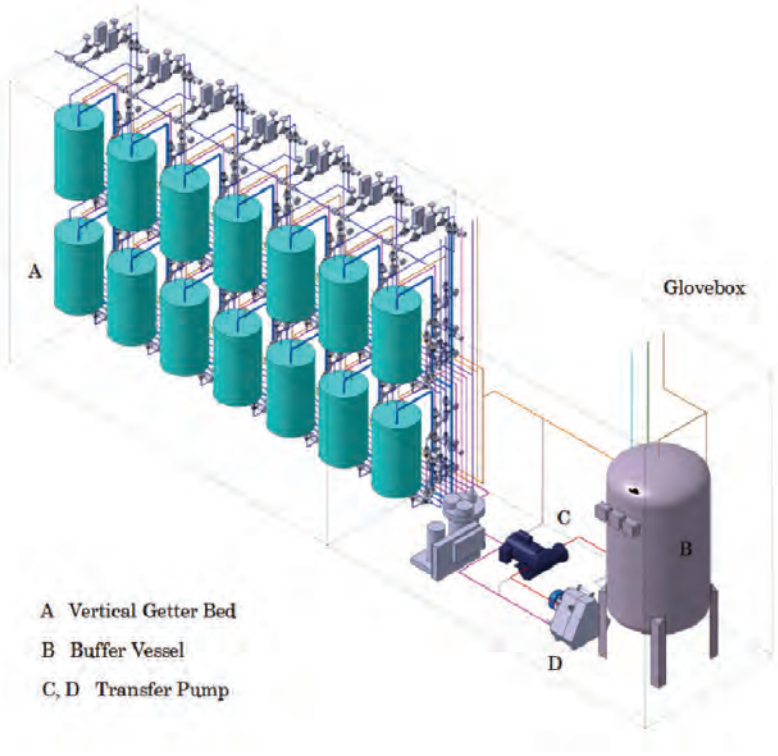

Fig. 7 Illustration of glovebox inside in SDS module (4~6 modules).

1 Series of Tanks
2 Buffer Tank
3 Reservoir Tank
4 Frame
5 Transfer Pump
6 Water Tank (Bed)
7 Level Indicator

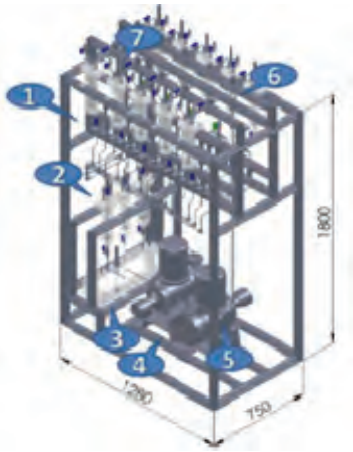

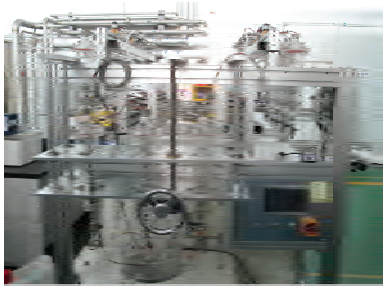

Fig. 8 Similarity test apparatus using multiple batch-wise efflux flow system instead of getter bed system. (Number means a detailed component in this system.)

2.4 He-3 recovery process

Recovery or separation of He-3 from the tritium storage system is one of major function in ITER SDS. Fig. 9 shows the schematic drawing of He-3 recovery system from the tritium storage getter bed as a basis of ITER SDS. Since the release of He-3 from the tritium absorbed in uranium is known to start at about 300 days age, the actual recovery of He-3 in ITER SDS' tritium storage does not seem to be realized. Moreover, the blanket effect is also well known phenomena in recovery of He-3 by concentration of tritium. However, the cyclic circulation of the He-3 mixture is recommended to increase the tritium concentration at the metal getter in Fig. 9. Thereafter, the initial He-3 blanket effect is expected to be diminished in gradual operation. There has been no quantitative result for the cyclic operation of this ITER concept (this concept will be studied also).

3. Verification of SDS Process

3.1 Cooling rate enhancement test

Metal hydride bed is one of the key components in ITER SDS and fusion fuel cycle. As mentioned in section 2.3 (experimental plan for the control logic development), SDS beds are heated for desorption of deuterium and tritium gases. At the same time, SDS beds must be ready for the absorption of DT gases recycled from the fuel cycle. In addition to some flocks of beds have to be ready for the emergency uptake of DT gases. For the better performance of absorption and emergency uptake of DT gases, therefore, the beds must be cooled down in a fast way. If the heating and cooling time of bed is too long, the turnover is delayed and results in enormous increase of SDS beds.

As a part of preparatory, systematic R&D work for the development of SDS bed, experimental study on various cooling of metal hydride bed is to be performed. A revised mock-up of metal hydride bed having the capacity of 70 g tritium storage is developed. ZrCo is used as a dummy material for the getter. The thermal mass is reduced and several active cooling methods are applied to the revised bed. Experimental apparatus for the independent circulation of several cooling circuit is installed as shown in Fig. 10 and Fig. 11. Fig. 10 shows three active cooling circulations. The first is circulation of helium loop which is inserted in the metal hydride layer for the in-bed calorimetry. The second is gas circulation inside outer jacket of the bed. And the last is water cooling jacket which is attached on the surface of outer jacket. Even though the direct water cooling of the getter bed for the purpose of safe tritium storage in priority is to be evaded in feelings, otherwise an indirect cooling should be necessary to maintain the constant glovebox temperature by removing the heat accumulation of heated getter beds. Preliminary test results shows that the outer jacket helium circulation reduces 25 % of cooling time comparing to the natural cooling by helium filled outer jacket. Various combination of active cooling method is under experiments and its results will be presented.

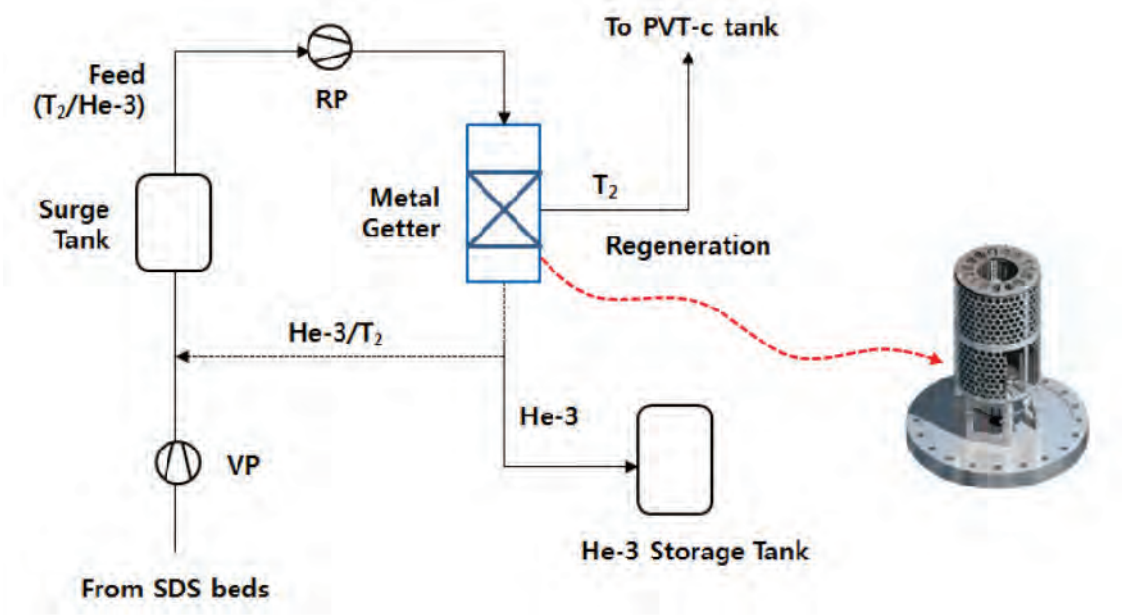

Fig. 9 Schematic He-3 recovery system in ITER SDS.

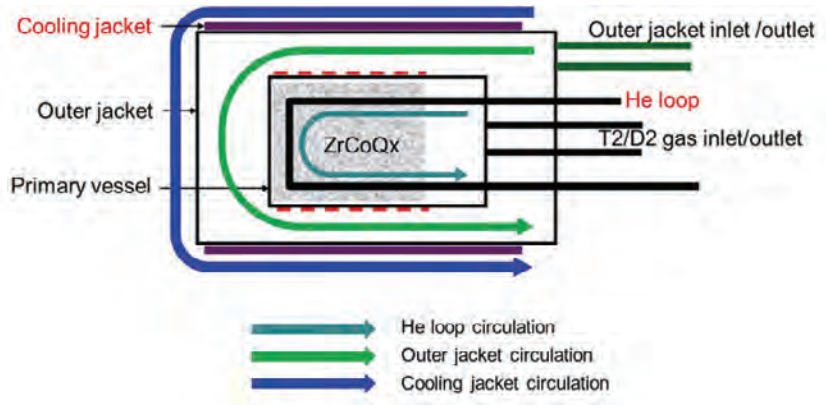

Fig. 10 Schematics of active cooling for hydride bed.

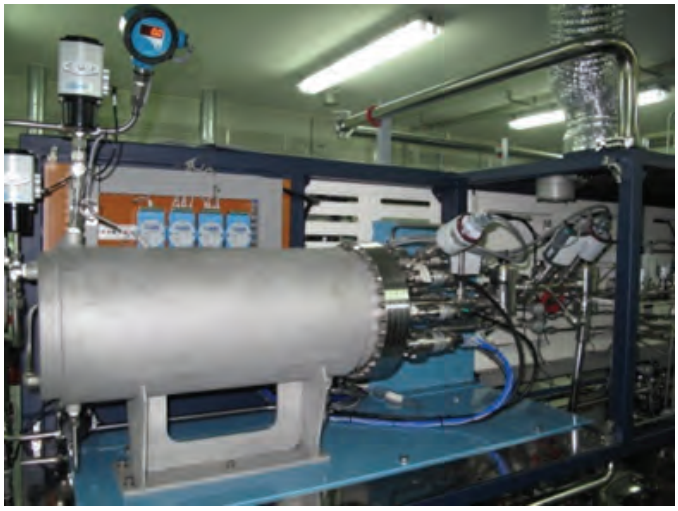

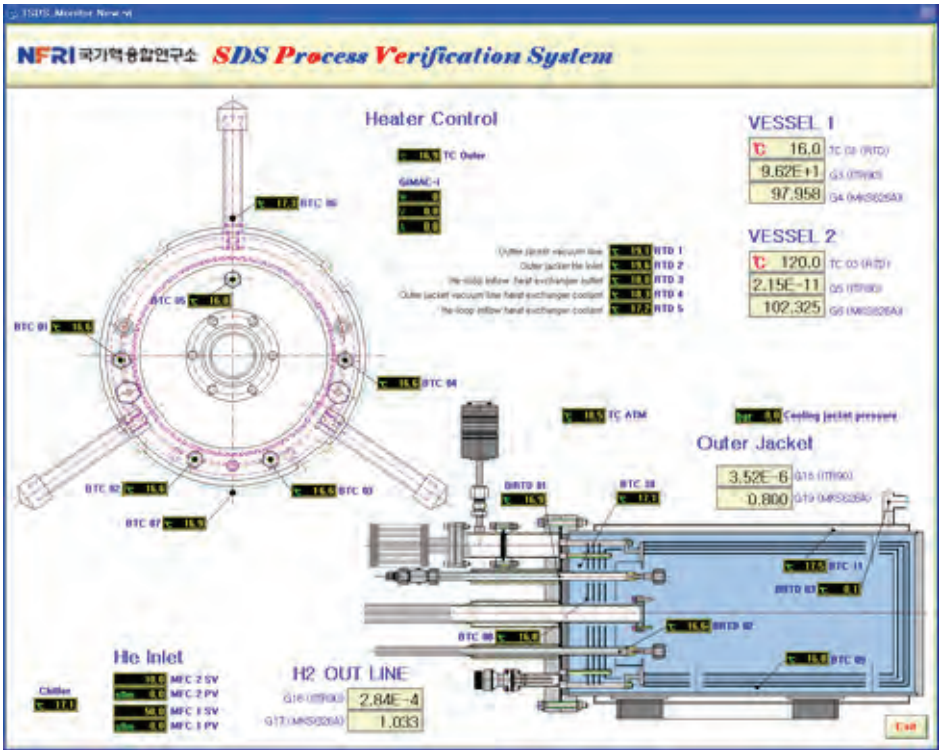

Fig. 11 Installation of improved design 1:1 mock-up bed with active cooling system.

3.2 1:1 scaled DU hydride bed system

SDS beds and major components including DU system has to be experimented to verify the current SDS technology. Fig. 12(a), 12(b), 12(c) show a schematic 3D installation drawing, an overall flow diagram, and one of the typical operation schemes for absorption/desorption performance test, respectively.

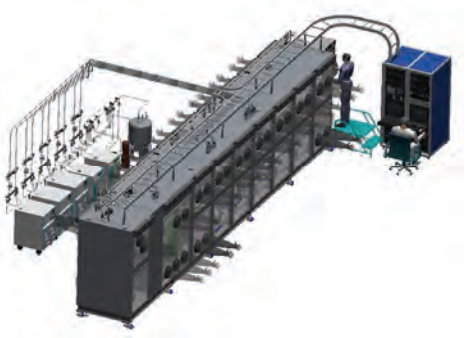

(a) Schematic 3D installation drawing

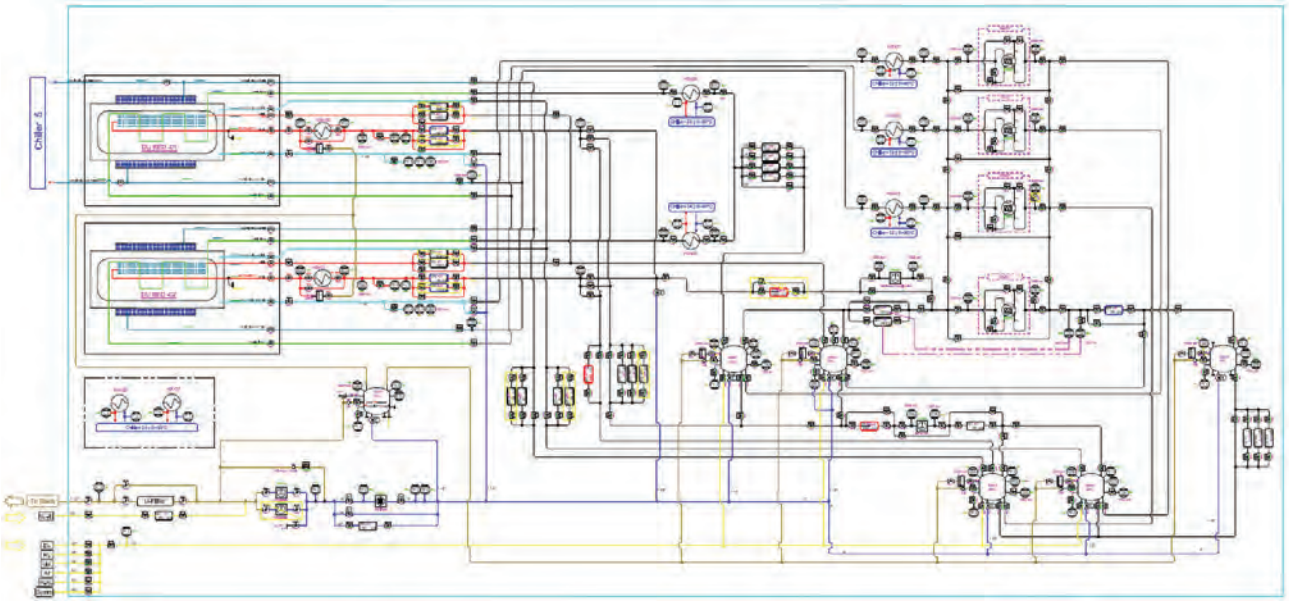

(b) Overall flow diagram for the SDS verification

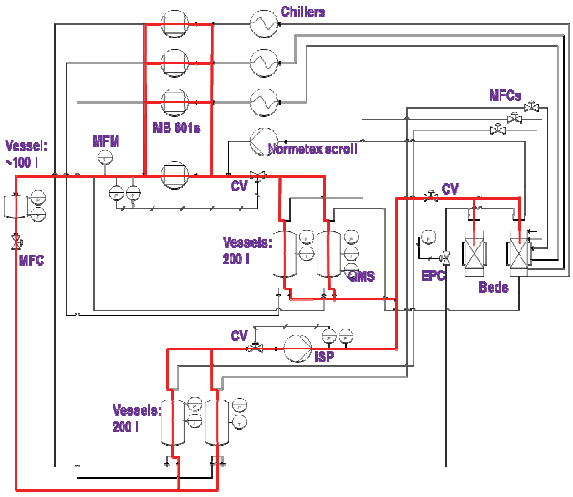

(c) Typical operation for absorption/desorption test

Fig. 12 DU hydride system (1:1 scaled system installation).

The SDS verification test apparatus (see Fig. 12(b)) has various kinds of SDS operation processes that should be verified for the technical completion of SDS. Moreover, through this verification test a clear distinction has to be shown the operability of this facility in two safety aspects: one for tritium and the other for DU.

Fig. 12(c) is one typical operation mode in this test apparatus. The other operation modes are to be tested as follows:

DU bed experiments with;

. Fuel receiving rate in absorption phase
. Fuel delivery rate in desorption phase (one bed)
. Fuel delivery rate with multiple beds
. Tritium accountancy using in-bed calorimetry
. Bed cooling with in-bed calorimetry circulation
. Bed cooling with outer jacket circulation
. Bed cooling with external cooling & circulation
. Bed cooling with overall combination
. He-3 recovery and collection
. Transfer pump performance and combinations
. PVT-c measuring and mass flow meter test
. Other instruments test.

4. Conclusion

The ITER SDS is on-going at pre-conceptual R&D phase. The SDS R&D is currently focused on DU getter bed system which requires careful approach to master and verify every component's performance and application skills. Basic approaches and 1:1 scaled process verification apparatus in SDS R&D are to be prepared on this basis.

The current status and activities, especially setup of handling procedure, test devices and facility design based on DU getter material was described in this report. Every R&Ds will be proceeding for the CD completion of the ITER SDS next year.

Acknowledgment

This research was supported by National R&D Program through the National Research Foundation of Korea (NRF) funded by the Ministry of Education, Science and Technology & Ministry of Knowledge Economy (2012-0000293).

5. References

[1] H. Chung *et al*., Fusion Engineering and Design **84**, 599 (2009).
[2] S. Cho *et al*., IEEE Transactions on Plasma Science **38**, 3, 425 (2010).
[3] S. Cho *et al*., Fusion Science and Technology **60**, 1077 (2011).
[4] M. Glugla *et al*., presented in Tritium 2010 Conference, Nara, Japan.
[5] H. Chung *et al*., Fusion Engineering and Design, doi:10.1016/j.fusengdes.2011.12.002 (2012).
[6] D. Chung *et al*., KNS spring conference, Jeju (2012).
[7] S.-H. Yun et al., Fusion Engineering and Design **86**, 2282 (2011).
[8] S.-H. Yun *et al*., Fusion Science and Technology **60**, 373 (2011).

Trapping of Tritium by Stainless Steel Exposed to Plasmas in Experimental Campaigns of LHD

M. Matsuyama[1)], S. Abe[1)], K. Nishimura[2)], Y. Ono[3)], Y. Oya[4)], K. Okuno[4)], T. Hino[5)] and A. Sagara[2)]
* masao@ctg.u-toyama.ac.jp

[1)] *Hydrogen Isotope Research Center, Univ. of Toyama, Gofuku 3190, Toyama 930-8555, Japan*
[2)] *National Institute for Fusion Science, 322-6 Oroshi-cho, Toki 509-5292, Japan*
[3)] *Center for Research and Development in Natural Sciences, Univ. of Toyama, Gofuku 3190, Toyama 930-8555, Japan*
[4)] *Radiochemistry Research Laboratory, Shizuoka Univ., Shizuoka 422-8529, Japan*
[5)] *Laboratory of Plasma Physics and Engineering, Hokkaido Univ., Sapporo 060-8628, Japan*

(Received: 7 May 2012 / Accepted: 5 October 2012)

Retention behavior of tritium by stainless steel exposed to plasmas in the Large Helical Device (LHD) has been studied by β-ray-induced X-ray spectrometry (BIXS) and an imaging plate (IP) technique. Plasma-exposed stainless steel samples were prepared by exposing the small plates at the location of 6.5L in LHD. X-ray photoelectron spectroscopy (XPS) was also applied to analyze deposition layers on the surface of a sample. XPS analyses showed that the deposition layers contain B, C, O and Ti as well as constituent elements of stainless steel. Chemical form of metallic elements was mainly oxides, but a part was metallic state. The plasma-exposed sample was exposed to tritium gas along with a bare stainless steel plate for comparison. The BIXS and IP measurements showed that the tritium retention largely increased by plasma exposure and it strongly depended on sample temperatures during vacuum heating and tritium exposure. In addition, it was seen from the IP images that non-uniform tritium distribution on the surface was formed even tritium exposure at room temperature.

Keywords: tritium retention, plasma exposure, BIXS, imaging plate, plasma-facing materials

1. Introduction

Reduction of tritium retention in the plasma-facing materials (PFMs) and the structural materials of fusion experimental device such as ITER is one of great important issues from viewpoints of the safety and economy of tritium as well as the fuel particle balance in the reactor core, since a huge amount of tritium is used in the device. These materials are exposed to various energy particles, and surfaces of them are modified. Deposition layers are formed on the surfaces as a result of plasma exposure. They will affect tritium retention. The tritium retention strongly depends on surface states such as chemical state and composition of constituent elements in the deposition layers. Namely, it is important to understand the correlation between tritium retention and surface states of deposition layers.

We have examined so far the trapping and release behavior of tritium in the PFM's of the Large Helical Device (LHD) as an example of the effects of exposure to plasmas for tritium retention [1]. Stainless steel plate is used as a protection plate in LHD. Small stainless steel samples were fixed at four different locations, which are 1.5U, 5.5U, 6.5L and 9.5L in LHD [2], and those samples were exposed to plasmas for one cycle in the 13th experimental campaign. After plasma exposure, they were applied to tritium exposure at 623 K for 4 hours after heating in vacuum at 673K.

It was seen that all of the stainless steel samples were covered with deposition layers, although their thickness was different from each other. Tritium retention in each sample was strongly dependent on the sample location [1]. In addition, significant non-uniform tritium distribution appeared in the plasma-exposed surface of the 6.5L sample, although other samples showed almost uniform distribution. Therefore, the present study was focused on the trapping behavior of tritium in the 6.5L sample.

2. Experimental

The samples used in this study are stainless steel type 316 (SS316), and size of the sample plates was 10×10 mm and 0.5 mm in thickness. These sample plates were finally electropolished, and they were fixed at four

different walls in LHD before beginning of the 13th plasma campaign, which was conducted for 13 weeks from October 2009. After plasma exposure, only 6.5L sample was provided for surface analyses and tritium exposure experiments in this study.

As a first step, the plasma-exposed surface was observed by a digital microscope. This sample was also used to analyze chemical states of surface elements by X-ray photoelectron spectroscopy (XPS). The XPS analysis was performed on a Thermo Fisher Scientific Model ESCLAB250Xi XPS system using Al(Kα) X-rays with an energy of 1486.6 eV.

Tritium exposure tests were conducted by the following procedures. The 6.5L sample and a bare SS316 plate with the same size as a reference sample were set in the tritium exposure device, and it was evacuated below $2x10^{-6}$ Pa at room temperature. The latter sample was used for comparison. In order to examine the effects of pre-heating in vacuum of the samples, at first, they were exposed to tritium gas at room temperature. After β-ray-induced X-ray spectrometry (BIXS) and imaging plate (IP) measurements of them, as the second examination, those samples were again set in the tritium exposure device and then it was evacuated below $6x10^{-6}$ Pa at 673 K. After this evacuation, the samples were exposed to tritium gas at room temperature for 4 hours. Subsequently, as the third examination, the samples were repeatedly set in the tritium exposure device, and those were heated at 673 K in vacuum and exposed to tritium gas at 623 K for 4 hours. Total pressure and tritium concentration of tritium gas used in this study were 2.66 kPa and 4.8%, respectively.

After each procedure of the tritium exposure, to estimate the amount and distribution of tritium retained in surface layers, both of 6.5L and bare SS316 sample were contacted with an IP along with a set of standard tritium sources, which were made of a polymer material labeled with tritium. In this procedure, a thin poy-phenylene-surfide film (PPS: 1.2 μm) was inserted between the samples and IP to avoid contamination of the IP surface. After exposure to IP for a given time, two-dimensional mapping of β-ray dose was obtained by measuring the intensity of photo-stimulated luminescence with the imaging analyzer (Fujifilm FLA-7000). The spatial resolution was 25×25 μm. Some examples of tritium measurements by a similar IP technique have been recently reported by Hatano [3-4]. The BIXS was also employed to evaluate the tritium retention in surface layers and the tritium distribution in depth of a sample. The details of BIXS are described elsewhere [5].

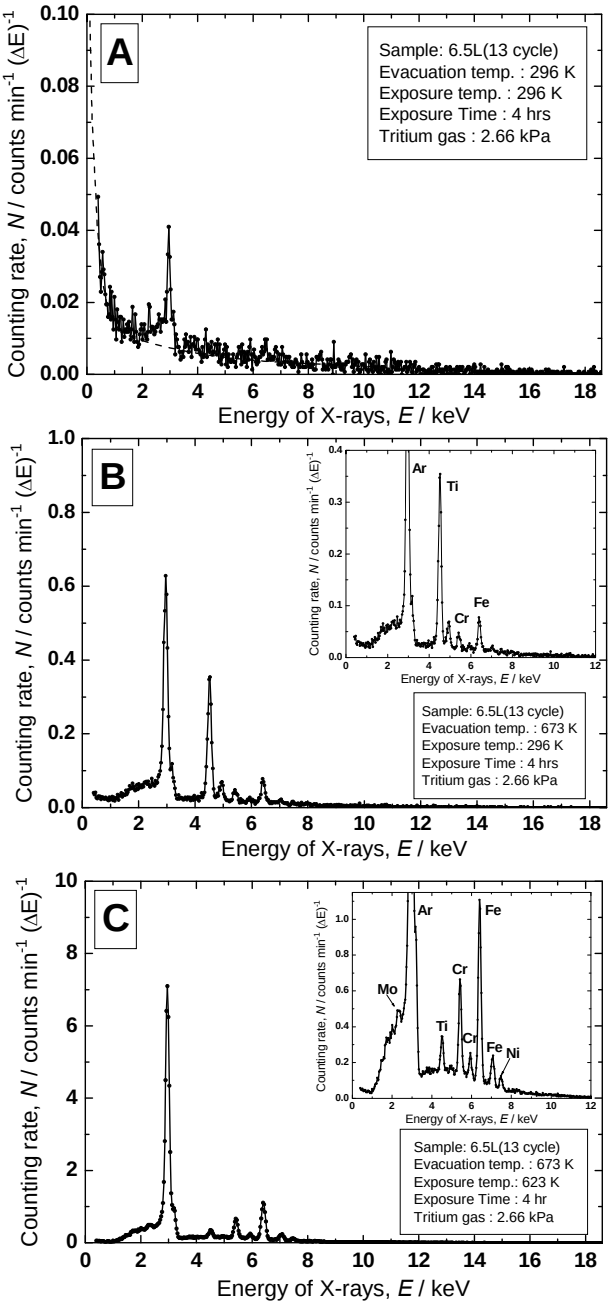

Fig. 1 X-ray spectra observed by BIXS for 6.5L sample.
Each of upper, middle and bottom figures was observed after vacuum heating and tritium exposure under the following conditions. (A) ; heated at 296 K and exposed at 296 K, (B); heated at 673 K and exposed at 296 K, and (C); heated at 673 K and exposed at 623 K. The dashed line in the figure (A) shows the background level of the present X-ray detector.

3. Results and discussion

3.1 Tritium measurements by BIXS

Figure 1 shows the X-ray spectra observed by BIXS measurements. All measurements by BIXS were carried out under the argon atmosphere. Each X-ray spectrum consists of characteristic X-ray peaks and a bremsstrahlung X-ray peak. Number of characteristic X-ray peak observed was dependent on conditions of the vacuum heating and exposure temperature. In the case that both temperatures

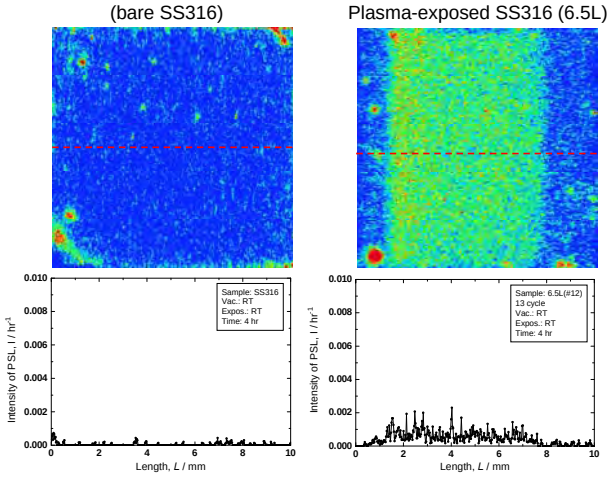

Fig. 2 IP images and line analyses for bare SS316 and 6.5L samples. Both temperatures in vacuum heating and tritium exposure were 296 K.

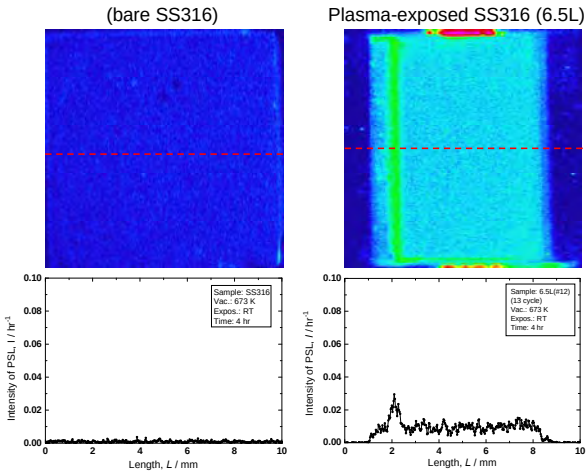

Fig. 3 IP images and line analyses for bare SS316 and 6.5L samples. Vacuum heating was 673 K and exposure temperature was 296 K.

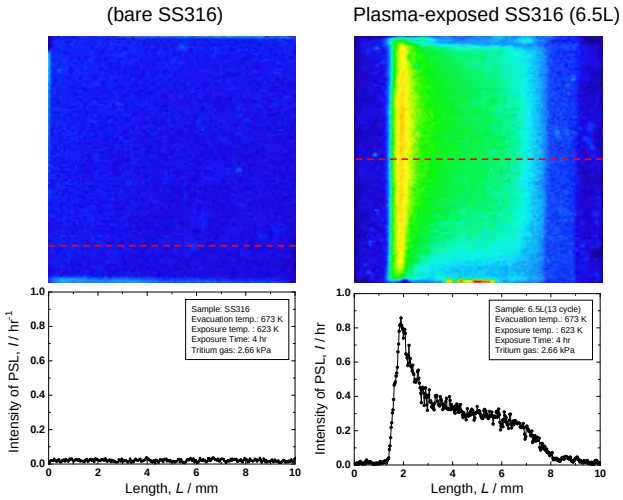

Fig. 4 IP images and line analyses for bare SS316 and 6.5L samples. Vacuum heating was 673 K and exposure temperature was 623 K.

during vacuum heating and exposure processes were room temperature as shown in Fig. 1 (A), only a single peak of Ar(Kα) X-rays was observed. On the other hand, plural characteristic X-ray peaks appeared as shown in Figs. 1 (B) and (C), when vacuum heating and/or exposure temperature were raised. Those X-ray peaks were assigned to Ti, Cr, Fe, Ni and Mo from energies of X-rays as shown in the inset of Figs. 1 (B) and (C). It is considered that appearance of a rather large titanium peak in Fig. 1 (B) is due to the use of a titanium sublimation pump as one of vacuum pumps in LHD. It should be noted that intensity of the Ti(Kα) peak in Fig. 1 (B) is 5 times larger than that of Fe(Kα) peak. Other characteristic peaks are due to constituent elements deposited on the surface by sputtering of stainless steel walls with plasmas in LHD.

It is known that intensity of an Ar(Kα) peak corresponds to the amount of tritium retained in surface layers of a sample because of a short escape depth of β-rays [6]. Intensity of an Ar(Kα) peaks in Figs. 1 (A), (B) and (C) was 0.13, 3.5 and 39 counts/min, respectively. The amount of tritium retained in surface layers largely increased with increasing temperatures of vacuum heating and tritium exposure: namely, tritium activity increased 27 times by elevating the temperature of vacuum heating, and it increased about 300 times by elevating both temperatures of vacuum heating and tritium exposure. The former increase may be due to removal of impurities adsorbed on the surface and diffusion of metallic species from bulk to the surface since the tritium exposure temperature was the same. On the other hand, it is expected that the latter increase was caused by acceleration of tritium diffusion into the deposited layers since the exposure temperature increased.

In addition, the shape of the bremsstrahlung X-ray peak in Fig. 1 (C) was different from that in Figs. 1 (A) and (B). Namely, the shape in Fig. 1 (C) was convex above 3.5 keV. This indicates the diffusion of tritium into the bulk as well as adsorption on the surface. It can be seen, therefore, that the amount of tritium retained in surface layers is strongly affected by both of vacuum heating and exposure conditions even though the surface is covered with the deposited layers.

3.2 Measurements of surface tritium distribution by IP technique

Surface tritium distribution was measured by an IP technique. To determine tritium activity in surface layers, seven standard polymer plates labeled with a given concentration of tritium were used. Main deposition of the surface of plasma-exposed sample was carbon described later and its thickness was thinner than about 1μm. Therefore, escape depth of β-rays in the sample was assumed to be almost same as the standard samples. Figure 2 shows the observed IP image (upper) and the result of

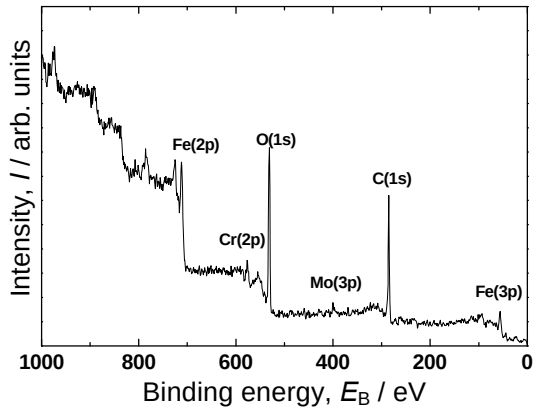

Fig. 5 An example of XPS spectra observed by wide scan.

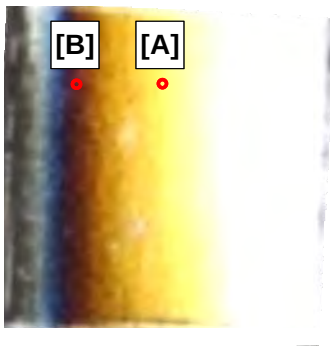

Fig. 6 Photograph of the sample surface and the analyzed spots by XPS.

line analysis (lower) at the red broken line in the image, where both the vacuum heating and exposure temperatures were room temperature. In comparison, similar measurements for a bare stainless steel that is not exposed to any plasma are also shown. Image of tritium distribution measured by IP technique is represented by a color measure. Red color shows the highest activity, while blue color does the lowest activity. Namely, tritium activity decreases relatively with the following color change: red, yellow, green and blue. Surface tritium activity of the 6.5L sample was estimated to be 128 MBq/m^2, while that of bare SS316 was 16 MBq/m^2. Difference in tritium activity was as large as 8 times. It is clear that such a large difference in tritium retention is due to the plasma exposure.

To examine the effects of vacuum heating, exposure to tritium gas was carried out at room temperature after vacuum heating at 673 K. After this, surface tritium distribution was similarly measured by IP technique. The results are shown in Fig. 3. Tritium retention in surface layers of the 6.5L sample was estimated to be 1.97 GBq/m^2 as an average, while that of bare SS316 sample was 0.16 GBq/m^2. The difference in tritium retention of both samples became larger by increasing in temperature of vacuum heating. In addition to this, high retention area appears in the left side of the 6.5L sample as green color.

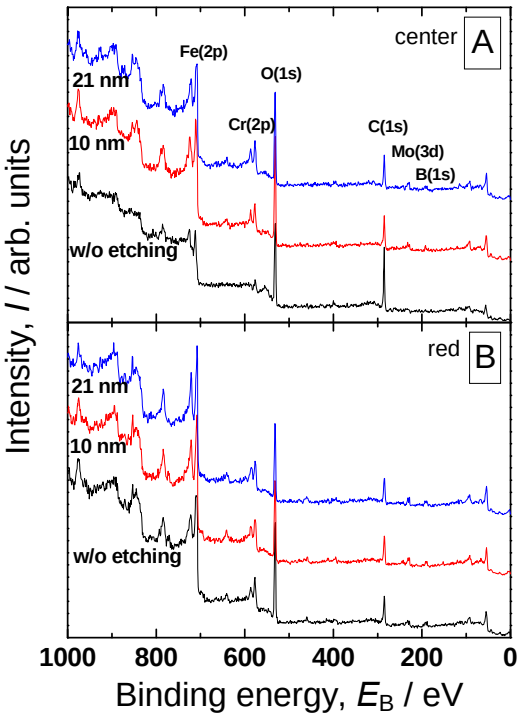

Fig. 7 Changes in XPS spectra for two spots with depth.

This is clearly shown by the result of line analysis. Tritium activity in the green region was 4.06 GBq/m^2, which is about twice of the average concentration. These indicate that high tritium retention appears even though exposure temperature is low, when the sample was pre-heated in vacuum at high temperature. It is considered, therefore, that the large increase in tritium retention is due to the change in adsorption properties of deposition layers by vacuum heating as mentioned above.

Further examination for the vacuum heating effects was carried out: namely, both samples were simultaneously exposed to tritium gas at 623 K after vacuum heating at 673 K. The results are shown in Fig. 4. Tritium retention in surface layers of the 6.5L sample was estimated to be 56.0 GBq/m^2 as an average. This activity was 437 times larger than that observed in Fig. 2, and it was close to the result observed by BIXS. On the other hand, tritium retention of bare SS316 was 3.23 GBq/m^2. Tritium retention of the 6.5L sample was about 17 times larger than that of bare SS316 sample. Furthermore, remarkably non-uniform tritium distribution appeared clearly in the left side of 6.5L sample and the tritium activity in the yellow region was as high as119 GBq/m^2.

3.3 XPS analyses of the plasma-exposed surface

In order to examine causes of non-uniformity in the tritium distribution on the deposition layers of the 6.5L sample, the plasma-exposed surface and its depth profile was analyzed by XPS without any heating treatment. Figure 5 shows an example of XPS spectra observed by

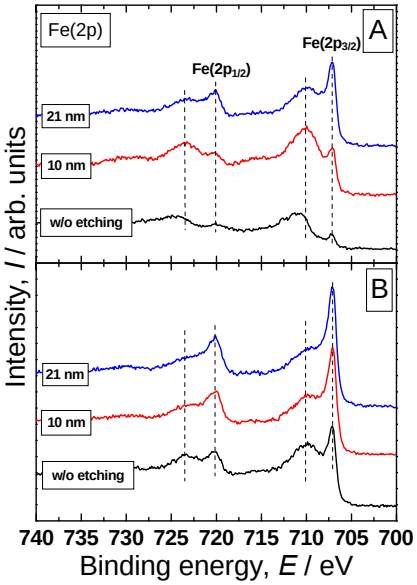

Fig. 8 Changes in Fe(2p) peak with depth.

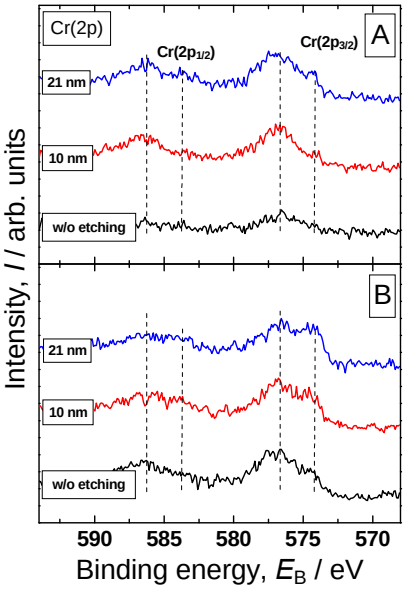

Fig. 9 Changes in Cr(2p) peak with depth.

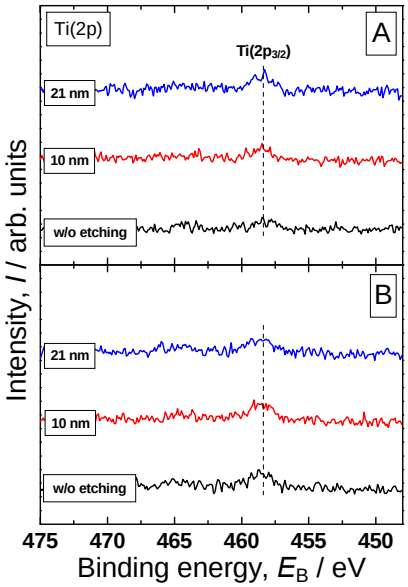

Fig. 10 Changes in Ti(2p) peak with depth.

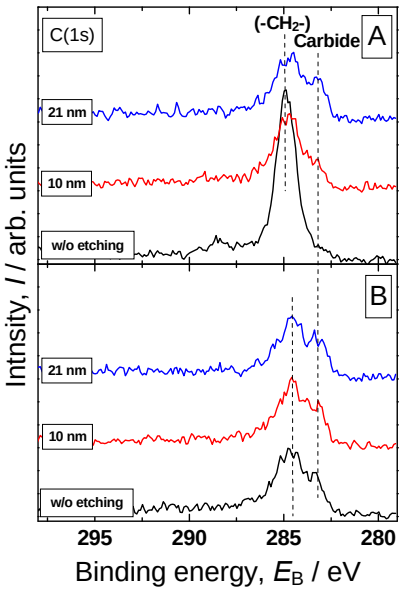

Fig. 11 Changes in C(1s) peak with depth.

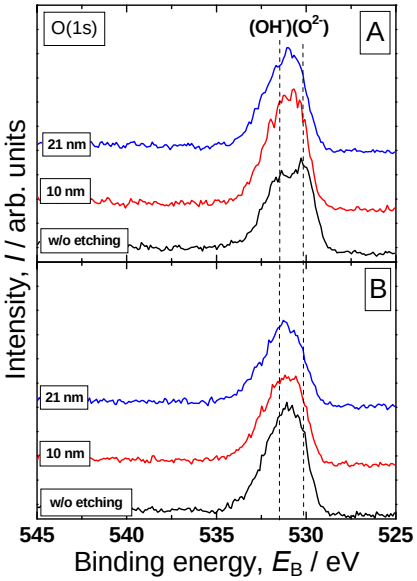

Fig. 12 Changes in O(1s) peak with depth.

wide scan from 0 to 1200 eV. The analyzed spot was almost center of the sample surface. As clearly seen from the spectrum, major elements on the surface are carbon and oxygen. In addition to these elements, small amount of elements such as iron, chromium and molybdenum also deposited on the surface. However, titanium was scarcely deposited in surface layers.

Depth profiles of two spots on the sample surface, [A] and [B], were measured as an example. Location of two spots is shown in Fig. 6. The former spot was the center of the surface, while the latter one is the region of left side, which corresponds to the region in which much tritium was retained as shown in Fig. 4. Changes in XPS spectra for two analyzed spots of the deposition layers were measured with etching by argon. The results are shown in Fig. 7. Etching rate by argon ions was assumed to be 1.0 nm/s, which was obtained from the sputtering of Ta_2O_5 by argon. Difference in peak intensity was observed between two spots: namely, intensity of a carbon peak in the spot [B] was less than that in the spot [A], while that of oxygen was contrarily larger. It should be noted that intensities of metallic Fe, Cr and Mo peaks in spot [B] is larger than those in spot [A], although oxygen peak in spot [B] is more intense than that in spot [A]. Such a remarkable difference in both measurement spots was observed for the as-received surface only, and it became small with depth.

Figs. 8 to 12 show the spectra observed by narrow scan of each element for two spots of [A] and [B]. The observed spectra for iron are illustrated in Fig. 8. It is seen from binding energy that chemical forms of iron consist of metallic iron (707.1 eV ($2p_{3/2}$) and 720.1 eV ($2p_{1/2}$)) and the mixed oxides of FeO, Fe_2O_3 and FeO(OH) (710.1 eV ($2p_{3/2}$) and 723.2 eV($2p_{1/2}$)) [7]. Peak of oxide assigned to the latter species shifted to the lower binding energy side with depth. This indicates that decrease in the amounts of FeO(OH) and Fe_2O_3 is larger than that of FeO with depth. Great difference in two analyzed spots is the fraction of metallic iron as mentioned above. Metallic iron, which is known as one of catalysts available for the adsorption of hydrogen, will contribute to the adsorption of tritium [8]. In addition, existence of iron carbide was also suggested from a C(1s) spectrum as described later.

The observed spectra for chromium are illustrated in Fig. 9. It was seen that chemical forms of chromium are metallic chromium (574.1 eV ($2p_{3/2}$) and 583.6 eV ($2p_{1/2}$)) and its oxides such as Cr_2O_3 and CrO(OH) (576.6 eV ($2p_{3/2}$) and 586.2 eV ($2p_{1/2}$)), although intensities of these peaks are fairly weaker than that of iron peaks. Fraction of metallic chromium increased with the increase in depth. This is a similar tendency to the changes in a peak intensity of iron.

The observed spectra for titanium are illustrated in Fig. 10. Only a weak peak appeared in the spectra. It was seen that a chemical form of titanium is TiO_2 (458.5eV ($2p_{3/2}$)), but metallic titanium (453.8 eV ($2p_{3/2}$) can not be found within a depth of 21 nm. However, an intense X-ray peak of titanium appeared as is shown in Fig. 1 (B), where the sample was heated at 673 K in vacuum and exposed to tritium gas at 296 K. It is considered that titanium atoms diffuse from bulk to the surface by vacuum heating, and tritium concentration near titanium atoms becomes high by annealing at high temperature in vacuum. Further investigations by XPS are required about the diffusion of titanium after vacuum heating at 673 K.

As is shown in Fig. 5, most of the surface was covered with carbon and oxygen atoms. Figure 11 shows the changes in C(1s) peak with depth. Two peaks apparently appeared in each spot. The peak of 283.2 eV was assigned to iron carbide [9], which may not contribute to the tritium adsorption. The higher energy peak (284.9 eV for the spot [A], 284.5 eV for the spot [B]) consists of plural peaks, and they were assigned to chemical forms such as graphite/ aromatics and (-CH_2-) [10]. There was a large difference in the as-received surface: namely, carbon content in the spot [A] is appreciably larger than that in the spot [B], and carbon species in the spot [B] consist of chemical forms of graphite, (-CH_2-) and carbide, although the content and chemical form of carbon in bulk is similar to each other. Tritium retention in point [B] was several times larger than that in point [A] as is shown in Figs. 3 and 4. It is considered, therefore, that the amount of carbon on the surface of deposition layers is one of key factors for tritium retention.

Figure 12 shows the changes in O(1s) peak with depth. At least, the peak of O(1s) consists of two kinds of oxygen species: O^{2-} (530.1 eV) and OH^- (531.5 eV) [11]. Assignment of these peaks coincides with that of oxide peaks of iron and chromium observed in Figs. 8 and 9. There are not large differences in a chemical state of oxygen for both analyzed spots.

4. Summary

Tritium retention behavior on the surface of a stainless steel plate, which was previously exposed to plasmas at the location of 6.5L in the Large Helical Device (LHD) during one cycle, has been studied. To clarify the effects of plasma exposure, the plasma-exposed sample along with a bare sample were exposed to tritium gas under the given temperature conditions. Three different temperature conditions of the vacuum heating and tritium exposure were applied to these samples.

It was seen from the BIXS and IP measurements that the amount of tritium retained in the plasma-exposed surface was larger than that in the bare surface irrespective of temperature conditions and it remarkably increased in increasing temperatures of vacuum heating and tritium exposure. Large heating effects for tritium retention appeared in the plasma-exposed sample than the bare sample of stainless steel. Furthermore, significantly intense X-ray peak of titanium was observed by vacuum heating at 673 K, although it did not appear at 296 K.

Non-uniformity of tritium distribution on the plasma-exposed surface was confirmed by the images of IP irrespective of temperatures of the vacuum heating and tritium exposure. XPS analyses of the as-received surface of the 6.5L sample indicated the existence of metallic chromium and iron, although the surface was exposed to ambient atmosphere after exposure to plasmas. It is considered, therefore, metallic species in the deposited layers are responsible for the non-uniformity of tritium distribution. This will be clarified by further XPS analyses of the sample processed at high temperatures.

Acknowledgement

This work was supported by the Collaboration Research Program of the National Institute for Fusion Science (NIFS10KUHR001).

References

[1] M. Matsuyama, *et al*., Plasma and Fusion Research **7**, 2405091-1 (2012).

[2] T. Hino, Y. Nobuta *et al.*, Fusion Eng. Design **82**, 1621 (2007).
[3] Y. Hatano, *et al*., J. Nucl. Mater. **386-388**, 569 (2009).
[4] Y. Hatano, *et al*., Fusion Sci. Technol. **60**, 982 (2011).
[5] M. Matsuyama, *et al*., J. Nucl. Mater. **290-293,** 437(2001).
[6] M. Matsuyama, *et al*., Fusion Sci. Technol. **41,** 505 (2002).
[7] C.R. Brundle, *et al*., Surface Sci. **68,** 459 (1977).
[8] G.C. Bond, "Catalysis by Metals", Academic Press, London, (1962), p.65.
[9] P.H-Fierro, *et al.*, J. Vac. Sci. Technol. **A11**, 354(1993).
[10] E. Desimoni, *et al*., Surface and Interface Analysis **15**, 627 (1990).
[11] T. Hanawa, *et al*., Materials Trans. **43,** 3088 (2002).

Simulating Tritium Retention in Tungsten with a Multiple Trap Model in the TMAP Code

[a]Brad J. Merrill, Masashi Shimada, Paul W. Humrickhouse

Fusion Safety Program, Idaho National Laboratory, Idaho Falls, ID, USA 83402

(Received: 10 May 2012 / Accepted: 1 September 2012)

Accurately predicting the quantity of tritium retained in plasma facing components is a key safety issue for licensing future fusion power reactors. Retention of tritium in the lattice damage caused when high energy neutrons collide with atoms in the structural material of the reactor's plasma facing components (PFCs) is an area of ongoing experimental research at the Idaho National Laboratory (INL) under the US/Japan TITAN collaboration. Recent experiments with the Tritium Plasma Experiment (TPE), located in the INL's Safety and Tritium Applied Research (STAR) facility, demonstrate that this damage can only be simulated by computer codes like the Tritium Migration Analysis Program (TMAP) if one assumes that the lattice damage produced by these neutrons results in multiple types of hydrogen traps (energy wells) within the material, each possessing a different trap energy and density. Previous attempts to simulate the quantity of deuterium released from neutron irradiated TPE tungsten targets indicated that at least six different traps are required by TMAP to model this release. In this paper we describe a recent extension of the TMAP trap site model to include as many traps as required by the user to simulate retention of tritium in neutron damaged tungsten. This model has been applied to data obtained for tungsten irradiated to a damage level of 0.025 dpa in the High Flux Isotope Reactor (HFIR) at the Oak Ridge National Laboratory (ORNL) after exposure to a plasma in TPE.

Keywords: fusion, safety, tritium, retention, trapping models, TMAP.

1. Introduction

Accurately estimating the quantity of tritium retained in plasma facing components (PFCs) is a key safety requirement for licensing future fusion power reactors, as well as for the International Thermonuclear Experimental Reactor (ITER) [1]. These components not only see the very harsh environment produced by a plasma, such as surface erosion, severe surface heat flux, and high rates of plasma ionic specie implantation, but the 14 MeV neutrons generated by the fusion process create significant damage to the PFC material lattice by atomic displacements and elemental changes through transmutations [2]. This damage acts as ideal traps for tritium retention as implanted tritium diffuses towards the surfaces of the PFC, where it is either released back into the vacuum vessel, or into the PFC's coolant.

Tritium retention in PFC materials is an area of experimental research at the Idaho National Laboratory (INL) under the US/Japan TITAN collaboration. Recent experiments with the Tritium Plasma Experiment (TPE), located in the Safety and Tritium Applied Research (STAR) facility at the INL, demonstrate that this damage can only be simulated by codes like the Tritium Migration Analysis Program (TMAP) [4] if multiple trap sites are used to simulate the damage generated by neutrons [3]. The TMAP code has been released as various versions, the most recent of which has the capability of modeling at most three user specified trap site types. However, even with this number of sites, TMAP was unable to adequately simulate deuterium release from tungsten targets exposed to TPE plasmas that had first been irradiated to a damage level of 0.025 dpa in the High Flux Isotope Reactor (HFIR) at the Oak Ridge National Laboratory (ORNL).

In this paper we describe recent extensions of the TMAP trap site model to treat as many traps as required by the code to simulate the retention of tritium in neutron damaged tungsten material. In the sections that follow, we describe the equations for these new trap site models, the experiments conducted at the INL to develop the data needed to benchmark the implementation of these models, and the application of these models to deuterium retained in neutron irradiated tungsten after exposure to a TPE plasma.

2. Trapping Models in TMAP

The TMAP calculates the time-dependent response any number of gaseous species in a system of solid structures or walls, and related gas filled enclosures by including:

- Implantation of species in structures,
- Movement of species through structure surfaces, governed by molecular dissociation and atomic recombination, or by a solution law such as Sieverts' or Henry's Laws
- Movement in the structure as treated by Fick's law of bulk diffusion with the possibility of specie trapping in material defects,
- Thermal response of structures to applied heating or boundary temperatures,
- Chemical reactions within the enclosures, and
- User specified convective flow between enclosures

Because the equations used to simulate these processes are highly nonlinear, a Newton-Krylov type solver is

[a]Brad.Merrill@inl.gov

used to update these equations at each point in time during a calculation.

The basic equation for movement of these species in the bulk material is the one-dimensional Fick's Second Law of diffusion written as follows:

$$\frac{\partial C_m}{\partial t} = \frac{\partial}{\partial x}\left(D \frac{\partial C_m}{\partial x} \right) + S_m - \sum_{i=1}^{n} \frac{\partial C_t^i}{\partial t} \tag{1}$$

where:

- C_m is the mobile specie concentration (m^{-3})
- D is specie diffusivity (m^2-s^{-1})
- S_m is a specie source term (m^{-3}-s^{-1})
- C_t^i is the trapped specie concentration in the "i^{th}" trap site (m^{-3})
- n is the number of traps allowed by TMAP

The rate at which the mobile species are entering trap defects in the bulk material is:

$$\frac{\partial C_t^i}{\partial t} = \alpha_t f_t^i C_m - \alpha_r C_t^i \tag{2}$$

where:

- α_t is the trapping rate coefficient (s^{-1})
- f_t is the probability of landing in a trap site (-)
- α_r is the release rate coefficient for exiting out of that trap site (s^{-1})

The definition of these terms is:

$$\alpha_t = \frac{D}{\lambda^2};\ f_t = \frac{c_t^o - C_t}{N};\ \alpha_r = \nu_o \exp\left(-\frac{E_t}{kT} \right) \tag{3}$$

and λ is the jump distance or lattice constant (m), c_t^o is the trap site concentration, N is the bulk material number density (atoms-m^{-3}), ν_o is the Debye frequency (s^{-1}), E_t is the trap binding energy (eV) and k is Boltzmann's constant (eV/K).

In order to allow the use of more than the three traps presently allowed by TMAP7, it was a trivial matter of merely changing the TMAP code to accept more than traps, which was also done for the purpose of this study. However, when viewing the Thermal Desorption System (TDS) data from neutron irradiated tungsten it became apparent that perhaps a more accurate approach would be to modify the TMAP code trapping model to accept any distribution of trap site energies; in particular for this study, a distribution based on previous work performed by the INL Fusion Safety Program (FSP) in developing aerosol resuspension models, which is a lognormal or bimodal lognormal distribution [5].

The density function for a lognormal trap distribution in terms of trap energy is written as:

$$\varphi\left(E{:}\mu,\sigma\right) = \frac{1}{\left(2\pi\right)^{1/2}\sigma E} \exp\left\{ -\frac{\left[\ln(E) - \mu\right]^2}{2\sigma^2} \right\} \tag{4}$$

where μ is the lognormal mean and σ is the lognormal standard deviation. Given this distribution, the total concentration of trap sites (c_t^o) at any location in the bulk material equals:

$$c_t^o = \int_{-\infty}^{\infty} c_t^o \varphi(E)\, dE \tag{5}$$

and the trapped concentration of a given specie C_t at that location, and at a given point in time equals:

$$C_t(x,t) = \int_{-\infty}^{\infty} C_t(x,t,E)\, dE \tag{6}$$

Differentiating Eq. 6 with respect to time and substituting from Eqs. 2 and 3, the result for the rate of change of the total trapped concentration of a given specie becomes:

$$\begin{aligned} \frac{\partial C_t}{\partial t} &= \int_{-\infty}^{\infty} \left(\frac{\alpha_t C_m}{N} \left(c_t^o \varphi(E) - C_t(E) \right) - \alpha_r(E) C_t(E) \right) dE \\ &\cong \sum_{i=1}^{N} \left(\frac{\alpha_t C_m}{N} \left(c_t^o \Delta\varphi_i - C_{t_i} \right) - \alpha_{r_i} C_{t_i} \right) \end{aligned} \tag{7}$$

While Eq. 7 could be used directly in Eq. 1, the TMAP code has always been meant to be a relatively fast running computer code capable of performing quick safety scoping and data reduction analysis tasks for the INL FSP. To accomplish this for the present trapping model, we again adopted the same approximation made for our dust resuspension model. By noting that high energy traps will be the last traps to release their trapped inventory, we assume that the traps of this distribution will fill from high energy to low energy in that order, that is from i = N to 1 as illustrated in Fig. 1. The advantage of this assumption is the TMAP is now only tracking the total trapped inventory in this distribution. Since the fraction of traps filled at any point in time equals the trapped inventory divided by the trap density (e.g., $F = C_t/c_t^o$), finding the trap site that is changing in concentration for this approximation is a simple matter of interpolating with respect to the Cumulative Distribution Function (CDF) for a lognormal distribution. This trap is assigned the net transient trapping and release rates for the entire distribution as its concentration is changing in time.

3. Experiments Conducted at the INL

Under the US/Japan TITAN collaborative agreement, tungsten samples that are 6 mm in diameter and 0.2 mm thick were irradiated to three different damage levels (0.025, 0.3 and 2.4 dpa) in the HFIR reactor at ORNL at a temperature of 50ºC.

Following an appropriate cool down period, these samples were exposed to the plasma of the Tritium Plasma Experiment (TPE) at INL's STAR facility. The TPE is a linear plasma device [6] capable of exposing target material to low-energy (100 eV) deuterons at a plasma ion flux of up to $(5–7)\times10^{21}$ m^{-2} s^{-1}. For the

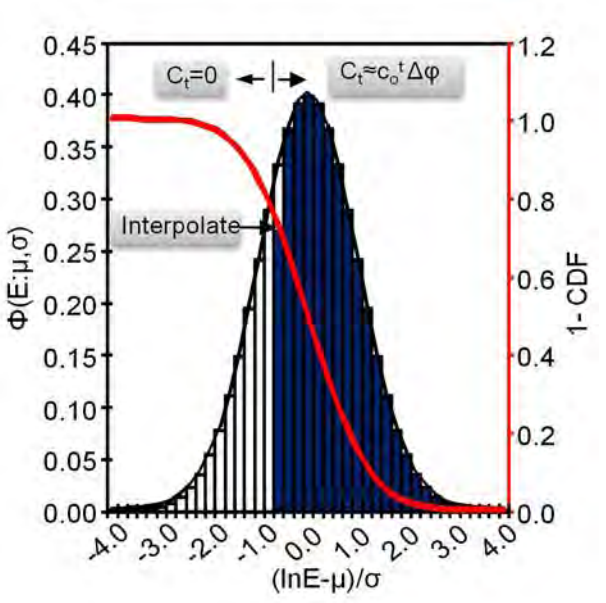

Fig. 1. Schematic of trap filling approximation for a lognormal trap density distribution.

irradiated tungsten samples the plasma was maintained until an ion fluence of (5–7)×10^{25} m^{-2} was achieved for sample temperatures of 100, 200 and 500ºC.

After the deuterium plasma exposure, the samples were removed from TPE and were transferred to the TPE Thermal Desorption System (TDS) in air, where the samples were heated to produce a controlled linear temperature change from 25 to 800ºC. The off-gas from the samples was passed through the Residual Gas Analyzer (RGA) of the TDS that was specially calibrated to measure the absolute concentration of off-gassing D_2. Only the peaks associated with HD (mass 3) and D_2 (mass 4) were considered in this analysis. Fig. 2 presents a TDS spectrum obtained for a 0.025 dpa sample used in this study.

Several of the exposed samples were sent to the Ion Beam Laboratory at University of Wisconsin, Madison for Nuclear Reaction Analysis (NRA) [7] prior to undergoing assay in the STAR facility's TDS. At this facility, a high energy 20 mA helium ion beam is directed at the target to create a D(^{3}He, p)^{4}He nuclear reaction with the deuterium implanted by a TPE plasma. The high energy protons emanating from the sample are used to estimate the depth profile of the deuterium retained in the sample. Given the relatively immobile nature of deuterium in tungsten at room temperature, this depth profile can also be used to infer the hydrogen trap site concentrations for those traps that saturate under TPE irradiation conditions. Fig. 3 contains a sample of NRA data as used in this study.

4. Application of Trapping Models to Irradiated Tungsten Deuterium Retention Data

A key component of any examination of experimental data is the validation of the physics models being solved by the computer code being applied. In order to verify TMAP's trapping models against TPE results, property data for tungsten diffusivity, solubility, and surface recombination are required.

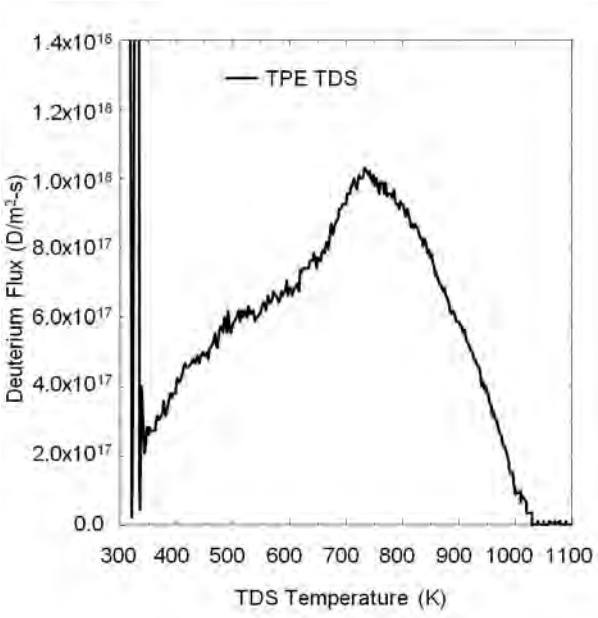

Fig. 2. TDS data of the deuterium retained by tungsten irradiated in HFIR to a damage level of 0.025 dpa after exposures to TPE plasma while maintaining the tungsten temperature at 200ºC.

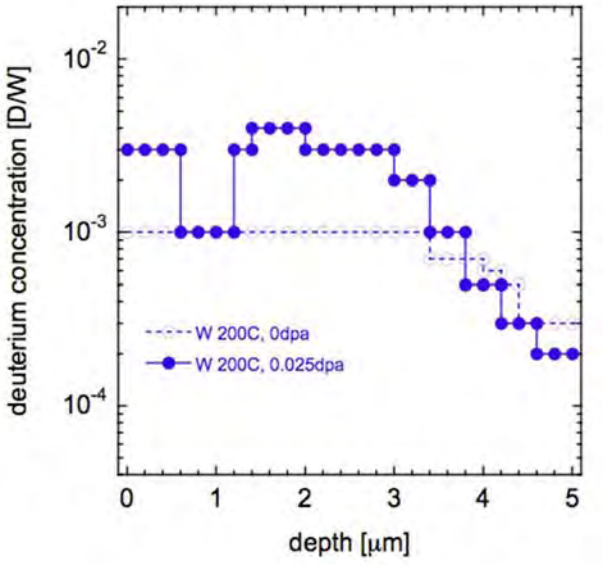

Fig. 3. Deuterium depth profiles for tungsten exposed to a TPE plasma at 200ºC as measured by NRA.

As was the case for Ref. [3], in this study we adopted the hydrogen diffusivity (corrected for deuterium) and solubility formulas proposed by Frauenfelder [8], where (D = 2.9×10^{-7} exp(-0.39 eV/kT) (m^2/s) and K_s = 1.79×10^{24} exp(-1.04 eV/kT) (D/m^3-$Pa^{1/2}$). In literature, surface recombination coefficient formulas can vary by several orders of magnitude [9]. However at this time, the only formula based on experimental data for tungsten is that by Anderl of K_r = 3.2×10^{-15} exp(-1.16 eV/kT)

(m^4/s) was adopted for this study as a representative value for a plasma vacuum environment [10].

Physical data of trap density, D^+ implantation depth, plasma surface flux intensity and target temperatures are also required. The NRA measured D/W atom fraction presented in Fig. 3 was used as a starting value for the total trap site density in neutron irradiated tungsten to a damage level of 0.025 dpa. An implantation depth of 3 nm, as estimated by Wampler [2], was used in our study. In addition, in order to understand if these new TMAP models accurately address the physics of plasma driven retention in tungsten, the actual TPE plasma operating history for the TDS data being examined must be used. For the data presented in Fig. 2, the TPE plasma flux (ramped up to 5×10^{21} D^+/m^2-s and held for 7200 s) and target temperature (under plasma heating to 200ºC) histories for the TPE run that resulted in the TDS data of Fig. 2 were follow in the TMAP model as reported by Shimada [3].

Our first goal is to verify the TMAP results obtained by Shimada [3], for this same TDS case. A good comparison between TMAP7 and TDS data was obtained by these authors by assuming six traps. However, because that version of TMAP only allowed a maximum of three user specified trap sites, the results of two separate TMAP simulations had to be manually added to obtain the result presented. The trap energies and total density for these traps were reported as 0.9, 1.1, 1.3, 1.5, 1.75 and 2.0 eV, and 1.3 at% D/W, respectively. As noted by these authors, the trap density required to match the TDS was much higher than the NRA D/W atom fraction measured for the 0.025 dpa sample that underwent the NRA in Fig. 3. There are a number of possible explanations for this difference, including losses of deuterium by diffusion and surface release between the time of TPE irradiation and NRA examination, uncertainty in the NRA results, or differences in TPE operating history for the TDS sample of Fig. 2 and NRA sample of Fig. 3, etc. However, because we do not have the NRA depth profile for the sample used in the TDS measurement of Fig. 3, it is equally plausible that the trap density is 1.3 at% for the sample analyzed by the TDS.

Fig. 4 contains the results of using six traps used in this study to simulate the TDS of Fig. 3 using the new multi-trap site TMAP model. Unlike the simulations of Ref. [3], where the decision to arbitrarily assign the trapped deuterium concentration profile as the initial condition for performing their TDS simulations, this result was obtained by simulating the implantation process of the TPE plasma, with the goal of determining if the adopted trap sites would actually saturate, as assumed by Ref. 3, at the irradiation temperature (200ºC) experienced by the target. The six traps required to simulate the TDS spectrum had energies of 0.9, 1.0, 1.1, 1.2, 1.4 and 1.6 eV, and a total trap density of 0.35 at%.

One aspect of this simulation that was not true to TPE plasma operation details deals with the filling of the lower energy trap sites. TMAP predicts that at 200ºC the 0.9 eV traps will not saturate. Since TMAP predicts that the mobile deuterium concentration in the tungsten target, which is several orders in magnitude less than the trapped concentration, is too low to fill these traps once the TPE plasma has been terminated, the TPE plasma ramp down had to be extended in time beyond what had actually occurred. The result marked "no overfill" in Fig. 4 illustrates the predicted TDS spectrum when the plasma was ramped down as reported. While additional validation of this new TMAP capability is still needed to verify the accuracy of this result, it does suggest that the deuterium being released in the TDS spectrum below 200ºC had nothing to do with trapping on dislocations but is more likely associated with the deuterium that resides in surface blisters known to develop in tungsten at the implantation fluence experienced by this TPE target (note discussion for Fig. 4 of Ref. [2]).

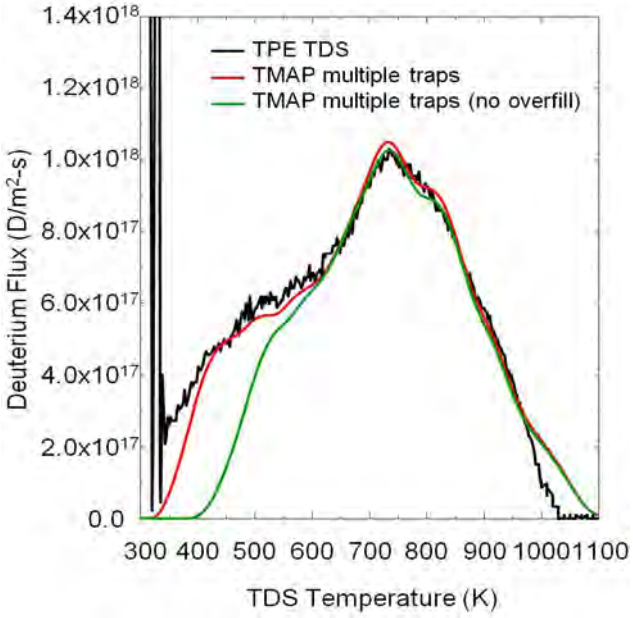

Fig. 4. Comparison of TMAP simulation with multiple traps and the TDS spectrum for neutron irradiated tungsten exposed to a TPE plasma at 200ºC.

Fig. 5 presents the results obtained for this same case with the new TMAP lognormal trap model. An adequate representation of the TPE TDS spectrum was obtained with a truncated (at 1.6 eV) bimodal lognormal distribution, which is a distribution that is the sum of two lognormal populations with proportions p and q, namely:

$$\varphi(E) = p\varphi_1(E{:}\mu_1,\sigma_1) + q\varphi_2(E{:}\mu_2,\sigma_2) \qquad (8)$$

For the comparison in Fig. 5, p and q were both set to 0.5, and the mean and standard deviations of the lognormal distribution φ_1 were set at 0.95 eV and 0.18 eV and for φ_2 set at 1.45 eV and 0.21 eV. The total trap density for this case was 0.47 at%. As can be seen, the simulation represents the data well. As was the case for the six trap model, the lower energy traps could only be filled by ramping TPE down more slowly that what actually occurred.

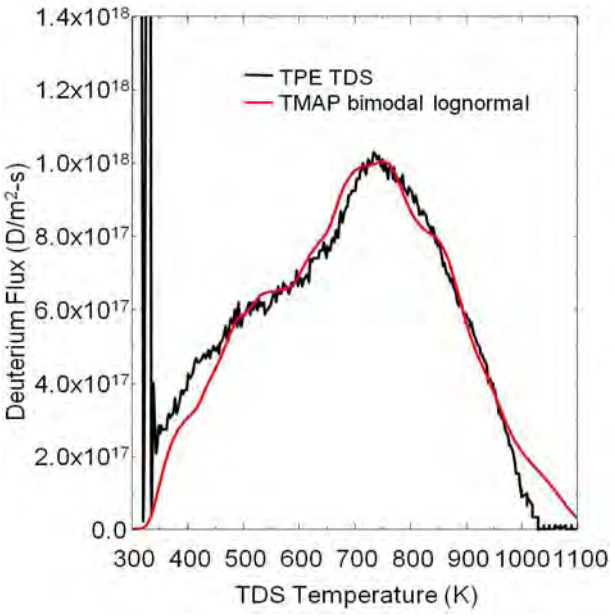

Fig. 5. Comparison of TMAP simulation with a bimodal lognormal trap distribution and the TDS spectrum for neutron irradiated tungsten exposed to a TPE plasma at 200ºC.

5. Summary and Conclusions

Accurately estimating the quantity of tritium retained in or permeating through PFCs is a key safety requirement for licensing future fusion power reactors. The magnitude of these processes is greatly affected by damage created in the structural materials of these PFCs by the 14 MeV neutrons generated by the fusion process. This damage acts as ideal trap sites for tritium retention within the PFCs.

In this paper, we have introduced two extensions to the TMAP computer code trap site model. These extensions allow the TMAP user to specify as many trap sites or a distribution of trap sites as needed to simulate the material damage being modeled. These models were benchmarked against data generated under the US/Japan TITAN collaborative research agreement in the INL's TPE device for retention of deuterium in tungsten that had been irradiated to a damage level of 0.025 dpa in the ORNL HFIR.

We found that the multi-trap extension to TMAP could reproduce the off-gassing data from a tungsten sample exposed to a TPE plasma by employing six traps of energies of 0.9, 1.0, 1.1, 1.2, 1.4 and 1.6 eV, and a total trap density of 0.35 at%. Alternatively, the data could also be matched if a bimodal lognormal trap site distribution is used that has proportions p and q equal 0.5, and mean and standard deviations of the lognormal distribution φ_1 of 0.95 eV and 0.18 eV and for φ_2 of 1.45 eV and 0.21 eV, respectively. The total trap density for this case was 0.47 at%.

While additional validation of these new TMAP capability is still needed to verify the accuracy of this result, the results appear to suggest that the deuterium being released in the TDS spectrum below a temperature of 200ºC had nothing to do with trapping on dislocations but is more likely associated with the deuterium that resides in surface blisters known to develop in tungsten at implantation fluence experienced by this TPE target. Future work in this area with a broader set of experimental data must be undertaken to confirm this conclusion.

Acknowledgments

This work was prepared under the auspices of the US Department of Energy, Office of Fusion Energy Science, under the DOE Idaho Field Office contract number DE-AC07-05ID14517.

References

[1] N. Taylor, D. Baker, S. Ciattaglia, P. Cortes, J. Elbez-Uzan, M. Iseli, S. Reyes, L. Rodriguez-Rodrigo, S. Rosanvallon, L. Topilski, "Updated safety analysis of ITER," Fusion Engineering and Design, **86,** 619-622 (2011).

[2] W. R. Wampler, R. P. Doerner, "The influence of displacement damage on deuterium retention in tungsten exposed to plasma," Nuclear Fusion, **49**, 11502 (2009).

[3] M. Shimada, G. Cao, Y. Hatano, T. Oda, Y. Oya, M. Hara, and P Calderoni, "The deuterium depth profile in neutron-irradiated tungsten exposed to plasma," Physica Scripta, **T145**, 014051 (2011).

[4] G. R. Longhurst, "TMAP7: Tritium Migration Analysis Program," User Manual, Idaho National Laboratory, INEEL/EXT-04–02352, Rev. 2 (2008).

[5] B. J. Merrill, P. W. Humrickhouse, J. P. Sharpe, "An aerosol resuspension model for MELCOR for fusion," Fusion Engineering and Design, **86**, 2686–2689 (2011).

[6] M. Shimada, R. D. Kolasinski, J. P. Sharpe, and R. A. Causey, "Tritium plasma experiment: Parameters and potentials for fusion plasma-wall interaction studies," Review of Scientific Instruments, **82**, 083503 (2011).

[7] M. Mayer, E. Gauthier, K. Sugiyama, U. von Toussaint, "Quantitative depth profiling of deuterium up to very large depths," Nuclear Instruments and Methods in Physics Research Section B, **267**, 506 (2009).

[8] R. Frauenfelder, "Solution and Diffusion of Hydrogen in Tungsten," J. Vac. Sci. Technol. **6** (3), 388 (1969).

[9] B. Lipshultz, et al., "An Assessment of the Current Data Affecting Tritium Retention and its Use to Project Towards T Retention in ITER," Massachusetts Institute of Technology Report, PSFC/RR-10-4, April (2010).

[10] R. A. Anderl, D. F. Holland, G. R. Longhurst, R. J. Pawelko, C. L. Trybus and C. H. Sellers, "Deuterium Transport and Trapping in Polycrystalline Tungsten," Fusion Technology, **21**, 745 (1992).

Implantation Energy Dependence on Deuterium Retention Behaviors for the Carbon Implanted Tungsten

Yasuhisa Oya[1)]*, Makoto Kobayashi[1)], Naoaki Yoshida[2)], Naoko Ashikawa[3)], Akio Sagara[3)], Yuji Hatano[4)], and Kenji Okuno[1)]

[1)] *Radioscience Research Laboratory, Faculty of Science, Shizuoka University, 836, Ohya, Suruga-ku, Shizuoka 422-8529, Japan.*

[2)] *Institute for Applied Mechanics, Kyushu University, Fukuoka 816-8580, Japan.*

[3)] *National Institute for Fusion Science, Gifu 509-5292, Japan.*

[4)] *Hydrogen Isotope Research Center, University of Toyama, 3190, Gofuku, Toyama 930-8555, Japan.*

(Received: 9 May 2012 / Accepted: 8 August 2012)

Effects of energetic carbon implantation on deuterium retention behavior in tungsten were studied. The dislocation loops and vacancies were introduced in tungsten as irradiation damages by energetic carbon implantation. The density of irradiation damages was almost saturated by C^+ implantation below 1 dpa according to TEM observations. The retentions of deuterium trapped by dislocation loops and vacancies were observed in TDS measurements, which were increased as increasing the carbon implantation energy. The deuterium desorption at higher temperature above 600 K was also found, corresponding to the desorption of deuterium retained in the intrinsic cavity in bulk region. However, this trapping was refrained by energetic C^+ implantation, concluding that the retained carbon would play a role as the diffusion barrier of deuterium, which would prevent deuterium penetration through bulk.

Keywords: Tungsten, TDS, TEM, Carbon, Irradiation damage, Diffusion, Simultaneous implantation

1. Introduction

Tungsten is a candidate for plasma facing materials (PFMs) in fusion devices due to its low hydrogen solubility, low sputtering yield and high melting point [1]. The usage of carbon fiber composite (CFC) is also considered in the high heat load region of divertor in fusion reactor, because of its high melting point [2]. These materials will be exposed to energetic particles from plasma during reactor operation. It is well known that carbon materials are easily eroded by energetic hydrogen isotopes by chemical or physical sputtering processes. Then, sputtered carbon will be implanted into tungsten with hydrogen isotopes during plasma operation, which will form the tungsten-carbon (W-C) mixed layer on the surface region of tungsten [3-5]. Hydrogen isotopes including tritium will be implanted simultaneously with formation of W-C mixed layer, and will dynamically interact with carbon in tungsten. In the view point of the fuel recycling, it is important to elucidate the retention behavior of hydrogen isotopes retained on tungsten materials in the fusion environment.

In our previous studies, deuterium retention behavior in tungsten with simultaneous 10 keV C^+ implantation was evaluated. Enhancement of deuterium retention by the introduction of irradiation damages was clearly observed because 10 keV C^+ implantation induced higher displacement damage in tungsten than that by deuterium [6]. On the other hand, it is reported that the carbon retained in tungsten plays a role of diffusion barrier for hydrogen isotopes toward the bulk, resulting in the decrease of hydrogen isotope retention in tungsten [7]. Recent ion-driven permeation experiments under carbon - deuterium simultaneous implantation indicate that deuterium permeation is promoted by simultaneous carbon implanted tungsten [8, 9]. These results indicate the estimation of hydrogen isotope retention in tungsten is complicated under fusion environment. Therefore, deuterium retention in tungsten implanted with carbon was investigated in this study to understand the effect of carbon implantation on deuterium retention behavior in tungsten. For this objective, two types of implantation were carried out. One was the simultaneous implantation (C^+ - D_2^+ sim. imp.) where carbon and deuterium were implanted into tungsten simultaneously. In the simultaneous implantation circumstance, deuterium was retained in tungsten with formations of irradiation defects and W-C mixed layer. The other implantation was the sequential implantation (C^+ - D_2^+ seq. imp.), meaning that

author's e-mail: syoya@ipc.shizuoka.ac.jp

carbon was implanted into tungsten prior to deuterium. In the sequential implantation, deuterium was implanted into tungsten after formations of irradiation defects and W-C mixed layer. In addition, implantation energy of carbon was changed to investigate dependences of the distribution of carbon and damage on deuterium retention behavior. The deuterium retentions were evaluated by means of Thermal Desorption Spectroscopy (TDS) measurements. The irradiation damages were also observed by Transmission Electron Microscopy (TEM) at Kyushu University.

2. Experimental

A disk-type polycrystalline tungsten with stress-relieved conditions (heated at 1173 K), which was supplied by Allied Material Co. Ltd was used. The sample size was 10 mm diameter and 0.5 mm thickness. The Sample was polished mechanically to the roughness of less than 1 μm by SiC abrasive papers and mono-crystalline diamond suspensions, and preheated at 1173 K for 30 minutes under ultrahigh vacuum to remove the impurities and damages introduced during the polishing processes. Then, simultaneous or sequential carbon ion (C^+) and deuterium ion (D_2^+) implantations were performed in the C^+-D_2^+ simultaneous implantation apparatus at room temperature. In this apparatus, the sample can be irradiated independently by two different ion guns, namely C^+ and D_2^+ guns. In the C^+ gun, CO_2 was used as the C^+ source gas to get rid of hydrogen impurities. The E × B mass separator was equipped at the head of the C^+ gun to extract pure C^+. The incident angles for the C^+ and D_2^+ guns were 15 degrees from the sample surface normal, forming an angle of 30 degrees between the two beams. The energy of C^+ was changed from 5 to 10 keV and that of D_2^+ was set to be 2 - 3 keV. The C^+ and D^+ flux were 0.1×10^{18} C^+ m^{-2} s^{-1} and 1.0×10^{18} D^+ m^{-2} s^{-1}, respectively. Therefore, for C^+-D_2^+ simultaneous implantation, the ion flux ratio was set to be $C^+/D^+ = 0.1$. The C^+ fleunce was constant to be 0.1×10^{22} C^+ m^{-2} in C^+-D_2^+ sequential implantation. D^+ fluence was changed in the range of $(0.1 - 1.8) \times 10^{22}$ D^+ m^{-2}. The only D_2^+ implantation was also performed to compare the deuterium retention in C^+ implanted tungsten. The chemical states of carbon and tungsten were studied by X-ray Photoelectron Spectroscopy (XPS). The TDS measurements were performed from room temperature to 1173 K with a heating rate of 0.5 K s^{-1}. The TEM observations were also performed to investigate the irradiation damages formed by the ion implantations. The depth profile of deuterium was analyzed by Glow Discharge Optical Emission Spectroscopy (GD-OES).

3. Results and discussion

Fig. 1 show TEM images of tungsten implanted by 3 keV D_2^+ with the fluence of 1.0×10^{22} D^+ m^{-2} and tungsten with 10 keV C^+ with different C^+ fluences in the range of $(0.001\text{-}0.1) \times 10^{22}$ C^+ m^{-2}. For all the samples, lots of dislocation loops were introduced in tungsten by ion implantations, which was quite different from pure tungsten where its density was low. In addition, since the irradiation vacancy and dislocation loop are pair defects, the formation of dislocation loops indicated the introduction of vacancies. It was also found that even higher fluence of D^+, density of irradiation defects in tungsten with 10 keV C^+ implantation was higher than that with 3 keV D_2^+ implantation, indicating that irradiation damages were easily introduced in tungsten by 10 keV C^+ implantation compared to that by 3 keV D_2^+ implantation due to higher implantation energy, higher mass and larger atomic radius. It was also found that density of irradiation damages in tungsten induced by 10 keV C^+ implantation was increased in the C^+ fluence range of $(0.001\text{-}0.01) \times 10^{22}$ C^+ m^{-2}, but its density was seen to be the same with C^+ fluence larger than 0.01 ×

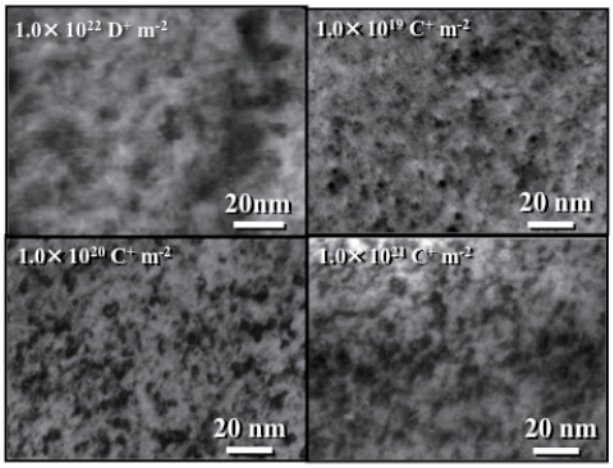

Fig. 1 TEM images of tungsten implanted with 3 keV D_2^+ or 10 keV C^+ at various ion fluences.

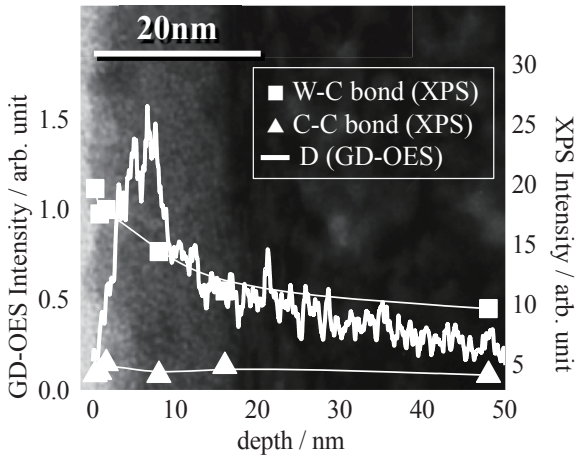

Fig. 2 Depth profiles of D observed by GD-OES and W-C and C-C bonds by XPS. The TEM image was also shown in this figure.

10^{22} C^+ m^{-2}, indicating that density of irradiation defects were saturated in the C^+ fluence of 0.01×10^{22} C^+ m^{-2}. By the SRIM (Stopping range of Ions in Matter) code calculation [10], irradiation defects in tungsten implanted by 10 keV C^+ with the C^+ fluence of 0.01×10^{22} C^+ m^{-2} were distributed within 30 nm beneath the surface, with the peak at around 5 nm (1.3 dpa), indicating that the density of irradiation defects would be saturated below 1.3 dpa. The depth profiles of D observed by GD-OES at University of Toyama and, W-C and C-C bonds evaluated by XPS were shown in Fig. 2. The TEM image was also overlapped in this figure. It was found that most of D was retained in W-C mixed layers and major chemical state of C in this layer was found to be W-C bond.

Fig. 3 shows D_2 TDS spectra for only 3 keV D_2^+ implanted tungsten and 10 keV C^+ - 3 keV D_2^+ sequentially implanted one with various D^+ fluences. These spectra were consisted of three desorption stages at around 370, 480 and 620 K which were named as Peaks 1, 2 and 3, respectively. In lower D^+ fluence of 0.1 ~ 0.3 x 10^{22} D^+ m^{-2}, the deuterium retentions as Peaks 1 and 2 were clearly increased by C^+ implantation, indicating that these desorption stages would be related to the deuterium interacted with the irradiation damages. The density of irradiation damages induced by 10 keV C^+ implantation was higher than that by 3 keV D_2^+ implantation as shown in Fig. 1, resulting in the higher deuterium retention for the 10 keV C^+ implanted tungsten. In general, trapping energy of deuterium by vacancy would be higher than that by dislocation loop [11,12], indicating that Peaks 1 and 2 could be assigned to the desorption stages of deuterium trapped by dislocation loops and vacancies, respectively. In higher fluence of 1.8×10^{22} D^+ m^{-2}, the deuterium retentions as Peaks 1 and 2 for C^+ implanted W were almost the same as that without C^+ implantation, indicating that deuterium trappings by irradiation damages should be almost saturated. However, the deuterium retention as Peak 3 for only D_2^+ implanted tungsten was higher than that for 10 keV C^+ - 3 keV D_2^+ sequentially implanted one. The amount of trapping site as Peak 3 was not induced by ion implantation because the retention of deuterium as Peak 3 was not increased by 10 keV C^+ implantation. Therefore, the promising trapping site for Peak 3 would be intrinsic sites such as cavities, grain boundary and/or oxygen impurity [13,14]. Lower deuterium retention as Peak 3 for 10 keV C^+ - 3 keV D_2^+ sequentially implanted tungsten would indicate that deuterium diffusion in tungsten was refrained by 10 keV C^+ implantation.

The retentions of deuterium retained as Peaks 1, 2 and 3 for tungsten with 10 keV C^+ - 3 keV D_2^+ sequential implantation or simultaneous implantations were compared in Fig. 4. The deuterium retentions for the samples with the D^+ fluence of 1.8×10^{22} D^+ m^{-2} were

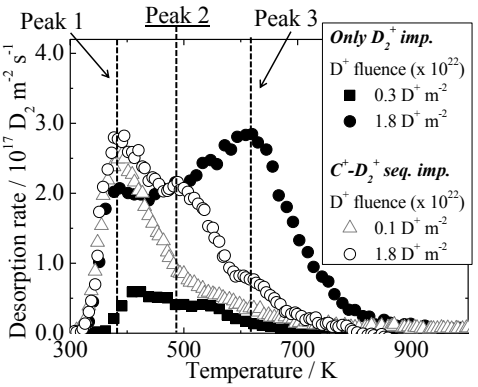

Fig. 3 D_2 TDS spectra of 3 keV D_2^+ implanted tungsten and 10 keV C^+- 3 keV D_2^+ implanted one.

compared. In the case of C^+- D_2^+ simultaneous implantation, the retention of deuterium retained as Peak 3 was decreased by C^+ implantation, which was almost the same with both of sequential and simultaneous implantations. However, the deuterium retentions as Peaks 1 and 2 for the simultaneous implantation were increased compared to those for the sequential implantation. The deuterium trappings as Peaks 1 and 2 for C^+- D_2^+ simultaneously implanted tungsten were higher than that for sequentially implanted tungsten, indicating that simultaneous implantation effects were contributed to the increase of deuterium retentions in these peaks.

To clarify the simultaneous implantation effects on deuterium retention behavior in tungsten, incident energy of C^+ was changed for both of sequential or simultaneous implantations. The implantation energy of D_2^+ was fixed to be 2 keV. Figs. 5 (a) and (b) show the D_2 TDS spectra for C^+ - D_2^+ simultaneously implanted tungsten and C^+ - D_2^+ sequentially implanted one as a function of C^+ incident energy, respectively. Both of D^+ and C^+ fluences were set to be 1.0 x 10^{22} D^+ m^{-2} and 0.1 x 10^{22} C^+ m^{-2}, respectively. The D_2 TDS spectra were slightly changed in simultaneous implantation case although little changes

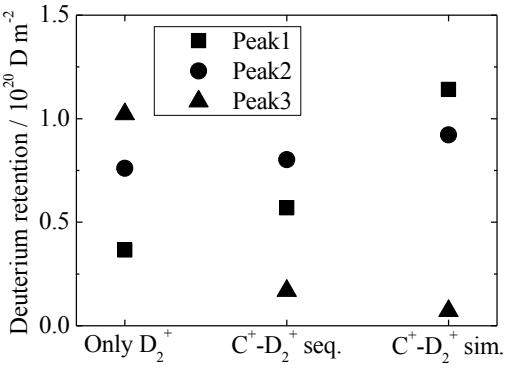

Fig. 4 Comparison of deuterium retentions as Peaks 1, 2 and 3 for tungsten implanted with various implantation procedure.

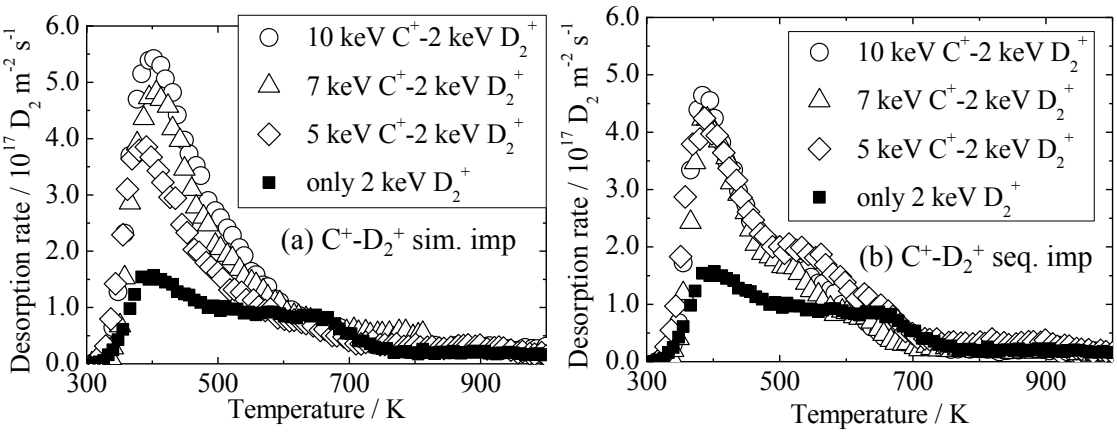

Fig. 5 D_2 TDS spectra of tungsten with (a) C^+- 2 keV D_2^+simultaneous and (b) C^+- 2 keV D_2^+ sequential implantation with various C^+ incident energies

were observed in that for C^+- D_2^+ sequentially implanted tungsten. Fig. 6 summarizes the retentions of deuterium retained as Peaks 1, 2 and 3. The deuterium retention as Peak 1 was clearly increased for C^+- D_2^+ simultaneously implanted tungsten. It was found that the no difference of deuterium retention for C^+- D_2^+ sequentially implanted tungsten was observed nonetheless C^+ incident energy was changed from 5 to 10 keV. By changing the C^+ incident energies from 5 to 10 keV C^+, the density of irradiation damages was estimated to be above 10 dpa, indicating that the density of irradiation defects was saturated in all the samples. However, distributions of irradiation defects induced by C^+ implantation were changed with incident energy from SRIM code calculation. With increasing C^+ incident energy, distribution of irradiation damages was expanded toward the depth. The irradiation damages induced by 10 keV C^+ were extended from surface to 30 nm of depth although those by 5 keV C^+ were limited with 20 nm from the surface, indicating that the increase of deuterium retention with increasing C^+ incident energy observed for the simultaneously implanted tungsten was resulted from distribution of irradiation damages. Deuterium trappings by irradiation defects in deeper region (20 - 30 nm beneath surface) would be contribution to these increases of deuterium retention as Peaks 1 and 2. However in the case of C^+ - D_2^+ sequential implantation, deuterium retention was not increased with increasing C^+ incident energy, considering that retained carbon would prevent deuterium penetration into bulk region. In C^+ - D_2^+ sequential implantation, the 2 keV D_2^+ was implanted into tungsten after C^+ implantation. Therefore, implanted deuterium should be affected by retained carbon in tungsten. On the other hand in C^+- D_2^+ simultaneous implantation, several portion of deuterium was implanted into tungsten before retaining carbon enough to prevent deuterium diffusion into bulk.

In summary, the retention of deuterium trapped by irradiation damages was enhanced by energetic carbon implantation. The deuterium retention by intrinsic cavity in bulk region was also found and was decreased by energetic carbon implantation. Therefore, it was

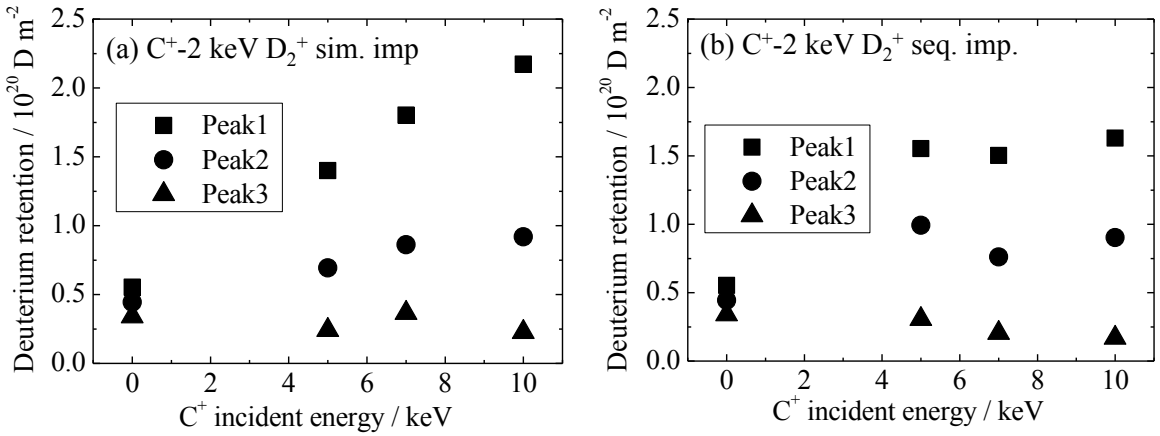

Fig. 6 Deuterium retention for each peak of tungsten with (a) C^+- D_2^+simultaneous and (b) C^+- D_2^+ sequential implantation with various C^+ incident energies.

considered that implanted carbon would play a role as the deuterium diffusion barrier leading the reduction of deuterium penetration toward the bulk. However, several experiments showed deuterium ion-driven permeation was promoted by carbon simultaneously implanted into tungsten. These facts can be explained by the project range of carbon and deuterium ions. In our experiments, the project range of 5 - 10 keV C^+ were almost the same as that of 2 - 3 keV D_2^+. As the project range of carbon reported in ref. [8,9] was shorter than that of deuterium, higher portion of deuterium was implanted deeper region of tungsten than carbon. The implanted deuterium was easily permeated through tungsten because of the decreased diffusivity in the implanted surface by carbon.

4. Conclusions

The effects of energetic carbon implantation on deuterium retention behavior in tungsten were investigated in this study. Dislocation loops and vacancies were formed in tungsten as irradiation defects by energetic carbon implantation. The density of irradiation damage was saturated below about 1 dpa by TEM observations. Deuterium retentions by dislocation loops and vacancies were observed in TDS measurements. Deuterium retentions by irradiation defects were increased by energetic carbon implantation. Deuterium retention by intrinsic cavity in bulk region was also found and was decreased by energetic carbon implantation. It was concluded that retained carbon would play a role as the diffusion barrier of deuterium, preventing deuterium to penetrating into bulk.

Acknowledgement

This study was supported by JSPS Kakenhi No. 22360389, NIFS collaboration program NIFS11KEMF022, University of Toyama collaboration program and the Center for Instrumental Analysis at Shizuoka University.

References

[1] R. P. Doerner et al., J. Nucl. Mater. **363-365**, 32-40 (2007).
[2] S. Pestchanyi et al., Fusion Eng. Des. **66-68,** 271-276 (2003).
[3] I. Bizyukov, *et al*., J. Nucl. Mater., **363-365**, 1184-1189 (2007).
[4] V. Kh. Alimov, Phys. Scr., **T108**, 46-56 (2004).
[5] H.T. Lee, *et al*., J. Nucl. Mater. **390-391,** 971-974 (2009).
[6] M. Kobayashi, et al., Phys. Scr. **T138**, 014050 (2009).
[7] V. Kh. Alimov, *et al*., J. Nucl. Mater., **375,** 192 (2008).
[8] Y. Ueda et al., J. Nucl. Mater., 2012 in press.
[9] H. Y. Peng et al., Phys. Scr. **T145,** 014046 (2011).
[10] J.F. Ziegler, 2006 SRIM code.
[11] M. Poon *et al.,* J. Nucl. Mater., **374**, 390 (2008)
[12] J. Roth and K. Schmid Phys. Scr. **T145,** 014031 (2011).
[13] V.Kh. Alimov *et al.,* J. Nucl. Mater. **337–339,** 619–623 (2005).
[14] T. Ahlgren et al., J. Nucl. Mater. In press.

Tritium distribution on the tungsten surface exposed to deuterium plasma and then to tritium gas

Kanetsugu ISOBE[1)*], Vladimir Kh. ALIMOV[1.2)], Akira TAGUCHI[2)], Makiko SAITO[1,3)], Yuji TORIKAI[2)], Yuji HATANO[2)], Toshihiko YAMANISHI[1)]

1) Tritium technology group, Japan Atomic Energy Agency, shirakatashirane 2-4, Tokai-mura, Ibaraki 319-1195, Japan.

2) Hydrogen Isotope Research Center, University of Toyama, Gofuku 3190, Toyama-shi, Toyama 930-8555, Japan.

3)ITER project Management group, Japan Atomic Energy Agency, mukooyama801-1, Naka-shi, Ibaraki 319-0193, Japan.

(Received: 12 May 2012 / Accepted: 5 October 2012)

Tungsten (W) samples were exposed to Low-energy (38 eV/D), high flux (10^{22} $D^+/m^2/s$) deuterium (D) plasma at 495, 545 and 550 K to a fluence of 10^{26} D/m^2. After the plasma exposure, tritium was introduced into the samples by exposure to deuterium-tritium gas mixture at 473K. Tritium distribution on the W surface was examined by the techniques of imaging plate and autoradiography. The results of the imaging plate revealed that tritium was concentrated mainly within the area exposed to the D plasma, and the concentration of tritium is slightly varied within the area. Autoradiography of the W surface showed that tritium was concentrated on the grain boundary and blisters.

Keywords: Tungsten, Plasma-surface interaction, Tritium, Imaging plate, Tritium autoradiography.

1. Introduction

Since tungsten (W) is one of the candidate materials for plasma-facing components of fusion reactor, many investigations relating to the plasma-W interaction have been carried out. From a view point of safety, the tritium inventory in plasma-facing materials is a one of key issues due to limitation of tritium inventory in the vacuum vessel. Most of the results on hydrogen isotope retention and recycling in W materials have been reviewed by Causey and Venhaus [1,2], and Skinner et al [3]. It has been reported that during exposure to D plasmas, blisters with various shapes and sizes depending on the exposure temperature are formed on the W surface [4-14]. Blister formation is accompanied by deformation of the near-surface layers [12, 13], and this deformation is thought to create additional traps for hydrogen isotopes. There is also a possibility that amount of hydrogen isotope which could be solved or trapped in the deformed W near-surface layer increases. In this study, W samples with D-plasma-induced blisters on the surface were exposed to D_2-T_2 gas mixture, and the distribution of tritium on the W surface was examined by the techniques of imaging plate and autoradiography.

2. Experimental

The W specimens exposed to D plasma were prepared from polycrystalline tungsten (A.L.M.T. Corp., Japan) with a purity of 99.99 wt%. The samples were fully recrystallized at 2070 K for 1 hour after cutting into $10 \times 10 \times 2$ mm^3 and polishing. The grain size was 20-200 μm.

The linear plasma generator used for delivering a plasma beam is described elsewhere [4]. A plasma beam highly enriched with a species of D_2^+ to over 80% was obtained. The bias voltage of -80 V was applied to the W sample resulting in a incident of 38 eV/D, taking into account the plasma potential of about -4 V measured by a Langmuir probe. The incident deuterium ion flux was fixed at 10^{22} $D^+/m^2/s$, and the samples were exposed to ion fluence of 10^{26} D/m^2. The sample was passively heated by the plasma itself and exposure temperature was set by the thermal contact between the sample and the cooled holder. D plasma exposure to recrystallized W was carried out at around 495, 545 and 550K. At the fluence of 10^{26} D/m^2, the deuterium inventory of tungsten exposed at temperature over the range of 500 - 550 K become higher than that at other temperature range [15]. The surface area of the W samples exposed to the plasma was 9 mm in diameter. For a comparison, as-received recrystallized W sample was also used for tritium loading. Note that the as-received sample was not exposed to the D plasma.

4 months after the D plasma exposure, the samples were loaded with tritium from gaseous phase. Fig. 1 shows a schematic view of a tritium exposure apparatus. The tritium exposure apparatus consisted of a vacuum pumping system, a quartz tube for gas exposure equipped with an external heater, quadrupole mass spectrometer

author's e-mail: isobe.kanetsugu@jaea.go.jp

(QMS), and a tritium source. The W samples were placed in the quartz tube, in doing so pieces of glass wool were inserted between samples to avoid a contact between them. The quartz tube with samples was heated in vacuum at 473K for degassing until termination of gas release that was controlled by QMS. At this temperature, we have already confirmed that deuterium in tungsten is not released to the vacuum by thermal desorption spectroscopy [15]. When high vacuum was obtained, tritium diluted with deuterium was introduced into the quartz tube from the tritium source. W samples were exposed at 473 K to D (92.2%)-T (7.8%) gas mixture at a total gas pressure of 1 kPa for 5 hours.

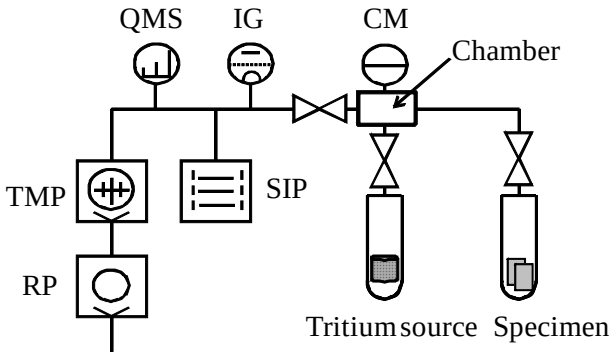

Fig. 1 Schematic view of tritium exposure apparatus.
QMS:Quadropole mass spectrometer,
IG:Ionization gauge, CM:Capacitance manometer
SIP:Suptter ion pump, RP:Rotary pump
TMP:Turbo molecular pump

The amount of tritium retained in the W near-surface layers was evaluated by the imaging plate technique. Imaging plate (IP) is a 2-dimensional radiation detector with high sensitivity. IP used in our experiments was BAS-TR2025 (Fuji Photo Film Co. Ltd.) which consists of 50 μm thickness photostimulable phosphor mounted on a plastic support. The IP surface was contacted to the W surface and exposed to tritium beta electrons in 1 week. After the exposure to tritium beta electrons, the IP was processed by an IP reader FUJIFILM BAS2500 (Fuji Photo Film Co. Ltd.) in order to obtain the digital image. Tritium activity is expressed as the photo-stimulate luminescence (PSL) intensity, which is proportional to the absorbed radiation energy.

Tritium autoradiography technique was applied to two specimens; recrystallized W exposed to the D plasma at 495K and as-received, non-exposed recrystallized W. At first, to avoid direct contact of the W samples with AgBr grains in radiographic emulsion, thin collodion film was deposited on the W surface by dipping the samples in collodion diluted by ethanol. The monolayer of the radiographic emulsion (ILFORD L4) was placed onto the collodion film by a wire-loop method. The specimens were kept in a light-tight box at around 273 K for 12 days to expose the emulsion to the tritium beta electrons. Then, specimens were dipped in a developer solution and then in a fixer solution. Under exposure to beta electrons, the AgBr grains were transformed into Ag grains. The distribution of Ag grains was observed by the scanning electron microscope (SEM).

3. Results and Discussion

Surface morphology of the recrystallized W after D plasma exposure at 495K is shown in Fig. 2. Grain boundary could be clearly observed in Fig. 2. Large blisters with sizes of a few tens of microns and small blisters with size of less than a few microns are observed. The large blisters demonstrate a multi-layered structure like steps. The small blisters are formed on the flat surface of crystal grains.

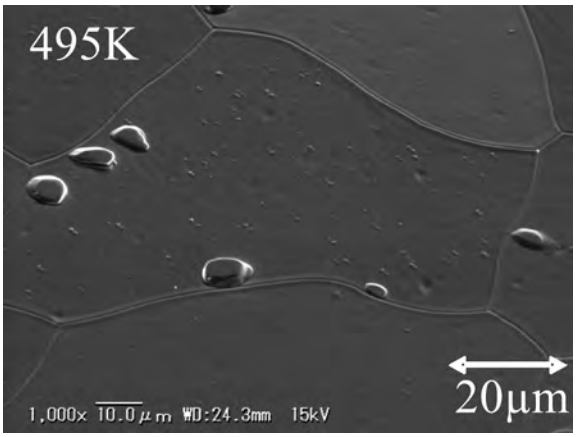

Fig. 2. SEM image of recrystallized W exposed at 495 K to low-energy high flux D plasma with fluence of 10^{26} D/m^2. The surface was tilted at an angle of 45ºto the electron beam.

Fig. 3 shows the results of IP measurements. IP measurement can easily observe tritium distribution of the whole of specimen as shown in Fig. 3. A level of darkness corresponds to a concentration of tritium in near-surface layer. As seen Fig. 3 (a, b, c), tritium is concentrated on the surface area exposed to the D plasma. It is known that under exposure to high flux D plasmas, vacancy-type defects, voids and cracks are generates in W, and these defects are responsible for accumulation deuterium [11-14, 16]. Obviously, subsequent exposure to tritium leads to isotope exchange in the near-surface layer [17] and accumulation of tritium at the defects created under previous D plasma exposure.

The average tritium concentration of the W surface exposed at 550 K is significantly higher than that for the W surface exposed at 545 K, although the difference in the exposure temperature is only 5 K. Obviously, a small variation in the exposure temperature within this temperature range has a significant influence on a

concentration of the D-plasma-induced traps generated in near-surface layer. This suggestion is supported by sharp temperature dependence of the D retention in the recrystallized W exposed to low-energy, high-flux D plasma [16].

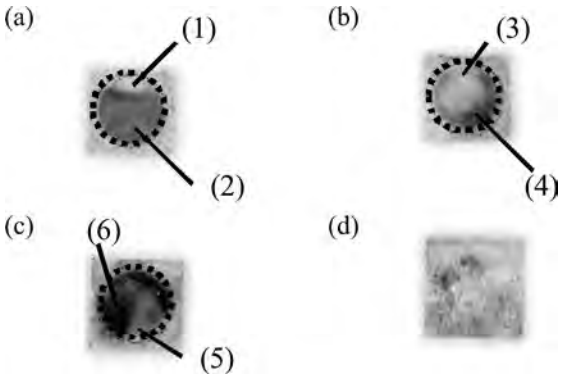

Fig. 3. IP images for recrystallized W exposed to low-energy, high flux D plasma at 495 K (a), 545 K (b), 550 K (c), and for as-received recrystallized W (d). Dashed circles (a-c) indicate the surface areas exposed to D plasma. Tritium was loaded into all samples at 473 K, 1 kPa D-T gas mixture for 5 hours.

However, within the exposed surface area the tritium distribution is not uniform. Intensities of PSL at points ((1)-(6)) in Fig. 3 are shown in Table I. The ratio between the maximum and minimum PSL intensities on the same exposed sample surface ((2)/(1), (4)/(3), (6)/(5)) varied from 4:1 to 6:1. It was reported recently that hydrogen isotopes can be retained by tungsten oxide layers [18]. Probably, the surfaces of the W samples were nonuniformly oxidized before tritium gas exposure.

Table I Intensity of photo-stimulate luminescence at some points on the plasma-exposed W surface

Point	(1)	(2)	(3)	(4)	(5)	(6)
PSL/mm^2	320	1800	500	2100	560	3200

Figure 4 demonstrates autoradiographic patterns, in which white spots correspond to Ag grains tracing the tritium beta electrons. The Ag grains, as white lines, were observed along grain boundary (Fig. 4 (a)). The Ag grains decorate also blisters and are distributed uniformly on the grain surface (Fig. 4 (b, c)). However, the Ag grains are not observed on the surface of as-received recrystallized W (Fig. 4 (d)). As was mentioned above, various types of trapping sites for hydrogen isotopes are generated in W under exposure to high-flux D plasma. Under subsequent exposure to tritium gas at elevated temperature, tritium is thought to be occupied these trapping sites. It should be noted that techniques of imaging plate and autoradiography allow detecting tritium retention in a shallow, near-surface layer because the escape depth of tritium beta electrons in

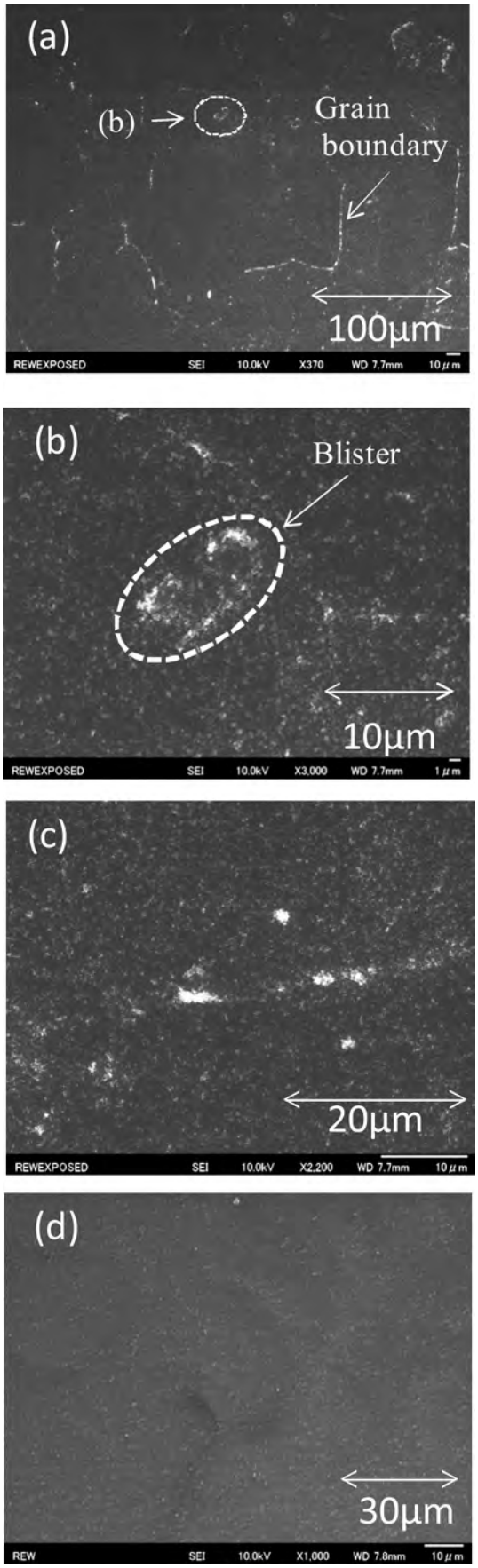

Fig. 4. Autoradiographic patterns of recrystallized W exposed with D plasma at 495K (a, b, c) and as-received recrystallized W (d). Tritium was loaded into these samples at 473 K, 1 kPa D-T gas mixture for 5 hours.

W does not exceed one micrometer [19, 20]. Thus, results of this study shows that under exposure to the D plasma at elevated temperatures, traps in the near-surface layer are generated mainly along grain boundaries and in layers subjected to tensile stress due to material migration above the surface during formation of blisters [12].

4. Conclusion

Techniques of imaging plate (IP) and autoradiography were applied to observe a distribution of tritium on the W surface preliminary exposed to low-energy, high-flux D plasma at elevated temperatures (495-550 K) and then to tritium gas at 473 K. According to IP images, tritium was highly concentrated within D-plasma-exposed surface area; however, the tritium concentration was varied within this area. With the use of autoradiography, it was found that tritium was concentrated on the grain boundary and along/on blisters formed under D plasma exposure. These results suggest that D plasma exposure generates traps for hydrogen isotopes in the W near-surface layer.

Acknowledgements

A part of this work is performed with the support and under the auspices of NIFS (NIFS11KUHR012) and a KAKENHI Grant-in-Aid for Scientific Research (B) (Project No. 21360458, No. 24360380). Authors really wish to acknowledge for these supports.

5. References

[1] R. A. Causey and T. J. Venhaus, Phys. Scripta T94 (2001) 9.
[2] R. A. Causey, J. Nucl. Mater. 300 (2002) 91.
[3] C. H. Skinner, A. A. Haasz, V. Kh. Alimov, *et al*., Fusion Sci. Technol. 54 (2008) 891.
[4] G.-N. Luo, W.M. Shu, H. Nakamura *et al*., Rev. Sci. Instrum. 75 (2004)4374.
[5] G. -N. Luo, W. M. Shu, M. Nishi, J. Nucl. Mater. 347 (2005) 111.
[6] G. -N. Luo, W. M. Shu, M. Nishi, Fusion Eng. Design 81 (2006) 957.
[7] W. M. Shu, A. Kawasuso, Y. Miwa et al., , Physica Scripta T128 (2007) 96.
[8] V. Kh. Alimov, J. Roth, Physica Scripta T128 (2007) 6.
[9] W. M. Shu, G. -N. Luo, T. Yamanishi, J. Nucl. Mater. 367-370 (2007) 1463.
[10] W. M. Shu, E. Wakai, T. Yamanishi, Nucl. Fusion 47 (2007) 201.
[11] V. Kh. Alimov, W. M. Shu, J. Roth and et al., Physica Scripta T138 (2009)014048.
[12] S. Lindig, M. Balden, V.Kh. Alimov et al., Phys. Scripta T138(2009)014040.
[13] S. Lindig, M. Balden, V.Kh. Alimov et al., Phys. Scripta T145(2011)014039.
[14] V. Kh. Alimov, B. Tyburska-Püschel, S. Lindig and et al., J. Nucl. Mater., 420(2012)519
[15] V.Kh. Alimov, S. Lindig, M. Balden and et al., Annual report of Hydrogen Isotope Research Center, Toyama University, 29-30(2010)71V.
[16] V.Kh. Alimov, W.M. Shu, J. Roth et al., J. Nucl. Mater., 417(2011)572.
[17] Y. Hatano, M. Shimada, V.Kh. Alimov et al., Proc. 20th Intern. Conf. on Plasma Surface Interactions, May 2012, Achen(submitted to J. Nucl. Mater.)
[18] V.Kh. Alimov, B. Tyburska, M. Balden et al., J. Nucl. Mater., 409(2011)27.K. Miyasaka, T. Tanabe, G. Mank and et al., J. Nucl. Mater., 290-293(2011)448
[19] T. Hoshihira, T. Otsuka and T. Tanabe, J. Nucl. Mater., 386-388(2009)776
[20] T. Hoshihira, T. Otsuka and T. Tanabe, J. Nucl. Mater., 390-391(2009)1029

Study on plasma – tungsten surface interactions using the new experimental device EXPRESS

Ryo Miura[1)*], Tetsuo Fujishima[1)], Yuto Miyahara[1)], Tomohisa Taguchi[1)], Masahiro Tanaka[2)], Akio Sagara[2)], Yasuhisa Oya [1)], and Kenji Okuno[1)]

1) Radioscience Research Laboratory, Faculty of Science, Shizuoka University

2) National Institute for Fusion Science

(Received: 25 May 2012 / Accepted: 5 December 2012)

An experimental apparatus named as EXPRESS (Effluence and Exchange Probe for Recycling Estimation at NIFS and Shizuoka University) has been designed and established in Shizuoka University to acquire laboratory data (well-conditioned data) needed for the design of an actual reactor. The behaviors of deuterium retention and the surface chemical state after EXPRESS plasma operation were evaluated and compared with that for LHD (Large Helical Device, NIFS) hydrogen plasma exposed sample. It was found that a thin impurity deposition layer with the thickness less than 0.3 nm was formed on the surface, which was one thirteenth thinner than that on LHD plasma exposed tungsten. The TDS experiment showed that major deuterium desorption stage for EXPRESS plasma exposed tungsten was located at the lower temperature less than 550 K, although that for LHD plasma exposed one was found at the temperature between 550 K – 1000 K. These facts suggest that the impurity concentration in the deposition layers have a large influence on the deuterium retention behavior in tungsten.

Keywords: deuterium plasma exposure, TDS, XPS, impurity deposition layer, tungsten

1. Introduction

Tungsten will be used as a plasma facing material in future fusion devices. Many studies have been devoted to elucidate fundamental tritium retention and transport behaviors in tungsten under well-controlled condition [1-3]. However, it is quite difficult to apply these data obtained under well-controlled condition to actual and larger-scale plasma devices or fusion devices where conditions are much more complex. For example, a wall temperature gradient will arise when the plasma is controlled. Therefore, the key parameters should be acquired to complete laboratory data (well-controlled condition data) needed for the design of an actual reactor design. The design of a new plasma experimental device, namely EXPRESS (Effluence and Exchange Probe for Recycling Estimation at NIFS and Shizuoka University) was designed to clarify the hydrogen isotope recycling dynamics. This devise has these following features: i) many samples can be placed on the sample stage for plasma exposure and the sample temperature gradient can be controlled, and ii) 1 GBq / day of tritium can be handled.

As a preliminary experiment, the deuterium plasma exposure to pure tungsten was performed in this study to characterize and evaluate the behaviors of the deuterium retention and the surface chemical state after EXPRESS plasma operation at R.T. These experimental results obtained at EXPRESS were compared with those in LHD (Large Helical Device, NIFS) plasma exposed tungsten and only D_2^+ implanted tungsten for the evaluation of fuel recycling during plasma-surface interactions in EXPRESS.

e-mail: r0232027@ipc.shizuoka.ac.jp

2. EXPRESS Apparatus

The recently designed plasma experimental device to investigate hydrogen isotope recycling behavior and plasma surface interaction, EXPRESS consists of three parts: i) a plasma generator and plasma exposure system, ii) a fuel storage and purification system, and iii) a fuel recovery-supply systems. Figure 1 shows the schematic view and picture of the plasma generator and plasma exposure system. The plasma generator and plasma

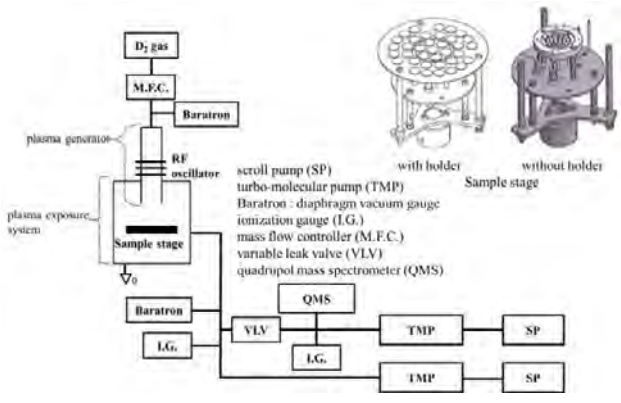

Fig. 1 Schematic view and picture of the plasma generator and plasma exposure system in EXPRESS.

exposure system can be evacuated to 1×10^{-5} Pa by a scroll pump (SP) and a turbo-molecular pump (TMP) combination. The pressure in the system is measured by Baratron and ionization gauge (I.G.). The source gas is supplied through a mass flow controller (M.F.C.) at a flow rate of 0.1-5.0 sccm into the plasma generation tube made by quartz with a size of 150 mm in length and 42 mm in diameter. The excitation frequency is fixed at 13.56 MHz by a RF matching box. The bias voltage can be changed from 0- 200 V between the chamber wall and the sample stage to control implantation energy similarly larger-scale plasma devices. The size of sample stage is 100 mm in diameter, which is made of tungsten. A heating unit is installed beneath the center of sample stage to generate a temperature gradient up to 200 K between the center and the edge of the sample stage as shown in Fig. 2. This apparatus is used to investigate the study of plasma-surface interactions on the first wall of actual reactor. The heating unit can heat up to 873 K at the center of stage. The ion flux can be measured by a faraday cup installed in the plasma exposure system.

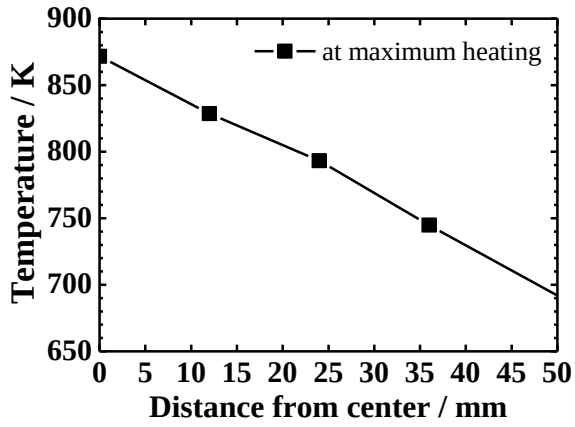

Fig. 2 The maximum temperature profile on the sample stage in EXPRESS.

3. Experimental

A disk-type polycrystalline tungsten with stress-relieved conditions (heated at 1173 K for 1 hour), which was purchased by Allied Material Co. Ltd, was used for all experiments. The sample size was 10 mm diameter and 0.5 mm thickness. The samples were polished mechanically to the roughness of less than 1 μm by SiC abrasive papers and 1-3 μm diamond suspensions, and preheated at 1173 K for 30 minutes under ultrahigh vacuum (< 10^{-6} Pa) to remove the impurities and damages introduced during the polishing processes.

After preheating, the sample was introduced into the plasma exposure system of EXPRESS. The deuterium gas was supplied at a flow rate of 3.0 sccm and the pressure of 3.5 Pa. The D plasma was exposed to the samples with the D_2^+ energy of 63 eV to implant at the lowest possible energy for the stable plasma operation. The ion flux was 3.4×10^{19} D^+ m^{-2} $s^{-1}$and the fluence was 1.0×10^{24} D^+ m^{-2} at R.T. This sample was named as EXPRESS sample.

After plasma exposure, TDS (Thermal Desorption Spectroscopy) were performed from R.T. to 1173 K with a heating rate of 0.5 K s^{-1} to investigate the deuterium desorption and retention behaviors. The chemical states and the thickness of the impurity layer on tungsten were evaluated by XPS (X-ray Photoelectron Spectroscopy) (ESCA1600 system, ULVAC-PHI Inc.) using a Mg - Kα X-ray source (1253.6 eV) and 1 keV Ar^+ sputtering technique [4]. The thickness of impurity deposition layer was defined as the depth where impurity concentration was reached to be half compared to that on the surface. The sputtering rate by Ar^+ implantation was estimated by AFM (Atomic force microscope).

Two types of tungsten samples, namely D_2^+ imp. sample and LHD sample, were prepared to compare the deuterium retention behavior. In the D_2^+ imp. sample, 3.0 keV D_2^+ implantation was performed for tungsten with flux of 1.0×10^{18} D^+ m^{-2} s^{-1} and fluence of 1.0×10^{22} D^+ m^{-2} at R.T. In the case of LHD sample, the sample was exposed to 134 shots (exposure time 271 seconds) of hydrogen plasma in LHD, with the ion energy of about 10-100 eV and the temperature of less than 373 K, at a first wall position in the plasma operation campaign of 2011.

4. Results and discussion

Figure 3 shows the TDS spectra for EXPRESS and LHD and D_2^+ imp. samples. The TDS spectrum for the D_2^+ imp. sample consists of two desorption stages at 400 K and 550 K, attributing to the desorption stages of deuterium adsorbed on the surface and/or trapped by dislocation loops (Peak 1), [5,6] and deuterium trapped by vacancies (Peak 2) [7] respectively. In the D_2 desorption stages for the EXPRESS sample, Peak 1 was the dominant stage which is similar for the D_2^+ imp. sample, but the ratio of Peak 1 to

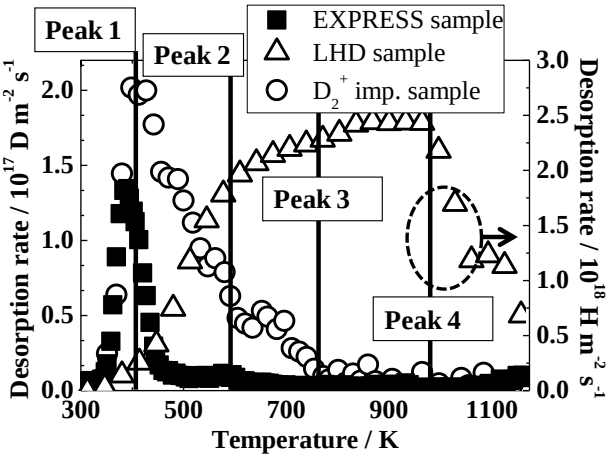

Fig. 3 TDS spectra for the EXPRESS, LHD and D_2^+ imp. samples

Peak 2 was quite different among these samples, It can be said that the plasma exposure hardly produces the irradiation defects in tungsten due to lower D^+ implantation energy according to SRIM code calculation [8], indicating that the formation of irradiation defects was limited for EXPRESS sample, and most of deuterium would be accumulated on the sample surface. In the LHD sample, additional desorption stages were observed at around 750 K (Peak 3) and 900 K (Peak 4). It was reported that the W-O bond in WO_3 was one of the stable deuterium trapping sites with a desorption temperature of around 750 K [9]. In our previous study, the deuterium implanted into HOPG was trapped as C-D bond after dissociation of C-C bond, which was desorbed at 900 K [10]. Therefore, the desorption stages of deuterium at these higher temperatures in the LHD sample may be assigned to that bound to oxygen as O-H (Peak 3) and carbon as C-H bonds (Peak 4), respectively.

Figure 4 shows W-4f XPS spectra for the top surfaces of the EXPRESS, LHD and D_2^+ imp. samples. The W- $4f_{7/2}$ XPS spectra consisted of two chemical states located at 30.8 eV for metallic W and 35.8 eV for WO_3. [11,12]. The abundance of WO_3 for total W-4f XPS peak area was 23% for the EXPRESS sample, and 63% for the LHD sample as shown in Table 1. In the EXPRESS sample, the major chemical state of tungsten was the metallic state which was different from the LHD sample, indicating that most of deuterium for the EXPRESS sample would be interacted with metallic W rather than WO_3. Figure 5 shows the depth profiles of W, WC, WO_3 and C for the EXPRESS sample. The impurities were accumulated within the depth of ~ 0.3 nm for the EXPRESS sample. Table 2 summarizes atomic concentrations on the top surface and thickness of impurity deposition layers on the EXPRESS and LHD samples. Large amount of oxygen and carbon were accumulated on the surface for both samples and its impurity concentrations were almost the same. However, the thickness of the impurity deposition layer for the EXPRESS sample was about one thirteenth thinner than that for the LHD sample. It can be said that the thin impurity deposition layer was achieved by EXPRESS device and the formation of impurity deposition layer hardly affected on deuterium retention as O-D bonds for the EXPRESS sample, resulting in decrease of Peak 3 in the TDS spectrum of the EXPRESS sample compared to the LHD sample.

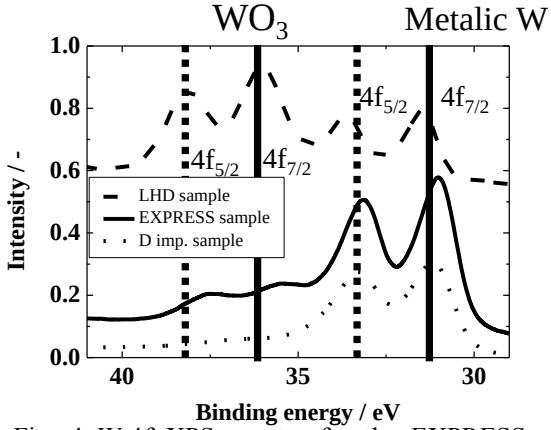

Fig. 4 W-4f XPS spectra for the EXPRESS, LHD and D_2^+ imp. samples

Table 1 Ratios of W and WO_3 on the top surface of W

	W	WO_3
EXPRESS	77%	23%
LHD	37%	63%
D imp.	86%	14%

Figure 6 shows C-1s XPS spectra of EXPRESS, LHD and D_2^+ imp. samples. Three chemical states were found at the binding energies of 286.1 eV, 284.8 eV and 283.3 eV, attributing to C-O, C-C and C-W bonds, respectively [13-15]. C-O and C-C bonds were major chemical states in the LHD sample, although C-C bond was formed by plasma exposure for the EXPRESS sample. However, implantation depth of carbon was limited within the surface region and the total amount of carbon for the EXPRESS sample was quite small compared to that for the LHD sample indicating that carbon would hardly affect the behavior of hydrogen isotope retention in the EXPRESS sample.

It was concluded that the EXPRESS sample had the thinner impurity deposition layer compared with LHD sample and hydrogen isotope retention is affected by carbon and oxygen chemical states and the amounts of impurity in deposition layer. In the EXPRESS sample, most of the impurities were adsorbed on the top surface

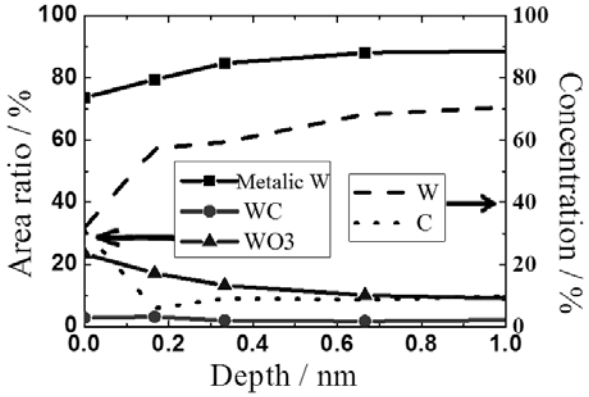

Fig. 5 Depth profiles of W and C for the EXPRESS sample

Table 2 Atomic concentrations for the surface of the EXPRESS and LHD samples and the thickness of the impurity deposition layers.

	W	C	O	Thickness
EXPRESS	34%	30%	36%	0.3 nm
LHD	18%	34%	48%	4 nm

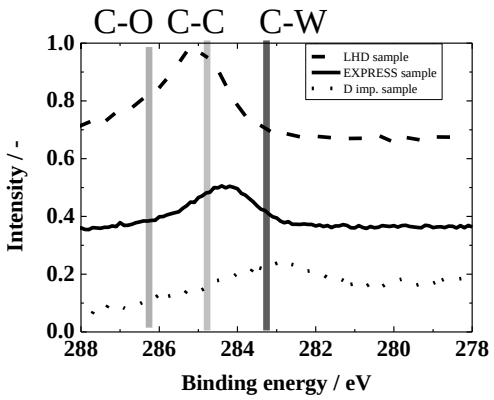

Fig. 6 C-1s XPS spectra for the EXPRESS, LHD and D_2^+ imp. samples.

after deuterium plasma exposure. However, the amounts of impurities beneath the surface were too small to affect the deuterium retention behavior. In addition, the deuterium was hardly trapped by irradiation defects because the formation of defects was limited due to low energy ion irradiation. Therefore, the deuterium was only retained by surface adsorption during deuterium plasma exposure in EXPRESS.

In further experiments, longer time (higher fluence) plasma exposure and oxygen and carbon contaminated plasma exposure will be needed to make impurity deposition layers that have a variety of thickness and chemical state in order to clarify the influence of impurity deposition layer on deuterium retention behavior.

5. Conclusions

A new equipment to acquire laboratory data (well-conditioned data) needed for the design of an actual reactor named EXPRESS has been designed and is establishing. The deuterium plasma exposure was performed to characterize and evaluate the behaviors of deuterium retention and surface chemical states after the EXPRESS plasma operation. The deuterium retention behaviors for tungsten after EXPRESS plasma exposure was studied and these results were compared to those for the LHD and D_2^+ imp. samples. It was found that most of deuterium was desorbed at the lower temperature less than 550 K for the EXPRESS sample, which was almost the same with the D_2^+ imp. sample. However, the TDS spectrum for the LHD sample was quite different from that for the EXPRESS and D_2^+ imp. samples, which would be caused by the formation of thick impurity deposition layer on the surface for the LHD sample. These facts indicate that the amounts of impurity in the deposition layer could affect on the deuterium retention behavior in tungsten used in actual plasma devices and fusion reactors.

Acknowledgement

This study was supported by NIFS collaboration program, NIFS11KOBA025 and the Center for Instrumental Analysis at Shizuoka University.

References

[1] P.S. Krstic et al,. Nucl. Inst. and Meth. B **267**,704(2009).
[2] K. Ohya et al., Fusion Eng. Des.**85**,1167(2010).
[3] Y. Oya et al,, J. Nucl. Mater. **390**, 622 (2009).
[4] K. Okuno et al.,Fusion Eng. Des. **85**, 2328(2010).
[5] H. Eleveld et al., J. Nucl. Mater, **191** 433(1992).
[6] H. Iwakiri et al., J. Nucl Mater., **307 ,**135(2002).
[7] M. Poon et al., J. Nucl. Mater., **374**, 390(2008).
[8] Ziegler J F 2006 SRIM code.
[9] N. Matsunami et al., J. Nucl. Mater. **390** , 693(2009)
[10] T. Suda et al., Fusion Eng. Des. **82** , 1762(2007)
[11] B.F. Dzhurinskii et al., Russian J. Inorganic Chem., **20**, 2307(1975).
[12] D.R. Chopra et al.,J. Vac. Sci. Technol. B, **10**, 1218(1992).
[13] B. Rousseau et al .,J. Phys. Chem., **53**, 419(1992).
[14] A. Fahlman et al.,J. Phys. Chem. Solids, **30**, 1835(1969).
[15] CH. Cardinaud et al., Applied Surface Science, **68**, 595(1993).

Hydrogen incorporation into tungsten deposits growing under hydrogen and argon mixed plasma

Kazunari KATAYAMA, Yasuhito OHNISHI, Satoshi FUKADA and Masabumi NISHIKAWA

Interdisciplinary Graduate School of Engineering Sciences, Kyushu University,
6-10-1, Hakozaki, Higashi-ku, Fukuoka, 812-8581, Japan

(Received: 10 May 2012 / Accepted: 9 October 2012)

Tungsten deposits were produced by exposing a tungsten tube to hydrogen and argon mixed plasma in different deposition conditions. The erosion rate of the tungsten tube decreased with increasing hydrogen concentration in the working gas. This indicates that the erosion was mainly caused by argon ion incident. In order to release hydrogen incorporated into the tungsten deposit, the tungsten deposit has to be heated up to 600 ^{o}C. While the tungsten deposition rate was promoted by the increase of negative target bias supplied to the tungsten tube, the influence of the target bias on hydrogen retention in the tungsten deposit was different in the deposition condition. However, it was found that hydrogen retention increases with the ratio of the energetic hydrogen flux reflected on the tungsten tube to the tungsten deposition flux. The flux ratio of hydrogen to tungsten toward the growing surface of the tungsten deposit is an important parameter to evaluate the amount of hydrogen incorporated into tungsten deposits growing under the plasma containing hydrogen ions.

Keywords: tungsten, deposition, hydrogen retention, sputtering

1. Introduction

It is important to understand the accumulation phenomena of hydrogen isotopes in a plasma confinement vessel of a fusion reactor from viewpoints of tritium economy and safety. Plasma-facing wall is eroded by energetic particle incident and sputtered atoms would form deposition layers. It has been known that carbon deposition layer can contain a large amount of hydrogen isotopes. Tungsten is a candidate material for plasma-facing wall because of low solubility and low sputtering yield for hydrogen isotopes. In a long time operation of a fusion reactor, a certain amount of tungsten deposits would be formed in the plasma confinement vessel. Erosion and deposition will be promoted if a noble gas such as argon is introduced around plasma-facing wall for a reduction of heat load. It has been reported by the present authors that a large amount of hydrogen isotopes are incorporated into tungsten deposition layer formed by hydrogen isotope plasma sputtering [1,2]. The empirical equation has been proposed from a systematic study of the influence of the deposition conditions on the deuterium retention by using magnetron sputtering and linear plasma devices [3]. The influence of oxygen on hydrogen isotope retention in tungsten deposition layers has been investigated [4,5]. Nevertheless, experimental data for hydrogen isotope retention in tungsten deposits are still insufficient. In this study, the influence of the deposition condition on hydrogen incorporation in tungsten deposits growing under hydrogen and argon mixed plasma was investigated.

author's e-mail: kadzu@nucl.kyushu-u.ac.jp

2. Experimental

A schematic diagram of the experimental apparatus is shown in Fig.1. A cylindrical quartz tube, 13 mm in outer diameter, 10 mm in inner diameter and 400 mm in length, which has a horizontal branch tubule, 6 mm in outer diameter, 4 mm in inner diameter and 30 mm in length, was used as a plasma sputtering chamber. A tungsten tube, 1.4 mm in outer diameter, 0.2 mm in thickness and 99.95% in purity (Nilaco Co.), was inserted to the branch tubule as a sputtering target. A copper tube, 3 mm in outer diameter, was rolled on the outer surface of the quartz tube in the upstream side as an inductive coil. The distance from the edge of the coil to the tungsten tube was set to be 35 mm. In order to collect a part of sputtered tungsten, a quartz substrate, 10 × 5 mm^2 in size and 1 mm in thickness, was placed beneath the tungsten tube. The detail of the sputtering-deposition region is illustrated in Fig.2. The distance from the center of the quartz tube to the surface of the substrate was 3.3 mm. The angle θ is about 113^{o} which is 31 % of the all circumferences. The length of the quartz substrate is 5 mm which is 50 % of the tungsten tube length in the longitudinal direction. Therefore the plasma-facing area of the quartz substrate views approximately 16 % of the plasma-facing area of the tungsten tube. The mixture gas of hydrogen and argon was introduced via a mass flow controller (SEC-E40, HORIBA

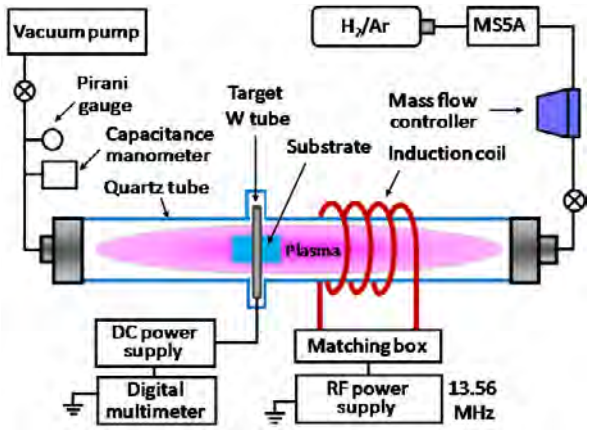

Fig.1 The schematic diagram of the experimental apparatus.

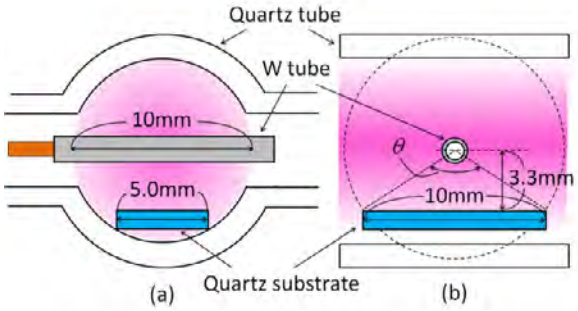

Fig.2 The illustration of the sputtering-deposition region. (a) : a view from the gas flow direction. (b) : a view from the cross-section direction of the W tube.

Ltd.) calibrated with pure hydrogen gas. Hydrogen concentrations in the mixture gas used in this study were 2, 20, 50 and 80 %. A packed bed of adsorbent, MS5A was installed between the gas cylinder and the mass flow controller to exclude a small amount of impurity water vapor in the gas cylinder. Plasma was inductively generated inside of the quartz tube by supplying the RF power of 40 W or 100 W with 13.56 MHz (NR05N-06, NRF Co.) to the copper coil via matching box (NM05AL-05, NRF Co.). In order to promote erosion of the tungsten tube, a negative bias of 200 V or 300V was supplied in the tungsten tube by a DC power supply (PWR400H, KIKUSUI Co.). The target current was measured by a digital multi-meter (PC520M, SANWA Inc.). Evacuation of the quartz tube was performed by a rotary pump (GLD-201B, ULVAC Inc.). The working gas pressure during sputtering-deposition process was monitored by a Pirani gauge (GP-1G, sencer:WPB-10-034, ULVAC Inc.). After the process, the absolute pressure was measured by a capacitance manometer (Baratron 626B, MKS Ltd.) in same deposition condition. The true flow rate of the mixture gas was obtained from the absolute pressure in the quartz tube and the exhaust velocity by the rotary pump. The temperature in the vicinity of the quartz substrate during sputtering-deposition process was measured by a thermocouple fixed on the outer surface of the quartz tube. In order to confirm the temperature inside the quartz tube, a thermocouple was inserted from the downstream side of the quartz tube to the position of the substrate. Both temperatures were almost same. The deposition conditions were summarized in Table 1. In cases that temperature is just 100 ^{o}C, the temperature was controlled by a ribbon heater. The sputtering-deposition region was wrapped by the ribbon heater except in Ex.1 and Ex.2. The temperatures in Ex.1 and Ex.2 are lower than that in the others because there is no effect of heat retention by the ribbon heater.

The amount of deposited tungsten was obtained from the weight change of the substrate before and after sputtering-deposition process. The weight change was measured by an electric balance with sensitivity of 0.01 mg (CP225D, Sartorius Inc.), whereas the original weight of the substrate was about 100 mg. The cross section observation of the tungsten deposit was performed by the scanning electron microscopy (SEM:SU8000, HITACHI Co.). The weight percent of oxygen in the tungsten deposit was analyzed by energy dispersive X-ray equipment (EDX:Genesis2000, EDAX Inc.). SEM and EDX used in this study were installed at the Center of Advanced

Table 1 The summary of deposition conditions.

	H_2 [%]	Flow rate [sccm]	Pressure [Pa]	RF power [W]	Target bias [-V]	Flux to target [ions/m^2/s]	Temperature [^{o}C]	Deposition period [h]
Ex.1	2	3.8	7.6	40	200	1.30×10^{20}	58	20
Ex.2	2	3.8	7.6	40	300	1.53×10^{20}	58	17
Ex.3	20	6.7	7.1	100	200	1.31×10^{20}	104	20
Ex.4	20	6.7	7.1	100	300	1.96×10^{20}	94	21
Ex.5	20	3.1	4.6	100	300	1.62×10^{20}	100	14
Ex.6	20	6.7	7.1	100	300	2.72×10^{20}	96	36.5
Ex.7	20	3.1	4.6	40	200	1.23×10^{20}	100	24
Ex.8	50	3.8	5.4	100	200	2.61×10^{20}	146	25
Ex.9	50	3.8	5.4	100	300	2.77×10^{20}	106	46
Ex.10	80	2.5	4.2	100	200	3.99×10^{20}	156	30

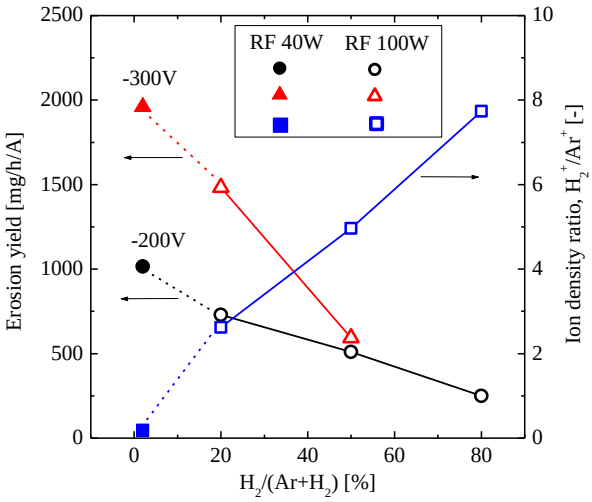

Fig.3 The dependence of hydrogen concentration in the working gas on the erosion yield of the tungsten tube and on the ratio of hydrogen ions to argon ions.

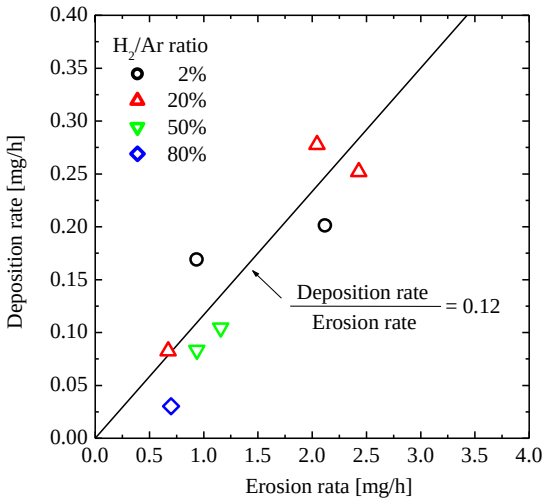

Fig.4 The deposition rate on the substrate with the erosion rate of the tungsten tube.

Instrumental Analysis, Kyushu University.

Ion densities at the vicinity of the substrate under pure hydrogen plasma and pure argon plasma were measured by the double probe method. The probes were inserted from the branch tubule to plasma without the target tube. Additionally, the emission intensities from H_2^+ and Ar^+ in plasma at the vicinity of the substrate were measured for pure hydrogen, pure argon and hydrogen-argon mixed plasma by a plasma process monitor (PlasCalc-2000, Mikropack). Ion densities of hydrogen and argon in the mixed plasma were estimated from the double probe measurement and the emission intensity measurement assuming the emission intensity is proportional to the ion density and H_2^+ is dominant in hydrogen ions.

After sputtering-deposition process, the substrates were placed into a separate quartz tube connected to a gas chromatograph (GC:GC-8A, SHIMAZU Co.). The quartz tube was filled with argon gas and heated from 200 ^oC to 800 ^oC in 200 ^oC step by an electric furnace. Argon gas was introduced into the reaction tube every 20 minutes in order to transport the released hydrogen into GC. Since the amount of hydrogen released at 800 ^oC was comparable to the background level, the hydrogen released by 600 ^oC was regarded as the hydrogen incorporated in the tungsten deposit.

3. Results and discussions

Fig.3 shows the dependence of hydrogen concentration in the working gas on erosion yield of the tungsten tube which was derived from dividing the erosion rate (mg/h) by the target current (A). The right axis indicates the ratio of hydrogen ion density and argon ion density under each deposition condition. The hydrogen ion ratio increased approximately proportionally to hydrogen concentration. It was observed that the erosion yield decreases with increasing hydrogen concentration. Additionally, the weight loss of the tungsten tube was undetectable in several-hour exposure under pure hydrogen plasma. These results indicate that the erosion of tungsten was caused by argon ion incident. Impinging energy of argon ions obtained from negative bias is mitigated by collisions with neutral molecules. Therefore the erosion yield is considered to decrease with decreasing the argon ion density. The erosion yield at a negative bias of 300 V was quite lager than that at a negative bias of 200 V in 2 % and 20 % of hydrogen concentration but these are close in 50 % of hydrogen concentration. This indicates that the negative bias effect on erosion is large when argon ion density is high.

The deposition rate against the erosion rate in each deposition condition is plotted to Fig.4. The ratio of the deposition rate to the erosion rate was 0.12 on the average. This value is smaller than 0.16 which is estimated geometrically. This difference is due to the erosion of the tungsten tube in the branch tubule, the slip of the substrate from the designed position and the scattering of sputtered tungsten atom by collision with neutral molecules.

SEM image of the cross-section of the tungsten deposit formed under hydrogen and argon mixed plasma, 20 % in hydrogen concentration, 7.1 Pa in working gas pressure, 100 W in RF power, 300 V in negative bias, 96 ^oC in temperature and 36.5 h in deposition period (Ex.6) is shown in Fig.5. The quartz substrate was broken in half and the surface was observed. It was found that the tungsten deposit has a columnar structure. The weight percent of oxygen in the tungsten deposit formed under hydrogen and argon mixed plasma, 20 % in hydrogen concentration, 4.8 Pa in working gas pressure, 40 W in RF power, 200 V in negative bias and 100 ^oC in temperature (Ex.7), is 2.0 wt%.

An example of hydrogen release behavior from tungsten

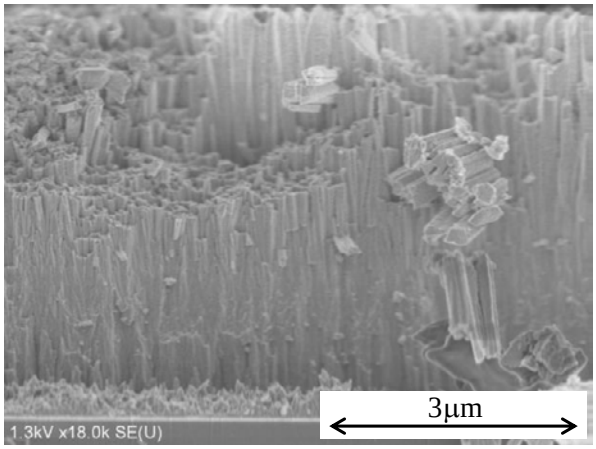

Fig.5 SEM image of the cross-section of the tungsten deposit formed in Ex.6.

deposits is shown in Fig.6. For all samples, the release behavior of hydrogen was similar. The hydrogen release began at 200 °C and continued until 600 °C. The highest release rate was observed at 400 °C. It was found that a high temperature of 600 °C is necessary to remove hydrogen incorporated in the tungsten deposit.

The dependence of negative bias on hydrogen retention (mol-H_2/g) and deposition rate (g/hour) are shown in Fig.7 for three deposition conditions. It was observed that the deposition rate at 300 V is obviously higher than that at 200 V. This means that the impinging energy of ions to the tungsten tube at 300 V is higher than that at 200 V. On the other hand, the change of hydrogen retention with negative bias was different in the deposition condition. A part of hydrogen and argon impinging to the target is considered to be reflected and implanted into the growing surface of the tungsten deposit. These reflected particles are considered to have relatively-high energy as compared with ions which impinge to the growing surface of the tungsten deposit with the sheath potential although its energy is reduced by the collision with neutral molecules

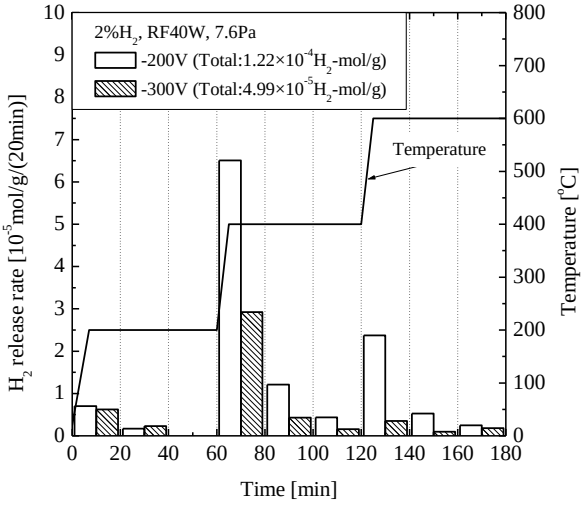

Fig.6 Hydrogen release behavior from the tungsten deposit formed in Ex.1 and Ex.2.

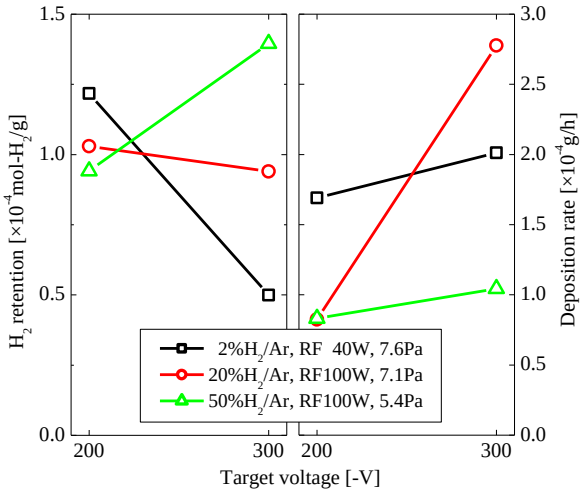

Fig.7 The dependence of target bias on hydrogen retention and deposition rate for three deposition conditions.

between the target and the substrate. Therefore, the bias of the target is considered to be one parameter that affects on hydrogen retention in tungsten deposits forming by sputtering method. However, the result shown in Fig.6 suggests that other parameter also contributes to hydrogen retention. The present authors considered that the ratio of hydrogen flux to tungsten flux from the target to the growing surface, f_H/f_W contributes to hydrogen retention. The hydrogen flux reflected from the tungsten target was estimated from the hydrogen ion flux and the fraction of backscattered particles, R_N [6]. The hydrogen ion flux was estimated from the target current and the ratio of hydrogen ion density to argon ion density. The tungsten flux was estimated from the deposition rate. The relationship between the ratio of hydrogen flux to tungsten flux and hydrogen retention as H/W is shown in Fig.8. The amount of tungsten deposited on the substrate was obtained from the deposition weight. Data from the parallel plate RF sputtering device [2,7] are also indicated. Although the tungsten deposit reported in [2] contained not only deuterium but also hydrogen, the reflected particle is assumed to be only deuterium because the working gas is pure deuterium. The expression obtained from fitting all of data is as follows:

$$\frac{H+D}{W} = 6.9\times10^{-3}\left(f_H/f_W\right)^{0.42} \quad , \qquad (1)$$

where $7.3 \le f_H/f_W \le 4780$, $65 \le E_n \le 652$ eV, $331 \le$ Temperature ≤ 429 K. E_n is the average energy of the reflected particles on the target. The value of E_n was estimated using the following formula [6]:

$$E_n(E_0) = E_0 \frac{R_E(E_0)}{R_N(E_0)} \quad , \qquad (2)$$

where E_0 is the energy of the ions impinging on the tungsten target, R_E is the energy reflection coefficient. The

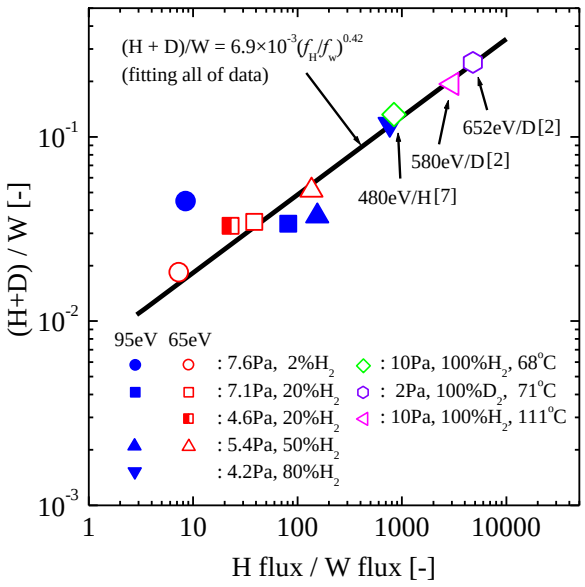

Fig.8 The dependence of the ratio of hydrogen flux to tungsten flux on hydrogen isotope retention.

obtained value, 0.42 is close to the value of 0.4±0.1 reported by De Temmerman and Doerner [3], where $2 \leq (f_H/f_W) \leq 500$, $60 \leq E_n \leq 280$eV, $293 \leq$ Temperature ≤ 600 K. The dependence of E_n on the retention was not observed in this work while they suggest in [3] that the retention is proportional to $E_n^{1.88}$. Strictly speaking, the impinging energy of reflected hydrogen to the growing surface of the tungsten deposit is abated by collisions with neutral molecules between the target to the substrate. That is to say, hydrogen retention depends on the working gas pressure as has been reported in [2]. Especially, the influence of the pressure would be large in the parallel plate RF sputtering device [7] because the distance from the target to the substrate is long. The impinging energy of hydrogen isotope to the growing surface in the parallel plate RF sputtering device might be comparable with that in the device used in this work. Hydrogen retention depends on temperature as has been reported in [3,4,8]. For the data summarized in Fig.8, these effects would be able to ignore because the temperatures are relatively low and the range is narrow.

4. Conclusions

The influence of deposition condition on hydrogen incorporation into tungsten deposits growing under hydrogen and argon mixed plasma was investigated by exposing a tungsten tube to the plasma. The erosion of the tungsten tube is mainly caused by the incident of argon ions. The tungsten deposit has a columnar structure. In order to remove the hydrogen incorporated into the tungsten deposit, a high temperature of 600 °C is necessary. While the tungsten deposition rate is promoted by the increase of negative target bias from 200 V to 300 V, the influence of the target bias on hydrogen retention is different in the deposition condition. Hydrogen concentration in the tungsten deposit increases with the ratio of the flux of the hydrogen reflecting from the tungsten target to tungsten deposition flux. The flux ratio of hydrogen and tungsten toward the growing surface of the tungsten deposit is an important parameter to evaluate hydrogen accumulation amounts.

Acknowledgments

This work was supported by a Grant-in Aid for Young Scientists (B) from the Japan Society for the Promotion of Science (KAKENHI21760691).

5. References

[1] K. Katayama, K. Imaoka *et al.*, Fusion Sci. Technol. **54**, 549 (2008).
[2] K. Katayama, S. Kasahara *et al.*, Fusion Eng. Des. **86**, 1702 (2011).
[3] G. De Temmerman and R.P. Doerner, J. Nucl. Mater. **389**, 479 (2009).
[4] V.Kh. Alimov, J. Roth *et al.*, J. Nucl. Mater. **399**, 225 (2010).
[5] T. Fujiki, K. Katayama *et al.*, Fusion Eng. Des. **85**, 1094 (2010).
[6] W. Eckstein, Calculated Sputtering, Reflection and Range Values, Report of theMax-Planck-Institute fr Plasmaphysik, IPP-Report 9/132, Garching, Germany (2002).
[7] S. Ishikawa, K. Katayama *et al.*, Fusion Eng. Des. **87**, 1390 (2012).
[8] K. Katayama, Y. Uchida *et al.*, J. Nucl. Mater. **390-391**, 689 (2009).

Hydrogen Storage Properties of Nanocrystalline Mg_2Ni Based Alloys Prepared by Ball-Milling

Yifu XIONG, Jingwen BA, Wuwen QING，Wenyong JING

China Academy of Engineering Physics, Mianyang, 621900, China

(Received: 15 May 2012 / Accepted: 26 November 2012)

Nanocrystalline hydrides are a new class of material in which outstanding hydrogen sorption may be obtained by proper engineering of the microstructure and surface. The nanocrystalline Mg_2Ni alloy is a promising hydrogen storage material. In the present work, nanocrystalline Mg_2Ni alloy powders with grain size of about 50 nm were prepared by high-energy ball-milling, and its phase, crystal structure and hydrogen storage properties were investigated by X-ray diffraction analysis, transmission electron microscopy and pressure-composition isotherms, respectively. The hydrogen storage characteristics of Mg_2Ni are also presented. Nanocrystalline Mg_2Ni can readily absorb hydrogen at temperature lower than 523 K. The reversible hydrogen capacity is up to 3.5 wt.%.

Keywords: Mg_2Ni, nanocrystalline, mechanical alloying, ball-milling, hydrogen storage

1. Introduction

Many metallic materials are known to form hydrides reversibly. Intermetallic Mg_2Ni with its high hydrogen capacity (up to 3.6 wt.%) is the prime candidates among hydrogen storage systems [1–5]. However, Mg_2Ni cannot absorb hydrogen under normal conditions (i.e. room temperature and atmospheric pressure), and the ability of hydrogenation appears in temperature range from 523–623 K with hydrogen pressure of 1.5–5 MPa. Moreover, even if Mg_2Ni is heated more than 523 K, it also needs to be activated before hydrogenation. The activation process usually involves a heating process at a high temperature (598 K) under a high hydrogen pressure (2 MPa). The activation process has to be carried out several times to obtain reproducible hydrogen absorption/desorption characteristics. Improvement of the hydrogenation conditions of Mg_2Ni is therefore essential to produce a suitable material for practical hydrogen storage [6–8].

The mechanical alloying (MA) may give various homogeneous composite particles. Since 1970, the MA process via the ball-milling (BM) technique has been used to prepare several dispersion-strengthened alloy powders. The application of the MA process has been expanded recently to produce several hydrogen storage metals using a method called the reactive ball-milling.

Metal hydrides are usually prepared by passing a flow of reactive hydrogen over the metallic material under high pressure and at temperatures usually above room temperature. In our study, the single-phase Mg_2NiH_4 alloy powders with grain size about 50nm has been synthesized by milling an equiatomic mixture of elemental Mg and Ni powders under hydrogen atmosphere. Mg_2Ni alloy powder has been followed by X-ray diffraction (XRD) and transmission electron microscopy (TEM), and the values of enthalpy and entropy changes for hydrogen absorption and desorption were evaluated from the pressure-composition isotherms on van't Hoff equation.

2. Experimental

In order to produce Mg_2Ni, a mixture of magnesium (99.95%, 150 mesh) and nickel (99.95%, 250 mesh), purified hydrogen and argon gas (H_2O and O_2, less than 20 ppm) has been used. The mixed powders were charged and sealed in a cylindrical stainless steel shell together with stainless steel rods in a laboratory high-energy mill SPEX 8000 (from SPEX Industries). The rod-to-powder weight ratio was controlled to be about 20 to 1.The inlet of the shell was connected to a rotary pump and evacuated for about 4 Pa. After evacuation, a flow of hydrogen gas was passed into the rod mill through a bellows pipe. Once the rod mill was filled with hydrogen at 0.25 MPa, the inlet of the vial was closed and the reactive rod-milling (RRM) process was carried out at ambient temperature by mounting the rod mill on a rotator at the rate of 2.0 s^{-1}. The RRM was stopped at selected intervals and a small amount of the rod-milled powder was taken out under argon atmosphere in a glove box.

3. Results and discussion

Mg_2Ni is difficult to prepare by conventional metallurgy because of the great difference in melting

author's e-mail: xiongyifu@yeah.net

temperature and vapor pressures of Mg and Ni. Mechanical alloying by ball-milling requires no melt process of the elements and yields the compound through a solid-state reaction. Although this ball-milling is quite a common technique, published results on ball-milled Mg and Ni powders have not yet been shown to produce single-phase [2,5].

Under the ball-milling conditions (high-energy mill and high ball-to-powder mass ratio) in the present work, Mg_2Ni alloy powder was formed directly. The ball-milling parameters were as follows: The ratio of rod and metallic powder was 20 to 1, rotational speed of ball-milling per minute was 0.2 s^{-1} and processing control reagent is stearic acid.

Fig. 1 shows the X-ray diffraction patterns of Mg_2Ni after mechanically ball-milling for 2 h and 50 h under hydrogen atmosphere. Fig. 1 (a) shows an intermediate stage of mechanical alloying reaction (after 2 h of ball-milling), and this diffraction pattern includes the peaks of the Mg_2Ni compound, Mg and Ni. After milling for 50 h, the diffraction peaks of Mg_2NiH_4 become broader and none of the peaks corresponding to MgH_2 and NiH_2 are seen. It is worth noting that the broadness of these peaks can be attributed to the formation of Mg_2NiH_4 solid solution powder, as shown in Fig. 1 (b). We should emphasize that this solid solution phase has not changed to any other phase, even after milling for as long as 50 hours.

The size of nanocrystalline Mg_2Ni alloy was calculated by Scherrer formula as follows:

$$D = K\lambda/\beta_{1/2}\cos\theta, \quad (1)$$

where D is the size of nanocrystalline, K is Scherrer constant (0.89), λ is the wavelength of CuKα X-rays (0.15405 nm), $\beta_{1/2}$ is the width of half-height for diffraction peak (rad). Those of (101) and (105) of common Mg_2Ni alloy are 0.3062° and 0.2879°, respectively. In our work, those of (101) and (105) of nanocrystalline Mg_2Ni alloy were 0.3204° and 0.2950°, respectively. The size of nanocrystalline Mg_2Ni alloy was evaluated from XRD patterns to be about 50 nm.

Detailed TEM analyses were performed in order to understand the change in the fine structure of mechanically alloyed Mg_2NiH_4 particles during above-mentioned stages of milling (Fig. 2). The powder have large grains of about 50 nm diameter and the selected-area diffraction patterns (SADPs) taken at the center of this micrograph shows sharp rings coexisting with spot patterns of nanocrystalline Mg_2Ni alloy powder in Fig. 2 (c).

Figs. 3 and 4 show pressure-composition isotherms of nanocrystalline Mg_2Ni prepared with 50 h of ball-milling. The absorption/desorption temperature was in a range from 473 K to 623 K, and the nanocrystalline Mg_2Ni-H_2 system has obvious and wide plateau region. Reversible hydrogen capacity amounts to 3.5 wt.% within the

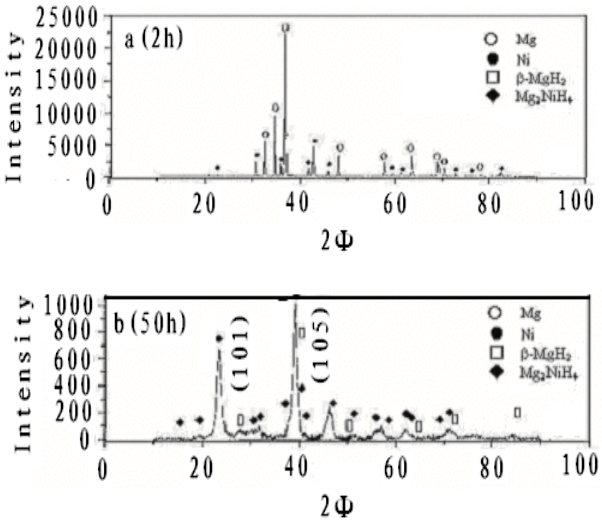

Fig. 1 XRD patterns of Mg-Ni alloys prepared by ball-milling for 2 h and 50 h.

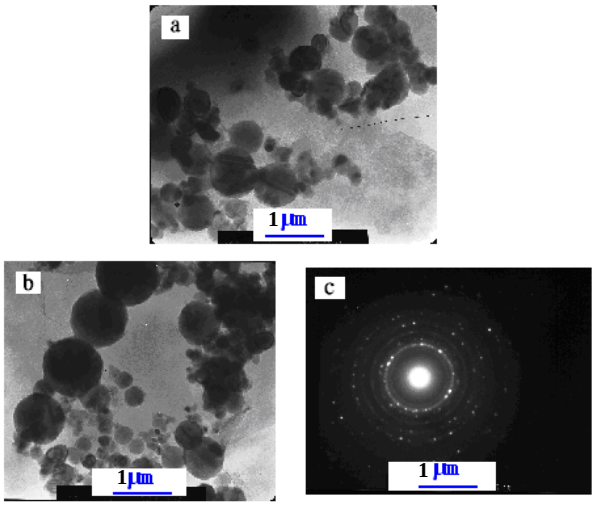

Fig. 2 TEM images of Mg-Ni alloys prepared by ball-milling under different conditions (a-2h, 120 K; b-50h, 150 K; c-electron diffraction pattern n (50h)).

applied hydrogenation time, and the capacity agreed with the literature [5]. The amount of absorbed hydrogen is usually 3.0–3.45 wt.% in the reversible hydrogenation cycles as reported in [5, 6]. The hydrogenation of the high-temperature phase of Mg_2NiH_4 is apparently much easier than for the low-temperature phase. The low-temperature phase of Mg_2NiH_4 is very difficult to obtain by the direct hydrogenation under moderate pressure conditions. The plateau pressures difference between absorption and desorption at the same temperature was observed (Fig. 5). The phenomenon was referred to hysteresis (its represents by hysteresis factor H_f), H_f increases with temperature. The hysteresis originates duo to the presence of transformation strains during both hydride formation and decomposition.

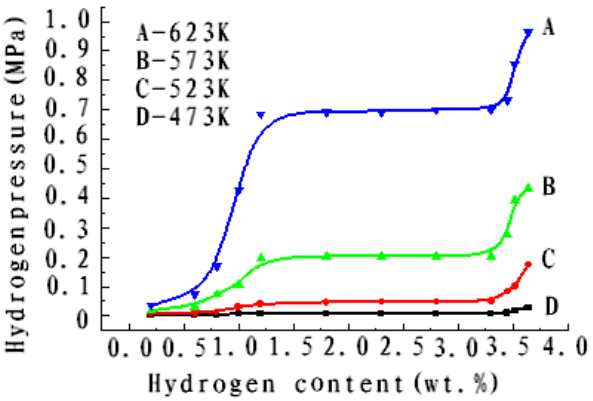

Fig. 3 Pressure-composition isotherms of hydrogen absorption for nanocrystalline Mg_2Ni alloy.

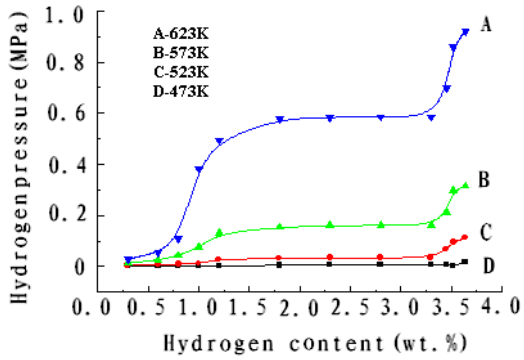

Fig. 4 Pressure-composition isotherms of hydrogen desorption for nanocrystalline Mg_2Ni alloy.

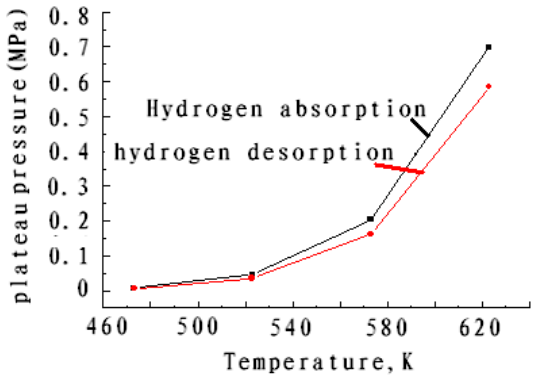

Fig. 5 The relationship between plateau pressure and temperature for nanocrystalline Mg_2Ni alloy.

According to van't Hoff equation, the relationship between temperature and hydrogen equilibrium pressure can be expressed as

$$\log(P_{H_2}) = \frac{-\Delta H^{\Theta}}{RT} + \frac{\Delta S^{\Theta}}{R}, \quad (1)$$

where ΔH^{Θ} is the standard enthalpy changes ($J \cdot mol^{-1}$) of hydriding reaction, ΔS^{Θ} is the standard entropy changes ($J \cdot mol^{-1} \cdot K^{-1}$) of the reaction, R is the gas constant, T is the given measurement temperature, and P_{H2} is the equilibrium hydrogen pressure.

The van't Hoff plots of the nanocrystalline Mg_2Ni alloy ($\log(P_{H2})$ versus $1/T$) were shown in Fig. 6. The best–fitting equations for ΔH^{Θ} and ΔS^{Θ} are given by hydrogen absorption process:

$$\log(P / 0.1\ \text{MPa}) = -3843/T + 7.012, \quad (2)$$

and by hydrogen desorption process:

$$\log(P / 0.1\ \text{MPa}) = -3992/T + 7.173. \quad (3)$$

The values of enthalpy and entropy changes for hydrogen absorption are $-73.58\ kJ \cdot mol^{-1}$ and $-134.26\ J \cdot mol^{-1} \cdot K^{-1}$, and those for hydrogen desorption are $76.44\ kJ \cdot mol^{-1}$ and $137.34\ J \cdot mol^{-1} \cdot K^{-1}$, respectively. The results agreed well with the literature [8].

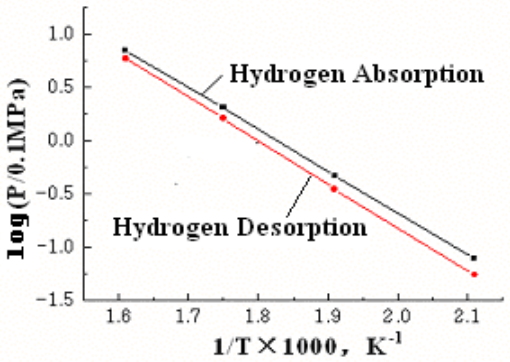

Fig. 6 Temperature dependence of plateau for nanocrystalline Mg_2Ni alloy.

Hydrogen absorption properties for ball-milled nanocrystalline Mg_2Ni alloy were better than those for conventional Mg_2Ni alloy. The as-produced powder readily absorbs hydrogen with no activation, and the final hydrogen content was found to be about 3.5 wt.% after the first hydrogenation cycle at 573 K (Fig. 7). In successive cycles, the absorption kinetics of Mg_2Ni prepared was reproducible and about four times faster than that of conventional Mg_2Ni. The results imply that the nanocrystalline Mg_2Ni alloys would be a promising hydrogen storage material.

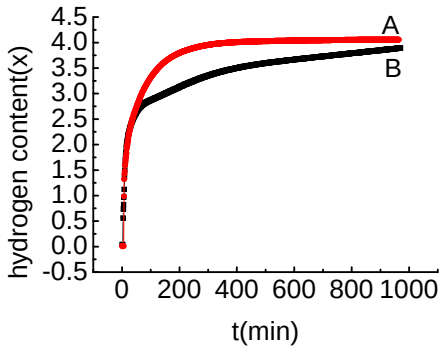

Fig.7 Absorption rate of hydrogen at 573K A-nanocrystalline Mg_2Ni alloy (50h) and B- conventional Mg_2Ni alloy

4. Conclusions

The Mg_2Ni alloys were prepared by ball-milling, which was composed of nanoparticles with grain size of about 50 nm. The structures and the hydriding behavior of Mg_2Ni prepared were studied. The absorption and desorption thermodynamic properties of Mg_2Ni alloys were improved by a ball-milling method. The reversible hydrogen capacity was found to be to 3.5 wt.%. The values of the enthalpy and the entropy for hydrogen absorption are −73.58 $kJ \cdot mol^{-1}$ and −134.26 $J \cdot mol^{-1} \cdot K^{-1}$, and those for hydrogen desorption are 76.44 $kJ \cdot mol^{-1}$ and 137.34 $J \cdot mol^{-1} \cdot K^{-1}$, respectively. The nanocrystalline Mg_2Ni alloy will be a promising hydrogen storage material for hydrogen energy and fuel cell systems.

References:

[1] L. Zaluski et al., J. Alloys Compd., **217**, 245 (1995).
[2] S. Orimo et al., J. Alloys Compd., **232**, L16 (1996).
[3] L. E. A. Berlouis et al., J. Alloys Compd., **305**, 82 (2000).
[4] L. Zaluski et al., J. Alloys Compd., **70**, 253 (1997).
[5] S. Orimo et al., J. Alloys Compd., **217**, 287 (1995).
[6] S. Orimo et al., J. Alloys Compd., **253**, 94 (1997).
[7] H. Imamura et al., J. Alloys Compd., **386**, 211 (2005).
[8] P. Selvam et. al, Int. J. Hydrogen Energy, **11**,169 (1986).

Hydrogen generation property on the surface of plasma sintered $Be_{12}Ti$

Kohei WADA[1)], Kenzo MUNAKATA[1)], Yusuke AKIMOTO[1)], Haruki TAKEDA[1)], Jae-Hwan KIM[2)], Daisuke WAKAI[2)],Kazuo YONEHARA[2)] and Masaru Nakamichi[2)]

[1)]*Faculty of engineering and resource science, Akita university, 1-1, Tegatagakuen-cho, Akita, 010-8502, Japan*

[2)]*Fusion Research and Development Directorate, Japan Atomic Energy Agency, 2-166, Omotedate, Obuchi, Rokkasho, Kamikita, Aomori, 039-3212, Japan*

(Received: 9 May 2012 / Accepted: 5 December 2012)

Central and peripheral parts of a plasma sintered titanium beryllide disc were exposed to water vapor at temperature rising up to 1273 K. Hydrogen generation on and oxidation properties of the titanium beryllide ~~surfaces~~ were investigated. According to electron probe microanalysis, the titanium beryllide parts were characterized by different surface area fractions of Be, $Be_{12}Ti$, $Be_{17}Ti_2$, and Be_2Ti phases, and the central part contained lower fraction of Be phase than the peripheral part. H_2 gas generation rate in the central part was found to be lower than that in the peripheral part, and this difference can be attributed to larger fraction of the Be phase. Secondary electron microscopy and X-ray diffraction revealed that the parts of the plasma sintered $Be_{12}Ti$ disc had higher oxidation resistance than metallic beryllium.

Keywords: beryllide, plasma sintering, hydrogen generation, oxidation, gas chromatograhphy

1. Introduction

Metallic beryllium has been considered as a leading candidate for a neutron multiplier in water- or helium-cooled solid breeder blankets in future fusion reactors. In these blankets, beryllium will be subjected to a high neutron flux and located in high temperature environment. However, beryllium is highly reactive with water vapor at temperatures above 873 K, producing hydrogen that may lead to accidents due to H_2 gas explosion.

$$Be + H_2O = BeO + H_2 \quad (1)$$

Titanium beryllides such as $Be_{12}Ti$ have many advantages over beryllium from the perspectives of higher melting point, lower chemical reactivity, lower swelling, etc. Therefore, $Be_{12}Ti$ material has attracted attention as an alternative of beryllium, and could be used as an advanced neutron multiplier in the fusion reactor blankets [1].

Titanium beryllides have been fabricated by various methods. Nakamichi et al. [2, 3] have developed new synthesis process of $Be_{12}Ti$ material called “plasma-sintering method”. This process consists of loading raw material powder in the punch and the die unit, direct current pulse plasma generation to activate the surface of powder particles, and uniaxial pressing to enhance the sinterability [2,3].

In this study, we report results on H_2 generation caused by interaction of water vapor with titanium beryllides. Besides, oxidation resistance of the titanium beryllides with slightly different phase compositions was studied.

2. Experimental

Be and Ti powders, characterized by average grain sizes of 27 μm and 28 μm, respectively, were mixed for 60 min by using a mortar grinder RM200 (Retsch, Germany). The mixed ratio was adjusted to the stoichiometric composition of $Be_{12}Ti$ (69.3:30.7 wt.%). The mixed powder was placed in a plasma electrical discharge sintering device KE-PAS III (manufactured by KAKEN Co. Ltd), and $Be_{12}Ti$ disc, 20

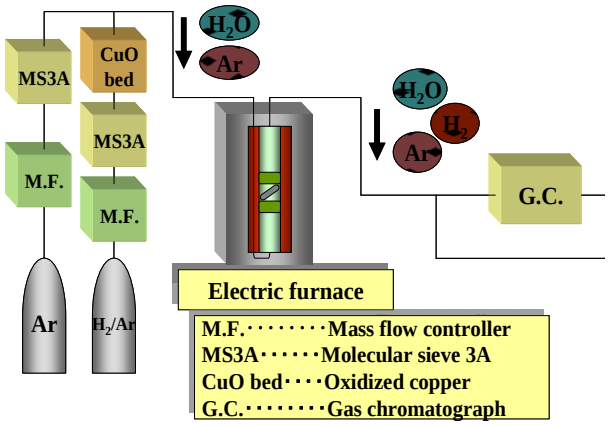

Fig. 1 Schematic flow diagram of test apparatus.

authors e-mail : kohei.wada1986@gmail.com

mm in diameter and 5 mm in thickness, was synthesized by sintering for 40 min at a temperature of 1273 K and a pressure of 50 MPa. Then the disc was cut into two small samples to separate central and peripheral parts of the disc for comparative analyses. The surface area of the central parts was 83 mm^2 while that of the peripheral part was 128 mm^2. The samples were mechanically polished with a #2400 SiC abrasive paper.

The surface morphology of the $Be_{12}Ti$ samples was examined by secondary electron microscopy (SEM) combined with the electron probe microanalysis (EPMA) in a SEM/EPMA instrument JXA-8230 (JEOL Co.)

Schematic flow diagram of apparatus for a measurement of the hydrogen generation rate is shown in Fig. 1. The $Be_{12}Ti$ sample was wrapped by platinum mesh to avoid direct contact with the test tube, and then placed between silica wools. 10,000 ppm H_2O/Ar gas was generated by passing 10,000 ppm H_2 /Ar gas through copper oxide bed heated at 623 K, and then introduced to the test tube with a flow rate of 300 cm^3/min. An electric furnace was used to heat the test tube at a heating rate of 5 K/min, and a temperature inside the tube was raised up to 1273 K. This temperature was kept constant until hydrogen generation terminated.

The concentrations of hydrogen in the outlet streams of the reactor were measured with a gas chromatograph GC-8A manufactured by SHIMADZU Co. The state of oxidized sample surface was characterized by X-ray diffraction (XRD) analysis with the Ultima IV instrument (RIGAKU Co.) and electron probe micro analysis (EPMA) with the SEM/EPMA JXA-8230 instrument (JEPL Co.).

3. Result and discussion

Figure 2 shows the SEM images using back-scattered electron for central and peripheral parts of the plasma sintered titanium beryllide disc prepared in this study. The results of EPMA analysis demonstrated that the titanium beryllide is composed of four different phases such as Be, $Be_{12}Ti$, $Be_{17}Ti_2$, and Be_2Ti with different fractions. Percentages of the surface areas of the phases for each part of the disc, evaluated with the use of an image analyzer, are shown in Table 1. It is evident that the central part is composed mainly of $Be_{12}Ti$ phase with relatively large fraction of $Be_{17}Ti_2$ phase. Additionally, smaller fractions of Be and $Be_{12}Ti$ phases were observed. Note that phase compositions for the central and peripheral parts were slightly different. This observation is in good agreement with results obtained by Kim et al. [4] proposing that the phase difference for the central and peripheral parts can be explained by a temperature gradient maintained during the sintering process.

Experiments on generation of H_2 gas on the surfaces of the plasma sintered titanium beryllides were carried out to investigate the effect of the phase composition. Fig. 3 shows changes in hydrogen concentrations in the outlet stream of reactor with central and peripheral part of the plasma sintered titanium beryllide disc exposed to a 10,000 ppm H_2O/Ar gas. In case of the central part, generation of hydrogen started at a temperature of 673 K and continued for about 27 h. The total amount of hydrogen generated for 24 h is 1.2×10^{-4} mol/cm^2. For the peripheral part, however, the hydrogen generation started at a temperature above 423 K and continued for 40 hr. The total amount of hydrogen generated on the peripheral part for 24 h is 3.0×10^{-4} mol/cm^2. As mentioned above, the samples used in this work included the phase of Be_2Ti (Table 1) that is known to

Table 1 Surface area fractions (in %) of phases constituent central and peripheral parts of titanium beryllide disc.

	Beryllide (a) (%)	Beryllide (b) (%)
Be	0.96	2.53
$Be_{12}Ti$	89.40	90.8
$Be_{17}Ti_2$	8.16	5.87
Be_2Ti	1.88	1.25

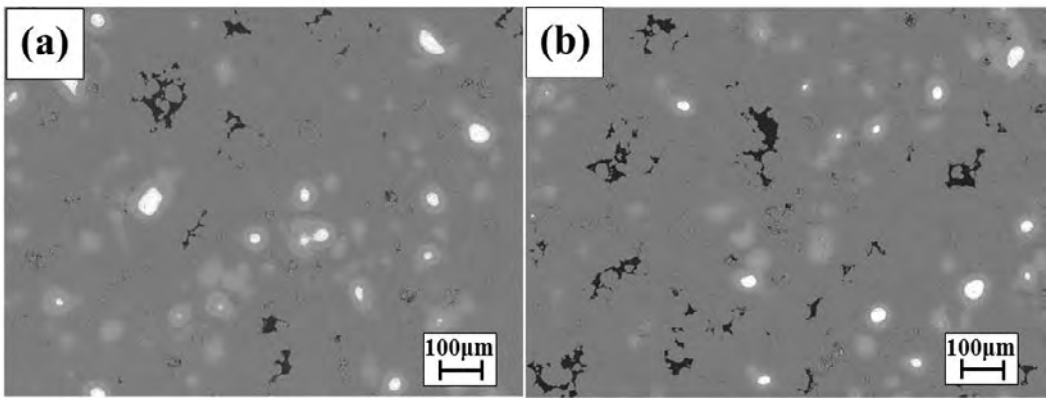

Fig. 2 SEM images of central part (a) and peripheral part (b) of plasma sintered titanium beryllide disc.

have capability of hydrogen storage [5]. The existence of this phase might affect the hydrogen generation of the samples, while the fractions of the phase in the both samples were almost the same. The $Be_{17}Ti_2$ phase could also affect the hydrogen generation, but this phase is probably stable and tolerant to oxidation as much as the $Be_{12}Ti$ phase [Kim paper Numat]. Thus, it is thought that the sample with larger fraction of Be phase generates more amounts of H_2, since Be is known as highly reactive with oxygen [6] and water vapor [7]. As shown in the EPMA analysis (Table 1), the edge sample was composed of larger fraction of Be, which affect the amount of generated H_2 gas. This agrees with the report by Anderl et al. [8], demonstrating that the rate of the reaction between beryllium surface and water vapor is associated with differences in the specific surface areas for the tested materials.

The weight gain for the $Be_{12}Ti$ and beryllium samples indicate that the center sample part increased by 3.6 % of the initial weight for the central part of the titanium beryllide and 4.7 % for the peripheral part. However, as reported in our previous study [9], for metallic beryllium used as a reference material, the weight gain was 50 % of the initial weight. Data on the weight gain and amount of generated hydrogen for the titanium beryllide parts indicate that the peripheral part is more oxidized.

SEM observation and XRD analysis were performed to investigate the surface state of the two samples after exposure to 10,000 ppm H_2O/Ar gas. Fig. 4 shows the SEM images of central (a) and peripheral (b) parts of the plasma sintered titanium beryllide disc and metallic beryllium (c) after exposure to water vapor. The Be sample (shown in Fig. 4 (c)) was used in our previous work and the surface of the sample was observed using the SEM/EPMA apparatus [9]. The result of the SEM analysis clarified that after oxidation the surfaces of the titanium beryllide parts are covered with dense and protective oxide scales (see Fig. 4 (a) and (b)). Gray and white areas in the SEM pictures correspond to BeO and TiO_2, respectively. Comparison of the oxidation behavior of $Be_{12}Ti$ and beryllium metal indicate that more protective BeO scales are present on the surface of the $Be_{12}Ti$ sample parts. In contrast, it could be stated that metallic Be possesses poor oxidation resistance due to cracked and fractured BeO scales present of the surface. Sato et al. [10] had demonstrated that BeO formed on the surface of metallic Be is affected by compressive stress caused by coherency of the lattice structures between the scale and the bulk metal, since the atomic distances in the BeO scale are smaller than those in the metallic Be substrate.

The results of the XRD analysis (Fig. 5) demonstrated that the intensity of peaks corresponding to BeO formed on the peripheral part are higher than those for the central part. This is in good agreement with the result of the weight gain

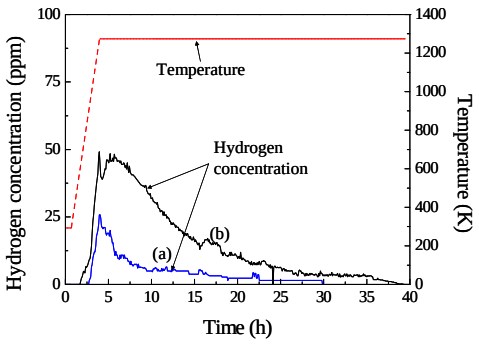

Fig. 3 Change in concentration of hydrogen in the outlet stream of reactor with central part (a) and peripheral part (b) of the plasma sintered titanium beryllide disc exposed to a 10 000 ppm H_2O/Ar gas.

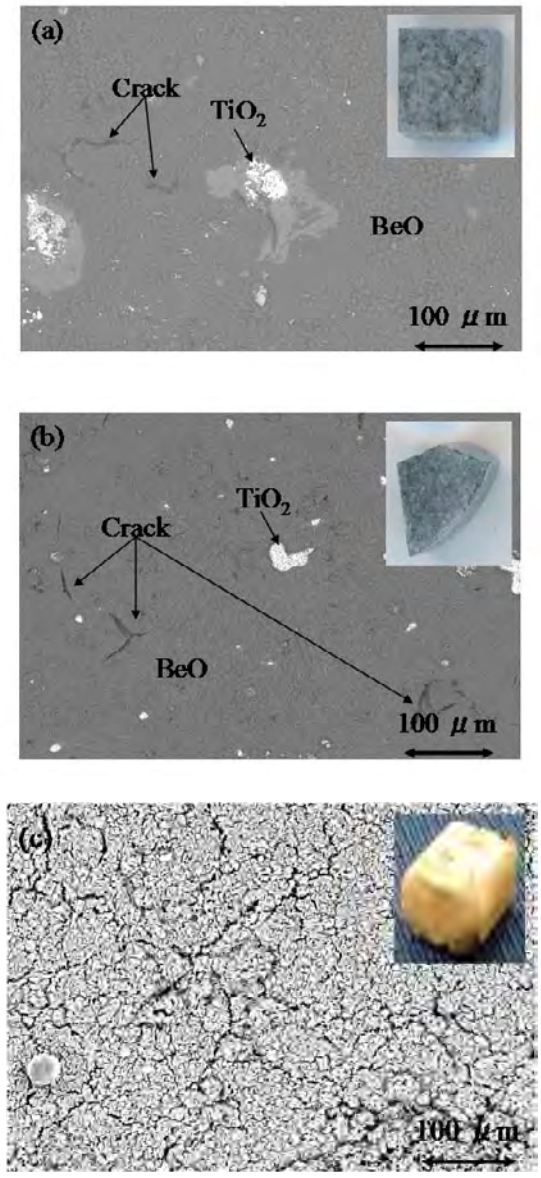

Fig. 4 SEM images of central (a) and peripheral (b) parts of the plasma sintered titanium beryllide disc and metallic beryllium [8] (c) after exposure to water vapor.

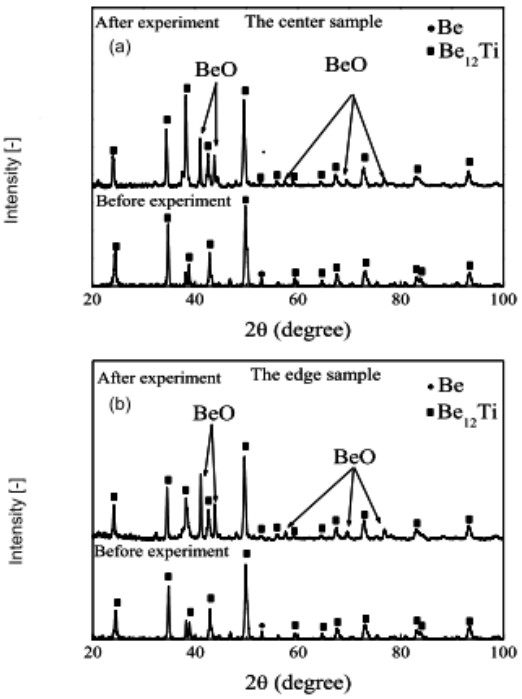

Fig. 5 XRD spectra of central (a) and peripheral (b) parts of the plasma sintered titanium beryllide disc after exposure to water vapor.

and H_2 gas generation. These results obviously suggest that the oxidation resistance for the central sample part of the plasma sintered beryllide disc is higher than that for the peripheral part. Therefore, as mentioned above, larger fraction of highly reactive Be in the titanium beryllide leads (i) to increase in the amount of H_2 gas generated under exposure to water vapor and (ii) to poor oxidation resistance of the surface.

4. Conclusion

Center and peripheral parts (with different surface area fractions of Be, $Be_{12}Ti$, $Be_{17}Ti_2$, and Be_2Ti phases) were cut and extracted from a plasma sintered $Be_{12}Ti$ disk in order to investigate the effect of the surface area fraction difference on not only the H_2 gas generation under exposure to water vapor but also oxidation property. It has been shown that the amount of hydrogen generated for the surface of the central part of the titanium beryllide disc was smaller than that for the peripheral part. This difference can be explained by lower fraction of the Be phase surface area on the surface of the central part in comparison with that for the peripheral part. The oxidation property for both parts did not exhibit big difference, while both titanium beryllides parts demonstrated higher oxidation resistance compared to metallic beryllium.

5. Acknowledgments

This work was supported by Japan Atomic Energy Agency under the Joint Work contract 23K131, as a part of Border Approach activities.

6. References

[1] H. Kawamura, H. Takahashi, N. Yoshida, V. Shestakov, Y. Ito, M. Uchida, H. Yamada, M. Nakamichi and E. Ishitsuka, Fusion Eng. Des. **61-62**, 391-397 (2002).

[2] M. Nakamichi, K. Yonehara and D. Wakai, Fusion Eng. Des. **86**, 2262-2264 (2011).

[3] M. Nakamichi and K. Yonehara, J. Nucl. Mater. **417**, 765-768 (2011).

[4] J.-H. Kim, K. Yonehara and M. Nakamichi, Thermal Stability of Plasma Sintered Beryllides, Proc. 15th Int. Conf. on Fusion Reactor Materials, Charleston, USA, October 2011 (submitted to J. Nucl. Mater.).

[5] A. J. Maeland and G. G. Libowits, J. Less Common Met. **89, 197-200** (1983).

[6] D. W. Aylmore, S. J. Gregg and W. B. Jepson, J. Nucl. Mater. **2, No.2**, 169-175 (1960).

[7] D. W. Aylmore, S. J. Gregg and W. B. Jepson, J. Nucl. Mater. **3, No.2**, 190-200 (1961).

[8] R. A. Anderl, K. A. McCarty, M. A. Oates, D. A. Petti, R. J. Pawelko and G. R. Smolik, J. Nucl. Mater. **258-263**, 750-756 (1998).

[9] K K. Wada, K. Munakata, M. Nakamichi, J. H. Kim, K. Yonehara and D. Wakai, Oxidation Resistance of $Be_{12}Ti$ Fabricated by Plasma-Sintering, Proc. 15th Int. Conf. on Fusion Reactor Materials, Charleston, USA, October 2011 (submitted to J. Nucl. Mater.).

[10] Y. Sato, M. Uchida, H. Kawamura, High Temperature Oxidation Behavior of Titanium Beryllide in Air, Proc. 6th IEA Int. Workshop on Beryllium Technology for Fusion, Miyazaki, Japan, December 2003, JAERI-Conf 2004-006, p. 203.

Journal of Plasma and Fusion Research SERIES
(JPFR SERIES) : ISSN 1883-9630

Link (URL): http://www.jspf.or.jp/JPFRS/index_vol10.html